UNIVERSIDAD POLITÉCNICA DE MADRID
Escuela Técnica Superior de Arquitectura

Capacidad de carga a la hienda de uniones con clavijas cargadas perpendicularmente a la fibra en madera de frondosas.

Análisis experimental y numérico bajo el enfoque de la mecánica de fractura

TESIS DOCTORAL

Presentada para optar al título de Doctor por:

José Luis Gómez Royuela
Arquitecto

Madrid, 2024

UNIVERSIDAD POLITÉCNICA DE MADRID
ESCUELA TÉCNICA SUPERIOR DE ARQUITECTURA
DE MADRID

Doctorado en Estructuras de la Edificación

Capacidad de carga a la hienda de uniones con clavijas cargadas perpendicularmente a la fibra en madera de frondosas.

Análisis experimental y numérico bajo el enfoque de la mecánica de fractura

TESIS DOCTORAL

Presentada para optar al título de Doctor por:

José Luis Gómez Royuela
Arquitecto

Bajo la dirección de:
Dra. Mª Almudena Majano Majano
Dr. José Manuel Cardoso Xavier

Madrid, 2024

Título: Capacidad de carga a la hienda de uniones con clavijas cargadas perpendicularmente a la fibra en madera de frondosas. Análisis experimental y numérico bajo el enfoque de la mecánica de fractura

Autor: José Luis Gómez Royuela

Programa de Doctorado: Estructuras de la Edificación

Dirección de tesis:

Dra. Mª Almudena Majano Majano, Profesora Titular de Universidad, Universidad Politécnica de Madrid

Dr. José Manuel Cardoso Xavier, Associate Professor, Universidade NOVA de Lisboa

Tribunal de tesis:

Presidente: _____

Vocal 1: _____

Vocal 2: _____

Vocal 3: _____

Vocal secretario: _____

Fecha de defensa:

Los trabajos numéricos han sido desarrollados en el marco del proyecto de I+D+i PID2020-112954RAI00, financiado por MCIN/AEI/10.13039/501100011033. Asimismo, parte de los trabajos de la tesis fueron llevados a cabo durante una estancia científica de corta duración (3 meses) en la Facultad de Ingeniería Mecánica de la Universidad de Oporto financiada por el Programa Propio de I+D+i 2021 de la Universidad Politécnica de Madrid.

A mi novia y a mis abuelos

Agradecimientos

A lo largo de mi vida he tenido el inmenso privilegio de cruzarme con personas extraordinarias, tanto en el ámbito personal, como profesional y académico. Cada una de ellas me ha aportado algo único que ha impulsado mi crecimiento y mejora continua. Sus aportes han contribuido, de una manera u otra, a que llegue hasta aquí y sin ellos esta tesis no habría sido posible. Por eso, quiero aprovechar estas líneas para expresar mi más sincero agradecimiento a todas aquellas personas que una vez se fijaron en mí, decidiendo regalarme un pequeño, pero muy valioso, pedacito de su tiempo y que de manera directa o indirecta han participado en el desarrollo de esta tesis.

En primer lugar, y de manera muy especial, quiero expresar mi más profundo agradecimiento a mi directora de tesis, la profesora Almudena Majano, por su entusiasmo, apoyo constante, disponibilidad, exquisito rigor, paciencia y dedicación inagotable. Aprecio especialmente la oportunidad que me brindó en la primavera del año 2017 para iniciar un nuevo y emocionante camino en la investigación y la docencia, introduciéndome en el fascinante mundo de las estructuras de madera. A lo largo de este camino, no han faltado contratiempos para llevar a buen puerto este trabajo, algunos especialmente difíciles. Aun así, he tenido la fortuna de poder inclinar la balanza gracias a los buenos momentos disfrutados. Si algo me gustaría agradecerle es, sobre todo, su cariño y amistad en los momentos más complicados.

Así mismo, quisiera destacar mi agradecimiento al codirector de esta tesis, el profesor José Xavier, por su enorme paciencia, disponibilidad, dedicación y la gran amabilidad con la que siempre me ha ayudado a lo largo de esta etapa. He tenido la suerte de disfrutar junto a él aprendiendo las virtudes de la técnica de correlación de imágenes digitales. En especial, quiero agradecerle la hospitalidad recibida durante mi estancia de investigación en la Universidad de Oporto, ciudad de extraordinario encanto que me cautivó y a la que reservo, con mucho cariño, un rinconcito de mi corazón. Si algo tengo que destacar es su bondad en los momentos personales más duros.

Con un cariño muy especial quiero mostrar mi gratitud al profesor Marcelo de Moura, tutor de mi estancia en la Faculdade de Engenharia da Universidade do Porto (FEUP) por su amabilidad, disponibilidad y hospitalidad, con quién he tenido la suerte de aprender los fundamentos de la mecánica de fractura. Del mismo modo, quiero agradecer al profesor Raul Moreira su amabilidad, atención y todo el tiempo que dedicó a enseñarme los conceptos esenciales para modelar la fractura en programas de elementos finitos durante mi estancia en la FEUP.

Mi agradecimiento también muy especial a mis compañeros y amigos de la Escuela de Arquitectura de Valladolid (ETSAVA), Alfonso Basterra y Gamaliel López, por enseñarme el camino del rigor profesional y despertar en mí la curiosidad científica.

En mi nueva etapa en la Escuela de Arquitectura de Madrid (ETSAM) he tenido la fortuna de conocer a personas maravillosas y que, sin lugar a duda, debo mi gratitud. Empezando por los profesores María Dolores García y Mariano Vázquez por su cariñosa acogida, apoyo constante y preocupación en los momentos complicados. A los profesores José Ignacio Hernando y Pedro Dávila por la gran amabilidad con la que siempre me han tratado, sus consejos y los buenos ratos que me han regalado en Estructuras II, sin olvidar las partidas de ping-pong. Por último, no me puedo olvidar de mi compañero el profesor

Antonio Lara, a quien debo tantas cosas que no se pueden expresar con palabras. Por encima de todo, quisiera subrayar su amabilidad, disposición, vitalidad y el entusiasmo que pone en cada proyecto que inicia. Son incontables los buenos momentos que me ha regalado en lo personal y profesional, destacando la oportunidad de viajar a Lugo para colaborar en la ejecución y montaje de la PEMADE gridshell. Allí vivimos grandes momentos y comenzó el inicio de una gran relación. En esta breve etapa tuve la suerte de conocer al amable personal de la Plataforma de Ingeniería de la Madera Estructural (PEMADE), resaltando las fructíferas conversaciones con el profesor Manuel Guaita sobre el potencial y futuro de la madera.

Quiero expresar también mi agradecimiento a los integrantes del Grupo de Investigación Construcción con Madera, en especial, a Francisco Arriaga, Miguel Esteban y Guillermo Íñiguez por su cálida acogida en el mismo y la simpatía con la que siempre me han tratado.

Al cerrar este capítulo de mi vida no me puedo olvidar de mis padres y mi hermana. Ellos han sido las verdaderas estrellas que han guiado siempre mi camino y quiero darles las gracias por inculcarme el valor del esfuerzo y la superación constante. A mis sobrinos Diego, Julia y Lucas por ser una fuente inesperada de alegría, fuerza y energía. Sus risas, ocurrencias y abrazos me han llenado de vitalidad en el último tramo de esta etapa. Gracias a ellos y a cada minuto que hemos pasado jugando juntos, he recordado que la verdadera magia de la vida se encuentra en esos pequeños momentos de felicidad que van más allá del trabajo o la investigación. Sin olvidarme, por supuesto, del resto de mi familia y amigos por haberme acompañado durante este desafío.

Mi más profundo amor y gratitud a mi novia Miriam, pilar fundamental de mi vida, por su inagotable bondad y generosidad. Sin su apoyo incondicional nunca hubiera conseguido reunir las fuerzas necesarias para terminar esta tesis doctoral. Además, aprovecho para pedirle mis más sinceras disculpas porque este viaje nos ha separado en muchas ocasiones y cada minuto dedicado a esta tesis ha sido un minuto que no hemos podido disfrutar juntos.

Por último, quiero rendir un emotivo homenaje a mis abuelos, Pepe y Visi, quienes, aunque ya no están, siempre han sido y serán mi modelo a seguir. Su cariño, sabiduría y alegría han sido un regalo invaluable y siempre los llevaré en lo más profundo de mi corazón.

Abstract

Mechanical dowel connections are a widely used solution in timber structures due to their ease of assembly and disassembly, rapid execution, and high load-bearing capacity. Their potential to develop ductile failure behaviour makes them particularly interesting. However, under certain conditions, stress concentrations perpendicular to the grain and shear stresses can arise, potentially leading to brittle failure by splitting, especially in dowel connections loaded at an angle to the grain.

Splitting failure in these types of connections is directly related to the fracture processes of the material. However, there is no general consensus on how to adequately address this issue, either in terms of analytical expressions for estimating their load-bearing capacity or in terms of characterising the fracture properties of the material. Eurocode 5 provides a very simplified expression, based on fracture mechanics, to determine the splitting capacity of dowel joints loaded at an angle to the grain. However, this expression does not consider the influence of many geometrical parameters of the connection, material properties, and is limited in its applicability to softwood.

The primary objective of this thesis is to contribute to overcome these limitations in the case of European beech (*Fagus sylvatica* L.) beams loaded perpendicularly to the grain using dowel connections, by adopting a non-linear fracture mechanics approach. To this end, both experimental work and numerical simulations are carried out to investigate the influence of different parameters related to the connection geometry. In particular, the impact of using one or two dowels to transfer the load to the beam, the spacing between the dowels in the longitudinal direction of the beam, and their proximity to the supports are analysed. Additionally, the influence of beam slenderness and the effect of arranging a second connection symmetrically with respect to the centre of the beam are also studied.

In the numerical simulations carried out to reproduce the splitting failure in beams, cohesive zone models are employed to simulate both damage initiation and crack propagation. These models require the implementation of the elastic and fracture properties of the material, which have been obtained experimentally in this thesis. The twelve elastic constants that define the orthotropic compliance matrix of the European beech are determined by compression tests with strain measurements using digital image correlation techniques. Fracture properties in loading modes I and II are obtained from DCB (*Double Cantilever Beam*) and ENF (*End-Notched Flexure*) tests, respectively. The cohesive laws describing the fracture behaviour of the material are obtained by applying the direct method using the CBBM (*Crack Based Beam Method*) procedure to determine the fracture energy. This method has the advantage of not requiring crack growth measurement during the test, which is particularly beneficial for wood. The numerical results are compared with the experimental results and with those obtained from the formula included in Eurocode 5 and two other analytical reference models for the estimation of the splitting capacity.

Based on the work carried out, the influence of the studied parameters on the splitting capacity is demonstrated, highlighting the need to update the current code expression. The comparison between the experimental, numerical and theoretical failure loads reveals that the analytical models tend to estimate splitting capacity conservatively, particularly the expression included in Eurocode 5.

Finally, the proposed numerical model proves to be an effective tool to reliably predict the splitting capacity of European beech beams with dowel connections and different configurations.

This doctoral thesis is presented as a compendium of publications. Its content is articulated through four contributions made by the author and published in indexed scientific journals (JCR Q1).

Resumen

Las uniones mecánicas con clavijas son una solución ampliamente utilizada en estructuras de madera debido a su facilidad de montaje y desmontaje, rapidez de ejecución y elevada capacidad de carga. La posibilidad de desarrollar un comportamiento de fallo dúctil las hace especialmente interesantes. Sin embargo, bajo determinadas condiciones, se generan concentraciones de tensiones rasantes y perpendiculares a la fibra que pueden provocar un fallo frágil por hienda, como en el caso de las uniones con clavijas cargadas con ángulo respecto de la fibra.

El fallo por hienda en este tipo de uniones está directamente relacionado con los procesos de fractura del material. Sin embargo, no existe un consenso generalizado sobre cómo abordar adecuadamente el problema, tanto en lo referente a las expresiones analíticas para estimar su capacidad de carga, como a nivel de caracterización de las propiedades de fractura del material. El Eurocódigo 5 ofrece una expresión muy simplificada, basada en la mecánica de la fractura, para estimar la capacidad de carga frente a la hienda. Sin embargo, no considera la influencia de muchos parámetros geométricos de la conexión, de las propiedades del material, y restringe su aplicabilidad a las especies coníferas.

El objetivo general de la presente tesis es contribuir a superar dichas limitaciones, para el caso de vigas de madera de haya europea (*Fagus sylvatica* L.) cargadas perpendicularmente a la fibra mediante conexiones con pasadores, bajo el enfoque de la mecánica de fractura no lineal. Con este fin, se realizan trabajos experimentales y simulaciones numéricas para investigar la influencia de diferentes parámetros relacionados con la geometría de la conexión. En particular, se analiza el efecto de la colocación de uno y dos pasadores para transferir la carga a la viga, la separación entre los pasadores en la dirección longitudinal de la viga y su proximidad a los apoyos. Asimismo, se estudia la influencia de la esbeltez de la viga y el efecto de disponer una segunda conexión de manera simétrica respecto al centro de la viga.

En las simulaciones numéricas se emplean modelos de zona cohesiva, que permiten simular el inicio y la propagación de la fisura. Estos modelos requieren la implementación de las propiedades elásticas y de fractura del material, las cuales han sido obtenidas experimentalmente en esta tesis. Las constantes de elasticidad se determinan mediante ensayos de compresión con mediciones de deformaciones utilizando técnicas de correlación de imágenes digitales. Por su parte, las propiedades de fractura en los modos de carga I y II se obtienen a partir de ensayos DCB (*Double Cantilever Beam*) y ENF (*End-Notched Flexure*), respectivamente. Las leyes cohesivas que describen el comportamiento a fractura del material son obtenidas aplicando el método directo utilizando el procedimiento CBBM (*Crack Based Beam Method*) para obtener la energía de fractura. Los resultados numéricos se comparan con los experimentales y los obtenidos a partir de la expresión del Eurocódigo 5 y de otros dos modelos analíticos de referencia para la estimación de la capacidad de carga frente a la hienda.

En base a los trabajos realizados, se demuestra la influencia en la capacidad de carga a la hienda de los parámetros estudiados, sugiriendo la conveniencia de actualizar la expresión normativa vigente. La comparación entre las cargas de fallo experimentales, numéricas y teóricas revela que los modelos analíticos tienden a estimar de forma conservadora la capacidad de carga frente a la hienda, especialmente la expresión incluida en el Eurocódigo 5.

Por último, el modelo numérico propuesto demuestra ser una herramienta eficaz para predecir de manera fiable la capacidad de carga a la hienda de vigas de haya europea con uniones con pasadores y diferentes configuraciones.

La presente tesis doctoral se articula a través de cuatro contribuciones realizadas por el autor y publicadas en revistas científicas indexadas (JCR Q1).

Índice

Lista de Figuras

Lista de Tablas

Estructura de la Tesis

La presente tesis doctoral se presenta bajo la modalidad de *Compendio de publicaciones*, según el reglamento de la Universidad Politécnica de Madrid (UPM) aprobado por Consejo de Gobierno de 30 de noviembre de 2017.

La tesis doctoral se estructura en dos partes y dos anexos con los siguientes contenidos:

Parte I: se compone de seis capítulos en los que se ofrece una visión general del estado de la cuestión y una síntesis de los trabajos desarrollados. Puede entenderse como un resumen extendido de las cuatro publicaciones que componen la Parte II de esta tesis. En el Capítulo 1 se presenta una breve revisión de los conocimientos básicos del fallo por hienda en vigas cargadas perpendicularmente a la fibra mediante uniones con clavijas, incluyendo un resumen de los enfoques de diseño analíticos y numéricos basados en la mecánica de fractura. Este capítulo incluye una descripción del interés de la madera de *Fagus sylvatica* L. como material estructural. En el Capítulo 2 se establecen los objetivos generales y específicos que orientan el desarrollo de la tesis. En el Capítulo 3 se describe brevemente el método experimental y numérico aplicado a los diferentes trabajos. En el Capítulo 4 se presentan sintéticamente los principales resultados obtenidos en cada línea de trabajo que justifican la consecución de los objetivos, cuyas conclusiones finales se exponen en el Capítulo 5. Por último, el Capítulo 6 introduce propuestas de futuras líneas de investigación derivadas de la experiencia acumulada durante el desarrollo de la tesis. La literatura referenciada en esta Parte I se detalla en el correspondiente capítulo de Bibliografía.

Parte II: contiene el compendio de publicaciones del autor vinculadas con los objetivos de investigación planteados en la tesis doctoral. La Publicación I aborda la determinación experimental de las doce constantes de elasticidad que configuran la matriz de flexibilidad del haya europea permitiendo definir la matriz de rigidez en cualquier simulación numérica. En las Publicaciones II y III se presentan las principales propiedades de fractura del material en los modos I y II determinadas experimentalmente, validando numéricamente las leyes cohesivas del material bajo el enfoque de la mecánica de fractura no lineal. La Publicación IV abarca la investigación experimental y numérica de la influencia en la capacidad de carga frente a la hienda de cinco parámetros relacionados con la geometría de la conexión en vigas de haya europea cargadas perpendicularmente a la fibra mediante uniones con pasadores, aplicando el enfoque de la mecánica de fractura no lineal. Las cuatro publicaciones son artículos publicados en revistas científicas que figuran en los listados JCR o Scopus en posiciones Q1, cumpliendo así con los criterios de calidad exigidos según el reglamento de *Tesis por compendio* de la UPM.

Anexo A: ofrece un resumen de los fundamentos teóricos, incluyendo una visión general sobre las propiedades resistentes de la madera y de los criterios de fallo basados en tensiones límite. Asimismo, proporciona un resumen de los antecedentes de la teoría de la mecánica de fractura, así como una descripción breve de los enfoques basados en esta teoría y sus conceptos básicos.

Anexo B: Incorpora un listado completo de las publicaciones del autor relacionadas con la tesis doctoral.

Parte I

1. Introducción

1.1. El interés del haya europea como material estructural

La madera es un material de construcción resistente, ligero, fácil de trabajar y abundante en todo el mundo. A lo largo de la historia ha desempeñado un papel crucial en el desarrollo de la construcción siendo utilizado, entre otros fines, como material estructural, de manera que se convirtió en un elemento clave en la evolución de la arquitectura e ingeniería, estando presente en la mayoría de los edificios arquitectónicos clásicos que conocemos. La madera ha sido ampliamente utilizada tanto en elementos estructurales principales (vigas, pilares, etc.) como secundarios (cimbras, puntales, andamios…) y actualmente continúa siendo uno de los materiales de construcción de estructuras más relevantes, debido a su versatilidad y diversas ventajas. Aun así, en el último siglo, su presencia en la construcción de edificios ha sido relegada progresivamente en favor de otros materiales de construcción de estructuras poco respetuosos con el medio ambiente como el hormigón o el acero, desplazando el uso de la madera a un segundo plano.

En los últimos años, el desarrollo de materiales de construcción renovables y sostenibles ha experimentado un gran crecimiento impulsado por la necesidad de mitigar los efectos del cambio climático. El sector de la construcción es uno de los responsables del daño medioambiental actual ya que utiliza mucha energía primaria y libera grandes cantidades de dióxido de carbono a la atmosfera (CO_2), entre otras razones, debido al crecimiento masivo de la nueva construcción en las economías en transición y las ineficiencias del parque inmobiliario existente (Gustavsson & Sathre, 2006; UNEP, 2009). Estudios muestran que el sector de la construcción aporta hasta el 30% de las emisiones anuales de gases de efecto invernadero y consume hasta el 40% de toda la energía (UNEP, 2009). El uso de la madera y los productos derivados de la madera en la construcción de edificios, puede ayudar a reducir de manera considerable la demanda de energía y las emisiones de CO_2 durante el proceso de fabricación, en comparación con otros materiales ampliamente utilizados como el acero, el hormigón, el aluminio o el ladrillo (Buchanan & Levine, 1999; Eriksson et al., 2012; Sathre & Gustavsson, 2009). De este grupo, la madera, es el único material que cuenta con la condición de recurso renovable (Buchanan & Honey, 1994) y que se compone de cantidades sustanciales de carbono capturadas de la atmósfera en el proceso de crecimiento de los árboles (alrededor del 50% de su peso seco) (UNECE & FAO, 2023), actuando de almacén de carbono durante toda la vida. Por esta razón, la madera y los productos derivados de la madera han despertado un gran interés para su utilización en la arquitectura e ingeniería civil, convirtiéndose en un aliado para combatir la crisis medioambiental en la que estamos sumergidos.

Actualmente, la mayoría de la madera o productos derivados de la madera usados en la construcción de estructuras para edificios están fabricados con madera de coníferas, como son el pino o el abeto, pero en los últimos años ha crecido el interés por usar las especies frondosas con fines estructurales. Las razones de este creciente interés son múltiples y se deben, entre otras cosas, al incremento de la demanda de madera por parte del ector de la construcción y la carpintería, la infrautilización de los bosques de frondosas envejecidos y sus elevadas propiedades mecánicas en comparación con las coníferas (Aicher et al., 2014; Camú & Aicher, 2018). En este contexto, *Fagus sylvatica* L. es una de las especies frondosas más prometedora, importante y extendida en Europa, cuyo nombre común es haya europea. Es un árbol

de gran tamaño que suele alcanzar los 30-40 m de altura y tiene la capacidad de crecer en ambientes muy diferentes, desde climas atlánticos hasta continentales y la zona mediterránea. Esto queda reflejado en su área de distribución natural, la cual se extiende desde el sur de Escandinavia al norte de Sicilia y desde el noroeste de Turquía hasta el noroeste de España, cubriendo más de 11 millones de hectáreas en Europa (Antonucci et al., 2021; De Rigo & Caudullo, 2016; FOREST EUROPE et al., 2011) (Figura 1.1)

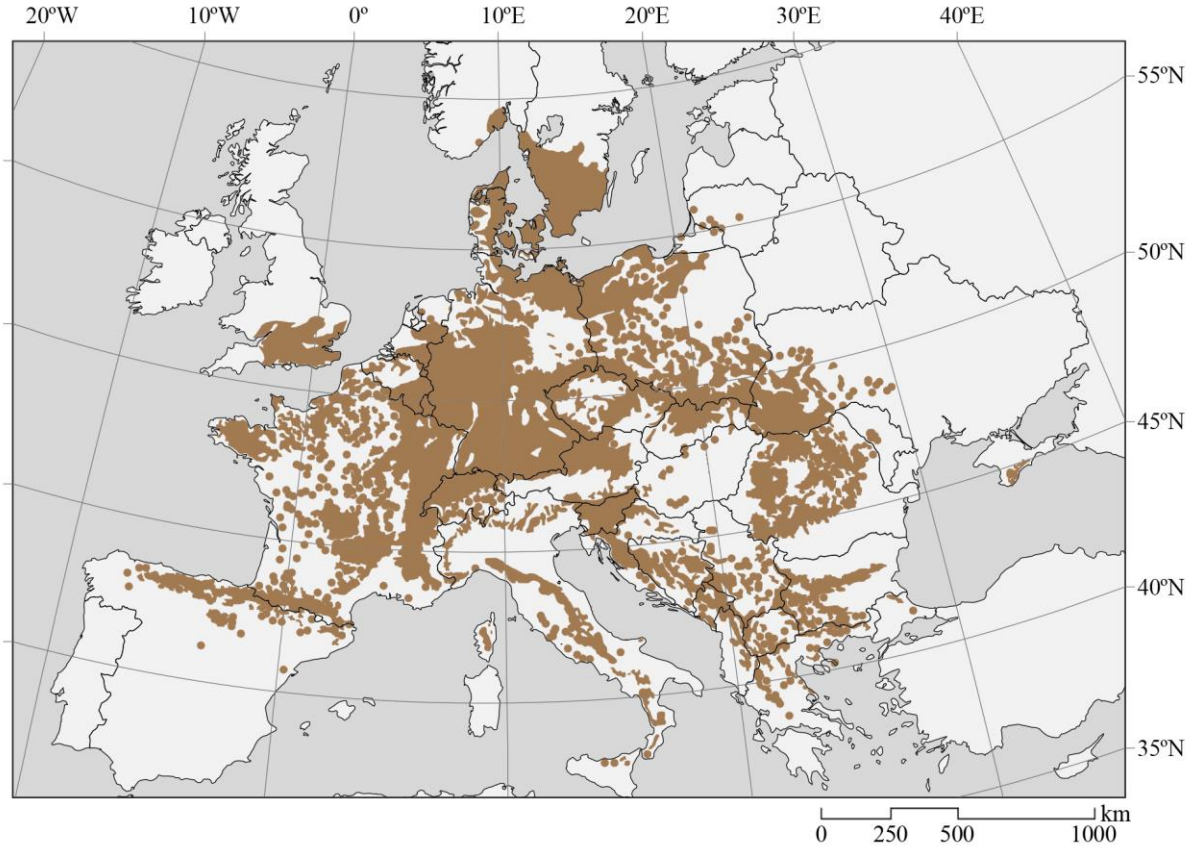

Figura 1.1:Presencia de *Fagus sylvatica* L. en Europa (adaptado de (Ehrhart, 2019)).

Históricamente, la madera de haya ha sido utilizada para diferentes aplicaciones, como por ejemplo la elaboración de herramientas agrícolas y artesanales. Actualmente, la mayor parte de la madera se destina principalmente para usos energéticos (leña, carbón vegetal…) y la madera en rollo de alta calidad se transforma en madera aserrada y contrachapada, desempeñando un papel esencial en la industria del mueble. Sin embargo, la investigación y el desarrollo de productos de ingeniería a partir de haya para la industria de la construcción ha ganado fuerza en la última década (Pramreiter & Grabner, 2023), ya que *Fagus sylvatica* L. es una de las tres especies frondosas con crecimiento en Europa con mayor clase resistente asignada (D40, según la norma (UNE EN 1912:2012), junto con el fresno (*Fraxinus excelsior* L.) y el eucalipto (*Eucalyptus globulus* L.). Por lo tanto, su buena resistencia y rigidez la convierte en una excelente alternativa para el desarrollo de productos con uso estructural, especialmente para situaciones donde se requieran altas prestaciones, como las conexiones mecánicas con clavijas y los elementos de grandes luces, permitiendo reducir el tamaño de los elementos principales. Presenta una alta contracción y una baja durabilidad natural contra insectos y hongos (clase 4, según la norma (UNE EN 350:2016)), por lo que no es adecuado utilizarla en ambientes exteriores sin tratamientos protectores.

Aun así, tiene la ventaja de ser fácil de tratar gracias a su buena impregnabilidad (clase 1, según (UNE EN 350:2016)).

La disponibilidad de haya en los bosques europeos y la posibilidad de aprovechar sus ventajas en términos de resistencia y rigidez han impulsado la caracterización del material con fines estructurales, determinando sus propiedades elásticas (Ozyhar et al., 2013; Ozyhar et al., 2013) y mecánicas (Franke & Magnière, 2014; Ozyhar et al., 2012; Widmann et al., 2012) a nivel de probeta pequeña, lo que permite realizar simulaciones numéricas con haya europea para analizar su comportamiento ante diferentes situaciones de carga y usos de ingeniería.

Con relación a los diferentes productos estructurales fabricados con haya europea, existe una investigación activa sobre madera laminada encolada (GLT, del inglés *Glued Laminated Timber*), madera microlaminada (LVL, del inglés *Laminated Veneer Lumber*), madera contralaminada (CLT, del inglés *Cross Laminated Timber*) y otros productos como son los tableros de fibras orientadas (OSB, del inglés *Oriented Strand Board*) o los tableros de partículas. Algunos de estos productos se muestran en la Figura 1.2. Estudios recientes revelan que el GLT de haya puede alcanzar una clase resistente de hasta GL55 (resistencia característica a flexión de 55 N/mm^2), con valores medios del módulo de elasticidad a flexión de 16.200 N/mm^2 (Ehrhart et al., 2020). Considerando que el GLT de especies coníferas se utiliza habitualmente en la clase GL24, resulta evidente cómo la madera de haya puede mejorar notablemente las aplicaciones en la construcción. En cuanto al LVL, se han publicado valores medios de resistencia y módulo de elasticidad a flexión de 78,8 N/mm^2 y 15.900 N/mm^2, respectivamente (Knorz & van de Kuilen, 2012). Investigaciones sobre CLT de haya europea mostraron un buen rendimiento, obteniendo valores medios de 43,8 N/mm^2 y 12.306 N/mm^2 para la resistencia a flexión y el módulo de elasticidad, respectivamente (Franke, 2016). Existen también estudios sobre caracterización de las propiedades mecánicas de otros productos derivados, como tableros OSB (Akrami et al., 2014) y tableros de partículas (Breinig et al., 2019). Esto refleja el creciente interés en desarrollar productos fabricados con esta especie para su uso en estructuras. En la última década, se han expedido homologaciones técnicas europeas para productos de GLT y LVL fabricadas con haya europea (ETA 14/0354:2021; ETA 18/1018:2018). No obstante, en (Pramreiter & Grabner, 2023) se puede encontrar una revisión exhaustiva de la utilización del haya europea en Europa y las líneas de investigación abiertas actualmente. Aun así, es necesario seguir profundizando en el conocimiento del comportamiento de esta especie para su uso como elemento estructural en diferentes aplicaciones, como las uniones con clavijas cargadas perpendicularmente a la fibra objeto de esta tesis.

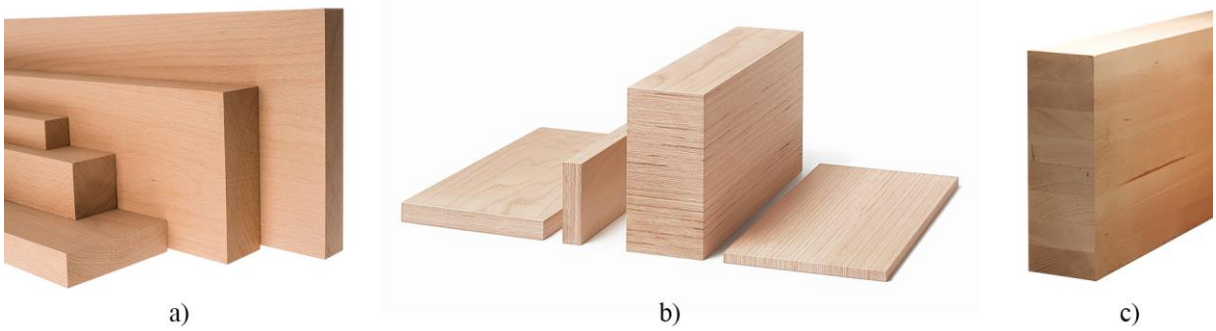

Figura 1.2: Productos de haya europea: a) madera aserrada; b) madera microlaminada (LVL); c) madera laminada encolada (GLT).

1.2. Fallo por hienda en uniones con clavijas cargadas con un ángulo respecto de la fibra

Generalmente, las uniones constituyen los puntos más débiles de una estructura, ya que son zonas sometidas a grandes concentraciones de tensiones y, por lo tanto, fomentan la aparición de fendas. Por ello, para evitar situaciones críticas que pongan en riesgo la estabilidad global de la estructura, es necesario realizar un análisis minucioso de la conexión y prestar especial atención a su diseño, estableciendo mecanismos que garanticen la adecuada transferencia de esfuerzos entre los diferentes elementos de madera que conecta.

La evolución de las uniones en estructuras de madera ha sido un proceso marcado por hitos cruciales que han transformado la arquitectura y la ingeniería. A lo largo de la historia se han desarrollado y perfeccionado diversas técnicas de unión para mejorar su eficiencia (Figura 1.3). Desde hace milenios, las conexiones carpinteras tradicionales, como la caja y espiga, han sido esenciales en la construcción de estructuras de madera. Sin embargo, la incorporación de uniones mecánicas en el siglo XIX y el desarrollo de las uniones encoladas en el siglo XX marcaron dos puntos de inflexión en la evolución, conduciendo a técnicas de unión más sofisticadas.

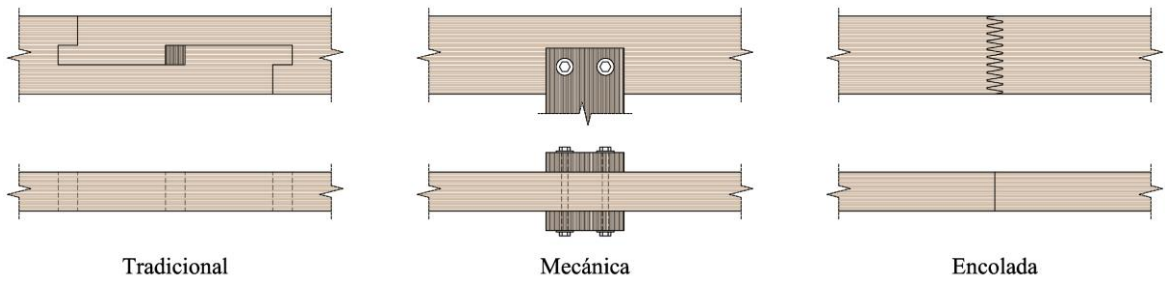

Figura 1.3: Tipos de uniones según el medio de conexión.

Las uniones encoladas facilitan una distribución uniforme de los esfuerzos, lo que contribuye a disminuir las concentraciones de tensiones. Aun así, el empleo de uniones encoladas en obra no es habitual debido, entre otros factores, a la dificultad de asegurar las condiciones óptimas de temperatura y humedad que garanticen un correcto proceso de curado de los adhesivos.

Las uniones con conexiones mecánicas mediante clavijas se ven menos afectadas por las condiciones climáticas y, una vez ejecutadas, están listas para trabajar a su máxima capacidad sin necesidad de tiempos de espera. Además, la prefabricación de los diferentes elementos que conforman la unión asegura una alta precisión de ensamblaje, y la posibilidad de realizar buena parte del montaje en taller permite una ejecución rápida y eficiente en obra, reduciendo el tiempo total de construcción. Por estas razones, las uniones mecánicas con clavijas se encuentran entre las uniones más utilizadas en obra, estando presentes en la mayoría de las construcciones con estructura de madera del siglo XXI (véanse ejemplos en la Figura 1.4).

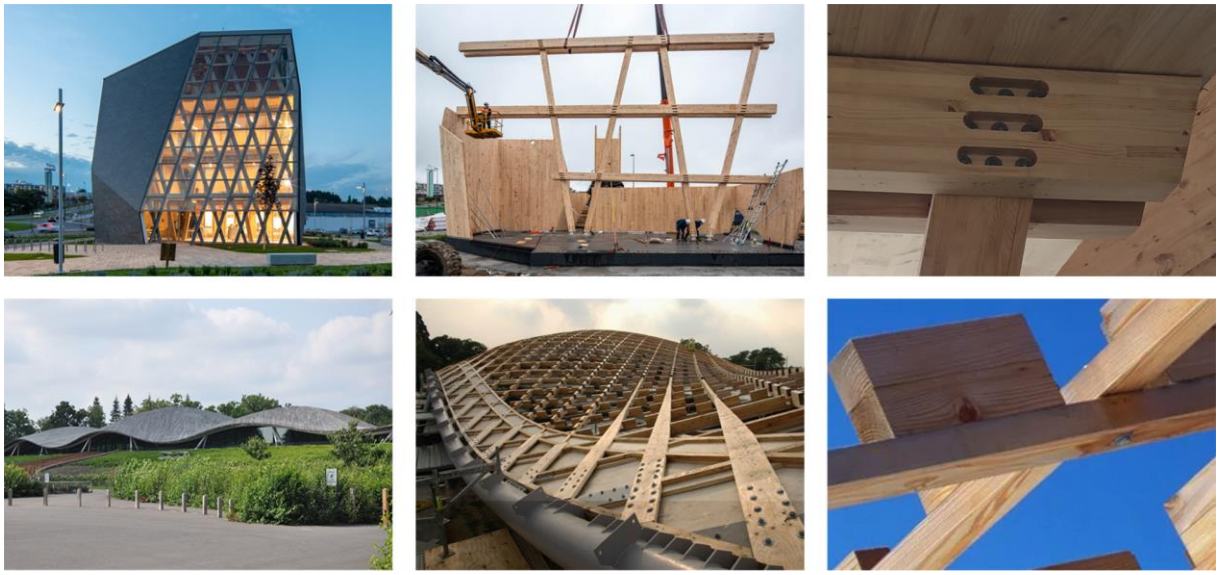

Figura 1.4: Ejemplos de edificios con estructura de madera y conexiones mecánicas con clavijas: Edificio Impulso Verde (arriba), The Savill Building (abajo).

En las últimas décadas, las uniones mecánicas con clavijas (pernos, pasadores, tirafondos…) han experimentado un gran impulso por parte de la comunidad científica. La industrialización de la construcción con madera y los nuevos avances tecnológicos, como por ejemplo el sistema de corte por control numérico (CNC) o la capacidad computacional de los ordenadores, han estimulado la evolución de las uniones estructurales. En consecuencia, se han desarrollado técnicas que facilitan la fabricación de uniones complejas y se han sofisticado las técnicas de análisis numérico consiguiendo mejorar las herramientas de diseño estructural. Aun así, todavía existen muchas lagunas en la previsión del comportamiento mecánico de las uniones con clavijas.

Los modos de fallo de las uniones con clavijas pueden caracterizarse como dúctiles, frágiles o una combinación de ambos (ver Figura 1.5). La posibilidad de ser diseñadas para tener un comportamiento dúctil es una de sus principales ventajas, ya que es muy deseable y apropiado en el diseño de estructuras. En este sentido, el modelo de plastificación Europeo (European yield model, EYM) o modelo de Johansen (Johansen, 1949) constituye una herramienta sencilla y fiable para estimar la resistencia última de las uniones que fallan de manera dúctil y está incluido en el Eurocódigo 5 (UNE EN 1995-1-1:2016). Este modelo siempre tiene en cuenta el comportamiento plástico de la madera y también el posible comportamiento plástico del pasador, en función del modo de fallo desarrollado por la conexión. Sin embargo, este modelo no resulta válido para dimensionar las situaciones en las que la madera falla de manera frágil, pudiendo sobrestimar peligrosamente la carga de rotura. Los modos de fallo frágiles conducen a una situación muy crítica, ya que desencadenan roturas repentinas que pueden aparecer incluso a bajos niveles de carga provocando el colapso parcial o total de la estructura, por lo que requieren un cuidado especial en la fase de diseño y dimensionado. Generalmente, el fallo de las uniones de madera con clavijas implica el crecimiento estable de zonas de fisuración, pero en algunas situaciones dichas fisuras crecen de manera inestable desencadenando uno de los modos de fallo frágil más comunes y peligrosos, el fallo por hienda.

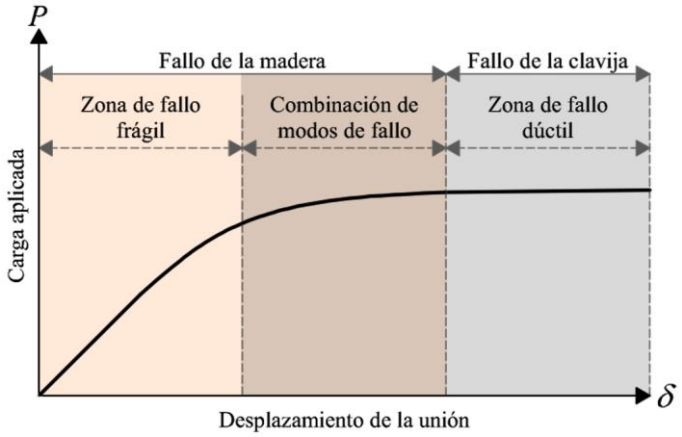

Figura 1.5: Zonas de aparición de los modos de fallo potenciales en las uniones de madera con clavijas.

El fallo por hienda es uno de los modos de fallo frágiles más observado en vigas con uniones con clavijas cargadas con un ángulo respecto de la fibra Figura 1.6. Este tipo de fallo se caracteriza por la aparición de una fisura que se propaga en la dirección paralela a la fibra separando el elemento de madera en dos partes. Esta fisura puede ser finita, llegando a estabilizarse en un punto, o propagándose de manera incontrolada a lo largo de todo el elemento de madera.

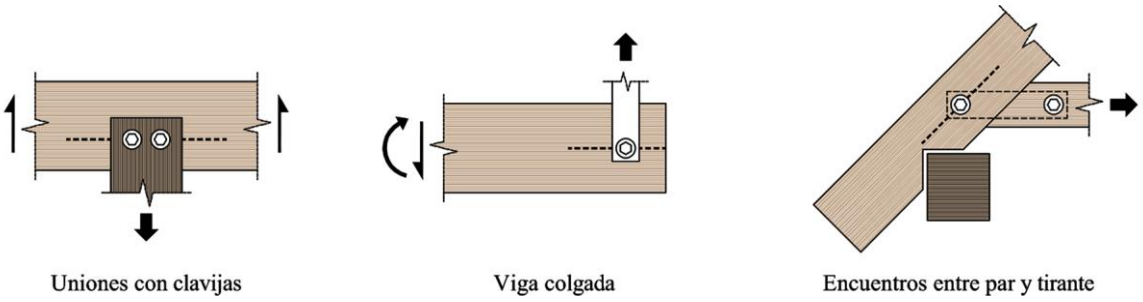

Figura 1.6: Soluciones estructurales con clavijas que pueden inducir el fallo por hienda.

Normalmente, el fallo por hienda se relaciona con la aparición de tensiones perpendiculares a la fibra, las cuales provocan el colapso por fractura del material. Sin embargo, este tipo de fallo también se produce debido a la concentración de tensiones de cortante.

Existen dos grandes enfoques para abordar el fallo por hienda. Uno de ellos se basa en el concepto de resistencia de los materiales, en el que la rotura del material se determina en base a criterios de tensión o deformación límite. Algunos de los más relevantes se pueden consultar en el Anexo A.1. Aun así, tal enfoque no resulta adecuado para analizar regiones con gradientes de tensión pronunciados ya que estos criterios suponen que el material está libre de defectos (Smith et al., 2003). Sin embargo, los enfoques basados en la mecánica de fractura asumen la presencia de un defecto inherente en el material, por lo que este planteamiento parece más adecuado para estudiar el daño por hienda. Un amplio desarrollo de las bases de la mecánica de la fractura puede consultarse en (Anderson, 2017; Bažant & Planas, 1998). Un resumen de los principales aspectos se recoge en el Anexo A.2.

La fractura implica la formación de una fisura que genera la perdida de contacto entre las partes de un elemento, de manera que se crean nuevas superficies incapaces de transmitir tensiones entre sí quedando

totalmente desenlazadas. De manera sencilla se podría decir que el proceso de fractura de un material suele desarrollarse en tres etapas. En primer lugar, se inician una o varias microfisuras que, en algunos casos, se desarrollan a partir de una imperfección o defecto preexistente. En segundo lugar, estas microfisuras crecen de forma estable y podrían unirse a otras microfisuras para alcanzar el tamaño de macrofisura. En tercer lugar, la macrofisura se propaga de manera inestable al alcanzar un nivel crítico de tensión. Esta fisura o defecto preexistente puede propagarse bajo tres modos de carga diferentes asociados a tres desplazamientos relativos, tal y como se muestra en la Figura 1.7. El modo I representa el modo de apertura de la fisura en la dirección perpendicular al plano de fractura. Los modos II y III están asociados a deslizamientos dentro y fuera del plano de fractura, respectivamente. Cada mecanismo de propagación está asociado a un estado de tensión diferente: tensiones de tracción perpendicular (modo I) y tensiones de cortante (II y III).

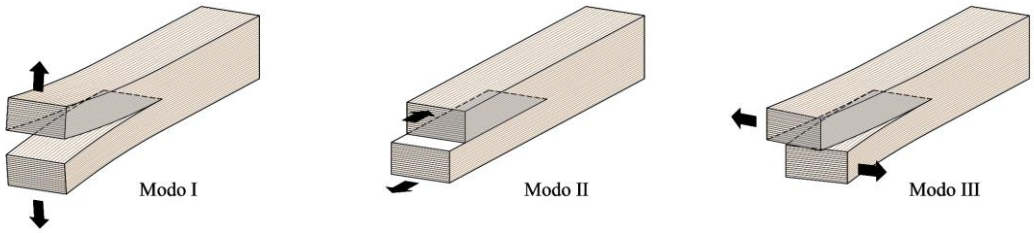

Figura 1.7: Modos de carga y fractura.

Las configuraciones del modo I son particularmente fáciles de encontrar en el diseño de estructuras habituales (flexión de vigas, vigas con entalle, uniones…) y, por tanto, son objeto de continuas investigaciones. En cambio, los modos relacionados con tensiones de cortante (II y III) son menos frecuentes, siendo el modo III particularmente inusual, ya que se trata de una configuración de carga muy poco común. En el caso particular de las uniones con clavijas, la mayoría de las configuraciones de conexión acaban desarrollando una combinación de los modos I y II en la punta de la fisura, lo que requiere considerar criterios de rotura en modo mixto para predecir con precisión el daño del material.

Por otro lado, suponer la madera como material ortótropo conduce a considerar seis sistemas de propagación de fisuras: RL, TL, LR, LT, RT y TR. La primera letra indica la dirección normal al plano de fractura y la segunda especifica la dirección de la propagación de la fisura. Estos posibles sistemas se esquematizan en la Figura 1.8.

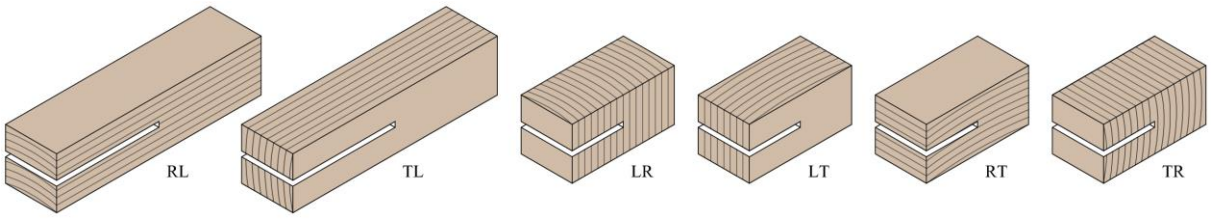

Figura 1.8: Sistemas de propagación de fractura en madera.

Actualmente existen dos criterios para analizar estructuras a través del enfoque de la mecánica de fractura (ver Anexo A.2). Uno de ellos está basado en criterios de energía y asume que el crecimiento de la fisura se produce cuando la energía de deformación disponible en la punta de la fisura (G) supera una tasa crítica de liberación de energía (G_c). G_c se considera una propiedad fundamental del material y

caracteriza su resistencia a fractura según cada modo de propagación de fractura (I, II y III). Por lo tanto, resulta conveniente determinar este parámetro de fractura de las especies de madera usadas con fines estructurales, de modo que se pueda modelizar con rigor su comportamiento mecánico.

Predecir el colapso de las estructuras de madera debido al fallo por hienda presenta desafíos significativos y actualmente no hay un consenso generalizado sobre cómo abordar el problema adecuadamente. Esto queda materializado por la ausencia de criterios de comprobación en las normas de diseño o la presencia de criterios cuestionables para comprobar elementos expuestos a tensiones de tracción perpendicular a la fibra y tensiones de cortante. No obstante, en la actualidad predominan dos enfoques teóricos para abordar la capacidad de carga frente a la hienda por tracción perpendicular a la fibra de la madera. Uno de ellos se centra en establecer criterios de rotura basados en tensiones límite. Las comprobaciones de la antigua norma alemana DIN 1052 (DIN 1052:2008) seguían este enfoque. El otro, se centra en aplicar la teoría de mecánica de fractura y, actualmente, las comprobaciones incluidas en el Eurocódigo 5 (UNE EN 1995-1-1:2016) están basadas en esta teoría.

Existen dos vías para profundizar en la aplicabilidad de dichos enfoques. Una se centra en el desarrollo de modelos de diseño analíticos, empíricos o semiempíricos. No obstante, desarrollar un modelo que pueda ser manejado con facilidad en el ejercicio práctico es una tarea difícil. A pesar de ello, muchos investigadores han realizado esfuerzos en este sentido y algunas de las propuestas más relevantes han sido aceptadas para formar parte de las bases de algunas normas de diseño de madera. Otra alternativa para profundizar en el comportamiento frente a la hienda es a través de simulaciones numéricas. En la siguiente sección se exponen los principales enfoques analíticos y numéricos basados en la mecánica de fractura para estimar la capacidad de carga frente a la hienda en uniones resueltas con clavijas.

1.3. Enfoques basados en la mecánica de fractura para estimar la capacidad de carga frente a la hienda de uniones con clavijas

1.3.1. Análisis por elementos finitos

Las simulaciones numéricas representan una herramienta fundamental en la ingeniería estructural, ofreciendo una alternativa eficaz y precisa a los ensayos experimentales tradicionales. Entre estas técnicas, el análisis por elementos finitos (FEA, del inglés *Finite Element Analysis*) se ha convertido en una de las herramientas de simulación computacional más utilizada en el diseño estructural (Figura 1.9), debido a su capacidad para predecir de manera fiable la respuesta de una estructura ante una combinación de cargas compleja.

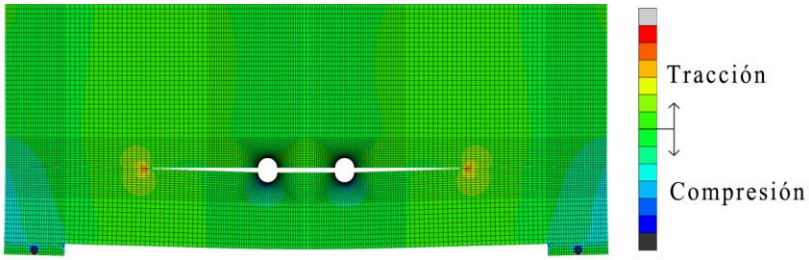

Figura 1.9: Simulación numérica del fallo por hienda y análisis de las tensiones perpendiculares a la fibra de una viga de haya carga perpendicularmente a la fibra mediante una conexión con dos pasadores.

Los resultados obtenidos con FEA son tan satisfactorios que algunos autores han desarrollado modelos empíricos basados en los resultados de los análisis numéricos para determinar la carga de rotura de vigas cargadas perpendicularmente a la fibra por medio de pasadores (Franke & Quenneville, 2011b).

1.3.1.1. Modelos de zonas cohesivas

Uno de los enfoques numéricos más sencillos, utilizados y aplicables a uniones en madera son los modelos de zonas cohesivas (CZM, del inglés *Cohesive Zone Models*) (ver subsección 1.3.1.4). Esta teoría tiene su origen en los trabajos de Dugdale (Dugdale, 1960), Barenblatt (Barenblatt, 1962) y concretamente en el modelo de fisura ficticia desarrollado por Hillerborg *et al.* (Hillerborg et al., 1976) (ver Anexo A.2). Todos ellos buscaban una herramienta para predecir el comportamiento a fractura de materiales con comportamiento dúctil (acero) o cuasifrágil (hormigón y madera). Este método, fácil de implementar en FEA, permite simular de manera realista el comportamiento frente a la hienda de vigas de madera cargadas perpendicularmente a la fibra por medio de uniones con clavijas. Los primeros trabajos que utilizaron este enfoque para reproducir la fisuración de la madera empleando una relación constitutiva del material en modo I se pueden encontrar en (Boström, 1992; Gustafsson, 1985). Desde entonces, numerosos trabajos han contribuido a su avance explorando la aplicabilidad de los CZMs en diferentes escenarios de carga y desarrollando criterios de rotura más sofisticados para mejorar la precisión de los resultados. Investigaciones llevadas a cabo en (Caldeira, 2011; Dourado et al., 2018; Franke & Quenneville, 2010), han incorporado criterios de rotura en modo-mixto para evaluar la rotura por fractura del material bajo diferentes condiciones de carga. Estas investigaciones han proporcionado información valiosa para el diseño y la evaluación de la integridad estructural.

En los modelos de zonas cohesivas (CZM), se considera que el material es capaz de transferir tensiones más allá de alcanzar la tensión máxima en el punto más solicitado. No obstante, esta capacidad disminuye a medida que evoluciona la zona en proceso de fractura (FPZ, del inglés *Fracture Process Zone*). Para ello, los CZMs combinan un criterio de resistencia basado en tensiones límite para determinar el inicio del daño, y la teoría de mecánica de fractura para describir la propagación de éste según una relación constitutiva. En consecuencia, no es necesario definir un defecto inicial para aplicar CZMs. El concepto clave de estos modelos es que usa dos relaciones constitutivas del material: una relación tensión-deformación para definir el comportamiento del material estructural de manera genérica y una ley de ablandamiento, asignada localmente a patrones de rotura predefinidos, que caracteriza el comportamiento a fractura del material en cualquiera de sus modos de carga (I, II y III), relacionando la tensión (f) con el desplazamiento relativo (u) entre las caras de la fisura. Esta última se conoce como ley cohesiva y se considera una propiedad del material. Por lo tanto, resultaría conveniente determinar

las leyes cohesivas de las especies de madera usadas con fines estructurales, de modo que se pueda predecir adecuadamente su comportamiento a fractura.

La desventaja de utilizar CZMs es que deben asociarse a patrones definidos geométricamente en los modelos de elementos finitos (FEM, del inglés *Finite Element Model*) y, por tanto, es esencial conocerlos de antemano. No obstante, una de las ventajas del comportamiento fuertemente ortotrópico de la madera es que los patrones de propagación de las fisuras suelen conocerse, y si no es así, pueden predecirse con FEA identificando los puntos propensos a generar fisuras. Estos patrones se introducen frecuentemente en FEM por medio de elementos finitos de interfaz (interface finite elements), a los cuales se asocian las leyes cohesivas de los modos de carga considerados (I, II, III).

Estos modelos requieren implementar las propiedades del material con el fin de simular con rigor el comportamiento estructural del material. Por ello es crucial determinar las constantes de elasticidad que definen la matriz de rigidez de ortotropía (ver subsección 1.3.1.3), así como las propiedades que definen el comportamiento a fractura, es decir, las leyes cohesivas (ver subsección 1.3.1.4).

1.3.1.2. Escalas de la madera y modelado

La madera es un material natural, con estructura heterogénea y celular, que cuenta con muchas propiedades atractivas a nivel estructural. Una de las desventajas inherentes a su origen natural es la alta variabilidad de sus propiedades mecánicas ya sea entre especies, troncos de la misma especie o dentro de una misma tabla. Además, su comportamiento mecánico se ve afectado, entre otras cosas, por la duración de la carga, el contenido de humedad y la temperatura. No obstante, las características del material pueden describirse a diferentes niveles, que van desde la composición de la pared celular hasta los elementos estructurales masivos. Las diferentes escalas en las que puede ser modelada la madera son: masiva, macro, meso, micro y nano (Smith et al., 2003) (ver Figura 1.10).

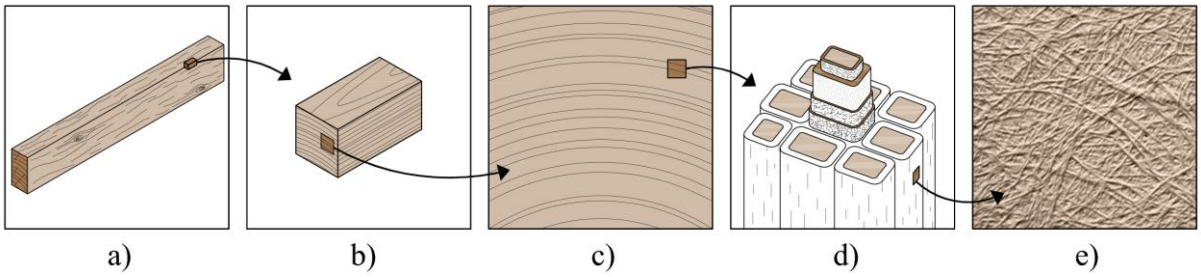

Figura 1.10: Escalas de la madera: a) elemento estructural (masiva); b) madera libre de defectos (macro); c) anillos de crecimiento (meso); d) estructura de la pared celular (micro) y d) forma microfibrilar de la pared celular primaria (nano). (Adaptada de (Majano-Majano, 2014))

A nivel estructural es de interés la escala masiva, ya que se refiere a madera aserrada o laminada de grandes dimensiones. Sin embargo, en esta dimensión, los elementos de madera contienen imperfecciones inherentes al material, como nudos, fendas, desviaciones de fibra, etc. Estos defectos debilitan localmente la madera dando lugar a concentraciones de tensiones que pueden causar una disminución de sus propiedades resistentes. Los fallos de la madera en la escala masiva están relacionados con procesos localizados, por lo que resulta esencial entender cómo se comporta la madera a escalas inferiores para poder comprender mejor algunos tipos de fallo, como por ejemplo el colapso

por fractura del material (Smith et al., 2003). Por consiguiente, la escala macro es la que se usa comúnmente para propósitos de diseño estructural en el análisis de tensiones y de fractura en 2D y 3D. La madera a esta escala corresponde con la madera libre de defectos y la caracterización de las propiedades a este nivel abre la puerta a investigaciones mediante simulaciones numéricas. En este contexto, los modelos en 3D suelen abordarse con ortotropía rectilínea o cilíndrica. En el caso particular de representaciones en 2D, se realizan análisis de tensión o deformación plana en los que la madera se modela, normalmente, como un material homogéneo y transversalmente isotrópico.

En la presente tesis se han realizado simulaciones numéricas empleando la técnica de análisis por elementos finitos (FEA). Para ello, se ha adoptado un enfoque de modelado de la madera a escala macro y análisis en tensión plana. A continuación, se exponen las propiedades mecánicas del material necesarias para simular con rigor el comportamiento estructural de la madera a escala macro.

1.3.1.3. Propiedades elásticas y de rigidez

La madera es un material anisótropo y, por tanto, sus propiedades de resistencia y rigidez varían en función de la orientación de la carga respecto a la orientación de las fibras. A efectos de diseño estructural, está ampliamente aceptado considerarla como un material cilíndricamente ortotrópico, caracterizado por tres direcciones principales: longitudinal (L), radial (R) y tangencial (T) (Figura 1.11).

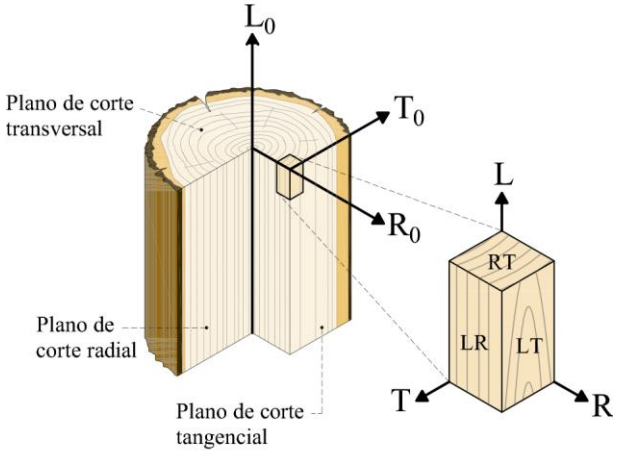

Figura 1.11: Planos y direcciones principales de ortotropía: direcciones principales de ortotropía en referencia al tronco del árbol (L_0, R_0 y T_0) y en referencia a la dirección de las fibras (L, R y T).

Las fibras de la madera rara vez están alineadas con las direcciones principales del cilindro del tronco del árbol (L_0, R_0 y T_0) debido al crecimiento en espiral o la forma cónica que suele tener el tronco. Esto es importante, ya que las propiedades mecánicas de la madera limpia se describen con referencia a la dirección de la fibra (L, R y T) y no a la dirección longitudinal del cilindro del tronco. Consecuentemente, las propiedades en la dirección L (conocida habitualmente como dirección fuerte) se denominan comúnmente como propiedades paralelas a la fibra, y las propiedades asociadas a las direcciones R y T como propiedades perpendiculares a la fibra. Entre estas direcciones existen grandes diferencias de rigidez y resistencia, siendo las propiedades en la dirección L bastante altas en comparación con las asociadas a las direcciones R y T. Estas diferencias también se encuentran dentro

de una misma dirección principal (L, R o T), ya que las propiedades de la madera varían en función de si la madera se tracciona o se comprime.

Asumiendo la hipótesis de pequeñas deformaciones y considerando ortotropía en las direcciones L, R y T, la respuesta elástica y lineal para la relación constitutiva del material en 3D puede expresarse mediante la ley de Hooke generalizada, la cual relaciona todos los componentes de tensión con todos los componentes de deformación. Esta ecuación constitutiva del material es una de las más simples, ya que se basa en la suposición de que las componentes de tensión (σ) y deformación (ε) se relacionan linealmente según la siguiente ecuación:

$$\{\sigma\} = [\mathrm{D}]\{\varepsilon\} \tag{1}$$

donde $\{\sigma\}$ es el vector de tensiones, el cual contiene las tensiones normales (σ) y las tensiones tangenciales (τ), $\{\varepsilon\}$ es el vector de deformaciones elásticas, que incluye los alargamientos (ε) y las deformaciones angulares (γ), y $[D]$ es la matriz de rigidez en las direcciones del material consideradas. De manera análoga, la relación entre $\{\varepsilon\}$ y $\{\sigma\}$ puede expresarse a través de la matriz de flexibilidad $[S]$ según la siguiente ecuación:

$$\{\varepsilon\} = [S]\{\sigma\} \tag{2}$$

La relación entre la matriz $[D]$ y $[S]$ es evidente, ya que la matriz de rigidez es la inversa de la matriz de flexibilidad y viceversa:

$$[D] = [S]^{-1} \tag{3}$$

Esta relación es importante ya que experimentalmente es más sencillo determinar la matriz $[S]$ y posteriormente obtener la matriz $[D]$ mediante la ecuación (3). De acuerdo con (Bodig & Jayne, 1982), la matriz $[S]$ y los vectores $\{\sigma\}$ y $\{\varepsilon\}$ quedarían definidos de manera extendida según la siguiente expresión:

$$\begin{Bmatrix} \varepsilon_{\mathrm{L}} \\ \varepsilon_{\mathrm{R}} \\ \varepsilon_{\mathrm{T}} \\ \gamma_{\mathrm{RT}} \\ \gamma_{\mathrm{LT}} \\ \gamma_{\mathrm{LR}} \end{Bmatrix} = \begin{bmatrix} \frac{1}{E_{\mathrm{L}}} & -\frac{\nu_{\mathrm{RL}}}{E_{\mathrm{R}}} & -\frac{\nu_{\mathrm{TL}}}{E_{\mathrm{T}}} & 0 & 0 & 0 \\ -\frac{\nu_{\mathrm{LR}}}{E_{\mathrm{L}}} & \frac{1}{E_{\mathrm{R}}} & -\frac{\nu_{\mathrm{TR}}}{E_{\mathrm{T}}} & 0 & 0 & 0 \\ -\frac{\nu_{\mathrm{LT}}}{E_{\mathrm{L}}} & -\frac{\nu_{\mathrm{RT}}}{E_{\mathrm{R}}} & \frac{1}{E_{\mathrm{T}}} & 0 & 0 & 0 \\ 0 & 0 & 0 & \frac{1}{G_{\mathrm{RT}}} & 0 & 0 \\ 0 & 0 & 0 & 0 & \frac{1}{G_{\mathrm{LT}}} & 0 \\ 0 & 0 & 0 & 0 & 0 & \frac{1}{G_{\mathrm{LR}}} \end{bmatrix} \begin{Bmatrix} \sigma_{\mathrm{L}} \\ \sigma_{\mathrm{R}} \\ \sigma_{\mathrm{T}} \\ \tau_{\mathrm{RT}} \\ \tau_{\mathrm{LT}} \\ \tau_{\mathrm{LR}} \end{Bmatrix} \tag{4}$$

donde E_i, G_{ij} y ν_{ij} son las constantes de elasticidad y corresponden, respectivamente, a los valores de los tres módulos de Young en la dirección *i* (*i* = L, R, T), los tres módulos de rigidez transversal en el plano *ij* (*ij* = RT, LT, LR) y los seis coeficientes de Poisson, siendo *i* (*i* = L, R, T) la dirección de aplicación de la tensión y *j* (*j* = L, R, T) la dirección de la deformación transversal, para i ≠ j. Consecuentemente, la matriz [S] se compone de doce componentes de flexibilidad que quedan determinadas en función de las doce constantes de elasticidad. Sin embargo, dado que la energía de deformación almacenada en un material es una cantidad única, usando este concepto se demuestra que la matriz [S] es simétrica (Bodig & Jayne, 1982). Esto implica que E_i y ν_{ij} quedan relacionados según la ecuación (5) y, por lo tanto, las constantes de elasticidad necesarias para determinar la matriz [S] quedan reducidas a nueve.

$$\frac{\nu_{ij}}{E_i} = \frac{\nu_{ji}}{E_j}; \qquad i \neq j; \qquad i,\ j = \mathrm{L,R,T} \tag{5}$$

La relación constitutiva para un estado de tensión plana se obtiene fácilmente de la ley tridimensional de Hooke, ya que los modelos bidimensionales se consideran un caso especial de la ley tridimensional, de modo que la ecuación (4) se simplificaría según la siguiente expresión:

$$\begin{Bmatrix} \varepsilon_i \\ \varepsilon_j \\ \gamma_{ij} \end{Bmatrix} = \begin{bmatrix} \frac{1}{E_i} & -\frac{\nu_{ji}}{E_j} & 0 \\ -\frac{\nu_{ij}}{E_i} & \frac{1}{E_j} & 0 \\ 0 & 0 & \frac{1}{G_{ij}} \end{bmatrix} \begin{Bmatrix} \sigma_i \\ \sigma_j \\ \tau_{ij} \end{Bmatrix}; \qquad i \neq j; \quad i,\ j = \mathrm{L,R,T} \tag{6}$$

siendo *i* y *j* las direcciones principales del plano *ij*. Debido a la simetría de [S], la relación de la ecuación (5) se mantiene para el modelo de tensión plana.

1.3.1.4. Propiedades de fractura: leyes cohesivas

La relación constitutiva entre la tensión máxima (f) y el desplazamiento relativo (u) entre las caras de la fisura se conoce habitualmente como ley cohesiva. La forma genérica de esta relación se ilustra de manera sencilla en la Figura 1.12, resultado de un ensayo uniaxial a tracción perpendicular a la fibra para una especie arbitraria de madera de frondosa. Esta curva tensión-apertura de fisura discretiza el comportamiento a fractura en tres etapas. En la primera (A), el material se comporta de manera elástica y lineal hasta alcanzar el límite elástico. La segunda (B), describe el posible comportamiento no lineal del material hasta alcanzar la tensión de rotura en el pico de la curva. Las no linealidades que tienen lugar en esta etapa suelen deberse al desarrollo de microfisuras, pero también pueden tener su origen en una respuesta elástica y no lineal del material o en el desarrollo de pequeñas deformaciones plásticas. La tercera etapa (C), corresponde con la formación de la zona en proceso de fractura (FPZ) justo después de alcanzar el pico de la curva y describe el ablandamiento gradual del material a medida que se separan progresivamente las caras de la fisura, es decir, describe la evolución del daño. Al final de esta etapa, las caras de la fisura se desconectan totalmente y pierden la capacidad de transmitir tensiones entre ellas y, por tanto, supone la rotura y separación del material creando dos superficies independientes. Esta

rama de ablandamiento pretende recoger y describir los efectos de los diferentes mecanismos de disipación de energía que tienen lugar en la FPZ, tales como el puenteo de fibras o las microfisuras.

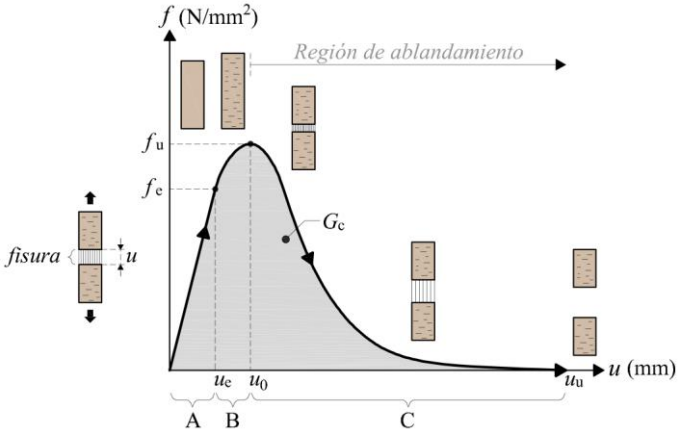

Figura 1.12: Esquema conceptual de la ley cohesiva para un ensayo estable a tracción uniaxial: respuesta elástica y lineal (A); comportamiento no lineal del material (B); ablandamiento del material, que describe los efectos de los mecanismos de disipación de energía que tienen lugar en la zona en proceso de fractura (C).

La ley cohesiva puede adoptar diferentes formas, pero contiene cuatro parámetros clave que marcan el inicio y la evolución del daño. El primero y más importante, es la tasa crítica de liberación de energía (G_c) que coincide con el área bajo la curva (sombreado gris en la Figura 1.12). La tensión máxima (f_u) y el desplazamiento relativo entre las caras de la fisura (u_0) definen el inicio del daño del material. Por último, el desplazamiento relativo máximo entre las caras de la fisura (u_u), que determina la rotura total del material.

Como se mencionó anteriormente, estas leyes cohesivas se asocian a patrones de rotura predefinidos geométricamente en FEM mediante elementos finitos de interfaz, para reproducir el inicio y la propagación del daño del material en el modo de carga considerado.

1.3.2. Modelos analíticos y empíricos

En la literatura se pueden encontrar varias propuestas de diseño para predecir la capacidad de carga frente a la hienda de vigas cargadas de manera perpendicular a la fibra por medio de uniones con clavijas. La mayoría de estos modelos han sido desarrollados de manera analítica o empírica, aunque algunas propuestas son una combinación de ambas siendo identificados como modelos semiempíricos. La Figura 1.13 ofrece una visión general de los modelos de diseño más relevantes y la relación entre ellos. Sin embargo, a pesar de los esfuerzos de la comunidad investigadora, todos los modelos han sido objeto de debate y ninguna propuesta ha sido ampliamente aceptada. Aun así, algunos de ellos han conseguido formar parte de las bases de algunas normas de diseño. El modelo propuesto por Ehlbeck et al. (Ehlbeck et al., 1989), basado en criterios de tensión, formó las bases de la expresión incluida en la antigua norma alemana (DIN 1052:2008). Por otro lado, el modelo desarrollado por van der Put y Leijten (Van der Put & Leijten, 2000) bajo el enfoque de la mecánica de fractura constituye las bases de la expresión incluida en el actual Eurocódigo 5 (UNE EN 1995-1-1:2016).

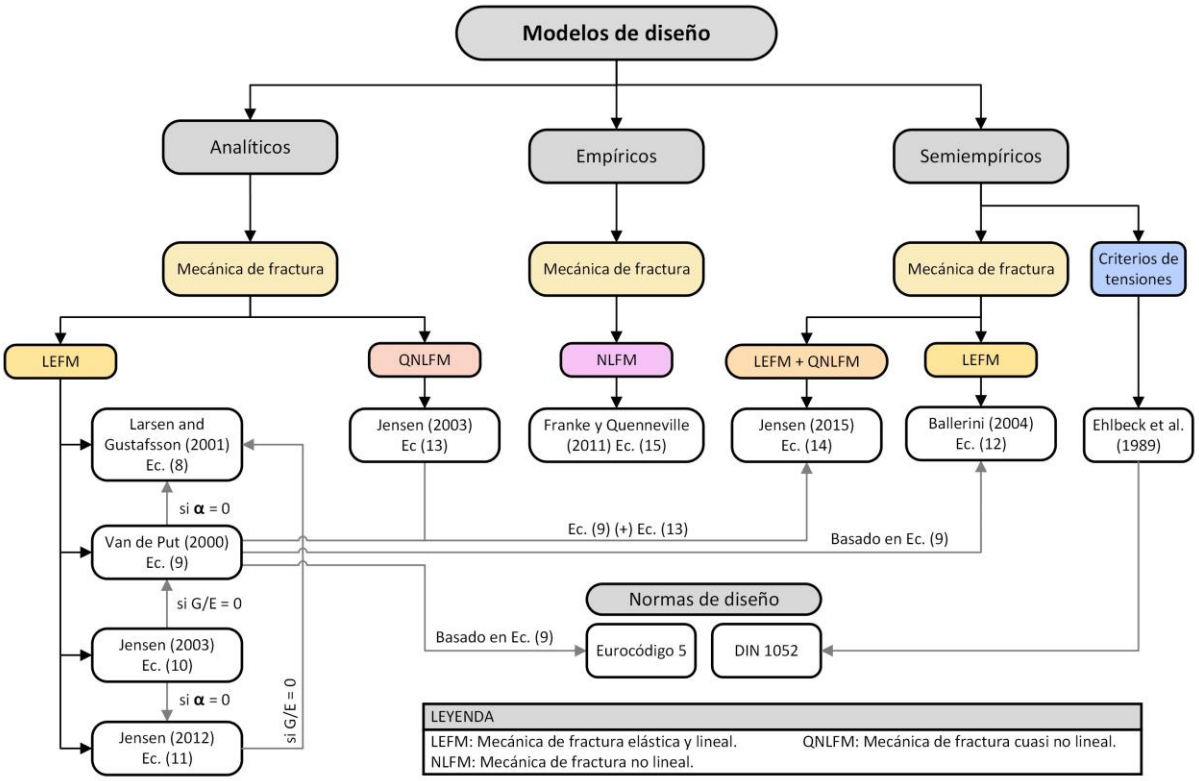

Figura 1.13: Diagrama de flujo de los modelos de diseño existentes para comprobar la capacidad de carga frente a la hienda de vigas cargadas perpendicularmente a la fibra por medio de uniones con clavijas.

En la presente tesis doctoral sólo se describen y aplican los modelos de diseño basados en la teoría de la mecánica de fractura. No obstante, en (Jockwer & Dietsch, 2018; Schoenmakers, 2010) se puede encontrar una revisión exhaustiva de la mayoría de los modelos existentes, su planteamiento teórico y su alcance en el diseño de conexiones de madera.

Uno de los principales inconvenientes de los modelos de diseño es que deben ser lo suficientemente simples y robustos como para ser manejados en la práctica y ajustarse bien a los resultados de los ensayos experimentales. Además, si es posible, deberían utilizar las propiedades de los materiales obtenidas a partir de ensayos normalizados. Sin embargo, desarrollar modelos de diseño con estas premisas no es una tarea sencilla (Jensen et al., 2015).

Los primeros modelos para predecir la carga de rotura (P_u) de una viga cargada perpendicularmente a la fibra se desarrollaron analíticamente en base a los principios de la mecánica de fractura elástica y lineal (LEFM, del inglés *Linear Elastic Fracture Mechanics*) y planteando el análisis de acuerdo con el enfoque de balance de energía (ver Anexo A.2.2.1). Estas propuestas destacan por ser las más sencillas, ya que consideran una sola fuerza externa (P) actuando en el centro del vano de la viga y sólo tienen en cuenta la influencia de algunas variables geométricas, tales como el canto de la viga (h), la distancia al borde cargado (h_e), el espesor de la viga (b) y la longitud de la fisura (a) (ver Figura 1.14). En este modelo, la viga es dividida por una fisura y la relación entre la distancia al borde cargado (h_e) y el canto total de la viga (h) se define como α (h_e/h).

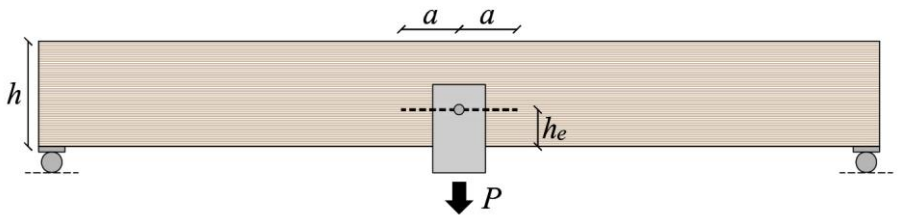

Figura 1.14: Viga fisurada cargada de manera perpendicular a la fibra por una conexión

En estos modelos, la carga de rotura (P_u) se determina aplicando el método de la flexibilidad, considerando que la fisura se propaga uniformemente a través del espesor de la viga (b) y crece de forma simétrica respecto de la posición de la carga con una longitud total de fisura de $2a$. De acuerdo con esto, el problema puede simplificarse a un análisis 2D y, combinando las ecuaciones (32) y (34) del Anexo A.2.2.1, se obtiene la carga crítica para la propagación de la fisura (P_u) según la siguiente expresión:

$$P_u = \sqrt{\frac{2bG_c}{\frac{dC}{da}}} \tag{7}$$

donde dC/da representa la variación de la deformación de la viga debido al incremento de la fisura.

Todos los modelos analíticos resumidos en la Figura 1.13 y basados en la LEFM son abstracciones del problema real, pero comparten el mismo punto de partida, es decir, se obtienen aplicando la ecuación (7). Por lo tanto, se pueden obtener varias soluciones diferentes planteando distintas hipótesis sobre cómo calcular la flexibilidad (C). En consecuencia, las soluciones derivadas están relacionadas entre sí de manera que cada una de las propuestas acaba siendo un caso especial de uno más general. Dicha relación queda recogida en la Figura 1.13.

El primer modelo analítico desarrollado bajo el enfoque de la LEFM se atribuye a Van der Put (Van der Put, 1990). Sin embargo, fue en la publicación de van der Put y Leijten (Van der Put & Leijten, 2000) donde la propuesta (ec. (9)) se mostró de manera clara. Este modelo fue diseñado sin tener en cuenta el tipo de conexión usado para transferir la carga a la viga, es decir, se analizó considerando una única fuerza aplicada en el centro del vano de la viga (Figura 1.14). Para la determinación de P_u se computó la flexibilidad debida al esfuerzo cortante y al momento flector. Además, fue calibrado para maderas de coníferas utilizando los resultados experimentales disponibles en la literatura. La propuesta ha sido ampliamente discutida, principalmente por su simplicidad. Algunas consideraciones adicionales acerca del alcance del modelo pueden encontrarse en (Leijten & Jorissen, 2001). Aun así, este modelo forma las bases de la comprobación frente a la hienda de elementos cargados perpendicularmente a la fibra incluida en el Eurocódigo 5 (UNE EN 1995-1-1:2016).

Jensen (Jensen, 2003) publicó un modelo ampliado (ec. (10)) para tener en cuenta algunas simplificaciones realizadas en el modelo original. Para el análisis se planteó una viga fisurada discretizada en cuatro elementos horizontales y dos verticales conectados rígidamente entre ellos (Figura 1.15a). En esta propuesta se tuvo en cuenta la contribución de las fuerzas normales en el equilibrio de la sección fisurada de modo que el modelo propuesto en (Van der Put & Leijten, 2000) aparece como un caso especial de este.

Larsen y Gustafsson (Larsen & Gustafsson, 2001) consideraron un mecanismo en el que la viga situada en la parte inferior de la fisura se comporta como una viga totalmente empotrada en sus extremos y sometida a una carga P, tal como se muestra en la Figura 1.15b. Esta hipótesis sólo considera las deformaciones debidas al esfuerzo cortante y está limitada a situaciones en las que la distancia h_e es pequeña en comparación con h, de modo que se pueda desarrollar el mecanismo considerado en la Figura 1.15b, es decir, que las deformaciones de la viga principal (superior) sean despreciables. Este planteamiento da como resultado la ecuación (8) y es interesante señalar que el parámetro que representa la longitud de la fisura (a) desaparece de la ecuación debido a que las deformaciones por cortante corresponden, en este caso, a una función lineal. Esta propuesta aparece como un caso especial del modelo de (Jensen, 2003) siempre y cuando se asuma que $\alpha \to 0$ y $G/E \to 0$ en la ecuación (10).

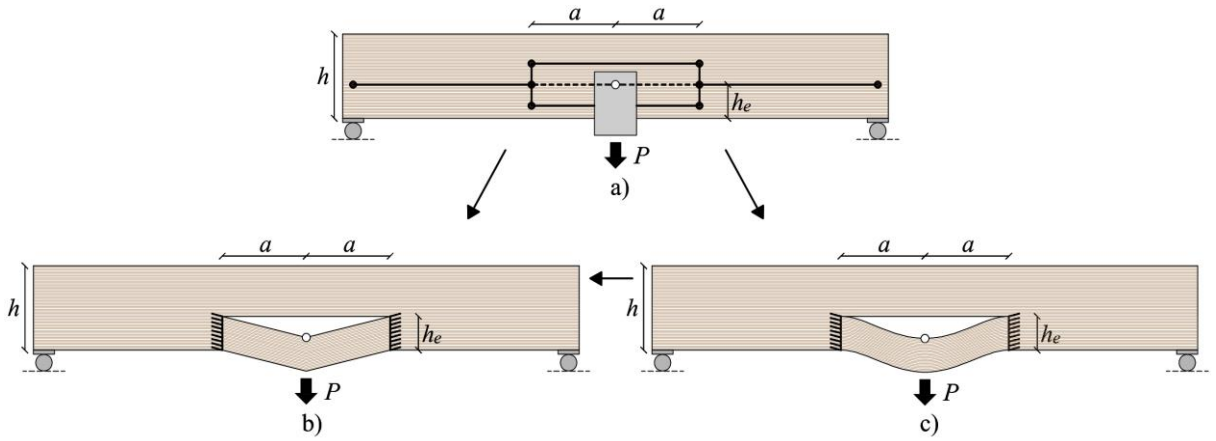

Figura 1.15: Modelos de vigas fisuradas consideradas para determinar la flexibilidad bajo el enfoque de la mecánica de fractura elástica y lineal: a) Jensen, 2003; b) Larsen & Gustafsson, 2001; c) Jensen et al., 2012.

Posteriormente, Jensen *et al*. (Jensen et al., 2012) consideraron el mismo punto de partida que en (Larsen & Gustafsson, 2001), pero esta vez se tuvieron en cuenta las deformaciones por flexión planteando el mecanismo que se muestra en la Figura 1.15c. Este modelo es dado por la ecuación (11) y es una versión más completa de la propuesta de (Larsen & Gustafsson, 2001), de manera que si en la ecuación (11) se asume que $G/E \to 0$ se obtiene la ecuación (8). Al existir esta conexión, la ecuación (11) también aparece como un caso especial del modelo de (Jensen, 2003) si se considera que $\alpha \to 0$ en la ecuación (10).

Por otro lado, Ballerini (Ballerini, 2004, 2006) en un esfuerzo por extender la aplicabilidad del modelo de van der Put y Leitjen (Van der Put & Leijten, 2000) desarrolló un modelo semiempírico dado por la ecuación (12). Inicialmente, modificó ligeramente la ecuación (9) para predecir mejor los ensayos experimentales con un solo pasador ubicado en el centro de la luz de la viga. Después incluyó dos factores de corrección (f_w y f_r) para considerar la influencia de vigas cargadas con múltiples filas de clavijas y/o más de una unión (Figura 1.16). El primer factor (f_w) tiene en cuenta la influencia del ancho de la conexión (a_r) y la separación entre conexiones independientes (l_c). El segundo (f_r) considera el efecto de la altura de la conexión (h_m) y el número de filas de clavijas (n_r). Cabe señalar que esta propuesta es muy similar a la incluida en la antigua norma alemana (DIN 1052:2008).

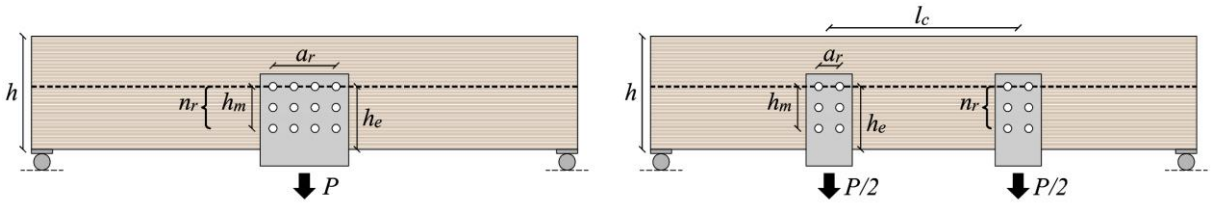

Figura 1.16: Definición de los parámetros considerados en el modelo de Ballerini.

Jensen *et al*. en (Jensen et al., 2003) desarrollaron otra propuesta analítica, pero utilizando esta vez la teoría de vigas de Timoshenko para cimentaciones elásticas. En este caso se plantea una viga dividida en dos partes por una fisura ficticia ubicada a una distancia h_e de la cara inferior de la viga (Figura 1.17a). Al fisurarse la viga, se considera que la parte inferior descansa sobre muelles elásticos conectados a la parte superior, la cual se supone infinitamente rígida. El análisis se aborda a través de una simplificación de la mecánica de fractura no lineal (NLFM, del inglés *Non-Linear Fracture Mechanics*), conocida como mecánica de fractura cuasi no lineal (QNLFM, del inglés *Quasi-Non-Linear Fracture Mechanics*). Este enfoque permite el análisis elástico lineal teniendo en cuenta la deformación, la resistencia y la energía de fractura del material en la zona en proceso de fractura. La base de esta aproximación es asumir que la forma de la ley cohesiva no influye en la carga de rotura y, por lo tanto, se puede utilizar una relación lineal tensión-apertura de fisura ($f-u$) como si fuese un material idealmente frágil. El punto clave de esta simplificación es que la pendiente (k) de la ley cohesiva se define de manera que el área bajo la curva es igual a G_c, tal como se muestra en la Figura 1.17b. Por lo tanto, se tienen en cuenta de manera correcta la tensión máxima a tracción perpendicular que puede resistir el material ($f_\mathrm{u,t}$) y G_c. Así la rigidez de los muelles (k) queda definida en función de las propiedades del material, siendo $k = f_\mathrm{u,t}^2/(2G_\mathrm{c})$. En base a QNLFM, la solución de P_u es dada por la ecuación (13). En esta propuesta, a diferencia de los modelos anteriores, se tiene en cuenta la resistencia a tracción perpendicular a la fibra ($f_\mathrm{u,t}$) y además P_u ya no es proporcional a la raíz cuadrada de G_c. Aun así, la solución de LEFM aparece como un caso especial de la solución de QNLFM. De hecho, la solución dada por la ecuación (13) podría expresarse como: $P_\mathrm{u} = \gamma P_\mathrm{u,LEFM}$, donde γ es un factor de efectividad dado en la Tabla 1.1 y $P_\mathrm{u,LEFM}$ corresponde con la solución analítica dada por la ecuación (8).

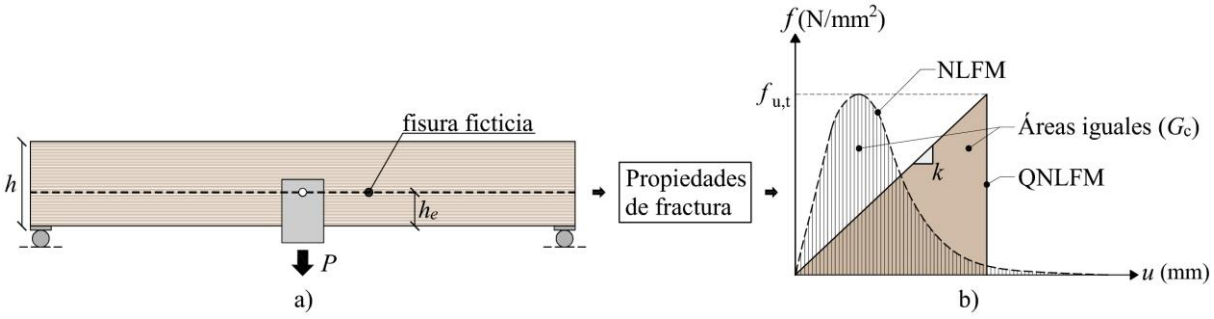

Figura 1.17: Enfoque de la mecánica de fractura cuasi no lineal (QNLFM): a) mecanismo de rotura; b) ley cohesiva.

Los modelos de diseño analíticos basados en LEFM dados por las ecuaciones (8) y (11) están limitados a situaciones en las que la distancia h_e es pequeña en comparación con h. Lo mismo ocurre con el modelo analítico desarrollado bajo el enfoque de QNLFM dado por la ecuación (13). Sin embargo, el

resto de los modelos analíticos ((9) y (10)) no tienen esta limitación. Dado que la ecuación (8) aparece como un caso especial de la ecuación (9) cuando $h \to \infty$, Jensen *et al.* (Jensen et al., 2015) realizaron una propuesta semiempírica fusionando la solución derivada de QNLFM y de LEFM sin la limitación de h_e. Como ya se ha comentado, la ecuación (13) puede expresarse como $P_{\mathrm{u}} = \gamma P_{\mathrm{u,LEFM}}$, donde $P_{\mathrm{u,LEFM}}$ es dado por la ecuación (8) y sustituido en esta propuesta por la ecuación (9), resultando la ecuación (14).

Franke y Quenneville (Franke & Quenneville, 2011b) presentaron uno de los modelos más completos que se puede encontrar en la literatura, el cual ha sido desarrollado bajo el enfoque de NLFM. Por primera vez se plantea un criterio de fallo que tiene en cuenta la energía de fractura en modo I y II (G_{Ic} y G_{IIc}, respectivamente) considerando la interacción entre los distintos modos según un criterio de fallo cuadrático. Esta propuesta es dada por la ecuación (15) y fue desarrollada empíricamente en base a un estudio paramétrico que involucraba tanto ensayos experimentales como numéricos, aunque fueron estos últimos los que más peso tuvieron. En el trabajo se evaluó la influencia de diferentes parámetros geométricos en la carga de rotura (P_{u}), analizando para tal fin más de cien configuraciones diferentes. Los resultados desvelaron el fuerte impacto de algunos de los parámetros estudiados, como el canto de la viga (h), la distancia al borde cargado (h_e), el ancho de la conexión (a_r) y el número de filas de clavijas de la conexión (n_r), formando parte del modelo propuesto. Los ensayos numéricos se llevaron a cabo utilizando CZMs mediante FEA, asumiendo que la viga estaba dividida en dos partes por una fisura ficticia ubicada en la fila de clavijas más alejada del borde cargado (Figura 1.18a). El patrón de fractura que une las dos partes de la viga fue introducido en FEM por medio de elementos finitos de interfaz, a los cuales se asoció la ley cohesiva mostrada en la Figura 1.18b. Los análisis numéricos fueron realizados en base a las investigaciones realizadas por los mismos autores en (Franke & Quenneville, 2010, 2011a) y cabe señalar que para definir la forma de la ley cohesiva se tomó como $f_{\mathrm{u,I}}$ la resistencia a tracción perpendicular a la fibra de la madera ($f_{\mathrm{t,90}}$) y como $f_{\mathrm{u,II}}$ la resistencia a cortante (f_{s}). Además, como valor de la rigidez inicial (k_i) se asumió el correspondiente con el módulo de elasticidad en la dirección aplicada (E_i), de manera que la forma de la ley cohesiva queda totalmente definida.

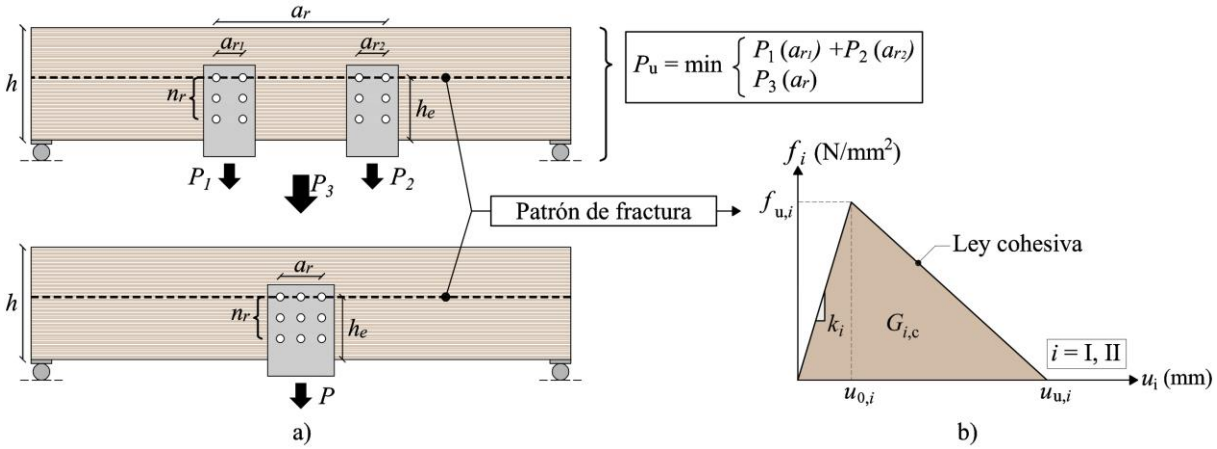

Figura 1.18: Modelo de Franke y Quenneville: a) mecanismo de rotura; b) ley cohesiva.

Tabla 1.1. Modelos de diseño de la capacidad de carga frente a la hienda de vigas cargadas perpendicularmente a la fibra por medio de uniones con clavijas.

Referencia	Modelo de diseño		Ecuación
LEFM			
(Larsen & Gustafsson, 2001)	$P_u = 2bC_1\sqrt{h_e}$	$C_1 = \sqrt{\frac{5}{3}GG_c}$	(8)
(Van der Put & Leijten, 2000)	$P_u = 2bC_1\sqrt{\frac{h_e}{1-\alpha}}$	$C_1 = \sqrt{\frac{5}{3}GG_c}$	(9)
(Jensen, 2003)	$P_u = 2bC_1\sqrt{\frac{h_e}{1-\alpha+\frac{15}{6}\frac{G}{E}\left(\frac{a}{h_e}\right)^2\left(1-\alpha^3\right)}}$	$C_1 = \sqrt{\frac{5}{3}GG_c}$	(10)
(Jensen et al., 2012)	$P_u = 2bC_1\sqrt{\frac{h_e}{1+\frac{15}{6}\frac{G}{E}\left(\frac{a}{h_e}\right)^2}}$	$C_1 = \sqrt{\frac{5}{3}GG_c}$	(11)
(Ballerini, 2004)	$P_u = 2bC_1\sqrt{\frac{h_e}{1-\alpha^3}}f_w f_r$	$C_1 = \sqrt{\frac{5}{3}GG_c}$ $f_w = \min\left\{1+0.75\left(\frac{a_r+l_c}{h}\right);\ 2.2\right\}$ $f_r = 1+1.75\frac{k}{1+k};\ k = \frac{n_r \cdot h_m}{1000}$	(12)
QNLFM			
(Jensen et al., 2003)	$P_u = \gamma 2bC_1\sqrt{h_e}$	$C_1 = \sqrt{\frac{5}{3}GG_c}$ $\gamma = \frac{\sqrt{2\zeta+1}}{\zeta+1}$ $\zeta = \frac{C_1}{f_{u,t}}\sqrt{10\frac{G}{E}\frac{1}{h_e}}$	(13)
LEFM + QNLFM			
(Jensen et al., 2015)	$P_u = \gamma 2bC_1\sqrt{\frac{h_e}{1-\alpha}}$	$C_1 = \sqrt{\frac{5}{3}GG_c}$ $\gamma = \frac{\sqrt{2\zeta+1}}{\zeta+1}$ $\zeta = \frac{C_1}{f_{u,t}}\sqrt{10\frac{G}{E}\frac{1}{h_e}}$	(14)

NLFM

(Franke & Quenneville, 2011b)

$$P_u = \frac{b \cdot 10^3}{\left(\frac{G_{I,norm}}{G_{Ic}} + \frac{G_{II,norm}}{G_{IIc}}\right)} \cdot k_r$$

$$P_u^* = \min \begin{cases} P_1(a_{r1}) + P_2(a_{r2}) \\ P_3(a_r) \end{cases}$$

* Consultar Figura 1.18

$$G_{I,norm} = e^{\left(h^{-1}\left(200 - 10 h_e \cdot h^{-0.25} - a_r\right)\right)}$$

$$G_{II,norm} = \left(0.05 + 0.12 \frac{h_e}{h} + 1 \cdot 10^{-3} a_r\right)$$

$$k_r = \begin{cases} 1 & \text{for } n_r = 1 \text{ fila} \\ 0.1 + \left(\arctan(n_r)\right)^{0.6} & \text{for } n_r > 1 \text{ filas} \end{cases}$$

(15)

1.3.3. Expresión del Eurocódigo 5

La expresión propuesta en el Eurocódigo 5 (UNE EN 1995-1-1:2016) para calcular la capacidad de carga frente a la hienda de un elemento de madera con conexiones tipo clavija sometido a tracción perpendicular a la fibra es la siguiente:

$$F_{v,Ed} \leq F_{90,Rd} \qquad \text{con} \qquad F_{v,Ed} = \max \begin{cases} F_{v,Ed,1} \\ F_{v,Ed,2} \end{cases}; \qquad F_{90,Rd} = \frac{F_{90,Rk}}{\gamma_M} k_{mod} \tag{16}$$

donde $F_{v,Ed,1}$ y $F_{v,Ed,2}$ son los esfuerzos de cortante del elemento principal a cada lado de la conexión en valor de diseño (Figura 1.19) y $F_{90,Rd}$ es el valor de cálculo de la capacidad de carga frente a la hienda, calculado a partir del valor característico ($F_{90,Rk}$) considerando los factores de modificación correspondientes, es decir, el coeficiente parcial para las propiedades del material (γ_M) y el factor de modificación que tiene en cuenta el efecto de la duración de la carga y del contenido de humedad (k_{mod}).

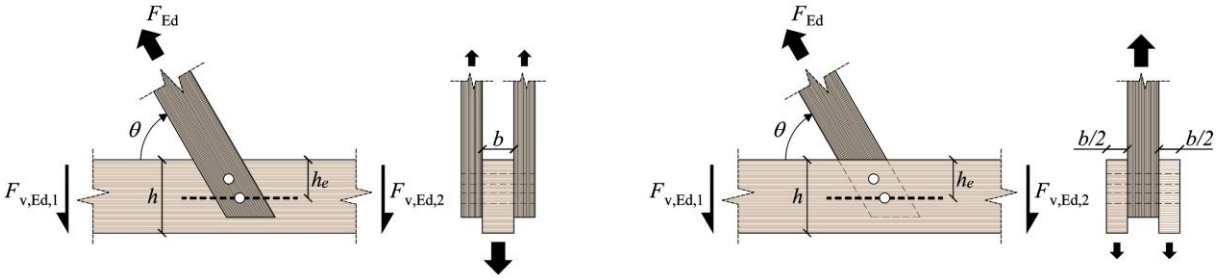

Figura 1.19: Esquema de diseño de una unión con pasadores con posibilidad de hienda por tensiones de tracción perpendicular a la fibra, según el Eurocódigo 5.

El valor característico, en N, de la capacidad de carga frente a la hienda de un elemento cargado mediante una unión con clavijas es dado por la siguiente expresión:

$$F_{90,Rk} = 14 b \sqrt{\frac{h_e}{1 - \alpha}} \tag{17}$$

donde b es el ancho del elemento de madera en mm y α (h_e/h) es un parámetro adimensional que tiene en cuenta la relación entre la distancia al borde cargado (h_e) y el canto del elemento a comprobar (h). El valor constante de 14 tiene unidades de $\mathrm{N/mm^{1.5}}$ y es sólo válido para maderas de coníferas.

La ecuación (17) es una simplificación de la versión original sugerida por van der Put y Leijten (Van der Put & Leijten, 2000) para comprobar la capacidad de carga frente a la hienda de elementos susceptibles de sufrir este tipo de fallo. El enfoque de diseño de esta propuesta está basado en los principios de LEFM y fue desarrollada para predecir el esfuerzo cortante máximo (V_{u}) que agotaba la sección de una viga biapoyada cargada en el centro de la luz por una fuerza puntual de valor igual a P, resultando la siguiente expresión:

$$V_{\mathrm{u}} = bC_1\sqrt{\frac{h_e}{1-\alpha}} \qquad con \qquad C_1 = \sqrt{\frac{5}{3}GG_{\mathrm{c}}} \tag{18}$$

dónde G y G_{c} son el módulo de rigidez transversal y la tasa crítica de liberación de energía en modo I, respectivamente. Para la hipótesis de carga considerada, $V_{\mathrm{u}} = P_{\mathrm{u}}/2$, la ecuación (18) corresponde con la mitad del valor de la ecuación (9) dada en la Tabla 1.1 de la subsección 1.3.2. La ecuación (18) se consideró válida para valores de $h_e < 0.7h$ y situaciones de diseño en las que se asuma que la fisura se propaga de manera uniforme a través de todo el ancho (b) del elemento. Por otro lado, los autores propusieron un valor característico de $C_1 \approx 10\ \mathrm{N/mm^{1.5}}$ para maderas de coníferas, el cual fue obtenido a partir de los resultados de un número limitado de ensayos experimentales disponibles en la literatura de vigas biapoyadas cargadas en el centro de la luz por medio de uniones con diferentes configuraciones de clavijas. Sin embargo, en la comprobación del Eurocódigo 5 (ec. (17)) se adoptó un valor de $C_1 = 14\ \mathrm{N/mm^{1.5}}$, sólo válido para maderas de coníferas. En consecuencia, la madera de frondosas queda fuera de dicha comprobación, ya que la expresión incluida en el Eurocódigo 5 no depende explícitamente de ninguna propiedad del material, como la resistencia, la rigidez o la tasa crítica de liberación de energía.

2. Objetivos

El objetivo general de la investigación presentada en esta tesis doctoral es ampliar el conocimiento sobre el fallo por hienda en vigas de haya europea (*Fagus sylvatica* L.) cargadas perpendicularmente a la fibra mediante conexiones con pasadores, bajo el enfoque de la mecánica de fractura no lineal (NLFM). Para alcanzar dicho objetivo se han llevado a cabo investigaciones en tres líneas de trabajo claramente diferenciadas pero complementarias.

Determinación de las propiedades elásticas (Publicación I)
En esta línea se plantea como objetivo específico la determinación experimental de las doce constantes de elasticidad de la madera de haya europea, que configuran la matriz de flexibilidad del material y permiten definir la matriz de rigidez en cualquier modelo numérico. Esto incluye tres módulos de elasticidad ($E_{\mathrm{L}}, E_{\mathrm{R}}, E_{\mathrm{T}}$), tres módulos de rigidez a cortante ($G_{\mathrm{LR}}, G_{\mathrm{LT}}, G_{\mathrm{RT}}$) y seis coeficientes de Poisson (ν_{LR}, ν_{LT}, ν_{RL}, ν_{RT}, ν_{TL}, ν_{TR}). Se llevan a cabo ensayos de compresión con medición de las deformaciones mediante técnicas de correlación de imágenes digitales (DIC). Se comparan los resultados con los obtenidos mediante técnicas de medición por ultrasonidos.

De manera complementaria al estudio principal, la publicación incluye un estudio adicional que extiende la determinación de las constantes de elasticidad a la madera de haya europea modificada a tres niveles de temperatura diferentes: 180 ºC (T1), 200 ºC (T2) y 230 ºC (T3).

Determinación de las propiedades de fractura (Publicación II y Publicación III)
En esta línea se plantean como objetivos específicos la determinación experimental y validación numérica de las principales propiedades de fractura del haya europea en los modos I y II de carga, para los sistemas de propagación de fractura TL y RL. Se determinan la tasa crítica de liberación de energía ($G_{\mathrm{Ic,TL}}$, $G_{\mathrm{IIc,TL}}$, $G_{\mathrm{IIc,RL}}$) y las leyes cohesivas del material para ambos modos. Estas propiedades son importantes y necesarias para analizar el comportamiento a fractura de elementos estructurales susceptibles de fallos frágiles por hienda, adquiriendo especial relevancia en análisis numéricos bajo el enfoque de la mecánica de fractura no lineal (NLFM).

Análisis de la capacidad de carga frente a la hienda (Publicación IV)
El objetivo específico de este trabajo consiste en el análisis de la influencia de diferentes parámetros relacionados con la geometría de la unión en la capacidad de carga frente a la hienda de vigas de haya cargadas perpendicularmente a la fibra mediante uniones con pasadores, colocados a una distancia del borde cargado (h_e) inferior a 0,7 veces el canto de la viga. Se analizan los siguientes parámetros: 1) número de pasadores (uno y dos); 2) esbeltez de la viga; 3) distancia de los pasadores a los apoyos; 4) separación entre los pasadores en la dirección longitudinal de la viga; 5) distancia entre conexiones dispuestas simétricamente respecto del centro de la viga. Para ello, se han llevado a cabo ensayos experimentales de las diferentes configuraciones, así como análisis numéricos por elementos finitos bajo el enfoque de la mecánica de fractura no lineal (NLFM) utilizando modelos de zona cohesiva (CZM), capaces de reproducir el fallo por hienda a partir de la implementación de las propiedades elásticas y de fractura determinadas para el material. Los resultados son comparados con los valores de las cargas de fallo por hienda estimadas aplicando la expresión incluida en el Eurocódigo 5 y dos de los modelos

analíticos disponibles en la literatura que ofrecen una formulación más completa en cuanto a la consideración de diferentes parámetros geométricos de la conexión y propiedades del material.

3. Materiales y métodos

Para la consecución de los objetivos de esta tesis doctoral se aplicaron diferentes métodos, tanto experimentales como analíticos y numéricos. En cada una de las respectivas investigaciones se llevó a cabo un análisis previo del estado de la cuestión, el cual se resume en la publicación correspondiente (ver Publicaciones I, II, III y IV).

3.1. Material

Para la realización de todos los ensayos experimentales, se utilizó haya europea (*Fagus sylvatica* L.) procedente de Austria. En cada grupo de ensayos se utilizaron probetas procedentes de diferentes tablas para poder tener en cuenta la variabilidad inherente al material. Todas las probetas de pequeño tamaño mecanizadas para los objetivos de caracterización de las propiedades elásticas y de fractura estaban libres de defectos (Publicaciones I, II y III). Las muestras de gran tamaño fabricadas para estudiar la capacidad de carga frente a la hienda (Publicación IV) se clasificaron visualmente según la norma (DIN 4074-5:2008), correspondiendo con una clase resistente D40 (UNE EN 1912:2012). No obstante, la descripción detallada de la preparación final, tamaño y geometría de las probetas para cada una de las investigaciones se puede encontrar en las publicaciones específicas.

Antes de realizar cada grupo de ensayos, la madera fue acondicionada a una temperatura de 20 ºC y un 65 % de humedad relativa hasta alcanzar el contenido de humedad de equilibrio. El contenido de humedad se determinó mediante el método de secado en horno utilizando una sección tomada de cada tablero siguiendo la norma (UNE EN 13183-1:2002) EN 13183-1:2002. La densidad se midió utilizando una sección tomada de cada tablero según la norma (UNE EN 408:2010+A1:2012).

A continuación, se resumen los aspectos más relevantes de los métodos aplicados para cada uno de los objetivos planteados. Para obtener información más detallada, se remite al lector a cada una de las publicaciones indicadas en cada caso.

3.2. Propiedades elásticas

Los trabajos realizados consistieron en la determinación de las propiedades elásticas del haya europea. Para ello, se determinaron las doce constantes de elasticidad que definen la matriz de flexibilidad del material: tres módulos de elasticidad, tres módulos de rigidez a cortante y seis coeficientes de Poisson. Se utilizaron técnicas de medición estáticas (ensayos de compresión) y se compararon los resultados con los obtenidos mediante técnicas de medición dinámicas (ultrasonidos) realizadas con material procedente del mismo lote (Majano-Majano, 2014).

Los detalles relativos a este trabajo se incluyen en la Publicación I.

Se realizaron series de ensayos a compresión en probetas con diferentes orientaciones de fibra respecto a la dirección de carga, según la constante de elasticidad a determinar.

Los ensayos de compresión paralela a la fibra fueron llevados a cabo siguiendo el procedimiento indicado en la norma ISO 13061-17 (ISO 13061-17:2017), utilizando probetas prismáticas de 30×30 mm^2 de sección y 60 mm de longitud. De estas probetas se determinaron E_{L}, ν_{LR} y ν_{LT}.

Los ensayos de compresión perpendicular a la fibra fueron llevados a cabo siguiendo el procedimiento indicado en la norma ISO 13061-5 (ISO 13061-5:2020), utilizando probetas prismáticas orientadas en la dirección radial y tangencial de 30×60 mm^2 de superficie de compresión y una altura de 30 mm. De la probeta orientada en la dirección radial se determinaron E_{R}, ν_{RL} y ν_{RT}, y de la orientada en la dirección tangencial E_{T}, ν_{TL} y ν_{TR}.

Los ensayos de compresión para determinar los módulos de rigidez a cortante fueron realizados utilizando probetas prismáticas con las direcciones principales orientadas a 45º respecto de la dirección de la carga. Para determinar G_{LR} y G_{RT} se utilizaron probetas de 30×30 mm^2 de sección y una longitud de 60 mm. Para obtener G_{RT} se utilizaron probetas de 30×30 mm^2 de sección y 38 mm de longitud, debido a la limitación del espesor del lote de tablas utilizadas.

Las deformaciones se midieron usando la técnica de correlación de imágenes digitales (DIC, por sus siglas en inglés, *Digital Image Correlation*). La técnica DIC es una técnica de medición de campo completo. Compara imágenes capturadas antes y después de la deformación mediante algoritmos de correlación analizando los desplazamientos de subpíxeles para obtener mapas detallados de la deformación. La técnica DIC ofrece gran precisión, versatilidad y una visualización completa de las deformaciones. Requiere un patrón moteado para tomar mediciones precisas, el cual se pintó en las caras de interés de las probetas con una granulometría y contraste óptimo para la correlación de imágenes. Este patrón se realizó en dos etapas: primero, se aplicó con spray una fina capa y homogénea de pintura blanca mate, y luego se proyectó un patrón de puntos negros sobre la superficie utilizando un aerógrafo.

El sistema de medición DIC utilizado fue ARAMIS® 3D (GOM GmbH, 2007), el cual consta de dos cámaras frontales con una resolución de 5 megapíxeles, acopladas a lentes de 35 mm. El sistema óptico se calibró según las especificaciones descritas por el fabricante (GOM GmbH, 2007). Para tal fin, se tomaron 13 imágenes y se verificó que los resultados de la calibración estuvieran dentro del rango aceptable establecido. El procedimiento de calibración se realizó utilizando el panel de calibración CP20 de acuerdo con el tamaño del área de estudio. Se seleccionó un tamaño de subconjunto de 15×15 píxeles^2 y un paso de subconjunto de 13×13 píxeles^2 para mejorar la resolución espacial en un compromiso con respecto a la precisión. Para obtener mediciones precisas, las cámaras se colocaron a 400 mm de la superficie de interés y se configuraron para un campo de visión de 80×65 mm^2. En consecuencia, se estableció un ángulo de 25° entre las cámaras. La separación entre ellas y el eje de referencia se fijó en 138 mm. Además, para asegurar el correcto enfoque de la superficie de la muestra, el dispositivo incorporó dos focos de luz blanca con intensidad lumínica regulable para evitar una exposición lumínica insuficiente o excesiva. Los focos y el tiempo de obturación se configuraron para garantizar un contraste e iluminación adecuados de la probeta.

Para aprovechar el potencial de las mediciones en 3D, las probetas fueron colocadas de manera que la superficie de dos caras adyacentes fuera visible por el equipo óptico (Figura 3.1) y así monitorizar las deformaciones de manera simultánea. Sin embargo, para obtener los módulos de rigidez a cortante, se grabaron las deformaciones en 2D ya que en estos casos sólo una de las caras de la probeta era útil para la obtención de los resultados.

Se estableció una velocidad constante de ensayo que varió entre 0,2 y 0,4 mm/min (dependiendo de la probeta) manteniendo el material en régimen elástico, de modo que se pudieran derivar todas las constantes elásticas posibles de una misma probeta. En consecuencia, sólo fueron necesarias ocho probetas para determinar los módulos de elasticidad y los coeficientes de Poisson, ya que estas probetas pueden compartir la misma geometría y orientación. Sin embargo, los módulos de rigidez a cortante requieren diferentes orientaciones de las probetas. En este caso se mecanizaron entre ocho y trece probetas por cada constante, llevando los ensayos hasta rotura.

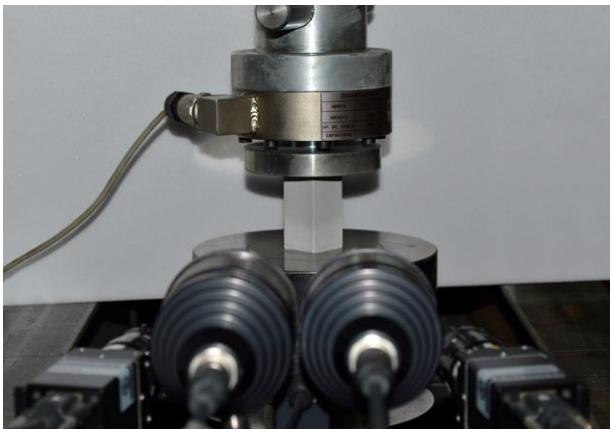

Figura 3.1: Ensayo de compresión con sistema de medición de deformaciones ARAMIS® 3D.

3.3. Propiedades de fractura

Los trabajos realizados consistieron en la determinación de las propiedades de fractura (tasa crítica de liberación de energía y ley cohesiva) del haya europea, para el modo I de fractura detalladas en la Publicación II, y modo II de fractura detalladas en la Publicación III.

3.3.1. Configuración de los ensayos

3.3.1.1. Modo I

Se realizaron un total de diecisiete probetas tipo DCB (del inglés *Double Cantilever Beam*), orientadas de acuerdo con el sistema de propagación de fractura TL. Las probetas consistían en pequeñas vigas rectangulares con una sección transversal de 20×20 mm^2 y una longitud de 250 mm (Figura 3.2a). En ellas se mecanizó una fisura de 1 mm de espesor y 110 mm de longitud total con una sierra de cinta en la mitad de su altura. Antes de los ensayos, esta fisura se prolongó 1 mm más usando una cuchilla. Se realizaron dos taladros de 3 mm de diámetro para introducir dos pasadores de acero en la probeta y fijarla al útil de carga (Figura 3.2b). Para transferir la carga a la probeta, se empleó una máquina de ensayos universal con control por recorrido y una velocidad constante de 2 mm/min.

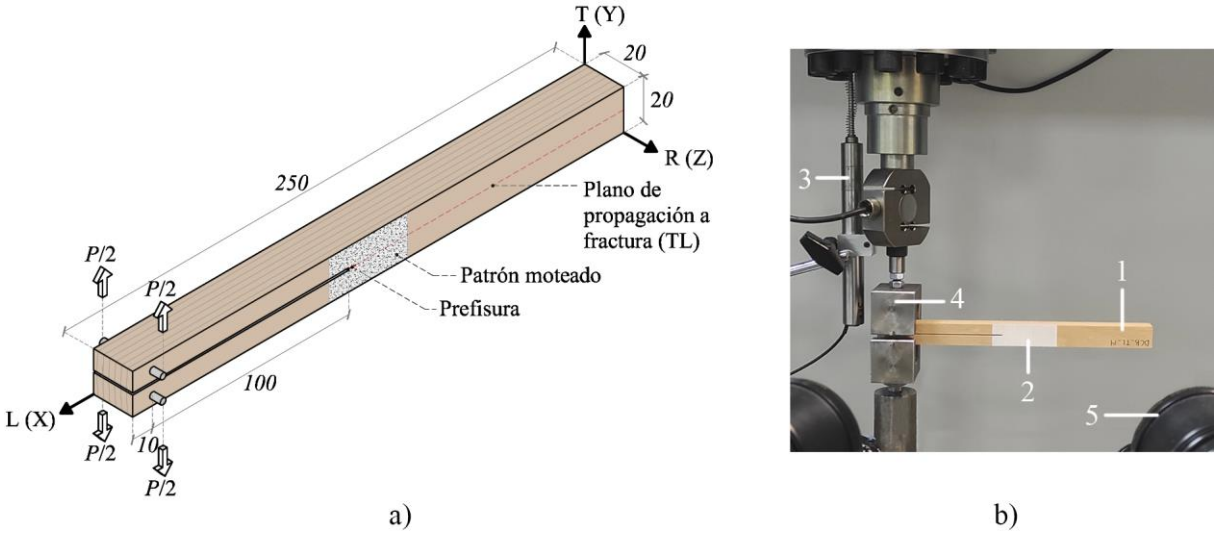

Figura 3.2: a) Geometría de la probeta. b) Configuración del ensayo para la probeta DCB: 1) probeta de haya; 2) patrón moteado; 3) LVDT; 4) útil de transferencia de carga; 5) equipamiento del sistema DIC.

El desplazamiento en la zona de aplicación de la carga se midió mediante un transformador de desplazamiento lineal variable (LVDT, del inglés *Linear Variable Displacement Transformer*). Los desplazamientos en torno a la punta de la fisura se midieron utilizando la técnica DIC (ver subsección 3.2).

3.3.1.2. Modo II

Se realizaron un total de doce probetas del tipo ENF (del inglés *End Notched Flexure*), orientadas según el sistema de propagación de fractura RL y catorce según el TL. Las probetas consistían en pequeñas vigas con una sección transversal de 20×20 mm^2 y una longitud total de 500 mm (Figura 3.3a). En ellas se mecanizó una fisura en la mitad de la altura utilizando una sierra de banda. Antes de realizar los ensayos, la fisura se prolongó 1 mm más usando una cuchilla afilada.

Las probetas se sometieron a ensayos de flexión a tres puntos a una velocidad constante de 2 mm/min. Para evitar los efectos de fricción durante el ensayo debido a la deformación de la probeta, se colocaron dos láminas de teflón rellenando la fisura en la zona de los apoyos, de modo que se garantizó el contacto entre los dos brazos de la probeta y su deslizamiento sin fricción.

El desplazamiento en el punto de aplicación de carga se registró mediante un LVDT (ver Figura 3.3b). Los desplazamientos en torno a la punta de la fisura se midieron utilizando la técnica DIC (ver subsección 3.2).

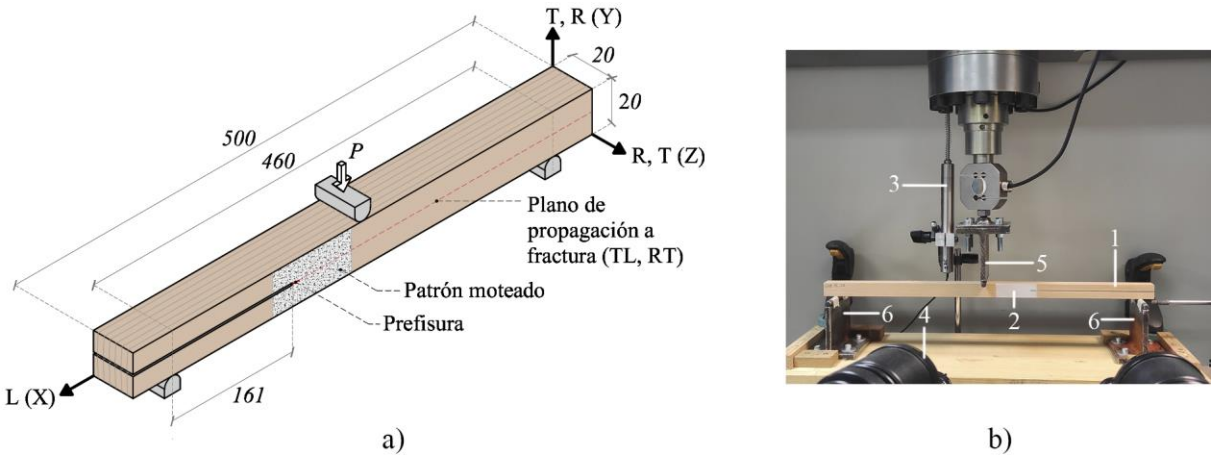

Figura 3.3: a) Geometría de la probeta. b) Configuración del ensayo para la probeta ENF: 1) probeta de haya; 2) patrón moteado; 3) LVDT; 4) equipamiento del sistema DIC; 5) útil de transferencia de carga; 6) apoyos.

3.3.2. Leyes cohesivas

Los datos recabados de los ensayos experimentales se utilizaron para determinar la tasa crítica de liberación de energía (G_c) y las leyes cohesivas del material en los modos I y II.

La tasa crítica de liberación de energía se obtuvo de las curvas de resistencia (curvas-*R*) aplicando el Método basado en la flexibilidad (CBBM, del inglés *Compliance Based Beam Method*). Este método está basado en la teoría de vigas y en el concepto de longitud de fisura equivalente. Tiene la ventaja de que sólo requiere la curva carga-desplazamiento del ensayo, por lo que no es necesario medir el crecimiento de la fisura durante el mismo, lo que supone una gran ventaja en madera. El método se aplicó de acuerdo con lo descrito en (de Moura et al., 2008) para el modo I y en (de Moura et al., 2006) para el modo II.

Las leyes cohesivas se determinaron aplicando el método directo, como la derivada de la curva que relaciona la tasa de liberación de energía de deformación (G, obtenida aplicando el CBBM) con el desplazamiento de apertura de fisura (CTOD para el modo I y CTSD para el modo II, del inglés *Crack Tip Opening Displacement* y *Crack Tip Shear Displacement*, respectivamente) medido con DIC, para el modo correspondiente. Para reducir el ruido introducido por los datos experimentales y disponer de una función continua que pueda derivarse, se ajustó una función del tipo logística a dicha curva (ec. (19)). La derivada de esta función da como resultado la ley cohesiva (ec. (20)), que describe la relación entre la tasa de liberación de energía, la tensión y la apertura de fisura en el modo considerado (I o II).

$$G_i = \frac{A_1 - A_2}{1 + (u_i / u_0)^p} + A_2 \qquad i = \mathrm{I, II} \tag{19}$$

$$f_i = -\frac{p(A_1 - A_2)(u_i / u_0)^{p-1}}{u_0 (1 + (u_i / u_0)^p)^2} \qquad i = \mathrm{I, II} \tag{20}$$

3.3.3. Análisis por elementos finitos

El procedimiento experimental se validó mediante análisis por elementos finitos (FEA) utilizando modelos de zonas cohesivas (CZM). Para tal fin, se realizó un modelo de elementos finitos (FEM) replicando el ensayo experimental (DCB o ENF) y se definió geométricamente en el modelo un patrón de propagación de la fisura siguiendo la dirección de la fisura existente, acorde con los resultados experimentales. Este patrón se introdujo en el modelo mediante elementos finitos de interfaz, a los cuales se asoció una ley cohesiva similar a la experimental, de modo que la tasa crítica de liberación de energía de la función implementada en FEA coincide con la determinada experimentalmente. Además, para considerar la variabilidad inherente de la madera, se implementaron dos leyes cohesivas adicionales que representaban el límite superior e inferior de las leyes cohesivas. Más detalles sobre las leyes cohesivas introducidas en FEA y el procedimiento de validación numérica empleado se pueden encontrar en la Publicación II (leyes que describen el modo I de fractura) y la Publicación III (leyes del modo II).

3.4. Capacidad de carga frente a la hienda

Los trabajos realizados consistieron en investigar de manera experimental y numérica la influencia en la capacidad de carga frente a la hienda de cinco parámetros relacionados con la geometría de la conexión en vigas de haya europea cargadas perpendicularmente a la fibra mediante uniones con pasadores. Todos los detalles de esta investigación se recogen en la Publicación IV.

3.4.1. Configuraciones analizadas

Se analizó el efecto que tiene la colocación de uno y dos pasadores para transferir la carga a la viga, la separación entre los pasadores en la dirección longitudinal de la viga y su cercanía a los apoyos. También se estudió la influencia de la esbeltez de las vigas y el efecto de colocar otra conexión dispuesta de manera simétrica respecto del centro de la viga, dando lugar a una viga con dos conexiones independientes. Las cargas de rotura de los ensayos experimentales se compararon tanto con las cargas estimadas por FEA como las deducidas a partir de algunos de los modelos de diseño más relevantes disponibles en la literatura, incluido el modelo recogido en el Eurocódigo 5.

Para conseguir el objetivo propuesto, la campaña de ensayos abarcó el análisis de 20 configuraciones geométricas diferentes (ver Figura 3.4), las cuales se dividieron en dos grupos de vigas en función de su canto: un primer grupo de vigas con 100 mm de canto y un segundo grupo con 200 mm de canto. Todas las vigas tenían una luz de 950 mm (1000 mm de longitud total) excepto las utilizadas para estudiar la influencia de su esbeltez, que se fabricaron con una luz de 450 mm (500 mm de longitud total). La carga se transfirió a las vigas por medio de uno o dos pasadores, dando lugar a 10 configuraciones de carga diferentes por cada grupo de vigas. En todas las geometrías propuestas, los pasadores se ubicaron en una misma fila y se colocaron a una distancia del borde cargado igual a cuatro veces el diámetro del pasador, que coincide con la distancia mínima que establece el Eurocódigo 5.

Para facilitar el análisis de la influencia de los diferentes parámetros propuestos, se establecieron dos configuraciones de referencia en cada grupo de vigas, correspondientes a las vigas de 950 mm de luz y una conexión con uno y dos pasadores ubicados en el centro de la luz. Los resultados de las vigas de referencia también se compararon con los disponibles en la literatura.

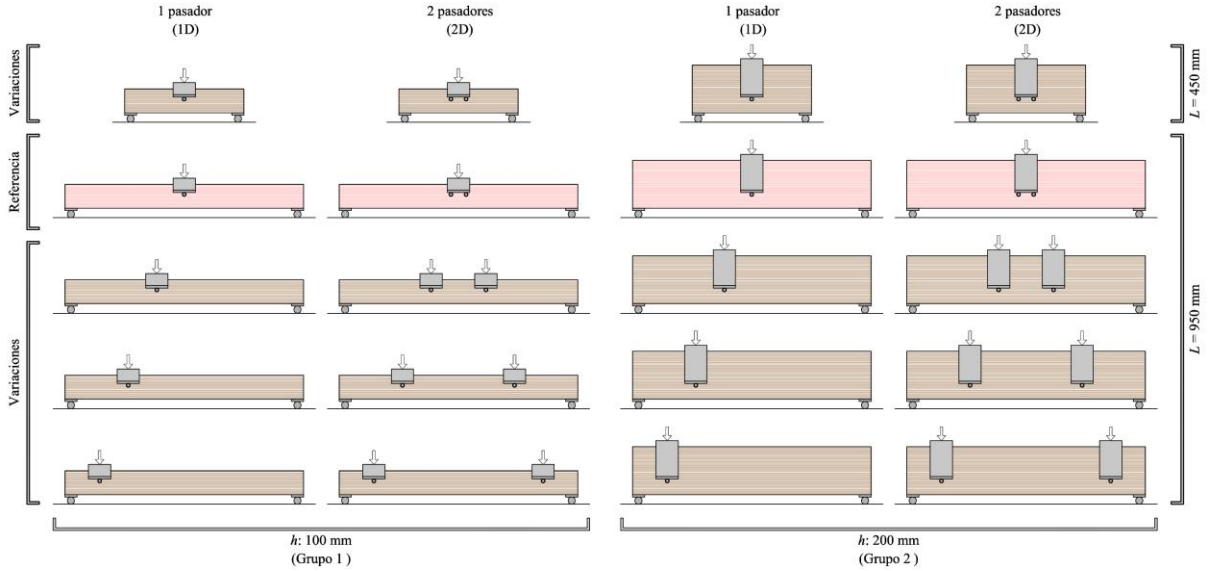

Figura 3.4: Configuraciones analizadas: configuraciones de referencia (en rojo) con conexiones de uno y dos pasadores colocadas en el centro de la luz para cada grupo de vigas y sus variaciones (en marrón) en cuanto a la posición de la conexión y la esbeltez.

3.4.2. Ensayos experimentales

Cada grupo de vigas se sometió a un ensayo de flexión a tres o cuatro puntos, dependiendo de la geometría ensayada (Figura 3.4). La velocidad del ensayo se ajustó a cada geometría para que el fallo se alcanzase en 5 min, aproximadamente. Se monitorizó tanto la deformación de las vigas como el deslizamiento de las uniones mediante LVDTs dispuestos en la cara inferior de la viga y en la parte inferior de las placas de carga, en este caso lo más cerca posible de los pasadores, registrándose así las curvas carga-desplazamiento de la cara inferior de la viga y la curva carga-deslizamiento de la unión.

Todas las vigas tenían un espesor de 48 mm y la orientación principal predominante de la sección transversal era la dirección tangencial, de modo que el sistema de propagación de fractura correspondía al TL. Para transferir la carga a las vigas se utilizaron pasadores de 16 mm de diámetro fabricados con acero de calidad S355 insertados sin holgura en las vigas.

3.4.3. Análisis por elementos finitos

Se realizaron modelos numéricos de elementos finitos de cada una de las geometrías estudiadas en la campaña experimental (ver Figura 3.4). El propósito fue desarrollar un modelo numérico lo más sencillo posible que proporcionase resultados suficientemente seguros desde el punto de vista del diseño estructural. De acuerdo con esto, la modelización del fallo por hienda se abordó utilizando CZMs para simular el inicio y la propagación de la fisura. Los modelos se realizaron en 2D, ya que los pasadores eran suficientemente rígidos para garantizar que la fisura se propagase de manera homogénea a través de todo el ancho de la viga.

Para minimizar el tiempo de cálculo y de acuerdo con las observaciones de (Franke & Quenneville, 2011a) sólo se modeló un patrón de propagación de fisura. De acuerdo con los patrones de rotura observados experimentalmente, la fisura se situó en la mitad de la altura de los pasadores. Esta fisura se introdujo en el modelo por medio de elementos finitos de interfaz, a los cuales se asoció una ley cohesiva bilineal con una relación de ablandamiento lineal, para reproducir el proceso de fractura en modo mixto I + II. La forma de las leyes cohesivas correspondientes a los modos puros implementadas en los modelos numéricos para reproducir el modo mixto fueron una versión simplificada, pero equivalente, a la forma de las leyes cohesivas determinadas experimentalmente (Publicaciones II y III).

El contacto entre los elementos de acero y la madera fue introducido a través de superficies de contacto considerando un coeficiente de fricción entre los materiales. Se consideró un material elástico isotrópico para los elementos de acero y ortotrópico para los elementos de madera, implementando las propiedades elásticas del material obtenidas experimentalmente (Publicación IV). Sin embargo, se despreció el comportamiento plástico de la madera a fin de desarrollar un modelo numérico sencillo.

El modelo numérico propuesto se validó comparando las curvas numéricas carga-desplazamiento con las obtenidas experimentalmente.

3.4.4. Modelos analíticos

Los resultados de los ensayos experimentales y numéricos se compararon con los valores de la capacidad de carga frente a la hienda obtenidos aplicando la comprobación incluida en el Eurocódigo 5 (ver subsección 1.3.3) y dos de los modelos de diseño más completos disponibles en la literatura y descritos en la subsección 1.3.2. Uno de ellos es un modelo semiempírico, dado por la ecuación (14), que fusiona la solución derivada de QNLFM y LEFM. El otro es un modelo empírico, dado por la ecuación (15), que ha sido desarrollado bajo el enfoque de NLFM a través de un estudio paramétrico que incluye tanto ensayos experimentales como numéricos.

Cabe señalar que para derivar la expresión incluida en el Eurocódigo 5 se utilizó un valor corregido de C_1 = 14 N/mm$^{1.5}$. En este trabajo se decidió aplicar la expresión original (ec. (18)) y determinar el valor de C_1 correspondiente al haya europea considerando el módulo de rigidez a cortante (G_{LT}) y la energía de fractura crítica ($G_{\mathrm{Ic,TL}}$) para el modo I obtenidos experimentalmente (subsecciones 4.1 y 4.2), resultando en C_1 = 23,27 N/mm$^{1.5}$.

4. Resultados y discusión

A continuación, se presentan algunos de los principales resultados de los diferentes trabajos desarrollados. Para obtener información más detallada, se remite al lector a cada una de las publicaciones individuales que constituyen el compendio de publicaciones de la tesis doctoral.

4.1. Propiedades elásticas

El programa experimental llevado a cabo en la Publicación I relativo a la caracterización de las propiedades elásticas del haya europea, condujo a la determinación de las doce constantes de elasticidad que definen la matriz de flexibilidad de ortotropía del material: tres módulos de elasticidad (E_{L}, E_{R}, E_{T}), tres módulos de rigidez a cortante (G_{LR}, G_{LT}, G_{RT}) y seis coeficientes de Poisson (ν_{LR}, ν_{LT}, ν_{RL}, ν_{RT}, ν_{TL}, ν_{TR}), mediante ensayos de compresión midiendo las deformaciones con la técnica DIC. Los valores se compararon con resultados obtenidos mediante la técnica de ultrasonidos utilizando material del mismo lote (Majano-Majano, 2014). En las Tablas 4.1 y 4.2 se muestran los correspondientes valores medios y el coeficiente de variación de las constantes elásticas.

Tabla 4.1. Valores medios (x) en N/mm^2 y coeficiente de variación (C.V.) en % de los módulos de elasticidad (E) y de rigidez a cortante (G) de haya europea obtenidos mediante ensayos de compresión y ultrasonidos.

		E_{L}	E_{R}	E_{T}	G_{LR}	G_{LT}	G_{RT}
Compresión	x	13811	1590	832	1108	706	349
	C.V.	9,6	34,0	13,9	18,3	19,7	15,3
Ultrasonidos	x	14078	2953	1339	1369	994	520
	C.V.	3,5	2,0	6,6	20,8	9,6	10,5

Tabla 4.2. Valores medios (x) y coeficiente de variación (C.V.) en % de los coeficientes de Poisson (ν) de haya europea obtenidos mediante ensayos de compresión y la técnica de ultrasonidos.

		ν_{LR}	ν_{RL}	ν_{LT}	ν_{TL}	ν_{RT}	ν_{TR}
Compresión	x	0,44	0,06	0,51	0,04	0,62	0,32
	C.V.	3,5	48,1	5,9	55,5	12,2	13,0
Ultrasonidos	x	0,27	0,05	0,63	0,06	0,55	0,24
	C.V.	41,9	41,5	21,3	18,0	16,5	12,2

Para facilitar la comparación, en la Figura 4.1 se ilustra de manera conjunta los valores medios y los rangos de variación de los módulos de elasticidad y rigidez a cortante del haya obtenidos con las dos técnicas de ensayo.

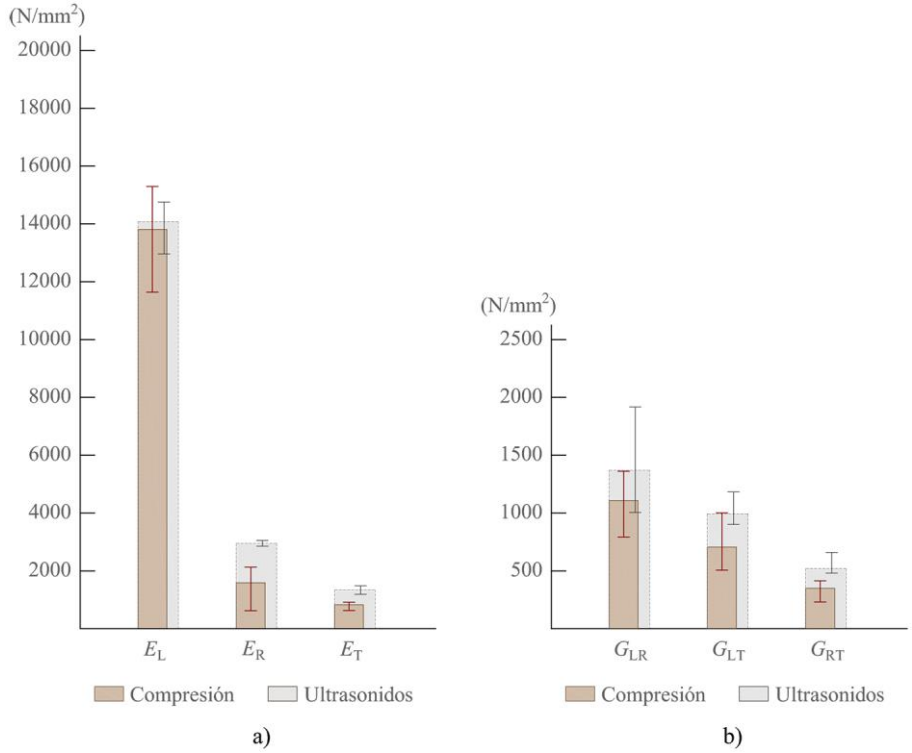

Figura 4.1: Valor medio y rango de variación de los módulos de elasticidad (a) y rigidez a cortante (b) del haya europea obtenidos a través de ensayos de ultrasonidos y de compresión.

Los valores de los módulos de elasticidad y de rigidez a cortante obtenidos mediante ultrasonidos resultaron mayores que con los derivados de ensayos estáticos y, para algunos casos, estas diferencias son importantes. Esto podría deberse a la variabilidad natural de la madera, ya que se utilizaron diferentes geometrías de muestras para los ensayos mecánicos y de ultrasonidos. En cualquier caso, los resultados de ambos tipos de ensayos para el haya están en el mismo rango que los publicados en la literatura (ver Publicación I). No obstante, es sabido que los módulos de elasticidad de la madera obtenidos a partir de ensayos dinámicos tienden a dar valores más altos que los obtenidos mediante ensayos estáticos (por ejemplo, (Hering et al., 2012; Keunecke et al., 2007)).

En la Figura 4.2 se representan los resultados de las seis relaciones de Poisson de la madera de haya europea.

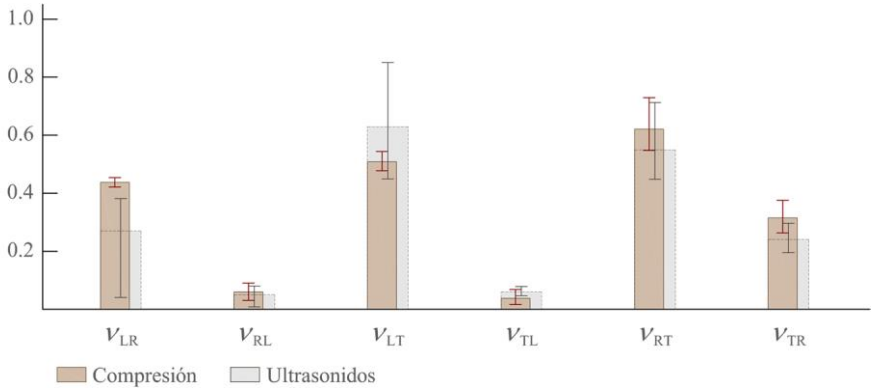

Figura 4.2: Valor medio y rango de variación de los coeficientes de Poisson del haya europea obtenidos mediante ensayos de ultrasonidos y de compresión.

Los coeficientes de Poisson más elevados se observaron en las muestras donde la dirección tangencial correspondía con la componente de deformación lateral pasiva (ν_{LT} y ν_{RT}), seguidos por los coeficientes de Poisson ν_{LR} y ν_{TR}, los cuales proporcionan la componente de deformación pasiva en la dirección radial. En cambio, los coeficientes de Poisson ν_{RL} y ν_{TL} mostraron valores significativamente inferiores a los anteriores, donde la dirección longitudinal del material correspondía con la componente de deformación lateral pasiva.

Los coeficientes de Poisson suelen caracterizarse por una alta variabilidad, que se observa por el elevado C.V. en algunos de los resultados (ver Tabla 4.2), especialmente cuando la dirección longitudinal corresponde a la componente de deformación lateral pasiva (ν_{RL} y ν_{TL}), superando el 50 % en algunos casos. Este es un problema bien conocido en los ensayos de madera, ya que las deformaciones en la dirección longitudinal son demasiado pequeñas para realizar mediciones satisfactorias y precisas. La alta variabilidad natural en los coeficientes de Poisson para la madera de haya europea también se puso de manifiesto en otros estudios (por ejemplo, (Hering et al., 2012; Ozyhar et al., 2012; Ozyhar et al., 2013), en los que se encontraron valores elevados con C.V. similares a los de este estudio.

A diferencia de lo observado en los módulos de elasticidad y de rigidez a cortante, los coeficientes de Poisson determinados mediante ensayos de ultrasonidos no muestran una tendencia general clara a ser más altos que los obtenidos por el método estático.

4.2. Propiedades de fractura

El programa experimental descrito en las Publicaciones II y III, enfocado en la caracterización de las propiedades de fractura del haya europea, permitió determinar la tasa crítica de liberación de energía (G_c) y la ley cohesiva del material para cada uno de los modos puros (I y II).

4.2.1. Tasa crítica de liberación de energía

En la Figura 4.3 se muestran los valores medios de G_c en modo I y II para los sistemas de propagación de fractura TL ($G_{Ic,TL}, G_{IIc,TL}$) y RL ($G_{IIc,RL}$) obtenidos experimentalmente a partir de las curvas de resistencia aplicando el método CBBM.

Tabla 4.3. Valores medios obtenidos experimentalmente de la tasa crítica de liberación de energía en modos I y II ($G_{Ic,TL}$, $G_{IIc,TL}$, $G_{IIc,RL}$), desviación estándar (Desv. Est.) y coeficiente de variación (C.V.) para los sistemas de propagación de fractura TL y RL.

	$\boldsymbol{G_{Ic,TL}}$ (N/mm)	$\boldsymbol{G_{IIc,RL}}$ (N/mm)	$\boldsymbol{G_{IIc,TL}}$ (N/mm)
Media	**0,46**	**2,29**	**1,17**
Desv. Est.	0,10	0,17	0,26
C.V. (%)	22,1%	7,5%	22,1%

En el caso del modo I, el valor de la tasa crítica de liberación de energía obtenido para el sistema de propagación de fractura TL (0,46 N/mm) es superior al de especies coníferas como *Picea abies* L., con un valor de 0,152 N/mm para $G_{Ic,TL}$ (Dourado et al., 2015). Sin embargo, es inferior al valor obtenido

para otras especies frondosas como *Eucalyptus globulus* L., que aplicando el mismo método presentó un valor de $G_{\mathrm{Ic,TL}}$ de 0,77 N/mm según (Majano-Majano et al., 2019).

En cuanto al modo II, el valor obtenido para el sistema de propagación de fractura RL (2,29 N/mm) es superior al obtenido en otras especies aplicando el mismo método. Por ejemplo, para la especie conífera *Pinus pinaster* se obtuvo un valor de $G_{\mathrm{IIc,RL}}$ de 1,15 N/mm en (Xavier et al., 2014). En el caso de *Eucalyptus globulus* L., el valor de $G_{\mathrm{IIc,RL}}$ fue de 1,54 N/mm (Majano-Majano et al., 2020).

Por otra parte, en el caso particular del modo II, el valor obtenido para el sistema de propagación de fractura RL (2,29 N/mm) es el doble del obtenido para TL (1,17 N/mm). Como se detalla en la Publicación III, el haya presenta un gran número de rayos leñosos en la dirección radial que cosen la superficie de fractura en el sistema de propagación RL. Esto podría explicar la gran diferencia entre los valores de $G_{\mathrm{IIc,RL}}$ y $G_{\mathrm{IIc,TL}}$.

4.2.2. Leyes cohesivas

Las leyes cohesivas describen la evolución de la tensión en función de la apertura de la fisura. El área bajo la curva corresponde con la energía de fractura (G_{c}). En la Figura 4.3 se muestran todas las curvas experimentales (en gris) y la ley cohesiva correspondiente con los parámetros medios de la función logística (en rojo), para el modo I de carga y el sistema de propagación de fractura TL.

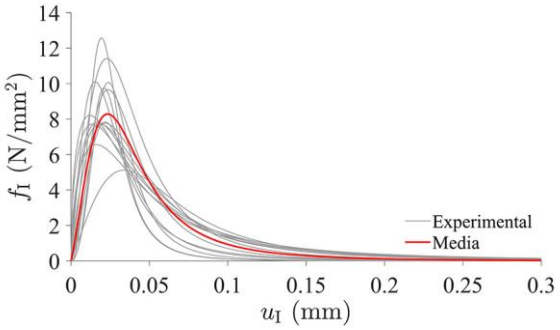

Figura 4.3: Leyes cohesivas experimentales (en gris) y ley cohesiva media (en rojo) para el modo I y sistema de propagación de fractura TL del haya europea.

Como puede observarse, los resultados obtenidos son consistentes. En la Tabla 4.4 se muestran los valores medios de los parámetros que definen la función logística (ec. (20)) que representa la ley cohesiva (A_1, A_2, u_0, p), la tensión de tracción máxima (f_{Iu}), el desplazamiento relativo que define el inicio del daño (u_{I0}), el desplazamiento relativo máximo (u_{Iu}) y la energía de fractura asociada a la ley cohesiva ($G_{\mathrm{I,ley}}$). Cabe señalar que la ley cohesiva media no representa los valores medios de $G_{\mathrm{I,ley}}$, f_{Iu}, u_{I0}, u_{Iu}.

Tabla 4.4. Valores de los parámetros que definen la función logística de la ley cohesiva (A_1, A_2, u_0, p), la tensión de tracción máxima (f_{Iu}), el desplazamiento relativo que define el inicio del daño (u_{I0}), el desplazamiento relativo máximo (u_{Iu}) y la energía de fractura asociada a la ley cohesiva ($G_{I,ley}$), para el modo I de carga y sistema de propagación de fractura TL del haya.

Modo I TL	A_1 (N/mm)	A_2 (N/mm)	u_0 (mm)	p (-)	f_{Iu} (N/mm^2)	u_{I0} (mm)	u_{Iu} (mm)	$G_{I,ley}$ (N/mm)
Media	**-0,005**	**0,46**	**0,037**	**2,16**	**8,74**	**0,020**	**0,416**	**0,46**
Desv. Est.	0,010	0,09	0,009	0,64	1,97	0,005	0,224	0,10
C.V.	-	20,9%	25,5%	29,8%	22,5%	27,1%	53,7%	21,3%

Es interesante señalar que el valor medio de f_{Iu} obtenido de las leyes cohesivas está en consonancia con el valor medio de resistencia a tracción perpendicular en la dirección tangencial de 8,9 N/mm^2 obtenido en (Ozyhar et al., 2012).

En cuanto al modo II de fractura, todas las leyes cohesivas experimentales (en gris) y media (en rojo) para los sistemas de propagación de fractura RL y TL se muestran en la Figura 4.4. Además, en las Tablas 4.5 (RL) y 4.6 (TL) se incluyen los valores medios de los parámetros que definen la función logística (ec. (20)) que representa la ley cohesiva (A_1, A_2, u_0, p), la tensión de cortante máxima (f_{IIu}), el desplazamiento relativo que define el inicio del daño (u_{II0}), el desplazamiento relativo máximo (u_{IIu}) y la energía de fractura asociada a la ley cohesiva ($G_{II,ley}$).

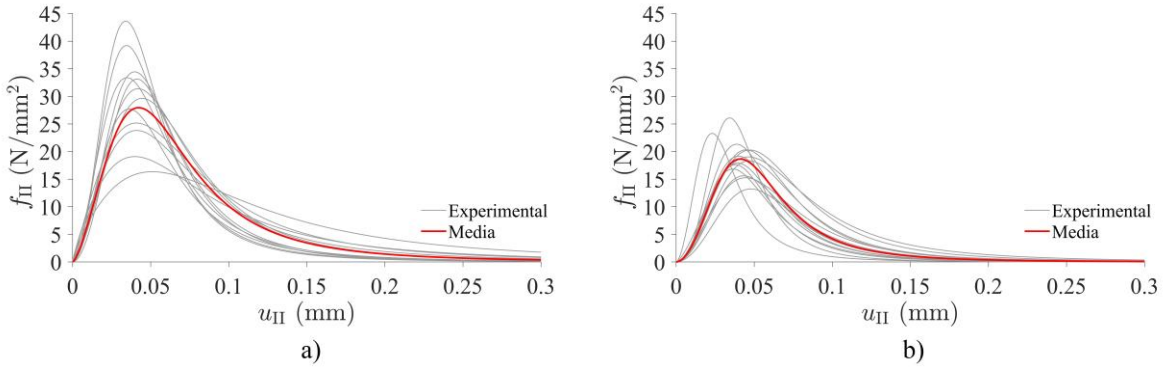

Figura 4.4: Leyes cohesivas experimentales (en gris) y ley cohesiva media (en rojo) para el modo II y el sistema de propagación de fractura RL (a) y TL (b) del haya europea.

Tabla 4.5. Valores de los parámetros que definen la función logística de la ley cohesiva (A_1, A_2, u_0, p), la tensión de cortante máxima (f_{IIu}), el desplazamiento relativo que define el inicio del daño (u_{II0}), el desplazamiento relativo máximo (u_{IIu}) y la energía de fractura asociada a la ley cohesiva ($G_{II,ley}$), para el modo II de carga y sistema de propagación de fractura RL del haya europea.

Modo II RL	A_1 (N/mm)	A_2 (N/mm)	u_0 (mm)	p (-)	f_{IIu} (N/mm^2)	u_{II0} (mm)	u_{IIu} (mm)	$G_{II,ley}$ (N/mm)
Media	**0,031**	**2,39**	**0,061**	**2,42**	**29,75**	**0,040**	**0,411**	**2,31**
Desv. Est.	0,025	0,21	0,016	0,37	7,89	0.005	0,153	0,18
C.V.	81,3%	8,8%	26,7%	15,3%	26,5%	12,3%	37,3%	7,9%

Tabla 4.6. Valores de los parámetros que definen la función logística de la ley cohesiva (A_1, A_2, u_0, p), la tensión de cortante máxima (f_{IIu}), el desplazamiento relativo que define el inicio del daño (u_{II0}), el desplazamiento relativo máximo (u_{IIu}) y la energía de fractura asociada a la ley cohesiva ($G_{II,ley}$), para el modo II de carga y sistema de propagación de fractura TL del haya europea.

Modo II TL	A_1 (N/mm)	A_2 (N/mm)	u_0 (mm)	p (-)	f_{IIu} (N/mm^2)	u_{II0} (mm)	u_{IIu} (mm)	$G_{II,ley}$ (N/mm)
Media	**0,029**	**1,25**	**0,053**	**2,86**	**18,88**	**0,041**	**0,320**	**1,22**
Desv. Est.	0,008	0,26	0,010	0,23	3,34	0,007	0,096	0,25
C.V.	29,4%	20,5%	18,3%	7,9%	17,7%	16,6%	30,2%	20,9%

El valor medio de la máxima tensión local de cortante (f_{IIu}) en el sistema de propagación de fractura RL resultó un 57% superior al del sistema TL.

4.2.3. Validación numérica

En la Figura 4.5 se presentan las curvas $P-\delta$ experimentales (en gris) obtenidas de los ensayos en modo I de carga y sistema de propagación de fractura TL, así como la curva $P-\delta$ numérica usando los valores medios de la ley cohesiva (en rojo), y las curvas obtenidas considerando las leyes cohesivas que representan el límite superior e inferior (en azul y verde, respectivamente) de las leyes cohesivas experimentales. Del mismo modo, en la Figura 4.6 se muestran las curvas $P-\delta$ obtenidas de los ensayos en modo II y los sistemas de propagación de fractura RL y TL.

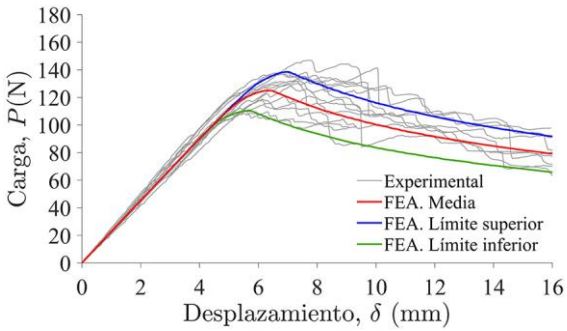

Figura 4.5: Curvas $P-\delta$ experimentales y numéricas para el modo I de carga y sistema de propagación de fractura TL.

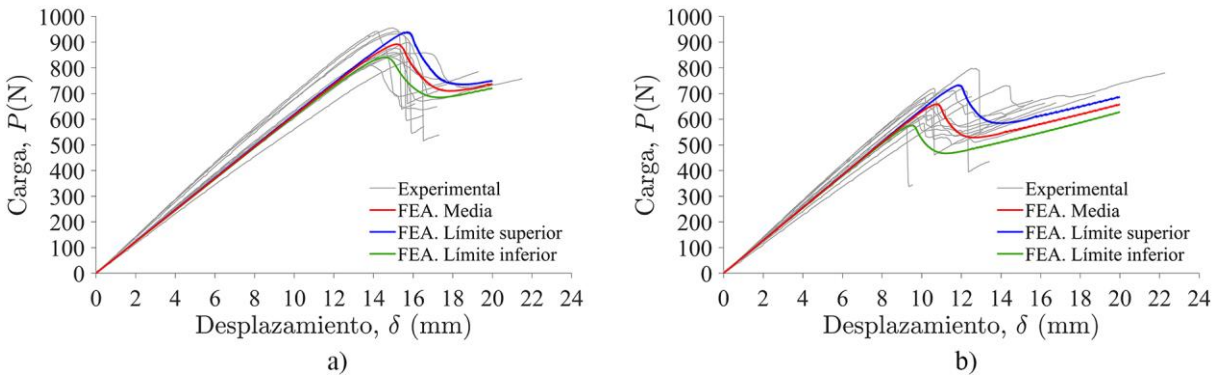

Figura 4.6: Curvas $P-\delta$ experimentales y numéricas para el modo II de carga y sistemas de propagación de fractura RL (a) y TL (b).

Las curvas experimentales ofrecen resultados coherentes teniendo en cuenta la variabilidad típica de la madera. La curva numérica determinada utilizando los valores de la ley cohesiva media se muestra representativa de los resultados experimentales. Las curvas obtenidas considerando los valores de las leyes cohesivas que representan el límite superior e inferior podrían dar cuenta de la variabilidad inherente de la madera.

Tanto en las curvas $P-\delta$ experimentales como numéricas de los modos I y II, se observa un comportamiento no lineal antes de que la curva alcance la carga máxima. Este hecho revela la influencia de una FPZ desarrollada en la punta de la fisura y su correcta implementación en FEA mediante CZMs.

4.3. Capacidad de carga frente a la hienda

En este apartado se muestran los principales resultados de la influencia en la capacidad de carga frente a la hienda de cinco parámetros relacionados con la geometría de la unión: 1) número de pasadores (uno y dos); 2) esbeltez de la viga; 3) distancia de los pasadores a los apoyos; 4) separación entre los pasadores en la dirección longitudinal de la viga; 5) distancia entre conexiones dispuestas simétricamente respecto del centro de la viga. Todos los detalles relativos a este estudio se recogen en la Publicación IV del compendio.

4.3.1. Ensayos experimentales

El fallo por hienda fue el tipo de fallo que gobernó el colapso de la mayoría de las vigas ensayadas. Sin embargo, algunas de las vigas fallaron por flexión. En la Tabla 4.7 se muestra el porcentaje de vigas con fallo por hienda/flexión por serie de ensayos, así como los valores medios de la carga de rotura de la conexión (P_{exp}) y el esfuerzo cortante correspondiente a la P_{exp} ($V_{cortante,max}$) para cada uno de los dos modos de fallo.

Tabla 4.7. Porcentaje de vigas con fallo por hienda/flexión por serie (%), valor medio de la carga de fallo de la conexión (P_{exp}) y máximo esfuerzo cortante correspondiente a la P_{exp} ($V_{cortante,max}$) para cada modo de fallo, coeficiente de variación (C.V.), relación entre la distancia de la conexión al apoyo (l_b) y el canto de la viga (h).

	Series	**Modo de fallo** Hienda / Flexión				
	h/nº pasadores/L/l_b	**%**	P_{exp} **(kN)**	$V_{cortante,max}$ **(kN)**	**C.V. (%)**	l_b/h
Grupo 1 (h: 100 mm)	100/1D/450/0,5L	100 / -	32,5 / -	16,3 / -	5,1 / -	2,25
	100/1D/950/0,5L	25 / 75	31,0 / 30,3	15,5/ 15,2	- / 4,1	4,75
	100/1D/950/0,38L	67 / 33	26,7 / 33,3	16,6/ 20,7	7,4/ 0	3,60
	100/1D/950/0,25L	67 / 33	26,3 / 28,3	19,7/ 21,1	5,7/ 0	2,40
	100/1D/950/0,13L	100 / -	23,9 / -	20,9 / -	6,0 / -	1,20
	100/2D/450/0,5L	100 / -	49,0 / -	24,5 / -	10,5 / -	1,93
	100/2D/950/0,5L	- / 100	- / 37,6	- / 18,8	- / 8	4,43
	100/2D/950/0,38L	33 / 67	23,7 / 23,9	23,7 / 23,9	0/ 0,4	3,60
	100/2D/950/0,25L	67 / 33	27,1 / 21,5	27,1 / 21,5	8,7/ 0	2,40
	100/2D/950/0,13L	100 / -	25,0 / -	25,0 / -	10,1 / -	1,20

Grupo 2 (*h*: 200 mm)	200/1D/450/0,5L	100 / -	27,2 / -	13,6 / -	7,8 / -	1,13
	200/1D/950/0,5L	100 / -	30,8 / -	15,4 / -	11 / -	2,38
	200/1D/950/0,38L	100 / -	24,3 / -	15,1 / -	10,0 / -	1,80
	200/1D/950/0,25L	100 / -	20,5 / -	15,3 / -	14,2 / -	1,20
	200/1D/950/0,13L	100 / -	27,4 / -	23,9 / -	6,5 / -	0,60
	200/2D/450/0,5L	100 / -	29,2/ -	14,6 / -	20,5 / -	0,97
	200/2D/950/0,5L	100 / -	33,6 / -	16,8 / -	5,1 / -	2,22
	200/2D/950/0,38L	100 / -	22,8 / -	22,8 / -	20,1 / -	1,80
	200/2D/950/0,25L	100 / -	26,9 / -	26,9 / -	18,9 / -	1,20
	200/2D/950/0,13L	100 / -	28,5 / -	28,5 / -	24,1 / -	0,60

Cabe señalar que todas las conexiones ensayadas tienen la misma distancia al borde cargado (h_e) pero diferentes valores de α. Este hecho conduce a que todas las series ensayadas en el grupo 2 fallaron por hienda, pero no las series del grupo 1. El fallo por flexión sólo se produjo en las vigas con mayor esbeltez y con relación α de 0,64, donde las cargas últimas mostradas en la Tabla 4.7 provocaron tensiones en las fibras de madera más tensionadas de alrededor de 90 N/mm^2. Este valor de tensión está en línea con los valores medios disponibles en la literatura (Widmann et al., 2012).

En las series investigadas, el fallo por hienda se caracterizó por la aparición de una fisura principal, la cual se extendió a lo largo de la longitud de la viga y a través de todo su espesor. Este modo de fallo apareció de manera repentina y frágil. En algunos ensayos, el fallo por hienda fue precedido por la formación de pequeñas fisuras alrededor del pasador, pero finalmente sólo una de ellas se propagó y de manera contundente.

4.3.2. Influencia del número de pasadores

En la Tabla 4.8 se resumen los resultados de las series estudiadas considerando conexiones compuestas por uno y dos pasadores (Figura 3.4), que incluyen los valores medios de las cargas de fallo por hienda y el porcentaje de incremento de carga en la conexión con dos pasadores respecto a sus homólogas con un solo pasador.

Tabla 4.8. Incremento de carga de las series con conexiones de dos pasadores en comparación con conexiones de un solo pasador.

Número de pasadores (nº pasadores)	**Serie h/nº pasadores/L/l_b**	**L (mm)**	**Esbeltez (L/h)**	**h_e (mm)**	**α h_e/h**	**P_{exp} (kN)**	**Incremento de carga (%)**
1D	100/1D/450/0,5L	450	4,50	64	0,64	32,5	51%
2D	100/2D/450/0,5L					49,0	
1D	200/1D/450/0,5L	450	2,25	64	0,32	27,2	7%
2D	200/2D/450/0,5L					29,2	
1D	200/1D/950/0,5L	950	4,75	64	0,32	30,8	9%
2D	200/2D/950/0,5L					33,6	

Como se puede observar, la ganancia de carga de las conexiones con dos pasadores en relación con las de un solo pasador nunca alcanza el doble del valor. Comparando series de esbeltez similar (4.75 y 4.5), la ganancia de carga para α = 0,32 es muy pequeña (9%) mientras que para α = 0,64 es mucho mayor

(51%), pero todavía lejos del doble esperado. Aunque en este caso α es el doble, la ganancia es más de cinco veces superior.

4.3.3. Influencia de la esbeltez de la viga

La Figura 4.7 muestra las cargas últimas de rotura en relación con la luz de la viga, para las series con conexión de uno y dos pasadores ubicados en la mitad de la luz y h = 200 mm.

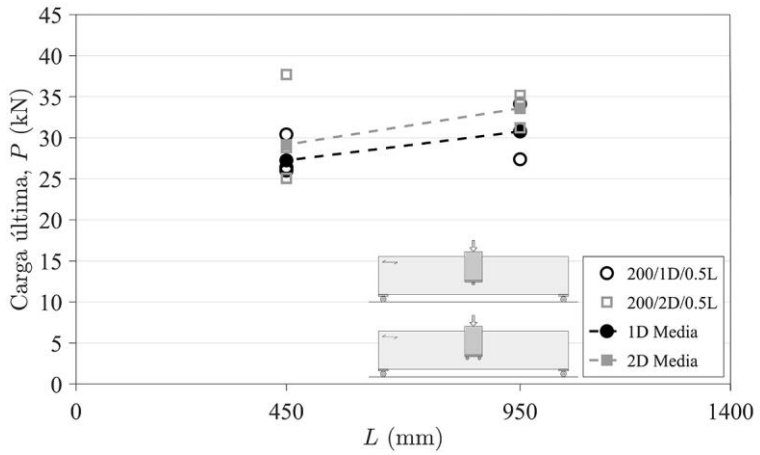

Figura 4.7: Cargas de fallo por hienda para conexiones de uno y dos pasadores en relación con la luz de la viga, para h = 200 mm.

Según los resultados, la capacidad de carga de la conexión aumenta ligeramente al aumentar la luz de la viga, correspondiendo con un incremento del 13% para 1D y 15% para 2D al duplicar la luz. En términos de esbeltez de la viga (L/h), a mayor esbeltez, mayor es la capacidad de carga resultante, lo que concuerda con los resultados para madera laminada de abeto disponibles en (Schoenmakers, 2010; Yasumura, 2001). En el caso de la serie con h = 100 mm, esta comparación no es posible debido a que las vigas con luces mayores fallaron por flexión.

4.3.4. Influencia de la distancia de los pasadores a los apoyos

En la Figura 4.8 se muestra la evolución de la carga de rotura por hienda para las conexiones con un pasador situadas a diferentes distancias del soporte más cercano (l_b) para los dos cantos de vigas estudiados. La serie con h = 200 mm presenta una disminución de la carga de rotura con la proximidad del pasador al apoyo, hasta la distancia l_b = 240 mm. Sin embargo, la carga vuelve a aumentar cuando el pasador se dispone a una distancia l_b = 120 mm, la más cercana a los apoyos de las estudiadas. Una tendencia similar se observa para las vigas con h = 100 mm, pero en este caso no se produce ningún aumento de la carga para la distancia l_b más pequeña.

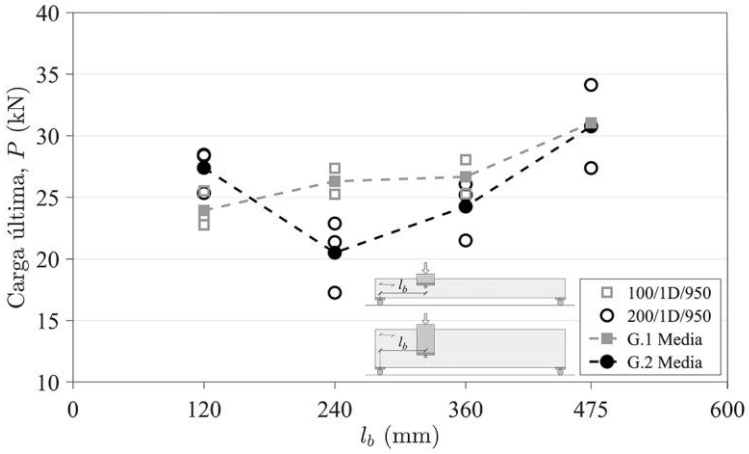

Figura 4.8: Cargas de fallo por hienda de las conexiones con un pasador en función de la distancia entre el pasador y el apoyo más cercano (l_b), para los dos cantos de viga diferentes.

No existen muchos estudios experimentales en la literatura que se enfoquen en la influencia de l_b. Algunas fuentes bibliográficas señalan que la capacidad de carga frente a la hienda es independiente de l_b (Jensen et al., 2012, 2015). Sin embargo, los resultados del presente estudio muestran una influencia clara.

4.3.5. Influencia de la separación entre pasadores en la dirección longitudinal a la viga

Respecto a la evolución de las cargas últimas de rotura por hienda en función de l_c para vigas de haya con conexiones de dos pasadores (Figura 4.9), los resultados muestran un aumento de las cargas con la separación de los pasadores, lo que es acorde con los resultados de los ensayos reportados en (Habkirk & Quenneville, 2006; Kasim & Quenneville, 2002; Leijten, 2018; Reshke, 1999; Schoenmakers, 2010).

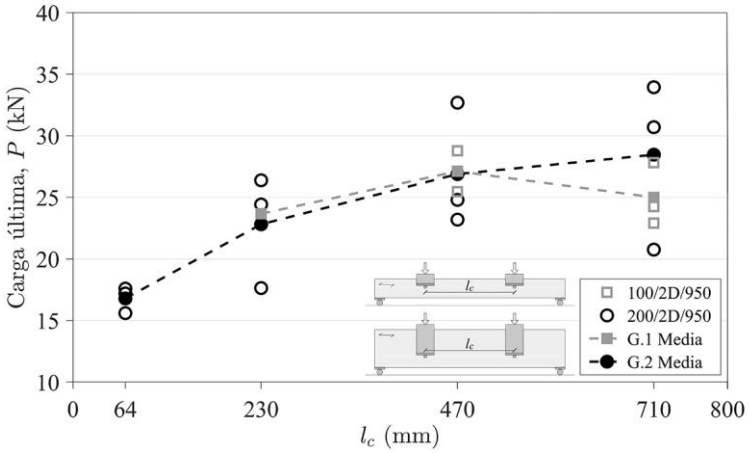

Figura 4.9: Cargas de fallo por hienda de las conexiones con dos pasadores en función de la distancia entre pasadores (l_c), para los dos cantos de viga estudiados.

En el caso particular de las series con h = 200 mm, cabe señalar que las cargas de rotura por hienda en las vigas con la separación entre pasadores más pequeña ($l_c = 4d$) no difieren significativamente de las cargas alcanzadas para vigas con un solo pasador colocado en el centro de la luz del vano. En la gráfica se observa claramente que la carga última aumenta con la separación entre pasadores (l_c). Pequeños incrementos de l_c conducen a un aumento pronunciado de la carga de rotura, pero ésta tiende a estabilizarse para separaciones l_c altas. Una tendencia similar se observa en el caso particular de las series con h = 100 mm, siendo los valores medidos casi idénticos entre los dos grupos.

4.3.6. Influencia del número de conexiones

La Figura 4.10 muestra la evolución de la carga por conexión en función de l_b para vigas con conexiones simples (1D) y dobles (2D) dispuestas simétricamente, para los dos grupos de cantos de viga ensayados (100 y 200 mm).

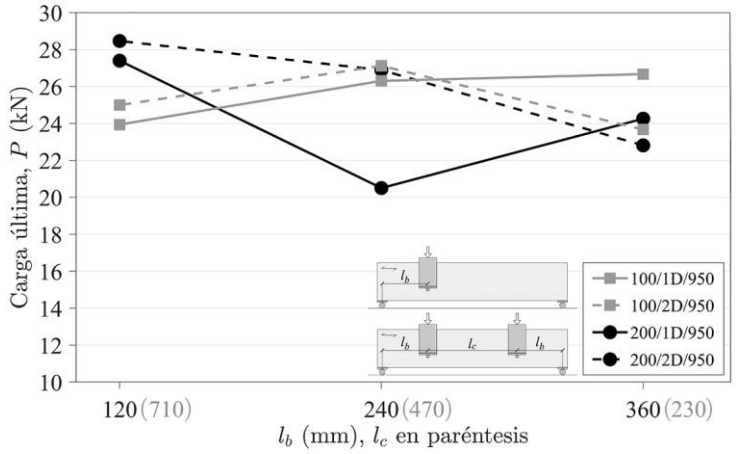

Figura 4.10: Cargas de fallo por hienda por conexión para conexiones asimétricas simples y dobles en función de la distancia al soporte l_b, para los dos cantos de viga diferentes.

Según los principales resultados descritos en la subsección 4.3.4, la carga total de una viga con dos pasadores ubicados de manera descentrada en la viga no duplica la carga de la conexión de referencia, es decir, una conexión con dos pasadores situados en el centro del vano. Sin embargo, como se observa en la Figura 4.10, al comparar geometrías semejantes, existe un cierto espaciamiento entre conexiones (l_c) donde los esfuerzos introducidos en la viga por cada conexión no interfieren entre sí y, en tales casos, la carga total de una viga con múltiples conexiones puede ser mayor que el doble de carga de su homóloga con una sola conexión.

4.3.7. Comparación entre las cargas de fallo experimentales, numéricas y teóricas

La Figura 4.11 muestra resultados representativos de las curvas carga-desplazamiento experimentales (líneas grises) y numéricas (líneas negras), considerando tanto el desplazamiento del pasador (líneas discontinuas) como el desplazamiento de la cara inferior de la viga (líneas continuas).

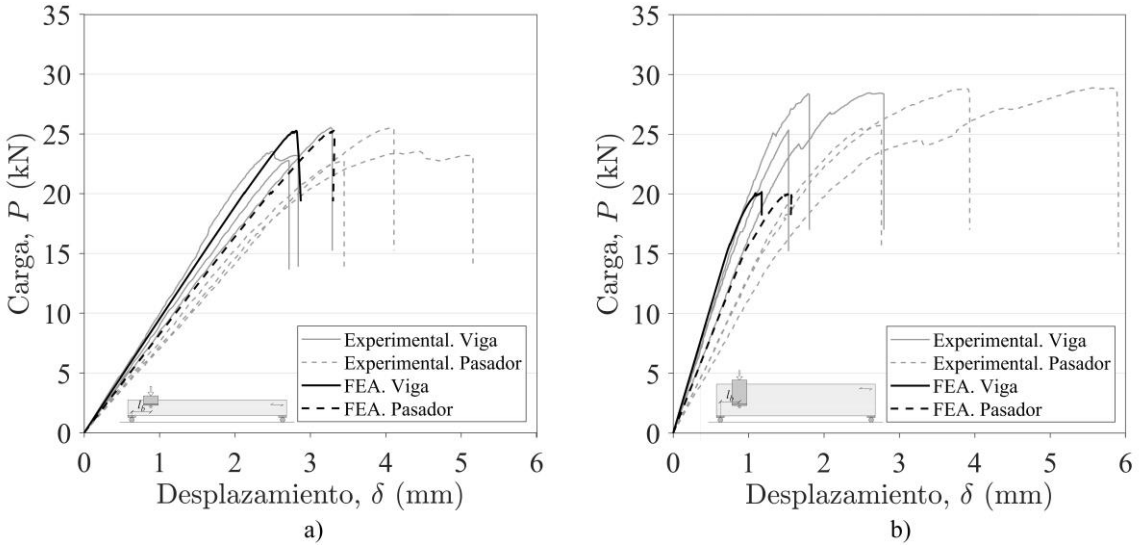

Figura 4.11: Curvas $P-\delta$ experimentales y numéricas representativas: (a) serie con h = 100 mm (100/1D/950/0,13L); (b) serie con h = 200 mm (200/1D/950/0,13L).

Como puede observarse, los resultados de FEA concuerdan bien con los resultados experimentales para los parámetros principales, como la rigidez y la carga última. La buena correspondencia entre la rigidez inicial experimental y la numérica demuestra que los valores promedio de las constantes elásticas utilizadas (ver subsección 4.1) son representativos del material. La capacidad de carga máxima frente a la hienda de las geometrías del grupo 1 (h= 100 mm) coincide bastante bien con los resultados experimentales, pero en el caso del grupo 2 (h = 200 mm) las cargas estimadas son siempre menores que las experimentales.

En la Tabla 4.9 se resumen los resultados de las cargas de fallo estimadas a partir de FEA y de los tres modelos de diseño considerados. También se incluyen los valores normalizados con respecto a los resultados experimentales para todos los casos. Estas proporciones se ilustran gráficamente en la Figura 4.12 para facilitar la comparación. Una proporción ≤1 representa una predicción segura y una proporción >1 una predicción insegura.

Tabla 4.9. Capacidad de carga frente a la hienda de los ensayos experimental (P_{exp}) frente a la estimada (numérica y teórica, P_{est}).

					Modelos de diseño					
	Serie	**Ensayos Exp.**	**FEA**		Eurocodigo 5 Ecuación (16)		(Jensen et al., 2015) Ecuación (14)		(Franke & Quenneville, 2011b) Ecuación (15)	
	h/nº pasadores/L/l_b	**P_{exp} (kN)**	**P_{est} (kN)**	**P_{est}/P_{exp}**	**P_{est} (kN)**	**P_{est}/P_{exp}**	**P_{est} (kN)**	**P_{est}/P_{exp}**	**P_{est} (kN)**	**P_{est}/P_{exp}**
G.1	100/1D/450/0,5L	32,5	27,0	0,83	29,8	0,92	29,2	0,90	21,6	0,66
	100/1D/950/0,5L	31,0	28,8	0,93	29,8	0,96	29,2	0,94	21,6	0,70
	100/1D/950/0,38L	26,7	30,2	1,13	24,0	0,90	29,2	1,10	21,6	0,81
	100/1D/950/0,25L	26,3	27,3	1,04	19,9	0,76	29,2	1,11	21,6	0,82
	100/1D/950/0,13L	23,9	25,3	1,06	17,0	0,71	29,2	1,22	21,6	0,90
	100/2D/450/0,5L	49,0	43,4	0,89	29,8	0,61	29,3	0,60	37,4	0,76
	100/2D/950/0,5L	-	-	-	-	-	-	-	-	-
	100/2D/950/0,38L	23,7	28,8	1,22	14,9	0,63	29,3	1,24	21,6	0,91
	100/2D/950/0,25L	27,1	25,4	0,94	14,9	0,55	29,2	1,08	21,6	0,80
	100/2D/950/0,13L	25,0	24,0	0,96	14,9	0,60	29,2	1,17	21,6	0,86

G. 1* ($P = 2P$)	100/2D/950/0,38L	47,3	57,6	1,22	29,8	0,63	29,3	0,62	92,6	1,96
	100/2D/950/0,25L	54,2	50,7	0,94	29,8	0,55	29,2	0,54	91,4	1,69
	100/2D/950/0,13L	50,0	48,0	0,96	29,8	0,60	29,2	0,58	67,6	1,35
G. 2	200/1D/450/0,5L	27,2	17,2	0,63	21,8	0,80	21,4	0,79	18,6	0,68
	200/1D/950/0,5L	30,8	18,1	0,59	21,8	0,71	21,4	0,70	18,6	0,60
	200/1D/950/0,38L	24,3	17,9	0,74	17,6	0,72	21,4	0,88	18,6	0,77
	200/1D/950/0,25L	20,5	17,5	0,85	14,6	0,71	21,4	1,05	18,6	0,91
	200/1D/950/0,13L	27,4	20,2	0,74	12,5	0,46	21,4	0,78	18,6	0,68
	200/2D/450/0,5L	29,2	26,8	0,92	21,8	0,75	21,5	0,74	24,7	0,85
	200/2D/950/0,5L	33,6	28,6	0,85	21,8	0,65	21,4	0,64	24,6	0,73
	200/2D/950/0,38L	22,8	17,5	0,77	10,9	0,48	21,5	0,94	18,6	0,82
	200/2D/950/0,25L	26,9	17,3	0,64	10,9	0,41	21,5	0,80	18,6	0,69
	200/2D/950/0,13L	28,5	23,5	0,83	10,9	0,38	21,4	0,75	18,6	0,65
G.2* ($P = 2P$)	200/2D/950/0,38L	45,6	35,0	0,77	21,8	0,48	21,5	0,47	45,1	0,99
	200/2D/950/0,25L	53,8	34,7	0,64	21,8	0,41	21,5	0,40	67,4	1,25
	200/2D/950/0,13L	56,9	47,1	0,83	21,8	0,38	21,4	0,38	64,1	1,13

* Esta comparación se realiza considerando que la viga tiene una sola conexión, es decir, $P = 2P$.

En el caso de la conexión descentrada de las series con dos pasadores (2D), se han considerado dos supuestos para el análisis de los resultados: cada pasador como parte de una conexión independiente (es decir, la viga tendría dos conexiones con un pasador cada una); y los dos pasadores como parte de la misma conexión. Los resultados de este segundo supuesto están marcados con * en la Tabla 4.9.

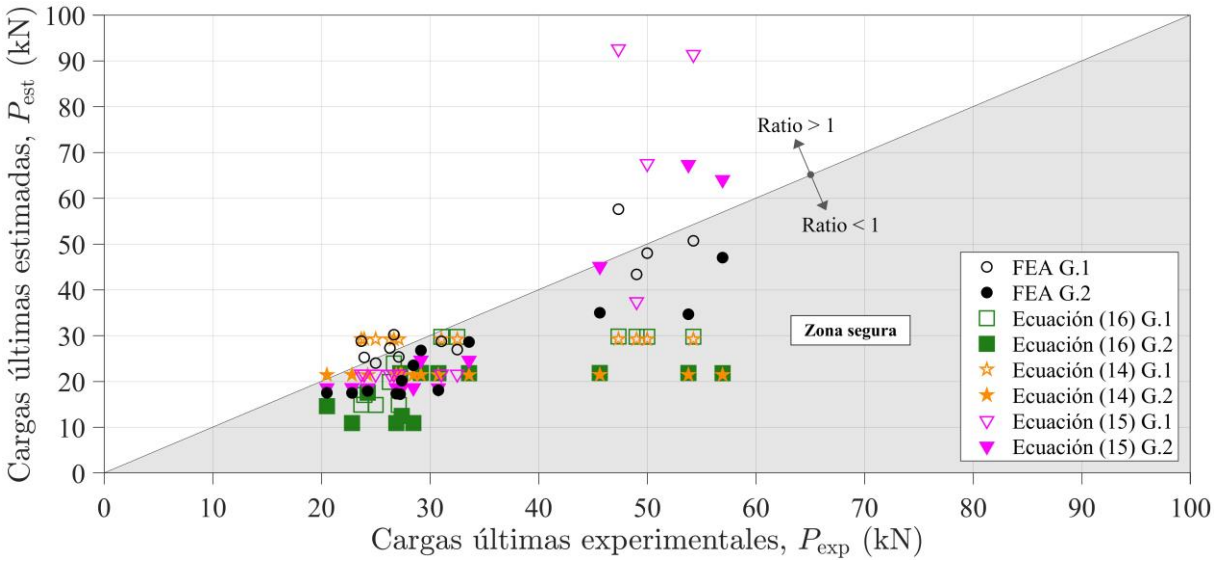

Figura 4.12: Cargas de fallo experimentales frente los valores estimados por FEA (símbolos negros) y por los modelos de diseño (símbolos en colores) para el haya europea.

En términos generales, los modelos de elementos finitos son los más versátiles, ofreciendo buenas estimaciones ante cualquier situación.

La formulación del Eurocódigo 5 (ec. (16)) siempre predice valores conservadores. Logra buenas predicciones de la capacidad de carga frente a la hienda de vigas cargadas por medio de una conexión con un pasador ubicado en el centro de la luz. Sin embargo, las estimaciones de las series con dos pasadores son demasiado conservadoras. Hay que tener en cuenta que el valor C_1 utilizado en la

expresión es el que corresponde al haya. Si se hubiera utilizado el valor fijo C_1 = 14 N/mm$^{1.5}$ que aparece en la ec. (16) para coníferas, las cargas estimadas serían aún más conservadoras (60% del valor mostrado en la Tabla 4.9).

En cuanto a los otros dos modelos, para vigas con un pasador y dos pasadores considerando cada pasador como parte de una conexión independiente (es decir, la viga tendría dos conexiones con un pasador cada una), predicen valores cercanos a los experimentales. Sin embargo, el modelo presentado en (Jensen et al., 2015) dado por la ecuación (14) tiende a sobreestimar la capacidad de carga frente a la hienda de las geometrías del grupo 1 (h=100 mm). En el caso de considerar que los dos pasadores forman parte de una misma conexión (resultados con * en la Tabla 4.9), la ecuación (14) predice valores muy conservadores, pero el modelo presentado en (Franke & Quenneville, 2011b) dado por la ecuación (15) sobreestima la capacidad de carga frente a la hienda de la mayoría de los casos, con algunos valores teóricos alejados de los experimentales, especialmente en las vigas con h = 100 mm.

5. Conclusiones | Conclusions

A continuación, se exponen las conclusiones más importantes extraídas del trabajo presentado en esta tesis doctoral, remitiendo al lector a las publicaciones individuales que constituyen el compendio de publicaciones para una revisión completa de las mismas:

- La matriz de flexibilidad del haya europea ha sido determinada a partir de ensayos de compresión con medición de deformaciones mediante DIC y por ensayos de ultrasonidos. En general, los módulos de elasticidad y de rigidez a cortante medidos por ultrasonidos resultaron más elevados. Sin embargo, esta tendencia no se observó en el caso de los coeficientes de Poisson.

- Las leyes cohesivas se obtuvieron aplicando el método directo, combinando el procedimiento CBBM para determinar la energía de fractura y mediciones DIC para monitorizar los desplazamientos en la punta de la fisura. El método ha resultado adecuado y presenta la ventaja de no requerir la medición de la propagación de la fisura durante el ensayo, lo cual es especialmente complejo en un material como la madera. Las propiedades de fractura en los modos I y II obtenidas experimentalmente se validaron mediante modelos de zonas cohesivas.

- Las leyes cohesivas en modo I y II obtenidas, permiten realizar simulaciones numéricas bajo el enfoque de la mecánica de fractura no lineal, pudiendo reproducir el inicio y la propagación de la fisura. Esta aportación, junto con la matriz de flexibilidad del material, son de gran interés para el diseño con haya europea de diversas aplicaciones en el ámbito de la ingeniería estructural con posibilidad de fallo frágil por hienda, como es el caso de vigas cargadas perpendicularmente a la fibra mediante uniones mecánicas analizadas en esta tesis.

- En los análisis por elementos finitos se han utilizado modelos de zonas cohesivas (CZM) para simular el inicio y la propagación del daño por fractura del material, los cuales han sido validados inicialmente a partir de los resultados de ensayos DCB y ENF. Los CZM se han utilizado de modo satisfactorio para desarrollar un modelo numérico 2D capaz de predecir de manera fiable la capacidad de carga frente a la hienda de uniones de madera con pasadores y diferentes configuraciones.

- Se ha analizado experimental y numéricamente la influencia de diferentes parámetros geométricos en la capacidad de carga frente a la hienda de vigas cargadas perpendicularmente a la fibra mediante uniones mecánicas. Los resultados muestran una influencia significativa de los parámetros estudiados, lo que sugiere la conveniencia de revisar la expresión incluida en el Eurocódigo 5.

- La comparación entre las cargas de fallo experimentales, numéricas y teóricas muestra que los modelos analíticos basados en la mecánica de fractura elástica y lineal (incluida la expresión del Eurocódigo 5) tienden a proporcionar estimaciones conservadoras de la capacidad de carga frente a la hienda, especialmente en configuraciones con dos pasadores considerados como una sola conexión. En términos generales, el modelo de elementos finitos propuesto ha ofrecido

buenas estimaciones ante cualquier configuración, proporcionando un mejor ajuste de los resultados cuanto más frágil es la rotura por hienda de la pieza de madera.

The main conclusions drawn from the work presented in this thesis are summarised below. For a comprehensive review, the reader is referred to the individual publications that constitute the compendium:

- The compliance matrix of European beech has been determined through compression tests with strain measurement using DIC and ultrasound tests. In general, the elastic and shear modulus measured by ultrasound were higher. However, this trend was not observed for the Poisson's ratios.

- The cohesive laws were obtained using the direct method, combining the CBBM procedure to determine the fracture energy and DIC measurements to record the crack tip displacement. This method has proven to be adequate and has the advantage of not requiring the measurement of crack propagation during the test, which is a particularly challenging task in a material such as wood. The modes I and II fracture properties obtained experimentally were validated using cohesive zone models.

- The cohesive laws obtained for modes I and II enable numerical simulations under the non-linear fracture mechanics approach, allowing for the simulation of damage initiation and crack propagation. This contribution, together with the compliance matrix of the material, is highly valuable for designing various structural engineering applications using European beech, particularly where there is a risk of brittle failure by splitting, such as beams loaded perpendicular to the grain through mechanical connections analysed in this thesis.

- Cohesive zone models (CZM) have been used in finite element analyses to reproduce the initiation and propagation of the material fracture damage. These models have been initially validated from the results of DCB and ENF tests. The CZMs have been successfully used to develop a 2D numerical model capable of reliably predicting the splitting capacity of timber dowel connections and different configurations.

- The influence of different geometrical parameters on the splitting capacity of beams loaded perpendicular to the grain by means of mechanical connections has been analysed experimentally and numerically. The results demonstrate a significant impact of the studied parameters, raising the need to review the expression included in Eurocode 5.

- A comparison of experimental, numerical and theoretical failure loads reveals that analytical models based on elastic and linear fracture mechanics (including the Eurocode 5 expression) tend to provide conservative predictions of the splitting capacity, especially in configurations with two dowels considered as a single connection. Overall, the proposed finite element model has provided accurate predictions across various configurations, with a better fit observed as the splitting fracture of the timber member becomes more brittle.

6. Futuros trabajos

A partir de los resultados obtenidos y de la experiencia adquirida durante el desarrollo de esta tesis, se proponen varias vías de investigación futura, las cuales se exponen brevemente a continuación:

- Determinar las constantes de elasticidad mediante ensayos mecánicos a tracción.

- Obtener la energía de fractura en modo I para el sistema de propagación RL. De este modo, estarían determinados los modos puros I y II para los dos sistemas de propagación de fractura más habituales en aplicaciones estructurales (RL y TL).

- Estudiar el crecimiento y propagación de la fisura bajo el modo mixto (I+II) de carga. Esto permitirá analizar con mayor precisión el comportamiento a fractura en diversas aplicaciones estructurales.

- Optimizar los parámetros que definen la ley cohesiva numérica mediante el estudio de formas sencillas equivalentes a la experimental en análisis por elementos finitos, evaluando su impacto en la carga de rotura, el margen de error y el tiempo de computación requerido.

- Desarrollar un modelo teórico que tenga en cuenta la influencia de los parámetros estudiados en esta tesis, considere la energía de fractura de la madera y sea lo suficientemente sencillo como para ser utilizado en la práctica profesional.

- Ampliar la campaña experimental para estudiar otras geometrías de conexión y profundizar en la influencia de la proximidad de la conexión a los apoyos y el uso de múltiples conexiones independientes en un mismo tramo de viga.

- Profundizar en el desarrollo de un modelo numérico sencillo, que sea eficiente y seguro para su uso en la práctica profesional, validando su eficacia ante otras configuraciones geométricas de la conexión y situaciones de carga más complejas.

- Llevar a cabo pruebas de carga con vigas de mayor esbeltez en las que se puedan desarrollar grandes deformaciones.

- Aplicar el método empleado en esta tesis doctoral para determinar las propiedades de fractura de productos tecnológicos de madera, como el microlaminado de haya y el microlamiando de *Eucalyptus globulus* Labill.

Bibliografía

Aicher, S., Christian, Z. & Dill-Langer, G. (2014). Hardwood glulams - Emerging timber products of superior mechanical properties. En: *Proceedings of the World Conference on Timber Engineering (WCTE)*, Quebec City, QC, Canada. doi: https://doi.org/10.13140/2.1.5170.1120.

Akrami, A., Barbu, M.C. & Fruehwald, A. (2014). Characterization of properties of oriented strand boards from beech and poplar. *European Journal of Wood and Wood Products*, 72, 393–398. doi: https://doi.org/10.1007/s00107-014-0793-9.

Anderson, T.L. (2017). Fracture Mechanics: Fundamentals and Applications (Fourth Edition). CRC Press. ISBN: 9781315370293.

Antonucci, S., Santopuoli, G., Marchetti, M., Tognetti, R., Chiavetta, U. & Garfì, V. (2021). What Is Known About the Management of European Beech Forests Facing Climate Change? A Review. *Current Forestry Reports*, 7, 321–333. doi: https://doi.org/10.1007/s40725-021-00149-4.

Ballerini, M. (2004). A new prediction formula for the splitting strength of beams loaded by dowel-type connections. En: *Proceedings of the International Council for Research and Innovation in Building and Construction (CIB-W18)*, Edinburgh, Scotland.

Ballerini, M. (2006). A new prediction formula for the splitting strength of beams loaded perpendicular-to-grain by dowel-type and nail-plates connections. En: *Proceedings of the World Conference on Timber Engineering (WCTE)*, Portland, Oregon, USA.

Barenblatt, G.I. (1962). The Mathematical Theory of Equilibrium Cracks in Brittle Fracture. *Advances in Applied Mechanics*, 7, 55–129. doi: https://doi.org/10.1016/S0065-2156(08)70121-2.

Bažant, Z.P. & Planas, J. (1998). Fracture and Size Effect in Concrete and Other Quasibrittle Materials (1st Editio). CRC Press. ISBN: 9780203756799.

Bodig, J. & Jayne, B.A. (1982). Mechanics of wood and wood composites. Van Nostrand Reinhold Company.

Boström, L. (1992). Method of determination of the softening behaviour of wood and the applicability of a nonlinear fracture mechanics model. PhD Thesis, Lund University, Sweden.

Breinig, L., Linsenmann, P., Brüchert, F., Weidenhiller, A. & Sauter, H. (2019). Mechanical properties of roundwood and boards of European beech and ash and their relationships. *Holztechnologie*, 2, 35–48.

Buchanan, A.H. & Honey, B.G. (1994). Energy and carbon dioxide implications of building construction. *Energy and Buildings*, 20, 205–217. doi: https://doi.org/10.1016/0378-7788(94)90024-8.

Buchanan, A.H. & Levine, S.B. (1999). Wood-based building materials and atmospheric carbon emissions. *Environmental Science and Policy*, 2, 427–437. doi: https://doi.org/10.1016/S1462-9011(99)00038-6.

Caldeira, T. (2011). Caracterização experimental e numérica do comportamento frágil de ligações com cavilhas em estruturas de madeira. PhD Thesis, Universidade de Trás-os-Montes e Alto Douro.

Camú, C.T. & Aicher, S. (2018). A stochastic finite element model for glulam beams of hardwoods. En: *Proceedings of the World Conference on Timber Engineering (WCTE)*, Seoul, Republic of Korea.

de Moura, M.F.S.F., Morais, J.J.L. & Dourado, N. (2008). A new data reduction scheme for mode I wood fracture characterization using the double cantilever beam test. Engineering Fracture Mechanics, 75, 3852–3865. doi: https://doi.org/10.1016/j.engfracmech.2008.02.006.

de Moura, M.F.S.F., Silva, M.A.L., de Morais, A.B. & Morais, J.J.L. (2006). Equivalent crack based mode II fracture characterization of wood. *Engineering Fracture Mechanics*, 73, 978–993. doi: https://doi.org/10.1016/j.engfracmech.2006.01.004.

De Rigo, D. & Caudullo, G. (2016). *Fagus sylvatica* in Europe: distribution, habitat, usage and threats. En: *European Atlas of Forest Tree Species*, 94–95. Publication Office of the European Union. ISBN: 978-92-76-17291-8

DIN 1052:2008. Design of timber structures – General rules and rules for buildings (In German).

DIN 4074-5:2008. Strength grading of wood-part 5: Sawn hard wood (In German).

Dourado, N., de Moura, M.F.S.F., Morel, S. & Morais, J. (2015). Wood fracture characterization under mode I loading using the three-point-bending test. Experimental investigation of *Picea abies* L. *International Journal of Fracture*, 194, 1–9. doi: https://doi.org/10.1007/s10704-015-0029-y.

Dourado, N., Silva, F.G.A. & de Moura, M.F.S.F. (2018). Fracture behavior of wood-steel dowel joints under quasi-static loading. *Construction and Building Materials*, 176, 14–23. doi: https://doi.org/10.1016/j.conbuildmat.2018.04.230.

Dugdale, D.S. (1960). Yielding of steel. *J. Mech. Phys. Solids*, 8, 100–104.

Ehlbeck, J., Görlacher, R. & Werner, H. (1989). Determination of perpendicular-to-grain tensile stresses in joints with dowel-type fasteners: a draft proposal for design rules. En: *Proceedings of the International Council for Research and Innovation in Building and Construction (CIB-W18A)*, Berlin, German Democratic republic.

Ehrhart, T. (2019). European beech glued laminated timber. PhD Thesis, ETH Zurich, Switzerland. doi: https://doi.org/10.3929/ethz-b-000402805.

Ehrhart, T., Steiger, R., Lehmann, M. & Frangi, A. (2020). European beech (*Fagus sylvatica* L.) glued laminated timber: lamination strength grading, production and mechanical properties. *European Journal of Wood and Wood Products*, 78, 971–984. doi: https://doi.org/10.1007/s00107-020-01545-6.

Eriksson, L.O., Gustavsson, L., Hänninen, R., Kallio, M., Lyhykäinen, H., Pingoud, K., Pohjola, J., Sathre, R., Solberg, B., Svanaes, J. & Valsta, L. (2012). Climate change mitigation through increased wood use in the European construction sector-towards an integrated modelling framework. *European Journal of Forest Research*, 131, 131–144. doi: https://doi.org/10.1007/s10342-010-0463-3.

ETA-14/0354:2021. Glued laminated timber made of hardwood – Structural laminated veneer lumber made of beech.

ETA-18/1018:2018. Glued laminated timber made of hardwood – Structural laminated veneer lumber made of beech.

FOREST EUROPE, UNECE & FAO. (2011). State of Europe's Forests 2011. Status and Trends in Sustainable Forest Management in Europe. ISBN: 978-82-92980-05-7.

Franke, B. & Quenneville, P. (2010). Analyses of the failure behaviour of transversely loaded dowel type connections in wood. En: *Proceedings of the World Conference on Timber Engineering (WCTE)*, Trentino, Italy.

Franke, B. & Quenneville, P. (2011a). Numerical Modeling of the Failure Behavior of Dowel Connections in Wood. *Journal of Engineering Mechanics*, 137, 186–195. doi: https://doi.org/10.1061/(ASCE)EM.1943-7889.0000217.

Franke, B. & Quenneville, P. (2011b). Design approach for the splitting failure of dowel type Connections loaded perpendicular to grain. En: *Proceedings of* the International Council for Research and Innovation in Building and Construction (CIB-W18), Alghero, Italy.

Franke, S. (2016). Mechanical properties of beech CLT. En: *Proceedings of the World Conference on Timber Engineering (WCTE)*, Vienna, Austria.

Franke, S. & Magnière, N. (2014). The Embedment Failure of European Beech Compared to Spruce Wood and Standards. En: Materials and Joints in Timber Structures, 221-229. Springer Netherlands. ISBN: 978-94-007-7810-8.

GOM GmbH. (2007). ARAMIS commercial software. Aramis 6.0.2; GOM GmbH: Braunschweig, Germany.

Gustafsson, P.J. (1985). Fracture mechanics studies of non-yielding materials like concrete: modelling of tensile fracture and applied strength analyses. PhD Thesis, Lund University, Sweden. Disponible online: https://lup.lub.lu.se/search/publication/37ef48d7-e415-43b7-9c7c-a4b103800454.

Gustavsson, L. & Sathre, R. (2006). Variability in energy and carbon dioxide balances of wood and concrete building materials. *Building and Environment*, 41, 940–951. doi: https://doi.org/10.1016/j.buildenv.2005.04.008.

Habkirk, R. & Quenneville, J.H.P. (2006). Bolted wood connections loaded perpendicular-to-grain: effect on wood species. En: Proceedings of the World Conference on Timber Engineering (WCTE), Portland, Oregon, USA.

Hering, S., Keunecke, D. & Niemz, P. (2012). Moisture-dependent orthotropic elasticity of beech wood. *Wood Science and Technology*, 46, 927–938. doi: https://doi.org/10.1007/s00226-011-0449-4.

Hillerborg, A., Modéer, M. & Petersson, P-E. (1976). Analysis of crack formation and crack growth in concrete by means of fracture mechanics and finite elements. *Cement and Concrete Research*, 6, 773–782.

ISO 13061-17:2017. Physical and Mechanical Properties of Wood – Test Methods for Small Clear Wood Specimens - Part 17: Determination of Ultimate Stress in Compression Parallel to Grain.

ISO 13061-5:2020. Physical and Mechanical Properties of Wood - Test Methods for Small Clear Wood Specimens - Part 5: Determination of Strength in Compression Perpendicular to Grain.

Jensen, J.L. (2003). Splitting strength of beams loaded by connections. En: *Proceedings of the International Council for Research and Innovation in Building and Construction (CIB-W18)*, Auckland, New Zealand.

Jensen, J.L., Girhammar, U.A., Quenneville, P. & Källsner, B. (2012). Splitting of beams loaded perpendicular to grain by connections: simple fracture mechanics models. En: *Proceedings of the World Conference on Timber Engineering (WCTE)*, Auckland, New Zealand.

Jensen, J.L., Gustafsson, P.J. & Larsen, H.J. (2003). A Tensile Fracture Model for Joints with Rods or Dowels Loaded Perpendicular to Grain. En: *Proceedings of the International Council for Research and Innovation in Building and Construction (CIB-W18)*, Colorado, USA.

Jensen, J.L., Quenneville, P., Girhammar, U.A. & Källsner, B. (2015). Brittle Failures in Timber Beams Loaded Perpendicular to Grain by Connections. *Journal of Materials in Civil Engineering*, 27, 4015026. doi: https://doi.org/10.1061/(ASCE)MT.1943-5533.0001275.

Jockwer, R. & Dietsch, P. (2018). Review of design approaches and test results on brittle failure modes of connections loaded at an angle to the grain. *Engineering Structures*, 171, 362–372. doi: https://doi.org/10.1016/j.engstruct.2018.05.061.

Johansen, K.W. (1949). Theory of timber connections. En: *Proceedings of the International Association for Bridge and Structural Engineering (IABSE)*, Zurich, Switzerland. doi: http://doi.org/10.5169/seals-9703.

Kasim, M. & Quenneville, P. (2002). Effect of row spacing on the capacity of bolted timber connections loaded perpendicular-to-grain. En: *Proceedings of the International Council for Research and Innovation in Building and Construction (CIB-W18)*, Kyoto, Japan.

Keunecke, D., Sonderegger, W., Pereteanu, K., Lüthi, T. & Niemz, P. (2007). Determination of Young's and shear moduli of common yew and Norway spruce by means of ultrasonic waves. *Wood Science and Technology*, 41, 309–327. doi: https://doi.org/10.1007/s00226-006-0107-4.

Knorz, M. & van de Kuilen, J.W.G. (2012). Development of a high-capacity engineered wood product-LVL made of european beech (*Fagus sylvatica* L.). En: *Proceedings of the World Conference on Timber Engineering (WCTE)*, Auckland, New Zealand.

Larsen, H.J. & Gustafsson, P.J. (2001). Dowel joints loaded perpendicular to grain. En: *Proceedings of the Proceedings of the International Council for Research and Innovation in Building and Construction (CIB-W18)*, Venice, Italy.

Leijten, A.J.M. (2018). Splitting of timber beams caused by perpendicular to grain forces of multiple connections. *Engineering Structures*, 171, 10–14. https://doi.org/10.1016/j.engstruct.2018.05.059.

Leijten, A.J.M. & Jorissen, A.J.M. (2001). Splitting strength of beams loaded by connections perpendicular to grain, model validation. En: *Proceedings of the International Council for Research and Innovation in Building and Construction (CIB-W18)*, Venice, Italy.

Majano-Majano, A. (2014). Madera termo-tratada de frondosas para uso estructural. PhD Thesis, Universidad Politécnica de Madrid, España.

Majano-Majano, A., Lara-Bocanegra, A.J., Xavier, J. & Morais, J. (2019). Measuring the cohesive law in mode I loading of *Eucalyptus globulus*. *Materials*, 12, 23. doi: https://doi.org/10.3390/ma12010023.

Majano-Majano, A., Lara-Bocanegra, A.J., Xavier, J. & Morais, J. (2020). Experimental evaluation of mode II fracture properties of *Eucalyptus globulus* L. *Materials*, 13, 1–13. doi: https://doi.org/10.3390/ma13030745.

Ozyhar, T., Hering, S. & Niemz, P. (2012). Moisture-dependent elastic and strength anisotropy of European beech wood in tension. *Journal of Materials Science*, 47, 6141–6150. doi: https://doi.org/10.1007/s10853-012-6534-8.

Ozyhar, T., Hering, S. & Niemz, P. (2013). Moisture-dependent orthotropic tension-compression asymmetry of wood. *Holzforschung*, 67, 395–404. doi: https://doi.org/10.1515/hf-2012-0089.

Ozyhar, T., Hering, S., Sanabria, S.J. & Niemz, P. (2013). Determining moisture-dependent elastic characteristics of beech wood by means of ultrasonic waves. Wood Science and Technology, 47, 329–341. doi: https://doi.org/10.1007/s00226-012-0499-2.

Pramreiter, M. & Grabner, M. (2023). The Utilization of European Beech Wood (*Fagus sylvatica* L.) in Europe. *Forests*, 14, 1419. doi: https://doi.org/10.3390/f14071419.

Reshke, R.G. (1999). Bolted timber connections loaded perpendicular-to-grain. Influence of joint configuration parameters on strength. PhD Thesis, Royal Military College of Canada, Canada.

Sathre, R. & Gustavsson, L. (2009). Using wood products to mitigate climate change: External costs and structural change. *Applied Energy*, 86, 251–257. doi: https://doi.org/10.1016/j.apenergy.2008.04.007.

Schoenmakers, J.C.M. (2010). Fracture and failure mechanisms in timber loaded perpendicular to the grain by mechanical connections. PhD Thesis, Universiy of Tecnology Eindhoven, Netherlands. doi: https://doi.org/10.6100/IR673053.

Smith, I., Landis, E. & Gong, M. (2003). Fracture and Fatigue in Wood. John Wiley & Sons Ltd, The Atrium, Chichester, England. ISBN: 0471487082.

UNE-EN 13183-1:2002. Contenido de humedad de una pieza de madera aserrada. Parte 1: Determinación por el método de secado en estufa. AENOR.

UNE-EN 1912:2012. Madera estructural. Clases resistentes. Asignación de calidades visuales y especies. AENOR.

UNE-EN 1995-1-1:2016. Eurocódigo 5: Proyecto de estructuras de madera. Parte 1-1: Reglas generales y reglas para edificación. AENOR.

UNE-EN 350:2016. Durabilidad de la madera y de los productos derivados de la madera. Ensayos y clasificación de la resistencia a los agentes biológicos de la madera y de los productos derivados de la madera. AENOR.

UNE-EN 408:2010+A1:2012. Estructuras de Madera. Madera aserrada y madera laminada encolada para uso estructural. Determinación de algunas propiedades físicas y mecánicas. AENOR.

UNECE & FAO. (2023). Circularity Concepts in Wood Construction. United Nations Publication. Disponible online: https://unece.org/forests/publications/circularity-concepts-wood-construction.

UNEP. (2009). Buildings and Climate Change: Summary for Decision-Makers. United Nation Environment Programme. UNEP DTIE, Sustainable Consumption & Production Branch. ISBN: 987-92-807-3064-7.

Van der Put, T.A.C.M. (1990). Tension perpendicular to the grain at notches and joints. En: *Proceedings of the International Council for Research and Innovation in Building and Construction (CIB-W18)*, Lisbon, Portugal.

Van der Put, T.A.C.M. & Leijten, A.J.M. (2000). Evaluation of perpendicular to grain failure of beams caused by concentrated loads of joints. En: *Proceedings of the International Council for Research and Innovation in Building and Construction (CIB-W18)*, Delft, The Netherlands.

Widmann, R., Fernandez-Cabo, J.L. & Steiger, R. (2012). Mechanical properties of thermally modified beech timber for structural purposes. *European Journal of Wood and Wood Products*, 70, 775–784. doi: https://doi.org/10.1007/s00107-012-0615-x.

Xavier, J., Oliveira, M., Morais, J.J.L. & De Moura, M.F.S.F. (2014). Determining mode II cohesive law of *Pinus pinaster* by combining the end-notched flexure test with digital image correlation. *Construction and Building Materials*, 71, 109–115. doi: https://doi.org/10.1016/j.conbuildmat.2014.08.021.

Yasumura, M. (2001). Criteria for Damage and Failure of Dowel-Type Joints Subjected To Force Perpendicular To the Grain. En: *Proceedings of the International Council for Research and Innovation in Building and Construction (CIB-W18)*, Venice, Italy.

Parte II

Constantes elásticas

Este trabajo se encuentra recogido en la Publicación I.

Publicación I

Determination of the elastic constants of thermally modified beech by ultrasound and static tests coupled with 3D digital image correlation

José Luis Gómez-Royuela, Almudena Majano-Majano, Antonio José Lara-Bocanegra, Thomas P.S. Reynolds.

Construction and Building Materials, 302: 124270, 2021
DOI: https://doi.org/10.1016/j.conbuildmat.2021.124270
Q1 (JCR). Impact factor: 7,693

Construction and Building Materials 302 (2021) 124270

Contents lists available at ScienceDirect

Construction and Building Materials

journal homepage: www.elsevier.com/locate/conbuildmat

Determination of the elastic constants of thermally modified beech by ultrasound and static tests coupled with 3D digital image correlation

José Luis Gómez-Royuela [a], Almudena Majano-Majano [a,*], Antonio José Lara-Bocanegra [a], Thomas P.S. Reynolds [b]

[a] Department of Building Structures and Physics, Higher Technical School of Architecture, Universidad Politécnica de Madrid (UPM), Avda. Juan de Herrera, 4. 28040 Madrid, Spain

[b] Institute for Infrastructure and Environment, School of Engineering, University of Edinburgh, The King's Buildings, Mayfield Road, Edinburgh, Scotland EH9 3FG, UK

ARTICLE INFO

Keywords:
Beech
Thermally modified timber
Heat treatment
Elastic constants
Orthotropy
Ultrasound
Compression
DIC

ABSTRACT

Fagus sylvatica L. (European beech) is one of the most widespread hardwood species growing in Europe, which is currently undergoing of in-depth research for the development of engineering products to use its excellent mechanical properties. As its natural durability is low, heat treatment is investigated as a means to enhance its biological durability, as well as its dimensional stability. Reliable models with a full material description including the elastic constants are necessary for material and structural modelling and design. The aim of this work was to comprehensively characterise European beech subjected to three different intensities of heat treatments. It is described as an orthotropic material by determining all of the independent elastic constants: three Young's moduli, three shear moduli and six Poisson's ratios. Both static (by compression) and dynamic (by ultrasound) experimental methods were considered for comparison purposes. The compression tests were coupled with 3D digital image correlation (DIC) technique to perform optical full-field analyses of strains. Characterization of untreated beech was also carried out and compared with literature values. The usual assumption of symmetry of the compliance matrix was verified. The results confirmed that heat treatment influenced the elastic behaviour of the material. However, the impact of the treatment differed among the elastic components, with non-uniform trends with the intensity of the heat treatments.

1. Introduction

Fagus sylvatica L. (European beech) is one of the most important and widespread hardwood species growing in Europe. There is a very high and steadily increasing share of this wood in European forests due mainly to forest policies and the progressing climate change [1]. Currently, beech is primarily used in the furniture industry. However, there is active research on the development of engineering products from beech for the construction industry taking into account the high mechanical properties of this species [1]. Even so, beech shows high shrinkage and low natural durability, so use in outdoor environments without protective treatments are not envisioned.

In this sense, heat treatment is considered one of the most effective preservative methods used to enhance mainly biological durability and dimensional stability of wood [e.g. [2–4]] and an established alternative to other treatments that may be harmful to the environment. A significant disadvantage is, however, a reduction in fracture toughness and strength [e.g. [5–7]], which can limit the range of structural applications, with the most common uses of thermally-treated wood as cladding, decking, garden furniture, and interior joinery. A better understanding of the effect of thermal treatment on mechanical behaviour could open new markets for timber construction. For example, research has been carried out into the use of thermally modified European beech in load bearing members for industrial buildings or noise protection barrier systems for roads [7,8]. Given the large resource of European beech, thermal treatment could allow it to be used for the development of new value-added products for outdoor applications, as an alternative to tropical hardwoods or impregnated softwoods.

If heat-treated European beech is to be used as a structural material, it will be necessary to carry out accurate structural analysis and modelling of its behaviour. Alongside strength parameters, the elastic constants which characterize its deformation under load are vital to such

* Corresponding author.
E-mail addresses: joseluis.gomez.royuela@upm.es (J. Luis Gómez-Royuela), almudena.majano@upm.es (A. Majano-Majano), antoniojose.lara@upm.es (A. José Lara-Bocanegra), T.Reynolds@ed.ac.uk (T.P.S. Reynolds).

https://doi.org/10.1016/j.conbuildmat.2021.124270
Received 7 June 2020; Received in revised form 9 July 2021; Accepted 14 July 2021

models, and so their determination is of considerable interest.

Wood is anisotropic, and is usually considered for engineering purposes as an orthotropic material, defined by its properties in three directions: longitudinal (L), radial (R), and tangential (T) [9,10]. Consequently, twelve elastic engineering parameters are required for a complete elasto-mechanical characterization in any computational model: three Young's moduli (E_L, E_R, E_T), three shear moduli (G_{LR}, G_{LT}, G_{RT}), and six Poisson's ratios (ν_{LR}, ν_{RL}, ν_{LT}, ν_{TL}, ν_{RT}, and ν_{TR}). These parameters can be reduced to nine when symmetry conditions in the stiffness matrix are applied. A theorical background of orthotropic elasticity in wood can be found in Bodig and Jayne [11].

The elastic characterization in wood involves therefore a great experimental effort, especially due to the need of several specimens oriented along the different orthotropic directions when commonly experimental testing methods are applied. Nonetheless, experimental work on the elastic behaviour of different species has been performed by numerous researchers.

Classical experimental methods for wood characterization are mechanical tests following compression or tension configurations. In them, displacement or strains used to be recorded by mechanical or electrical measurement systems (e.g. strain gauges, inductive strain devices, extensometers) [e.g. [12,13]]. However, recent development of full-field optical measurement techniques such as digital image correlation (DIC), grid/moiré method, speckle and moiré interferometry or shearography, have enabled novel mechanical tests for material characterization. Particularly 2D and 3D optical measurements systems based in DIC are being increasingly used in recent studies for the the determination of the elastic constants in wood [e.g. [14,15]]. This is a non-contact technique which shows clear advantages in comparison with conventional techniques: it is entirely non-intrusive, so does not influence the specimen during testing; and it measures accurate deformations over the whole visible surface of the specimen in three dimensions. The latter is crucial for heterogeneous materials and leads to more robust results considering the strong variability inherent to wood. In addition, these techniques have allowed the development of testing procedures to reduce the number of necessary specimens [16].

Another remarkable experimental method which has drawn increasing attention in elastic characterization of wood is ultrasonic testing. It is a very efficient non-destructive technique which allows fast measurements in small-size specimens, advantages highlighted by [17–19]. The development of fast measurement techniques is important to increase the number of available data for wood. In many studies, ultrasonic testing was limited to the determination of the elastic moduli. However, it is also possible to obtain all the elastic constants using specimens with the grain angles oriented to the different planes of ortotropy [e.g. [18,20,21]].

There is comprehensive research on the mechanical characterization of elastic properties in untreated European beech by different experimental techniques [e.g. [13,18,21–32]]. On the contrary, only few studies have dealt so far with the investigation of the influence of heat treatments on the elastic constants for this species. Widmann et al. [7] reported experimental data on different mechanical properties in order to benchmark the thermally treated beech at around 180–190 °C to the European EN 338 strength class system for structural timber. Regarding the elasticity constants, E_0 and E_{90} were derived from tension parallel to grain and compression perpendicular to grain tests respectively. Sebera et al. [33] provided the E_L values of thermally treated beech subjected to 180 °C and 200 °C obtained from compression tests. Fajdiga et al. [34] and Straže et al. [35] determined also from compression tests the E_L and E_T moduli of heat treated beech at 210 °C. Wetzig et al. [36] reported the three Young's moduli and two Poisson ratios (ν_{LR} and ν_{LT}) of heat-treated beech subjected to two different treatment atmostpheres from static and ultrasound tests, and the three shear moduli by ultrasound alone. Loidl et al. [37] carried out initial work on similar material to that used in the present study to derive the three Young and shear moduli (but not the Poisson's ratios) by means of the resonant beam technique method. However, to the authors' best knowledge, there are no research which provide a complete data set of the twelve elastic constants of thermally treated European beech: some of the Poisson's ratios have not been derived by any method; for other constants, namely the shear moduli, there are no reported values obtained from common static tests, taking into account that test method may affect the results.

The main objective of the present study is to provide a complete data set of elastic engineering constants (the three Young's moduli, the three shear moduli and the six Poisson's ratios) for untreated and thermally treated European beech (*Fagus sylvatica* L.) modified at three different heating temperatures. Dynamic and static measurement techniques were compared to this aim: ultrasound and compression tests. In the latter, optical full-field analysis of strains was performed by means of a 3D non-contact optical device based on the digital image correlation (DIC) method. In the process, the usual assumption of symmetry of the compliance matrix was verified. The determined elastic constants provide fundamental input parameters for reliable models with a full material description necessary for material and structural modelling and design.

2. Theoretical background

2.1. The compliance matrix [S]: Mechanical characterization

Derived from Voigt's [38] crystal elasticity theory, wood is regarded as a rhombic crystalline material with linear elastic mechanical properties which differ according to three orthotropic axes (L, R, T) orthogonal to each other. This elastic model of the material can be expressed by the generalized Hooke's law which considers a linear relationship between stresses and strains in the form (Eq. (1)):

$$[\varepsilon_{kl}] = [S_{ijkl}][\sigma_{ij}] \tag{1}$$

where $[\varepsilon]$ corresponds to the strain vector defined by elongations, ε, and shear strains, γ; $[\sigma]$ denotes the stress vector formed by the normal stresses, σ, and shear stresses, τ; and $[S_{ijkl}]$ is the compliance matrix composed of twelve compliance components, s_{ij}, which are function of the so-called elastic engineering parameters, also referred as elastic constants, expressed in Eq. (2). These parameters can be determined by mechanical tests as will be described in section 3.3.

$$\begin{pmatrix} \varepsilon_L \\ \varepsilon_R \\ \varepsilon_T \\ \gamma_{RT} \\ \gamma_{TL} \\ \gamma_{LR} \end{pmatrix} = \begin{bmatrix} \frac{1}{E_L} & -\frac{\nu_{RL}}{E_R} & -\frac{\nu_{TL}}{E_T} & 0 & 0 & 0 \\ -\frac{\nu_{LR}}{E_L} & \frac{1}{E_R} & -\frac{\nu_{TR}}{E_T} & 0 & 0 & 0 \\ -\frac{\nu_{LT}}{E_L} & -\frac{\nu_{RT}}{E_R} & \frac{1}{E_T} & 0 & 0 & 0 \\ 0 & 0 & 0 & \frac{1}{G_{RT}} & 0 & 0 \\ 0 & 0 & 0 & 0 & \frac{1}{G_{TL}} & 0 \\ 0 & 0 & 0 & 0 & 0 & \frac{1}{G_{LR}} \end{bmatrix} \begin{pmatrix} \sigma_L \\ \sigma_R \\ \sigma_T \\ \tau_{RT} \\ \tau_{TL} \\ \tau_{LR} \end{pmatrix} \tag{2}$$

In the previous expression, the twelve compliance components can be reduced to nine since symmetry condition may be satisfied according to the elasticity theory, where elastic deformation is non-dissipative [11]. In this regard, the off-diagonal terms are related as follows (Eq. (3)):

$$-\frac{\nu_{RL}}{E_R} = -\frac{\nu_{LR}}{E_L}; -\frac{\nu_{TL}}{E_T} = -\frac{\nu_{LT}}{E_L}; -\frac{\nu_{TR}}{E_T} = -\frac{\nu_{RT}}{E_R} \tag{3}$$

Accordingly, three Young's moduli, three shear moduli and just three Poisson's ratios instead of six are the independent elastic constans needed to build the compliance matrix of the material. Deeper fundamentals on the elastic constants in wood can be seen in [11,39].

2.2. The stiffness matrix [C]: Ultrasound characterization

The stiffness matrix and the compliance matrix have an inverse relation by the form $[C_{ijkl}]^{-1} = [S_{ijkl}]$. Accordingly, the material elastic model can be expressed by the generalized Hooke's law as (Eq. (4)):

$$[\sigma_{ij}] = [C_{ijkl}][\varepsilon_{kl}] \tag{4}$$

Assuming symmetry of the non-diagonal terms, the stiffness matrix is composed by nine independent terms (Eq. (5)) which can be determined by ultrasound tests.

$$\begin{bmatrix} C_{11} & C_{12} & C_{13} & 0 & 0 & 0 \\ C_{12} & C_{22} & C_{23} & 0 & 0 & 0 \\ C_{13} & C_{23} & C_{33} & 0 & 0 & 0 \\ 0 & 0 & 0 & C_{44} & 0 & 0 \\ 0 & 0 & 0 & 0 & C_{55} & 0 \\ 0 & 0 & 0 & 0 & 0 & C_{66} \end{bmatrix} \tag{5}$$

The relationship between elasticity and wave propagation theories has the origin in the Christoffel equation (Eq. (6)):

$$\left(C_{iklm}n_k n_1 - \rho V^2 \delta_{im}\right)u_m = 0 \tag{6}$$

This equation represents a set of three homogeneous first degree equations at u_1, u_2 and u_3. n denotes the components of the wave vector; δ_{im} is the unit tensor or the Kronecker delta which becomes 1 when $i = m$, and 0 if $i \neq m$. The term $C_{iklm}n_k n_1$ can be simplified by λ_{im}, known as Christoffel tensor.

By solving the corresponding equations and taking into account the displacement vectors of the particles or polarization (see [40] for more details), it is possible to determine the diagonal terms of the stiffness matrix [C] according to [17]:

$$C_{LL} = C_{11} = \rho V_{LL}^2$$

$$C_{RR} = C_{22} = \rho V_{RR}^2$$

$$C_{TT} = C_{33} = \rho V_{TT}^2$$

$$C_{RT} = C_{44} = \rho\left(V_{RT}^2 + V_{TR}^2\right)/2$$

$$C_{LT} = C_{55} = \rho\left(V_{LT}^2 + V_{TL}^2\right)/2$$

$$C_{LR} = C_{66} = \rho\left(V_{LR}^2 + V_{RL}^2\right)/2 \tag{7}$$

being ρ the material density (kg/m^3) and V the wave velocity (m/s), with the first subscript denoting the direction of propagation and the second one the direction of polarization.

The off-diagonal terms of the stiffness matrix are obtained as follows:

$$(C_{12} + C_{66})n_1 n_2 = \left[\left(C_{11}n_1^2 + C_{66}n_2^2 - \rho V_\alpha^2\right)\left(C_{66}n_1^2 + C_{22}n_2^2 - \rho V_\alpha^2\right)\right]^{1/2}$$

$$(C_{23} + C_{44})n_2 n_3 = \left[\left(C_{22}n_2^2 + C_{44}n_3^2 - \rho V_\alpha^2\right)\left(C_{44}n_2^2 + C_{33}n_3^2 - \rho V_\alpha^2\right)\right]^{1/2}$$

$$(C_{13} + C_{55})n_1 n_3 = \left[\left(C_{11}n_1^2 + C_{55}n_3^2 - \rho V_\alpha^2\right)\left(C_{55}n_1^2 + C_{33}n_3^2 - \rho V_\alpha^2\right)\right]^{1/2} \tag{8}$$

where α is the wave propagation angle outside the symmetry axes (45°); $n_1 = \cos\alpha$, $n_2 = \sin\alpha$, $n_3 = 0$ when α is taken in relation to axis 1 (plane 12); $n_1 = \cos\alpha$, $n_3 = \sin\alpha$ and $n_2 = 0$ when α is taken in relation to axis 1 (plane 13); and $n_2 = \cos\alpha$, $n_3 = \sin\alpha$ and $n_1 = 0$ when α is taken in relation to axis 2 (plane 23).

When all the terms of the stiffness matrix [C] are determined, the calculation of the compliance matrix [S] can be performed by the inverse matrix $[C]^{-1}$ and therefore obtain the whole set of elastic constants. This procedure is known as full-stiffness-inversion method. It requires specimens oriented at different angles with respect to the man directions L, R and T (see details in section 3.2). There are other simplified evaluation techniques that only require specimens oriented along the main directions thus increasing the time efficiency of the tests, such as the simplified-uncorrected technique in Bachtiar [41]. According to it, the off-diagonal terms of [C] are considered zero (and therefore also the Poisson's ratios), but it overestimates the values of Young's moduli [21]. In Bachtiar [41] the alternative simplified-corrected technique is also proposed to correct the Young's moduli by means of a k-factor expressed as a function of the Poisson's ratios, which could be taken from the literature. In the present study, the full-stiffness-inversion method was applied.

3. Materials and methods

3.1. Material

European beech (*Fagus sylvatica* L.) was provided by Mitteramskogler GmbH, Austria. The pre-dried (to approximately 8–12% MC) boards were modified at heating temperatures of 180° (Mezzo, hereafter referred as T1), 200° (Forte, referred as T2) and 230° (Forte exterior, referred as T3) in a dry three-stage heat-treatment process: phase 1) a fast increase of oven temperature is performed followed by a gradual increase using heat and steam until almost zero moisture content in wood is reached. Steam acts as protection gas, keeps process slightly pressurized and replaces oxygen inside chamber; phase 2) actual thermal modification is carried out with an increase of temperature to wanted level which is kept constant during some hours; phase 3) cooling and re-conditioning stage to bring moisture content of wood back to the desired level. More details on the process data are commercially sensitive and thus cannot be published. Both treated and untreated (control) specimens were obtained from the same "twin" board (one half thermally treated and the other half untreated) in order to reduce variability.

Small-clear specimens were prepared for each treatment batch (Fig. 1) oriented in the different anatomical directions as will be specified in next subsections. Prior to testing, the specimens were conditioned at 20 °C and 65% relative humidity until equilibrium moisture content was reached. Mean moisture contents of 11.6%, 6.2%, 4.3 and 4.1% were measured by T0, T1, T2 and T3 batches, respectively, of the specimens destined to ultrasound tests, and analogously 11.4%, 6.3%, 4.3 and 4.2% for the groups of compression tests. Densities were also measured from the conditioned specimens. The mean densities for the different batches of ultrasound tests were: 633 kg/m^3 (T0), 679 kg/m^3 (T1), 599 kg/m^3 (T2) and 648 kg/m^3 (T3). The mean densities of the specimens used in the compression tests were: 677 kg/m^3 (T0), 694 kg/m^3 (T1), 624 kg/m^3 (T2) and 640 kg/m^3 (T3). The difference in mean density is thought to be consistent with random sampling rather than an effect of the treatment.

3.2. Ultrasound tests

A series of five prismatic specimens following the orientations represented in Fig. 2 were required for ultrasound testing [20]. Specimens 1 and 2 of 20 × 30 × 70 mm^3 were oriented along the main axes to derive the diagonal terms of the stiffness matrix (only one of the two specimens

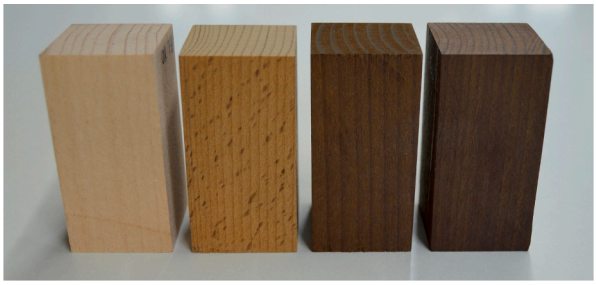

Fig. 1. Control and thermally treated beech samples. From left to right: untreated, Mezzo, Forte and Forte exterior.

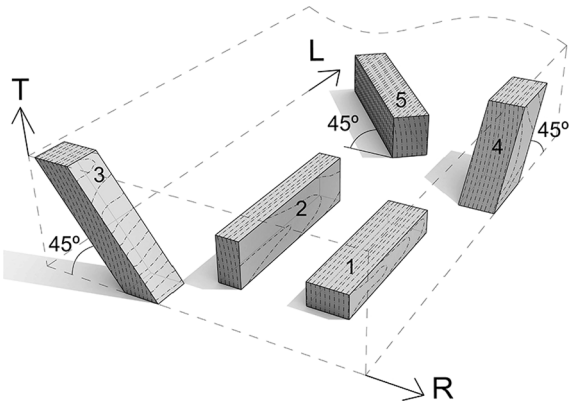

Fig. 2. Specimen orientations for ultrasound tests.

would be strictly necessary). Specimens 3, 4 and 5, with 30 × 30 mm^2 cross-section and length adapted to the board thickness (45 mm), were oriented 45° to the planes RT, LT and LR, so the remaining components of the stiffness matrix could be obtained. The 45° angle was chosen taking into account studies carried out by Bucur and Archer (1984) [18], which concluded that this angle produced the smallest relative error when finding the C_{13} term of the stiffness matrix (see section 2.2). Eight specimens per orientation in every batch of treatments (and untreated wood) were tested.

An Olympus Epoch 600 portable device (Fig. 3) equipped with longitudinal and transverse Panametrics-NDT Olympus plane transducers of 1 MHz nominal frequency and 15 mm external diameter was used.

The flight time of the waves propagating on each specimen was recorded. The wave velocity, V, for each specimen was derived from the measured time and the specimen length. The elastic constants were consequently obtained considering the wave velocity and the material density, ρ, according to the description specified in section 2.2.

When longitudinal transducers are positioned on the specimen faces parallel to the main axes L, R and T, a longitudinal wave is released which propagate and polarize directionally along such axes and consequently V_{LL}, V_{RR} and V_{TT} velocities can be obtained. Similarly, by placing the transverse transducers on the corresponding faces, the wave propagation takes place along the major axes and polarize along the perpendicular one. In this way V_{LR}, V_{RL}, V_{LT}, V_{LT}, V_{RT} and V_{TR} velocities are derived. From specimens oriented at 45°, V_{α} can be obtained for each plane by means of transverse transducers [18]).

Wavelengths (λ) of 5 mm in the longitudinal direction, 2.5 mm in the radial direction, and 1.8 mm in the tangential direction were selected, resulting in a minimum ratio of path length per wavelength (L/λ) of 18 (L values somewhat greater than λ are recommended to approximate to the hypothesis of infinite wave propagation mode [17,42]).

Both transducers had an outer diameter of 18 mm, which fitted to the specimen's dimensions. To improve coupling as much as possible and keep constant pressure throughout measuring, pure starch glucose was used as couplant gel between both transducers and the specimens.

3.3. Compression tests coupled with digital image correlation technique

Small clear prismatic specimens were also subjected to mechanical compression tests in order to get all the elastic constants of the untreated and heat-treated beech.

A 3D stereovison system based on the digital image correlation principle (DIC), ARAMIS® 3D [43], was used for strain measurements. Its coupling to universal testing machine is easy since it is a white-light technique and does not need any specific equipment such anti-vibration tables or laser, required by other interferometric measurement devices.

The system comprises two CCD cameras of 5 Megapixels resolution with 35-mm lens, positioned facing the specimen to be tested (Fig. 4). A stereovision angle of 25° between both cameras was set. A reference field of view of 65 mm × 55 mm was selected. The base distance between cameras was adjusted to 110 mm, making it match the centre of the especimen and the centre of the images. It corresponded to a working distance of 340 mm. The depth of field was adjusted to 46 mm to image each pair of orthogonal adjacent faces of the prismatic specimen. Two light sources were adjusted in order to guarantee an even illumination of the specimen and to avoid local over-exposure.

The DIC system was calibrated before testing using a calibration panel with a dimension similar to that of the region of interest. In the procedure, some images are taken successively by translating and rotating the calibration panel with respect to the optical device. In this way, a measurement volume is defined in which the specimen must fit.

The method requires a textured pattern (speckle pattern) created onto the specimen surface to be analysed. A thin coating of matt white aerosol spray paint was applied, followed by a spot distribution of airbrush black paint, which gave a suitable contrast.

Once the device and specimens were prepared, images of the surface of interest were recorded during testing. These images are mapped by correlation of facets formed by a group of pixels, within which an independent measurement of the displacement is calculated. The strain field is finally obtained by analyzing the geometrical deformation produced in the images. Therefore, it is important for the accuracy of the measurements, to decide an appropriate facet size. In the present work, a facet size of 15 × 15 pixel^2 was considered to offer a good compromise with the region of interest size and the pattern quality of the specimen. In order to enhance spatial resolution, a facet step size of 13 × 13 pixel^2 was chosen for an overlap of 2 pixels. The in-plane displacements were then numerically differentiated on a base computation size of 5 subsets.

The compression tests were carried out using a universal testing machine. The specimens were placed in such a way that the deformation field at two adjacent faces could be visible by the optical equipment and measured simultaneously. The specimens were loaded under displacement control between 0.2 and 0.4 mm/min. Synchronized stereo images of the patterned surface with the different loading stages were recorded

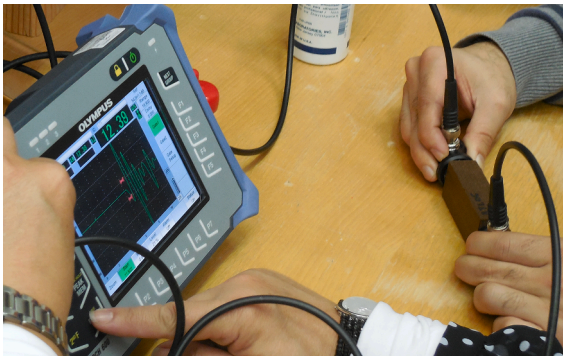

Fig. 3. Ultrasound testing device.

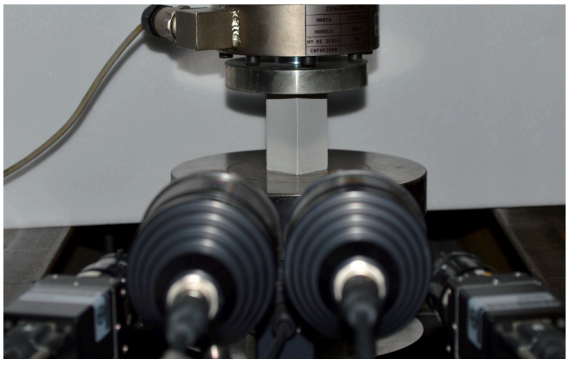

Fig. 4. Compression set-up coupled with ARAMIS® 3D.

every second. Most of the test were kept in the elastic range in order to derive all of the possible elastic constants from the same specimen. Some tests were continuted to failure.

The Young's moduli were processed afterwards as the ratio of the stress (σ_i) to the respective strain (ε_i) in the load direction (Eq. (10)). It corresponds to the slope of the elastic region in the stress–strain curve, and was evaluated as the result which provides the maximum coefficient of determination, R^2.

$$E_i = \frac{\Delta\sigma_i}{\Delta\varepsilon_i}, i \in R, L, T \tag{10}$$

The Poisson's ratios were determined by the relationship between two strain components optically recorded: the active strain component (ε_i) in the load direction, and the passive strain component (ε_j) normal to the load direction (Eq. (11)) in each of the two visible faces of the specimen by the optical device.

$$\nu_{ij} = -\frac{\varepsilon_j}{\varepsilon_i},\ i,j \in R, L, T \text{ and } i \neq j \tag{11}$$

Accordingly, three different compression set-ups were followed:

- Compression tests parallel to the grain as specified in ISO 13061-17:2017 [44] on specimens of 30 × 30 mm^2 cross-section and 60 mm length, from which E_L, ν_{LR} and ν_{LT} were derived.
- Two compression tests perpendicular to the grain by applying the load along the radial and tangential directions respectively following ISO 13061–5:2020 [45]. Prismatic specimens of 30 × 60 mm^2 of compression surface and 30 mm height were used in these cases. E_R, ν_{RL} and ν_{RT} (from radial test) and E_T, ν_{TL} and ν_{TR} (from tangential test) were calculated.

Eight specimens in every batch of treatments (and untreated beech) were tested to derive the Young's moduli and Poisson's ratios.

In order to determine the three shear moduli, three 45° off-axis compression tests relative to every of the three orthotropic directions were executed. To this aim, batches consisting of eight to thirteen prismatic specimens with the grain oriented 45° to the load direction were tested. Specimens of 30 × 30 × 60 mm^3 were used for LR and RT planes and 30 × 30 × 38 mm^3 for the LT plane due to the limitation thinckness of the board. Vertical strain in the load direction, ε_V, and horizontal strain in the transverse direction, ε_H, were recorded from the front face of the specimen visible by the optical device in every of the three configurations. The shear moduli G_{LR}, G_{LT} and G_{RT} were determined according to Eq. (12).

$$\begin{aligned} G_{LR} &= \frac{\tau_{LR}}{\gamma_{LR}} = \frac{\sigma_V}{2(\varepsilon_H - \varepsilon_V)}; \\ G_{LT} &= \frac{\tau_{LT}}{\gamma_{LT}} = \frac{\sigma_V}{2(\varepsilon_H - \varepsilon_V)}; \\ G_{RT} &= \frac{\tau_{RT}}{\gamma_{RT}} = \frac{\sigma_V}{2(\varepsilon_H - \varepsilon_V)} \end{aligned} \tag{12}$$

4. Results and discussion

4.1. Ultrasound parameters

Table 1 shows the ultrasonic wave velocities along different propagation and polarization directions from heat treated beech by the three treatments T1, T2 and T3 in comparison to the untreated beech wood (T0). The coefficient of variation (CoV) from all the specimens with each treatment is included in brackets.

As can be seen, the V_{ii} differ in each of the orthotropic directions. For the untreated material, the measured mean value of V_{LL} was double the mean V_{RR}, which is in agreement with the results obtained from beech by Ozyhar et al. [21]. This relation was similar in the case of heat-treated beech, with slightly higher mean V_{LL} value for the most severe heat treatments. The mean V_{TT} was approximately one third of the V_{LL} (1/4 was reported in Ozyhar et al. [21]).

Table 1
Mean values and coefficient of variations (percentage in brackets) for the wave propagation velocities in heat treated (T1, T2, T3) and untreated (T0) beech from ultrasound tests.

V [m/s]	T0	T1	T2	T3
$V_{11}\equiv V_{LL}$	4932 (2.0)	4986 (2.5)	5271 (3.9)	5339 (2.8)
$V_{22}\equiv V_{RR}$	2390 (1.8)	2448 (4.1)	2351 (6.5)	2334 (2.6)
$V_{33}\equiv V_{TT}$	1647 (2.0)	1840 (9.2)	1650 (5.7)	1671 (2.7)
$V_{44}\equiv V_{RT}\equiv V_{TR}$	905 (5.5)	913 (5.6)	884 (2.1)	905 (3.3)
$V_{55}\equiv V_{LT}\equiv V_{TL}$	1252 (5.0)	1391 (5.1)	1473 (3.7)	1336 (7.6)
$V_{66}\equiv V_{LR}\equiv V_{RL}$	1463 (11.0)	1627 (4.4)	1586 (4.4)	1630 (1.5)
$V_{12}\equiv V_{QLR}$	1836 (3.1)	1854 (3.1)	1821 (4.6)	1832 (1.8)
$V_{13}\equiv V_{QLT}$	1344 (2.2)	1490 (3.5)	1409 (4.7)	1374 (3.3)
$V_{23}\equiv V_{QTR}$	1036 (3.7)	989 (3.7)	940 (5.9)	1056 (6.0)

It is known that ultrasound velocity can be affected by factors such as moisture content, temperature or density, the latter being found one of the most dominant structural factors by some researchers. Increasing velocities trends with increasing densities were found in Bader et al. [23] from studies on different untreated hardwood species. Yilmaz and Aydin [46] did not report significant relation between V_{LL} and densities in heat treated oriental beech exposed to different temperatures in the process of determining the Young's modulus in longitudinal direction. In the present work, V_{LL} values were higher for heat-treated beech than for the untreated material. However, there is also no clear trend between wave velocities and heat treatment intensities, as there was neither trend between densities and treatment intensities. Even so, velocities from the different batches remained within a similar range.

Considering the average density of each group of treatment and the velocities specified in Table 1, the coefficients of the stiffness matrix were determined (Table 2).

4.2. Strain measurements

The 3D DIC system (ARAMIS® 3D) coupled with the compression tests for stereovision measurements provided 3D coordinates for each pair of images recorded during testing and then converted to relative displacements and strains. As mentioned above, the 3D system made it possible to measure two adjacent faces of the specimens simultaneously. This made it possible to check the uniformity of measurements on both sides and thus avoid possible defects in the testing or specimens manufacture. The measured working area was divided into a large number of facets (around 700 facets at the smallest faces and over 1500 at the largest) which provided corresponding strains. These strains at the working area data were finally averaged.

Figure 5 shows the results of strains on the two visible faces of a representative specimen subjected to a compression test with the load applied along the longitudinal direction. The time evolution of the strain during testing reveals an expected scenario, with increasing contraction

Table 2
Mean values and coefficient of variations (percentage in brackets) for the stiffness coefficients in heat treated (T1, T2, T3) and untreated (T0) beech from ultrasound tests.

C [MPa]	T0	T1	T2	T3
C_{11}	15,396 (3.6)	16,885 (6.3)	16,678 (8.9)	18,476 (4.1)
C_{22}	3617 (4.1)	4075 (10.1)	3329 (13.9)	3534 (6.5)
C_{33}	1672 (3.3)	2510 (17.5)	1627 (13.6)	1690 (6.3)
C_{44}	520 (11.2)	568 (11.4)	469 (6.2)	532 (8.1)
C_{55}	994 (10.2)	1315 (10.4)	1301 (5.2)	1164 (15.8)
C_{66}	1369 (22.3)	1801 (9.5)	1512 (10.4)	1721 (2.6)
C_{12}	1612 (19.1)	2253 (30.0)	1907 (27.5)	2029 (21.2)
C_{13}	1315 (12.9)	2098 (34.7)	1586 (21.9)	1439 (17.4)
C_{23}	1000 (13.7)	1819 (19.6)	1196 (10.8)	882 (21.8)

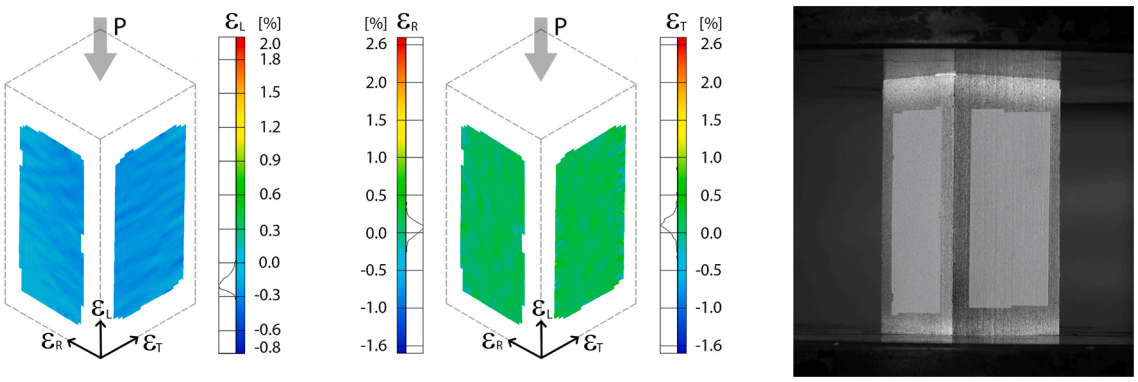

Fig. 5. Distribution of longitudinal (left), radial and tangential (middle) strains measured by DIC for a load of 22.9 kN in longitudinal direction. Measurement area marked on the specimen (right).

of the specimen in the axial direction (negative strain) and elongations in the transverse directions.

Similarly, Figs. 6 and 7 illustrate the three strain distributions on representative specimens subjected to compression perpendicular to the grain along the radial and tangential directions, respectively.

The horizontal and vertical strain distributions on a representative specimen subjected to oblique compression along the LR shear plane is exemplarity shown in Fig. 8.

As can be oberseved from Figs. 5-8, the strains were uniformally distributed on the specimens' faces. Possible boundary effects were avoided by restricting the strain measurements to the central area of the faces avoiding the edges. Even the small strains were reliably computed due to the subpixel accuracy of the DIC algorithm.

As indicated in the colourmaps and histograms in Figs. 5-8, there was a significant variation in strain across the surface of each specimen. Fig. 8 demonstrates that this variation is substantially due to real underlying variations in the strain in the material, rather than simply measurement noise, since it follows the orientation of the ring structure of the wood. In order to deal with measurement noise and material variation, it is valid to take the mean value of the strain on the face of the specimen.

A representative example of the curve-fitting process to determine the elastic constants determination is shown in Fig. 9.

In this example, an untreated beech specimen was loaded radially and mean strains on the RT surface were determined. As seen in Fig. 9 left, the E_R was derived from the slope of the elastic region in the stress–strain curve which provided the maximum R^2 (above 0.99). In Fig. 9 right, horizontal and vertical strains are plotted for the same data set. The values follow an acceptable narrow path. The slope of the linear regression corresponded to the Poisson's ratio ν_{RT} (0.73).

4.3. Elastic constants

Table 3 shows the mean values and the corresponding coefficient of variation of the different elastic constants that characterize untreated beech wood (T0) in comparison to modified beech at the three heat treatments (T1, T2 and T3) by ultrasound technique and compression tests.

The results grouped by Young's moduli, shear moduli and Poisson's ratios are discussed below.

4.4. Young's moduli

Figure 10 illustrates together the mean values and ranges of variation of Young's moduli obtained from the different heat treatments and the two testing methods for a better direct comparison.

In general, as can be deduced from the results, the stiffness of beech is not negatively affected by heat treatments. Sometimes the differences in elastic constants are not high, and in some cases the stiffness is increased in the heat-treated material compared to the untreated one. There is also no clear correlation among treatment intensities and values of elastic constants, although they all remain in the same range.

According to the Young's moduli results, the influence of heat treatments is more pronounced in the longitudinal direction than in radial or tangential. Overall, E_L values were higher for heat-treated beech than for untreated regardless of the measurement method, which support the general findings published for European heat-treated beech in [e.g. [7,33,34]].

In particular, there is an increase in the mean E_L values of approximately 12%, 23% and 20% between the untreated beech and T1, T2 and T3 treatments respectively, if we consider the static tests. These increases are somewhat lower than those reported by Sebera et al. [33] for beech treated in steam atmosphere at similar temperatures to T1 and T2 (increases of 15% and 38% respectively) from compression tests. Fajdiga et al. [34] reported an increase of 29% in E_L for heat-treated beech at 210 °C from compression tests. Meanwhile, the values reported by Wetzig et al. [36] for heat-treated beech in nitrogen atmosphere, also obtained from compression tests at normal environmental conditions,

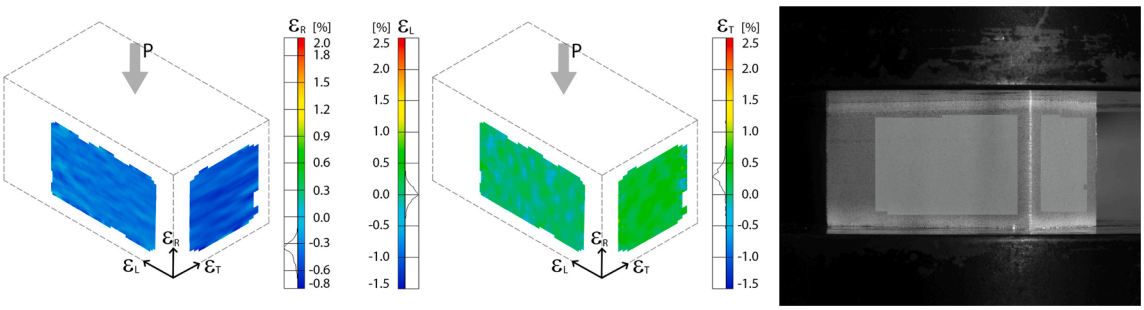

Fig. 6. Distribution of longitudinal (left), radial and tangential (middle) strains measured by DIC for a load of 14.5 kN in radial direction. Measurement area marked on the specimen (right).

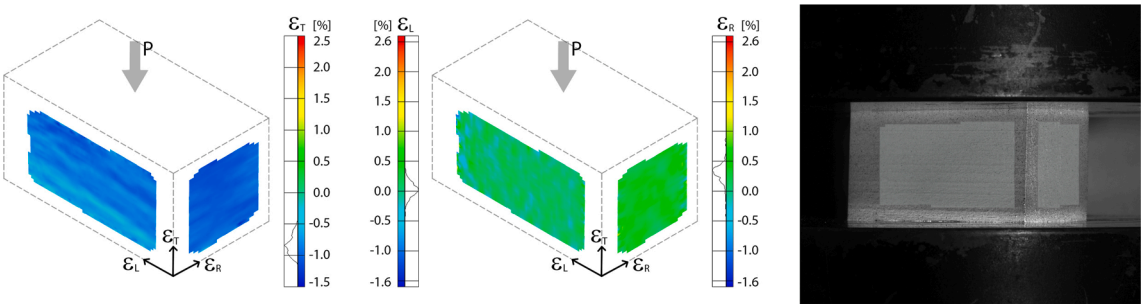

Fig. 7. Distribution of longitudinal (left), radial and tangential (middle) strains measured by DIC for a load of 12.8 kN in tangential direction. Measurement area marked on the specimen (right).

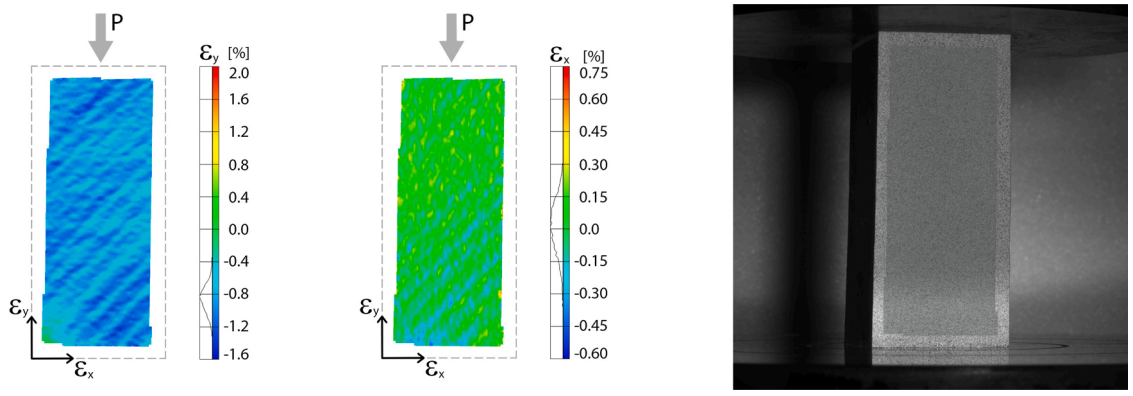

Fig. 8. Vertical (left) and horizontal (middle) strain distributions measured by DIC for a 45° LR loading configuration at 17.1 kN. Measurement area marked on the specimen (right).

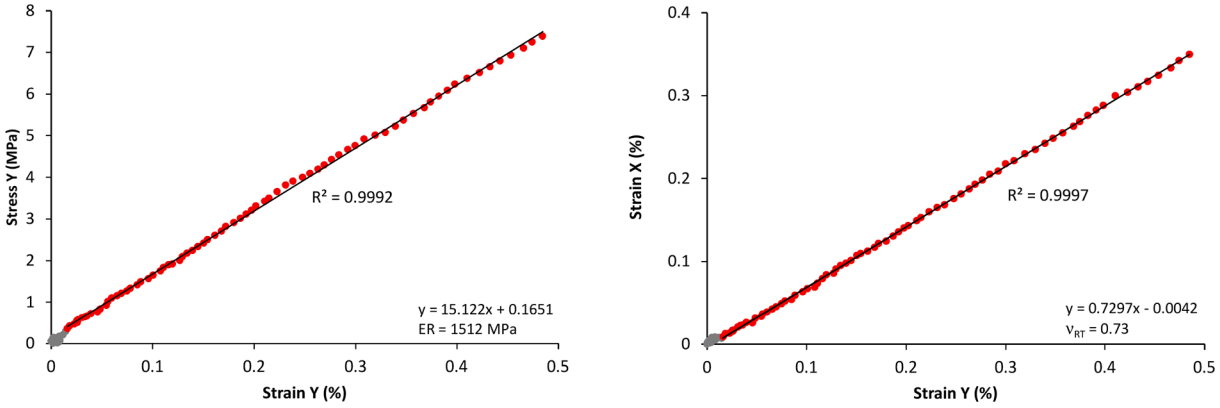

Fig. 9. Representative curves for T0 specimen loaded at radial direction: stress versus radial strain (left); horizontal (x) versus vertical (y) strains (right).

were rather similar to those of the reference material, and even reported lower values in the case of heat treated wood in steam atmosphere. This trend is similar to that obtained by Loidl et al. [37] using beech subjected to three treatments equal to those of the present work, where an increase in only 2% occurred with T1 (Mezzo) treatment. However, E_L of T2 (Forte) and T3 (Forte exterior) decreased by approximately 9.6% and 3.2%, respectively, with respect to the reference material. It should be noted that these latter results were obtained using the resonant beam technique and not from compression tests, so it can be deduced that the test method has a considerable influence on the results, even within different static tests themselves. This fact has already been proved by several authors. For example, greater E_L values from tensile than compression tests in heat-treated and untreated beech were reported in Wetzig et al. [36]. This tension–compression inequality of the elastic properties was also revealed in Ozyhar et al. [26] for untreated beech.

The non-linear increase in Young's moduli with treatment intensities is not only observed in the longitudinal direction, but also in the radial and tangential ones from static compression tests. This non-linear trend has already been shown in Yilmaz and Aydin [46], where elastic moduli in longitudinal direction seemed to increase for softer treatments and decrease for more severe ones. This may be related to the fact that lower moisture content of the specimens subjected to more intense treatments can positively affect the stiffness properties (a negative relationship between wood stiffness and moisture content is generally observed [e.g. [21,22,26]), but this effect may be surpassed by significant degradation of the chemical compounds [46], particularly the hemicellulose components of the polysaccharide complex [3]. This idea is supported by findings in heat treated wood presented by [e.g. [37,46,47]], where softer heat treatments showed and increase of this parameter while severe treatments tended to reduce it. As mentioned by Borůvka et al. [47],

Table 3
Mean values (x) in MPa and coefficient of variation (CoV) in % for the elastic constants of heat treated and untreated beech by compression and ultrasound tests.

		T0 Ultras.	T0 Compr	T1 Ultras.	T1 Compr	T2 Ultras.	T2 Compr	T3 Ultras.	T3 Compr
E_L [MPa]	x	14,078	13,811	14,821	15,443	14,798	16,930	16,619	16,559
	CoV	3.5	9.6	11.6	3.0	12.9	9.5	6.4	7.1
E_R [MPa]	x	2953	1590	2707	2031	2397	1866	2942	1811
	CoV	2.0	34.0	14.7	29.0	18.8	16.7	7.8	30.7
E_T [MPa]	x	1339	832	1586	1101	1132	834	1404	891
	CoV	6.6	13.9	12.5	32.2	14.9	13.2	7.7	19.2
G_{LR} [MPa]	x	1369	1108	1801	1433	1512	1479	1721	1344
	CoV	20.8	18.3	10.7	10.4	11.7	11.0	2.4	2.9
G_{LT} [MPa]	x	994	706	1315	723	1301	801	1164	929
	CoV	9.6	19.7	11.8	39.9	6.9	38.2	14.8	12.6
G_{RT} [MPa]	x	520	349	568	328	469	234	532	305
	CoV	10.5	15.3	12.8	17.9	7.7	17.2	7.6	17.2
ν_{LR}	x	0.27	0.44	0.25	0.43	0.29	0.39	0.40	0.45
	CoV	41.9	3.5	60.3	9.1	49.2	6.5	35.1	15.1
ν_{RL}	x	0.05	0.06	0.05	0.07	0.05	0.06	0.07	0.05
	CoV	41.5	48.1	72.9	39.7	62.9	52.5	46.1	33.0
ν_{LT}	x	0.63	0.51	0.62	0.51	0.76	0.49	0.65	0.46
	CoV	21.3	5.9	42.9	23.4	26.7	13.4	25.9	10.5
ν_{TL}	x	0.06	0.04	0.07	0.05	0.06	0.03	0.05	0.03
	CoV	18.0	55.5	49.3	62.2	25.8	27.4	27.2	28.0
ν_{RT}	x	0.55	0.62	0.68	0.55	0.69	0.66	0.45	0.64
	CoV	16.5	12.2	4.3	3.8	8.1	14.0	27.7	12.4
ν_{TR}	x	0.24	0.32	0.40	0.35	0.33	0.29	0.21	0.30
	CoV	12.2	13.0	20.4	15.3	18.4	14.7	28.4	18.4

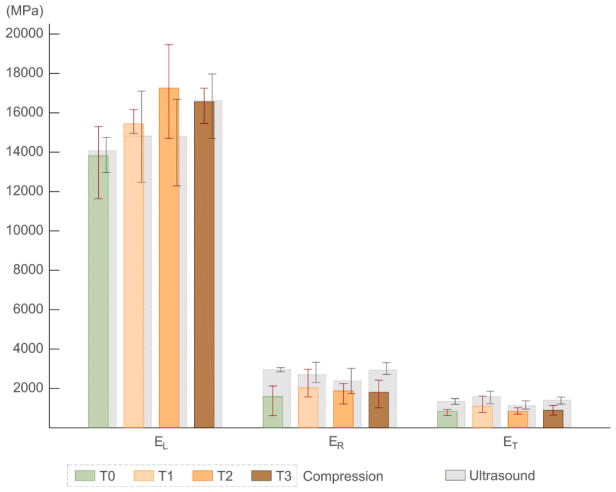

Fig. 10. Mean value and variation range for the Young's moduli of heat-treated and untreated beech obtained by ultrasound and compresion tests.

although changes in the polymerization degree may appear at low temperatures (above approx. 150 °C), it is proven by different studies that the decomposition of hardwood xylan of the hemicellulose begins at a temperature close to 200 °C in a normal atmosphere. Changes at temperatures below 200 °C have also been observed in lignin, despite it being a more thermally stable component [3].

If we look at the results from the dynamic tests, the increases in E_L appear to be less pronounced in comparison to static test results, approximately 5% for T1 and T2, and 18% for T3 in relation to T0, again without a clear trend regarding the intensity of the treatments.

Similarly, in the case of Young's moduli in transverse directions (E_R and E_T) slightly higher values can be associated with the heat-treated sets compared to the reference material from the static results. In particular, the increase in the mean E_R values was of approximately 28%, 17% and 14% for T1, T2 and T3 treatments, respectively, relative to untreated beech. The greatest improvement in E_T was also produced for T1 with 32%, whereas the improvement for T2 and T3 was smaller. Studies of Fajdiga et al. [34] in heat treated beech at 210 °C reported an increase in E_T by 16%, a little bit greater than that of the present work but still not too significant. Loidl et al. [37] reported and increase in stiffness with respect to reference material for Mezzo treatment, but a decrease in the cases of Forte and Forte exterior based on a resonant beam technique. Although the positive or negative effect with respect to untreated wood does not completely coincide with the present study, there is a similarity in terms of the decrease in the mean value of E_R and E_T with the severity of the treatment.

Unlike static results, the increasing stiffness is not expressed by E_R and E_T obtained from the dynamic tests, where heat treated beech offered greater or less values than untreated material depending on the treatment. In Wetzig et al. [36], the tangential modulus of elasticity in heat treated beech from ultrasound tests was clearly lower than in untreated material, but in the radial direction it depended on the type of heat treatment. Therefore, a clear overall statment on the influence of the heat treatment cannot be established in this case. A reason may be that micro-cracks and other inner faults might occur due to temperature exposure, so the prediction of the Young's moduli could be affected by these discontinuities [46]. Even so, the E_R and E_T values for the different treatments in the present work remain more or less in the same range.

These previous results clearly show that stiffness changes depend, in addition to the level of thermal treatment, also on the direction of mechanical loading and the cellular wood structure. The changes on a cellular level along the grain are presumably less affected during the thermal treatment so the compression stiffness is not negatively reduced in comparison with untreated material.

It is a known that Young's moduli for wood obtained by ultrasonic tests tend to give higher values than comparable ones obtained by static tests [e.g. [19,22]]. In heat-treated beech, Wetzig et al. [36] deduced E_L values up to 44% higher by ultrasound than compression methods. As shown, this general tendency is in accordance with the E_R and E_T results from this study (up to 62% higher values in heat treated beech by ultrasounds), but not entirely in E_L, although the high variability of these results must be taken into account.

The elastic anisotropy of wood expressed by the E_L:E_R:E_T ratio was stated by Bodig and Jayne [11] as approximately 20:1.6:1. The Young's moduli ratios obtained from the present study deviate slightly from this relationship (see Table 3). In this sense, it should be noted that the general relationship presented by Bodig and Jayne [11] comes from studies with different species.

The E_L:E_T ratios were different for each procedure: the ratios derived from ultrasound were around 1.6 times lower than those from static tests for all the heat treatments and reference groups. However, the E_R:E_T ratios remained widely unchanged regardless of heat treatment or testing procedure, with Young's moduli obtained in the radial direction ranging between 1.7 and 2.3 times greater than those corresponding to the tangential direction. This important difference beteween radial and tangential moduli in heat treated wood was also reported by Wetzig et al. [36]. This could be due to ray cells acting as reinforcements of the tissue in the radial direction.

Wood is a heterogeneous natural material, which implies great variability in mechanical properties [11]. It is exhibited by the Young's moduli coefficient of variation, especially in the radial direction. In longitudinal direction, the coeffient of variation exhibited lower values (below 10%).

In light of the scarce literature research on the determination of the elastic constants in heat-treated European beech and also considering the variability in the type of heat treatment, Table 4 presents a compilation of literature results of elastic moduli in untreated beech obtained in similar climatic conditions to the present study for comparison. It must be taken into account that moisture content, density, experimental method or specimen shapes are influencing factors that complicate direct comparisons.

Overall, the Young's moduli values obtained in the present research are of the same order of magnitude that those compiled from literature. Even the high values derived from ultrasound tests showed reasonable similarity with those in literature. In addition, as mentioned before, it is known from investigations that values determined by ultrasound methods are usually higher than those determined by static tests. From the literature compilation for unmodified beech, it becomes noticeable mainly in the radial moduli of elasticity. Also noticiceable is the remarkably wide range of variation of the longitudinal Young's modulus, varying from 9160 to 19100 MPa.

4.5. Shear moduli

Regarding the three shear moduli obtained from the compression and ultrasound tests performed in this work (Table 3), the effect of the three heat treatments in comparison to the untreated beech is illustrated in Fig. 11.

Overall, the mean shear moduli of heat-treated beech tended to be higher than those of the untreated material in LR and LT planes regardless of the measurement method, although the differences were not extremely large. That was not so clearly true in the TR plane, where

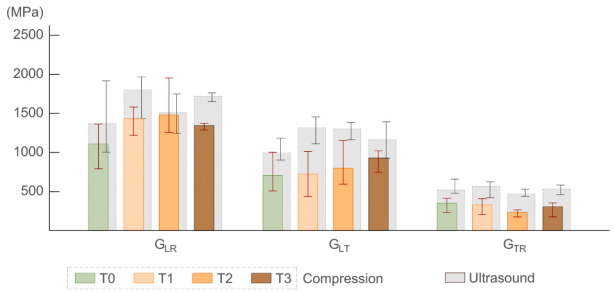

Fig. 11. Mean value and variation range for the shear moduli of heat-treated and untreated beech obtained by ultrasound and compression tests.

the shear modulus results were quite similar or even lower for heat treated beech than for the corresponding unmodified material. Higher shear values for heat treated beech than for unmodified beech under the same moisture conditions as here were also found by Wetzig et al. [36] from ultrasound tests when the treatment was performed in steam atmosphere. For the treatment performed under nitrogen atmosphere, higher shear modulus than that of the untreated material was exhibited in LR direction, but on the contrary G_{LT} and G_{TR} were found to be lower. In the case of Loidl et al. [37] using resonant beam technique, neither was a similar trend found for the three shear moduli, with slightly lower G_{LR} and G_{LT} for the three heat treatments than for untreated beech but equal or slightly higher G_{TR}.

Greater values were attained once more from ultrasound than static tests in the present work. Sometimes such differences are high. This could be due to natural variability of the wood as different specimens were used for ultrasound and mechanical tests. In any case, the results for untreated beech from both type of tests are in the same range than those reported in literature (Table 5). In the best knowledge of the authors, no shear moduli of heat treated beech from compression tests are reported in literature (just from ultrasounds mentioned before [36]), which prevents comparison within this material.

A ratio of approximately 3.2(LR):2(LT):1(TR) between the material planes of untreated beech is derived from compression tests in the present study. In the case of heat treated beech from the same tests, the ratios resulted slightly higher, that is, 4.4–6.3(LR):2.2–3.4(LT):1(TR).

The results from ultrasound tests also revealed little higher ratios for the modified material, and the three treatments show quite analogous ratios among them (2.6(LR):1.9(LT):1(TR) in untreated beech and 3.2 (LR):2.2–2.8(LT):1(TR) for the treated material). As can be seen from Table 5, similar ratios for shear moduli in untreated European beech

Table 4
Young's moduli of untreated beech from static and ultrasound tests and comparison with literature values.

	Test method	ρ (kg/m^3)	ω (%)	E_L (MPa)	E_R (MPa)	E_T (MPa)
STATIC TESTS						
This study	**Comp + DIC**	**677**	**11.4**	**13,811**	**1590**	**832**
[22]	Comp + DIC	691	12.5	13,900	1900	606
[25]	Comp + DIC	674	11.9	9690	1290	810
[26]	Comp + DIC	674	11.3	11,060	1650	750
[27]	Comp + DIC	678	–	15,020	1882	1132
[13]	Comp + gaug	629	10.8	12617–17980	1027–1537	642–1041
[26,28]	Tens + DIC	661	11.3	10,560	1510	730
[25]	Tens + DIC	674	11.9	10,460	1480	530
[29]	Flex & Tors	750	12	11,900	1700	1030
[30]	Torsion,static	–	12	–	1100	580
[48]	Compilation	740	10.5	14,000	2280	1160
ULTRASOUND TESTS						
This study	**Ultr 1 MHz**	**633**	**11.6**	**14,078**	**2953**	**1339**
[18]	Ultr 1 MHz	674	–	9160	1851	1037
[21]	Ultr 2.27 and 1 MHz	–	12.7	9560	2200	490
[23]	Ultr 100 kHz	700	10	14,650	–	–
[24]	ResoUltras	717	7–9	19,100	2700	1200

Table 5
Shear moduli of untreated beech from static and ultrasound tests and comparison with literature values.

	Test method	ρ (kg/m^3)	ω (%)	G_{LR} (MPa)	G_{LT} (MPa)	G_{TR} (MPa)
STATIC TESTS						
This study	**Comp + DIC**	**677**	**11.4**	**1108**	**706**	**349**
[13]	Comp + gaug	629	10.8	527–945	398–499	169–373
[29]	Flex & Tors	750	12	975	762	366
[30]	Torsion,static	–	12	1110	770	220
[31]	Torsion	631–708	12	977	757	–
[32]	Shear frame	697	8.6	953	688	234
[48]	Compilation	740	10.5	1640	1080	470
ULTRASOUND TESTS						
This study	**Ultr 1 MHz**	**633**	**11.6**	**1369**	**994**	**520**
[18]	Ultr 1 MHz	674	–	1396	978	356
[22]	Ultr 1 MHz	711	11.9	1280	855	486
[21]	Ultr 2.27 and 1 MHz	–	12.7	1240	930	380
[23]	Ultr 100 kHz	700	10	1430	1130	500
[24]	ResoUltras	717	7–9	1590	1100	530

were reported in literature, where approximately 3(LR):2(LT):1(TR) seems valid from various studies using ultrasound tests.

4.6. Poisson's ratios

Regarding Poisson's ratios, they are the less studied elastic constants due to the delicate instruments required to determine them. According to Bodig and Jayne [11], Poisson's ratios do not seem to be influenced by density or other anatomical material features in any clear way. On the contrary, there are other literature in which differences within and between species and also influence by factors, such as moisture content or specific gravity, are stated. However, there is a lack of information about the effects of heat tretament on Poisson's ratios for wood.

The six Poisson's ratios of beech wood as affected by the three heat treatments in comparison with the untreated material obtained from the present work are represented in Fig. 12.

The Poisson's ratios seem to be rather insensitive to heat treatments as no essential distinction between treated and untreated beech was observed. Also no great differences between treated and untreated beech were reported by Wetzig et al. [36] on the two Poisson's ratio that they studied. To the authors' knowledge, there are no other works that derive Poisson's ratios in heat-treated beech, but insensitivity to heat treatment intensities is also found in other species. For example, Yilmaz et al. [49] demostrated no significant effect of heat treatment on Poisson's ratio from oak wood despite small fluctuations in the values.

Passive lateral strain components along the tangential direction of the specimens led to the highest values of the Poisson's ratios (ν_{LT} and ν_{RT}), followed by Poisson's ratios from lateral strains along the radial direction (ν_{LR} and ν_{TR}). The smallest Poisson's ratios were those obtained from specimens where lateral passive strains were produced along the longitudinal direction (ν_{RL} and ν_{TL}).

The mean values of the Poisson's ratios obtained from static tests ranged from 0.03 (in TL plane) to 0.66 (in RT plane). The variation range in the case of ultrasound results was slightly greater, from 0.05 (in RL and TL planes) to 0.76 (in LT plane).

Namely, the mean ν_{LR} in the range of 0.39–0.45 for heat treated beech obtained from the present study is comparable to the result in Wetzig et al. [36] also for heat treated beech from compression tests (0.33). However, the mean $\nu_{LT,}$ ranging between 0.46 and 0.51, was significantly higher than the 0.08 reported by Wetzig et al. [36].

The Poisson's ratios are usually characterized by a high variability, wich is observed by the high CoV in some of the results from the present research, especially when the longitudinal direction corresponds to the passive lateral strain component (ν_{RL} and ν_{TL}), exceeding CoV's of 50% in some sets. This is a well-known problem in wood testing [11], since strains in longitudinal direction are too small for satisfactory and accurate measurments. Therefore, it is a common practise to derive these constants from relationships using the determined Young's moduli. Also in specimens tangentially oriented, it is difficult to guarantee growth rings to be completely parallel to the loading direction over the whole specimen.

The high natural variability in the Poisson's ratios for untreated European beech wood was also evidenced in other estudies [e.g. [22,26,28]], where similar high CoV's values for Poisson's ratios were reported.

Due to the high scatter, it is also not possible to make clear statements about the influence of heat treatment on the Poisson' ratios of beech wood. Higher number of specimens should be tested for better statistical significance.

Table 6 summarizes the obtained Poisson's ratios of untreated beech by static and ultrasound testing in comparison with corresponding results from literature.

In general, and considering the natural variation mentioned before, all determined Poisson's ratio measured at standard climatic conditions by static tests and DIC measurements correspond well with the respective literature values for beech listed in the table. However, this similarity is not exhibited by the sets of ultrasound results, with great differences especially within ν_{LR} and ν_{LT} ratios, which makes this

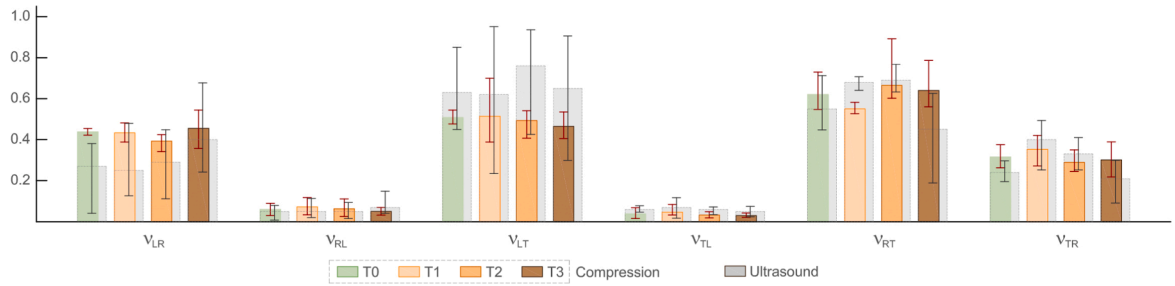

Fig. 12. Mean value and variation range for Poisson's ratios of heat-treated and untreated beech obtained by ultrasound and compression tests.

Table 6
Poisson's ratios of untreated beech from static and ultrasound tests and comparison with literature values.

	Test method	ρ (kg/m^3)	ω (%)	ν_{LR}	ν_{RL}	ν_{LT}	ν_{TL}	ν_{RT}	ν_{TR}
STATIC TESTS									
This study	**Comp + DIC**	**677**	**11.4**	**0.44**	**0.06**	**0.51**	**0.04**	**0.62**	**0.32**
[22]	Comp + DIC	691	12.5	0.27	0.07	0.24	0.09	0.64	0.27
[25]	Comp + DIC	674	11.9	0.13	0.06	0.22	0.08	0.65	0.33
[26]	Comp + DIC	674	11.3	0.55	0.15	0.51	0.09	0.75	0.32
[13]	Comp + gau	629	10.8	0.41–0.71	–	0.34–0.72	–	0.44–0.64	–
[26,28]	Tens + DIC	~661	11.3	0.43	0.04	0.58	0.04	0.61	0.31
[25]	Tens + DIC	674	11.9	0.24	0.07	0.18	0.04	0.61	0.27
[30]	Torsion	–	12	–	–	–	–	0.77	0.29
ULTRASOUND TESTS									
This study	**Ultra 1 MHz**	**633**	**11.6**	**0.27**	**0.05**	**0.63**	**0.06**	**0.55**	**0.24**
[18]	Ultra 1 MHz	674	–	1.24	0.25	0.90	0.10	0.26	0.15
[21]	Ultra 1 MHz	–	12.7	0.08	0.02	2.26	0.11	1.02	0.23

methodology less reliable. Highly accurate optical measurement techniques (as DIC) show more confidence to establish Poisson's ratios. Even so, it is worth noting the similarity between the static and dynamic Poisson's ratios from the research presented here.

Unlike the Young and shear moduli, the Poisson's ratios obtained from ultrasound tests do not exhibit a general tendency of higher values than those from ultrasound method.

Ozyhar et al. [26] revealed that the loading method had greater influence on the Poisson's ratios than the moisture content. They reported overall higher Poisson's ratios in compression than the corresponding values in tension. The differences were more pronounced for the ratios from specimens with the radial as the loading direction (ν_{RL} and ν_{RT}) and, to a lesser extend, for the specimens loaded in tangential direction (ν_{TR} and ν_{TL}). Even so, the lack of data on the tension–compression relationship of wood's Poisson's ratios prevents a deeper verification of the results, and a general statement can not be made by looking at all the data listed at the table. In fact, the mean ν_{TL} from the present work corresponds better with the results derived from tension tests by Ozyhar et al. [26].

4.7. Compliance parameters

Finally, the compliance matrix $[S_{ijkl}]$ of Eqs. (1) and (2) was derived using the data from Table 3. The measurement of the six Poisson's ratios enables a discussion of the material symmetry expressed by the corresponding non-diagonal compliance components.

Table 7 provides an overview of the determined compliance parameters for unmodified and thermally modified beech by the three treatments obtained both by static and ultrasound tests.

As can be seen by the results, there is no clear correlation between mean compliance values and treatment intensities. What is noticed is that thermo-treated beech values from compression tests are lower than those of untreated material except for the case of s_{44}, for wich the variations among batches are more significant. However, the compliance values derived from ultrasound method do not show an analogous behaviour, with some cases where the mean compliance parameter of the heat treated wood was greater than the untreated material.

For simplicity, in order to reduce the unknown coefficients for the material description, symmetry in the orthotropy compliance matrix of wood is usually assumed, so the non-diagonal parameters (s_{ij} and s_{ji}) are often taken as equal. It is relatively satisfied for various wood species. Even though, several studies have pointed out discrepancies between the corresponding values of such non-diagonal parameters [e.g. [11,19,22,25]], being sometimes almost decoupled.

Comparing the non-diagonal compliance parameters from the present work (Table 6), very low deviations are observed between the components in RT planes for T0, T2 and T3 batches obtained from compression tests, being in the range of 2–5%. However, beech treated by T1 amounted 17% of difference. In the case of the values related to the LT plane, deviations in approximately 20 to 37% are noticed. Finally, different magnitudes of deviations were found for the LR plane, being almost negligible for T3, and approximately 18%, 24% and 40% for T0, T1 and T2, respectively.

Even so, these deviation percentages are below those reported in other studies using European beech. Deviations up to 35% were derived for RT plane and even exceeded more than 100% for LR and LT planes (being almost decoupled) from static tests in [19,22,25].

Meanwhile, it is noticeable the very low deviations in the non-diagonal compliance elements obtained from ultrasound tests (Table 6) where a maximum of 13% was shown for untreated beech in LR plane. For most of the other pairs of non-diagonal elements, the difference was even less than 6%.

Therefore, the results indicate overall that the orthotropic symmetry for the three planes is largely satisfied for each of the heat treatment batches and test method, specially for the results from ultrasound tests.

Table 7
Compliance paramenters of heat treated and untreated beech determined by compression and ultrasound tests.

	T0 Ultras.	T0 Compr	T1 Ultras.	T1 Compr	T2 Ultras.	T2 Compr	T3 Ultras.	T3 Compr
$s_{11} = 1/E_L$	7.10	7.24	6.75	6.48	6.76	5.91	6.02	6.04
$s_{22} = 1/E_R$	33.86	62.89	36.94	49.24	41.72	53.59	33.99	55.22
$s_{33} = 1/E_T$	74.68	120.19	63.05	90.83	88.34	119.90	71.23	112.23
$s_{44} = 1/G_{RT}$	192.31	286.53	176.06	304.88	213.22	427.35	187.97	327.87
$s_{55} = 1/G_{LT}$	100.60	141.64	76.05	138.31	76.86	124.84	85.91	107.64
$s_{66} = 1/G_{LR}$	73.05	90.25	55.52	69.78	66.14	67.61	58.11	74.40
$s_{21} = -\nu_{LR}/E_L$	1.92	3.19	1.69	2.78	1.96	2.30	2.41	2.72
$s_{12} = -\nu_{RL}/E_R$	1.69	3.77	1.85	3.45	2.09	3.22	2.38	2.76
$s_{31} = -\nu_{LT}/E_L$	4.48	3.69	4.18	3.30	5.14	2.89	3.91	2.78
$s_{13} = -\nu_{TL}/E_T$	4.48	4.81	4.41	4.54	5.30	3.60	3.56	3.37
$s_{32} = -\nu_{RT}/E_R$	18.63	38.99	25.12	27.08	28.79	35.37	15.30	35.34
$s_{23} = -\nu_{TR}/E_T$	17.92	38.46	25.22	31.79	29.15	34.77	14.96	33.67

5. Conclusions

The elastic properties of European beech and thermally modified beech at three different treatment intensities were quantified using both compression tests, coupled with a 3D digital image correlation technique, and ultrasound method. The results confirm a general influence of the heat treatments. However, the impact of the heat treatment differs between the elastic components. Results indicate that the elastic moduli are affected by the heat treatment to a greater extend than the Poisson's ratios. However, no clear correlations among treatment intensities and elastic constants were observed.

Overall, the Young's moduli and shear moduli (except G_{TR}) exhibited and increase in mean value for heat-treated material (for the three heat treatment cases) with respect to the untreated one when static compression tests were considered. In the case of ultrasound results, all three treatments showed greater values of elastic constants except, once again, G_{TR} and additionally the two Young's moduli in the transverse direction.

No essential distinction between treated and untreated beech was observed for the Poisson's ratios, which did not follow uniform trends with heat treatments and were the paremeters of highest variability.

Good comparability of the current results with literature references can be ascertained. In particular, all determined Poisson's ratio (whose determination is usually more difficult) from compression tests corresponded well with the respective literature values for untreated beech. Therefore, the accuracy of strain measurement by DIC is satisfactory for his purpose, confirming it as a potential tool for wood characterization. However, this similarity was not exhibited by the sets of ultrasound results, which makes this methodology less reliable to establish Poisson's ratios. The mean values obtained by ultrasonic waves were in most of the elastic properties and batches clearly higher than those from static tests.

The compliance parameters of heat-treated beech values from compression tests were lower than those of untreated material except for that related to G_{TR}. Relatively low deviations were obtained between the respective non-diagonal compliance parameters, so the orthotropic symmetry for the three planes was largely satisfied for each of the heat treatment batches and test methods.

The twelve elastic constants provide a basis for modelling of thermally treated beech structures, thus giving added-value to this product in the construction industry.

CRediT authorship contribution statement

José Luis Gómez-Royuela: Conceptualization, Formal analysis, Investigation, Writing - original draft, Writing - review & editing. **Almudena Majano-Majano:** Conceptualization, Formal analysis, Investigation, Resources, Supervision, Writing - original draft, Writing - review & editing. **Antonio José Lara-Bocanegra:** Conceptualization, Investigation, Writing - original draft, Writing - review & editing. **Thomas P.S. Reynolds:** Supervision, Writing - original draft, Writing - review & editing.

Declaration of Competing Interest

The authors declare that they have no known competing financial interests or personal relationships that could have appeared to influence the work reported in this paper.

Acknowledgements

Part of the work was undertaken during a short-term scientific stay by the second and third authors at the School of Engineering (University of Edinburgh) in 2019, with the financial support of "Programa Propio de I + D + i 2019 de la Universidad Politécnica de Madrid". The authors would like to thank PEMADE Laboratory for ultrasound testing, and Dr. Raquel Gonçalves and Mr. Carlos Vázquez for their support with ultrasound analysis. The wood material was acquired within the IP-SME project HOLIWOOD (Holistic implementation of European thermal treated hard wood in the sector of construction industry and noise protection by sustainable, knowledge-based and value added products). This project was carried out with financial support from the European Community within the Sixth Framework Program (NMP2-CT-2005-IP 011799-2).

References

[1] T. Ehrhart, G. Fink, R. Steiger, A. Frangi. Strength grading of European beech lamellas for the production of GLT & CLT. In: Proceedings of International Network on Timber Engineering Research. Graz, Austria, 2016.
[2] E. Hermoso, J. Fernández-Golfín, M. Conde, M.T. Troya, R. Mateo, J. Cabrero, M. Conde, Characterization of thermally modified Pinus radiata timber (in Spanish), Maderas-Cienc Tecnol 17 (3) (2015) 493–504, https://doi.org/10.4067/S0718-221X2015005000044.
[3] C.A.S. Hill, Wood modification - chemical, thermal and other processes. Wiley Series in Renewable Resources, Wiley & Sons, Chichester, UK, 2006.
[4] B.M. Esteves, H.M. Pereira, Wood modification by heat treatment: a review, BioResources 4 (1) (2009) 370–404.
[5] E. Dizman Tomak, D. Ustaomer, S. Yildiz, E. Pesman, Changes in surface and mechanical properties of heat treated wood during natural weathering, Measurement 53 (2014) 30–39, https://doi.org/10.1016/j.measurement.2014.03.018.
[6] A. Majano-Majano, M. Hughes, J.L. Fernandez-Cabo, The fracture thoughness and properties of thermally modified beech and ash at different moisture contents, Wood Sci. Technol. 46 (2012) 5–21, https://doi.org/10.1007/s00226-010-0389-4.
[7] R. Widmann, J.L. Fernandez-Cabo, R. Steiger, Mechanical properties of thermally modified beech timber for structural purposesMechanische Eigenschaften von thermisch modifiziertem Buchenholz für tragende Bauteile, Eur. J. Wood Prod. 70 (6) (2012) 775–784, https://doi.org/10.1007/s00107-012-0615-x.
[8] R. Schöftner Holiwood—international research and development for innovative products made out of thermal modified timber. In: 3rd European Conference on Wood Modification, Cardiff, UK, 2007.
[9] N.T. Mascia, Concerning the elastic orthotropic model applied to wood elastic properties, Maderas-Cienc Tecnol 5 (1) (2003) 3–19, https://doi.org/10.4067/S0718-221X2003000100001.
[10] N.T. Mascia, F.A.R. Lahr, Remarks on orthotropic elastic models applied to wood, Mater. Res. 9 (3) (2006) 301–310, https://doi.org/10.1590/S1516-14392006000300010.
[11] J. Bodig, B.A. Jayne, Mechanics of Wood and Wood Composites, Krieger Publishing Company, Malabar, 1993.
[12] A. Sliker, Y. Yu, T. Weigel, W. Zangh, Orthotropic elastic constants for eastern hardwood species, Wood Fiber Sci. 26 (1) (1994) 107–121.
[13] W. Hu, H. Wan, H. Guan, Size effect on the elastic mechanical properties of beech and its application in finite element analysis of wood structures, Forests 10 (2019) 783, https://doi.org/10.3390/f10090783.
[14] J. Xavier, A.M.P. de Jesus, J.J.L. Morais, J.M.T. Pinto, Stereovision measurements on evaluating the modulus of elasticity of wood by compression tests parallel to the grain, Constr. Build. Mater. 26 (1) (2012) 207–215, https://doi.org/10.1016/j.conbuildmat.2011.06.012.
[15] M. Brabec, J. Tippner, V. Sebera, J. Milch, P. Rademacher, Standard and non-standard deformation behaviour of European beech and Norway spruce during compression, Holzforschung 69 (9) (2015) 1107–1116, https://doi.org/10.1515/hf-2014-0231.
[16] A. Majano-Majano, J.L. Fernandez-Cabo, S. Hoheisel, M. Klein, A test method for characterizing clear wood using a single specimen, Exp. Mech. 52 (8) (2012) 1079–1096, https://doi.org/10.1007/s11340-011-9560-6.
[17] V. Bucur, Acoustics of Wood, Springer-Verlag, New York, 2006.
[18] V. Bucur, R.R. Archer, Elastic constants for wood by an ultrasonic method, Wood Sci. Technol. 18 (4) (1984) 255–265.
[19] D. Keunecke, W. Sonderegger, K. Pereteanu, T. Lüthi, P. Niemz, Determination of Young's and shear moduli of common yew and Norway spruce by means of ultrasonic waves, Wood Sci. Technol. 41 (4) (2007) 309–327, https://doi.org/10.1007/s00226-006-0107-4.
[20] R. Gonçalves, A.J. Trinca, D.G.P. Cerri, Comparison of elastic constants of wood determined by ultrasonic wave propagation and static compression testing, Wood Fiber Sci. 41 (1) (2011) 64–75.
[21] T. Ozyhar, S. Hering, S.J. Sanabria, P. Niemz, Determining moisture-dependent elastic characteristics of beech wood by means of ultrasonic waves, Wood Sci. Technol. 47 (2) (2013) 329–341.
[22] S. Hering, D. Keunecke, P. Niemz, Moisture-dependent orthotropic elasticity of beech wood, Wood Sci. Technol. 46 (5) (2012) 927–938, https://doi.org/10.1007/s00226-011-0449-4.
[23] T. Bader, J. Eberhardsteiner, K. De Borst, Shear stiffness and its relation to the microstructure of 10 European and tropical hardwood species, Wood Mater. Sci. Eng. 12 (2) (2017) 82–91, https://doi.org/10.1080/17480272.2015.1030773.
[24] R. Longo, T. Delaunay, D. Laux, M. El Mouridi, O. Arnould, E. Le Clézio, Wood elastic characterization from a single sample by resonant ultrasound spectroscopy, Ultrasonics 52 (8) (2012) 971–974.

[25] T. Ozyhar, S. Hering, P. Niemz, Viscoelastic characterization of wood: time dependence of the orthotropic compliance in tension and compression, J. Rheol. 57 (2) (2013) 699–717, https://doi.org/10.1122/1.4790170.
[26] T. Ozyhar, S. Hering, P. Niemz, Moisture-dependent orthotropic tension-compression asymmetry of wood, Holzforschung 67 (4) (2013) 395–404, https://doi.org/10.1515/hf-2012-0089.
[27] J. Milch, J. Tippner, V. Sebera, M. Brabec, Determination of the elasto-plastic material characteristics of Norway spruce and European beech wood by experimental and numerical analyses, Holzforschung 70 (11) (2016) 1081–1092, https://doi.org/10.1515/hf-2015-0267.
[28] T. Ozyhar, S. Hering, P. Niemz, Moisture-dependent elastic and strength anisotropy of European beech wood in tension, J. Mater. Sci. 47 (16) (2012) 6141–6150, https://doi.org/10.1007/s10853-012-6534-8.
[29] R.F.S. Hearmon, W.W. Barkas, The effect of grain direction on the Young's moduli and rigidity moduli of beech and Sitka spruce, Proc. Phys. Soc. 53 (6) (1941) 674–680.
[30] A.J. Neumann. Ermittlung und Bewertung der elastischen Materialkennwerte von Vollholz in Abhängigkeit der Feuchte und der Anisotropie (in English: Identification and evaluation of the elastic properties of solid wood depending on th moisture and anisotropy). Master Thesis, Technische Universität Dresden, 1998.
[31] M. Brabec, R. Lagaña, J. Milch, J. Tippner, V. Sebera, Utilization of digital image correlation in determining of both longitudinal shear moduli of wood at single torsion test, Wood Sci. Technol. 51 (1) (2017) 29–45.
[32] R. Krüger, B. Buchelt, A. Wagenführ, New method for determination of shear properties of wood, Wood Sci. Technol. 52 (6) (2018) 1555–1568.
[33] V. Sebera, M. Redón-Santafé, M. Brabec, D. Děcký, P. Čermák, J. Tippner, J. Milch, Thermally modified (TM) beech wood: compression properties, fracture toughness and cohesive law in mode II obtained from the three-point end-notched flexure (3ENF) test, Holzforschung 73 (7) (2019) 663–672, https://doi.org/10.1515/hf-2018-0188.
[34] G. Fajdiga, B. Zafošnik, B. Gospodarič, A. Straže, Compression test of thermally-treated beech wood: experimental and numerical analysis, BioResources 11 (1) (2016) 223–234.
[35] A. Straže, G. Fajdiga, S. Pervan, Z. Gorišek, Hygro-mechanical behavior of thermally treated beech subjected to compression loads, Constr. Build. Mater. 113 (2016) 28–33, https://doi.org/10.1016/j.conbuildmat.2016.03.038.
[36] M. Wetzig, C. Heldstab, T. Tauscher, P. Niemz, Ermittlung ausgewählter mechanischer Kennwerte thermisch modifizierter Buche (in English: determination of select mechanical properties of heat-treated beech wood), Bauphysik 33 (6) (2011) 366–373, https://doi.org/10.1002/bapi.v33.610.1002/bapi.201110794.
[37] D. Loidl, S. Puchegger, N. Gierlinger, W. Beikircher, S. Stanzl-Tschegg. Elastic properties of thermally treated wood at elevated temperatures. In: Proceedings of Third International Symposium on Wood Machining. Lausanne, Switzerland, 2007.
[38] W. Voigt, Lehrbuch der Kristallphysik, B.G. Teubner, Leipzig, 1928.
[39] F.F.P. Kollmann, W.A. Côté Jr., Principles of Wood Science and Technology, Solid wood. Springer, München, Part I, 1968.
[40] A.J. Trinca. Metodologia para determinaçao das constantes elásticas da madeira por ultrassom. PhD Thesis. Universidade Estadual de Campinas, Facultade de Engenharia Agrícola, 2011.
[41] E.V. Bachtiar. Material characterization of wood, adhesive and coating of cultural heritage under various climatic conditions. Doctoral Thesis, ETH Zürich, 2017.
[42] A.J. Trinca, R. Gonçalves, Effect of the transversal section dimensions and transducer frequency on ultrasound dimensions and transducer frequency on ultrasound wave propagation velocity in wood, Revista Árvore 33 (1) (2009) 177–184.
[43] GOM mbH. ARAMIS commercial software. Aramis 6.0.2; 2000.
[44] ISO 13061-17:2017. Physical and Mechanical Properties of Wood – Test Methods for Small Clear Wood Specimens - Part 17: Determination of Ultimate Stress in Compression Parallel to Grain. International Organization for Standardization: Geneva, Switzerland, 2017.
[45] ISO 13061-5:2020. Physical and Mechanical Properties of Wood - Test Methods for Small Clear Wood Specimens - Part 5: Determination of Strength in Compression Perpendicular to Grain; International Organization for Standardization: Geneva, Switzerland, 2020.
[46] T. Yilmaz Aydin, M. Aydin, Comparison of temperature dependent Young's modulus of oriental beech (Fagus orientalis L.) that determined by ultrasonic wave propagation and compression test, Turk. J. For. 19 (2) (2018) 185–191, https://doi.org/10.18182/tjf.397907.
[47] V. Borůvka, A. Zeidler, T. Holeček, R. Dudík, Elastic and strength properties of heat-treated beech and birch wood, Forests 9 (4) (2018) 197, https://doi.org/10.3390/f9040197.
[48] D. Guitard, F. El Amri, Modèles prévisionnels de comportement élastique tridimensionnel pour les bois feuillus et les bois résineux, Ann. Sci. For. 44 (3) (1987) 335–358.
[49] T. Yilmaz Aydin, E. Güntekin, M. Aydin. Effects of heat treatment on some orthotropic mechanic properties of oak (Quercus petraea) wood. In: 1st International Mediterranean Science and Engineering Congress, Adana, Turkey, 2016.

Propiedades de fractura

Este trabajo se presenta en dos publicaciones: Publicaciones II y III.

Publicación II

Evaluation of R-curves and cohesive law in mode I of European beech

José Luis Gómez-Royuela, Almudena Majano-Majano, Antonio José Lara-Bocanegra, José Xavier, M. F. S. F. de Moura.

Theoretical and Applied Fracture Mechanics, 118: 103220, 2022
DOI: https://doi.org/10.1016/j.tafmec.2021.103220
Q1 (JCR). Impact factor: 5,3

Theoretical and Applied Fracture Mechanics 118 (2022) 103220

Contents lists available at ScienceDirect

Theoretical and Applied Fracture Mechanics

journal homepage: www.elsevier.com/locate/tafmec

Evaluation of *R*-curves and cohesive law in mode I of European beech

J.L. Gómez-Royuela [a,*], A. Majano-Majano [a], A.J. Lara-Bocanegra [a], J. Xavier [b], M.F.S.F. de Moura [c]

[a] Department of Building Structures and Physics, ETS of Architecture, Universidad Politécnica de Madrid (UPM), Avda. Juan de Herrera, 4., 28040 Madrid, Spain
[b] UNIDEMI, Department of Mechanical and Industrial Engineering, NOVA School of Science and Technology, NOVA University Lisbon, 2829-516 Caparica, Portugal
[c] Faculdade de Engenharia da Universidade do Porto, Departamento de Engenharia Mecânica e Gestão Industrial, Rua Roberto Frias, 4200-465 Porto, Portugal

ARTICLE INFO

Keywords:
Beech
Mode I
Cohesive law
Digital image correlation
FEM
Double cantilever beam

ABSTRACT

This work addresses the determination of the cohesive laws in Mode I and tangential–longitudinal (TL) crack propagation system of *Fagus Sylvatica* L. This species is one of the ever-growing and most widely used hardwood species in Europe for engineered timber products. Double Cantilever Beam (DCB) tests are performed. The strain energy release rate (G_I) is derived from the R-curves by applying the Compliance-Based Beam Method (CBBM), which has the advantage of not requiring the measurement of the crack length during propagation, but only the global load–displacement curves. The cohesive law of the material is determined from the relationship between G_I, and the crack tip opening displacement (CTOD) monitored for each specimen using Digital Image Correlation (DIC). Numerical finite element models are developed by implementing the average cohesive law through Cohesive Zone Models (CZM). An average G_I value of 0.46 kJ/m^2 is obtained for this species. The numerical load–displacement curves are consistent with the experimental results, which demonstrates the suitability of the method for the identification of the cohesive laws in beech. The fracture properties obtained are essential in the development of advanced and reliable numerical models in timber engineering design using this species.

1. Introduction

Recent studies show that the building sector contributes up to 30% of global annual greenhouse gas emissions and consumes up to 40% of all energy [1]. For this reason, the wood industry and therefore the construction of buildings with timber structure is undergoing strong growth. Part of this growth is driven by the need to provide environmentally friendly answers and, in this sense, wood is playing a very important role. The use of wood-based materials in building construction can reduce energy demand and CO_2 compared to other materials, such as steel, concrete, aluminum or brick [2–4]. Furthermore, wood is the only main building material that is a renewable resource as long as it is managed sustainably [5]. This interest in wood highlights the need for research to better understand its mechanical behavior. From a technical point of view, it is necessary to advance and deepen in the characterization of the material properties in order to address the design of timber structures in a safe way and develop advanced and reliable numerical models, which involves the study of the fracture behavior.

In the last decade, the use of hardwood species as a raw material for timber structures is gaining momentum over softwoods due to their advantages in term of mechanical performance and natural durability. Currently, beech wood (*Fagus sylvatica* L.) is one of the most widely used hardwoods for timber structures in Europe [6]. Therefore, predicting its fracture behavior becomes necessary, especially in design situations where brittle failures may occur, such as timber connections loaded perpendicular to the grain. For this particular case, Eurocode 5 [7] proposes a splitting resistance verification based on the fracture mechanics approach. The code expression derives from considering a critical fracture energy parameter, which was empirically calibrated based on several experimental studies on softwoods available in literature [8,9]. However, the design standard limits this verification to softwoods, so research is needed to extend its application to hardwoods, which requires determining their fracture properties.

It is well known that wood presents a high variability of elastic properties due to its natural origin. Furthermore, although it is an anisotropic material, it is widely accepted to be considered as orthotropic characterized according to three main directions: longitudinal

* Corresponding author.
E-mail addresses: joseluis.gomez.royuela@upm.es (J.L. Gómez-Royuela), almudena.majano@upm.es (A. Majano-Majano), antoniojose.lara@upm.es (A.J. Lara-Bocanegra), jmc.xavier@fct.unl.pt (J. Xavier), mfmoura@fe.up.pt (M.F.S.F.d. Moura).

https://doi.org/10.1016/j.tafmec.2021.103220
Received 21 October 2021; Received in revised form 17 December 2021; Accepted 19 December 2021
Available online 17 January 2022

(L), radial (R) and tangential (T) [Fig. 1]. This leads to consider six fracture propagation systems: RL, TL, LR, LT, RT and TR (the first letter indicates the direction normal to the crack plane and the second letter specifies the direction of crack propagation). In particular, the most relevant propagation systems from a structural point of view are RL and TL, so numerous research works focused on them in different wood species can be found in literature [10–17]. Each propagation mechanism can present a state of stresses in three different modes: mode I (in-plane tension), mode II (in-plane shear) and mode III (out-of-plane shear). Due to the low strength perpendicular to the grain of wood, the failure mode I requires special attention. In this sense, several types of experimental tests are available to characterize the mode I fracture parameters, such as the Compact Tension (CT) [18,19] the Single Edge Notched Beam (SENB) [15,20] or the Wedge Splitting Test (WST) [21,22]. One of the most suitable tests is the Double Cantilever Beam (DCB) as the specimen geometry is simple, it is able to adequately produce crack propagation, and allows the fracture energy to be determined mathematically according to the beam theory [23,24].

The complexity of wood makes that the fracture of the material is characterized by the occurrence of hardening phenomena such as multiple micro-cracks and fiber-bridging [24]. These non-linear phenomena take place in the region known as the Fracture Process Zone (FPZ) just ahead of the crack tip. Consequently, in order to adequately describe the fracture behavior of wood, it is necessary to make use of non-linear fracture theories, which were initially developed for elasto-plastic materials such as mild steel [25]. Currently, one of the simplest ways to address fracture in wood is by applying traction-crack opening laws to predefined crack propagation paths. Although wood is a strongly orthotropic material, the crack propagation pattern is usually known in advance. The first applications of this methodology correspond to the Fictitious Crack Models [26,27], today known as Cohesive Zone Models (CZM), being for the first time applied to wood in [28]. The traction-crack opening laws are considered material properties and relate the tractions with the total displacement at the crack tip. They consist of an initial branch corresponding to the elastic behavior of the material until the maximum traction is reached, followed by a softening branch describing the damage development [29]. These cohesive laws can be obtained experimentally by direct methods [11] or by inverse methods using numerical simulations [30].

The main objective of the present work is to experimentally estimate the resistance curves (*R*-curves) and the representative cohesive laws in mode I and TL crack propagation system of European beech wood (*Fagus sylvatica* L.) using DCB specimens. The *R*-curves are determined applying the Compliance-Based Beam Method (CBBM). This data reduction scheme is based on the beam theory and an equivalent crack length (a_{eq}) concept, which has the advantage of not requiring the measurement of crack growth during the test, which would be a difficult and complex task in wood. Instead, only the load–displacement curve is needed. The cohesive laws are derived directly from the relationship between the critical strain energy release rate (G_{Ic}) obtained from the R-curves, and the crack tip opening displacements (w) monitored using digital image correlation (DIC) technique. Numerical simulations by finite element models were performed to validate the experimental procedure. CZM were applied to predefined paths in the specimen geometry in order to implement the fracture mechanisms and validate the results.

2. Materials and methods

2.1. Raw material

Clear wood specimens made of European beech (*Fagus sylvatica* L.) were manufactured. All specimens were randomly cut from boards from a single log and machined in such manner that they are oriented according to the orthotropic directions (Fig. 2). Before testing, the specimens were stored at 20 °C and 65% relative humidity until equilibrium moisture content was reached. A mean density of 704 kg/m^3 and 10.5% average moisture content were measured. Constant values for the tangential modulus of elasticity E_T=832 MPa (St. Dev.=115 MPa) and for the shear modulus G_{LT}=706 MPa (St. Dev.=139 MPa) were taken from [31].

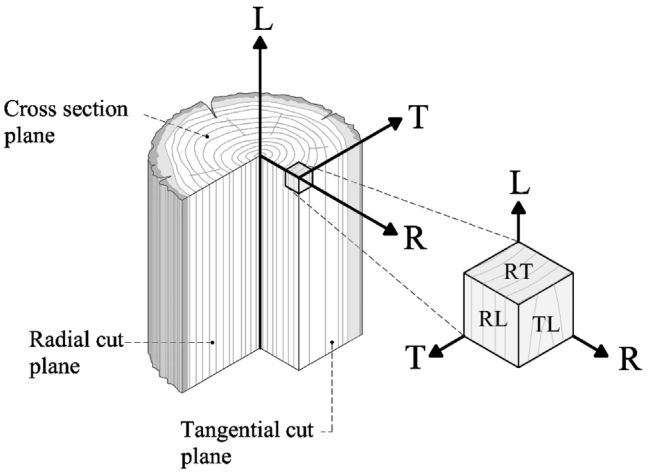

Fig. 1. Main orthotropic directions and planes in wood.

2.2. DCB test coupled with digital image correlation

In this work, seventeen DCB specimens oriented according to the TL crack propagation system as schematically represented in Fig. 2 were prepared for studying the fracture behavior in mode I of European beech. The specimens consist of small rectangular beams with nominal dimensions $L \times 2h \times B$ (250 mm × 20mm × 20mm). A notch of 1 mm thickness was machined at mid-height using a band saw. Prior to testing, this notch of initial length a_0 (100 mm) was lengthened by 1 mm using a very sharp blade to guarantee a sharped pre-crack surface before crack propagation. The pre-crack depth was controlled using a universal testing machine under displacement control of 10 mm/min. The pre-crack length was measured with a precision magnifying glass as shown in Fig. 3. A symmetrical pair of holes of 3 mm diameter were drilled at mid-height of the arm and 10 mm distance from the specimen test end (e in Fig. 2). Two steel pins of the same diameter were introduced into the holes to transfer the mode I load to the specimen. The resultant applied load was measured by a load cell of 5 kN maximum capacity. The DCB specimens were loaded by displacement control applying a constant load rate of 2 mm/min.

The DIC system ARAMIS® 3D [32] was used to record the crack tip opening displacements (Fig. 4). The device comprises two 5 megapixels resolution cameras coupled with 35 mm lens and two white light spotlights. They were calibrated using the CP20 90 × 72 calibration panel according to the target region of interest. To ensure correct focusing of the specimen surface, a field of view of 80 mm × 65mm and a distance of 400 mm between the cameras and the specimen were established. An stereo-vision angle of 25° between cameras was set. The base distance between cameras was locked at 138 mm. The shutter time and the spotlights were setup to enhance contrast and adequately lighting the specimen, avoiding insufficient or excessive light exposure. ARAMIS®3D was coupled to the universal testing machine to record synchronized data with a frequency of 1 Hz. Speckle pattern was applied on the specimen surface of interest to ensure the accuracy of the measurements using the DIC technique. This textured pattern was created in two phases. Firstly, a thin homogeneous layer of matte white paint was applied with a spray, and then a black dots pattern was projected using an airbrush. The created pattern guaranteed suitable

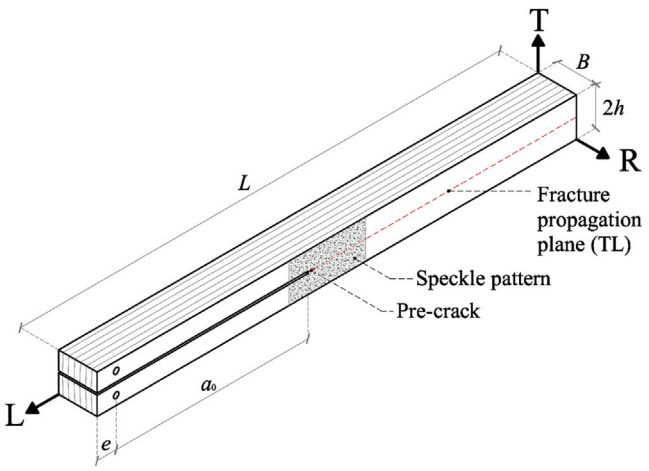

Fig. 2. Geometry of the DCB specimen.

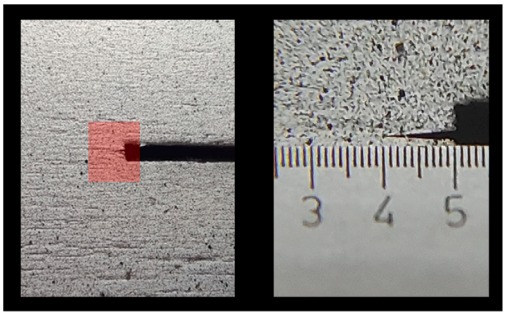

Fig. 3. Pre-crack measurement by a precision magnifying glass.

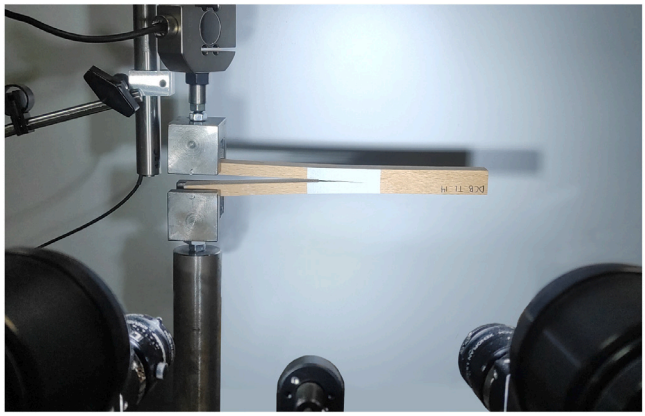

Fig. 4. DCB test set-up coupled with DIC.

contrast and granulometry of the surface according to the magnification scale of observation. Subset size of 15 × 15 pixel^2 and a subset step of 13 × 13 pixel^2 were selected for enhancing spatial resolution in a compromise with accuracy, since the DIC setting parameters can have a significant influence in the kinematics measurements [33,34].

2.3. R -curves: Compliance based beam method

The crack growth resistance curves (R-curves) describe the evolution of the strain energy release rate G_I as a function of the crack length a. A fracture process zone (FPZ) arises in the region close to the crack tip, where various toughening mechanisms take place, such as multiple micro-cracks, cracks-branching and fiber-bridging. These non-linear phenomena influence the fracture behavior of wood and therefore cannot be neglected. The R-curve is a useful tool to quantify the influence of the FPZ and obtain the critical fracture energy G_{Ic}, since this parameter is given by the plateau value of these curves.

The strain energy release rate can be obtained according to the Irwin–Kies equation,

$$G = \frac{P^2}{2B}\frac{\mathrm{d}C}{\mathrm{d}a}, \tag{1}$$

where P, B, C and a are the test load, the specimen width, the specimen compliance ($C = \delta/P$) and the crack length, respectively. It should be noted that the toughening mechanisms developing at the FPZ in wood make difficult an accurate measurement of a during testing. To avoid this problem, the Compliance-Based Beam Method (CBBM) [24] was applied in the determination of $\mathrm{d}C/\mathrm{d}a$. This methodology is based on the Timoshenko beam theory and an equivalent crack length (a_{eq}) concept. Accordingly, for a DCB test, the specimen compliance can be written as [24],

$$C = \frac{8a^3}{E_L B h^2} + \frac{12a}{5BhG_{LT}}, \tag{2}$$

where E_L and G_{LT} are the longitudinal and the shear modulus of elasticity in the LT plane, respectively. It should be noted that Eq. (2) does not take into account the stress concentrations and assumes that the rotation at the crack tip is zero, but actually this is not the case. To account for these effects, a correction to the initial crack length (Δ) is used, so that $a = (a_0 + \Delta)$, being Δ the William's correction factor [35],

$$\Delta = h\sqrt{\frac{E_f}{11G_{LT}}\left[3 - 2\left(\frac{\Gamma}{1+\Gamma}\right)^2\right]} \quad \text{where} \quad \Gamma = 1.18\frac{\sqrt{E_f E_T}}{G_{LT}}. \tag{3}$$

As mentioned before, another typical problem in wood is the variability of the elastic constants. To overcome this issue, a corrected bending modulus E_f is used for each specimen instead of E_L. The E_f value can be obtained from Eq. (2) considering the initial compliance $C = C_0$ estimated by linear regression of the $P - \delta$ curve using least squares method,

$$E_f = \left[C_0 - \frac{12\,(a_0+\Delta)}{5BhG_{LT}}\right]^{-1}\frac{8\,(a_0+\Delta)^3}{bh^3}. \tag{4}$$

Successive iterations between Eqs. (3) and (4) are performed until a convergent value of E_f is reached. It should be noted that no significant errors are made when neglecting the influence of the variability of the other elastic constants (E_T and G_{LT}) on the final value of G_I, so the average values of these constants can be used as input parameters [24]. During propagation, the current specimen compliance ($C = \delta/P$) is registered and used to obtain the equivalent crack length during crack propagation. With this aim, Eq. (2) is used to get a_{eq} as a function of C. The resultant cubic equation is solved with Matlab® software (see more details in [24]). This parameter accounts for the FPZ effects, i.e., $a_{eq} = a + \Delta + \Delta a_{FPZ}$, since the current specimen compliance reflects the influence of them. Finally, combining Eqs. (1) and (2), the energy release rate is reached according to the following expression,

$$G_I = \frac{6P^2}{2B}\left[\frac{2a_{eq}^2}{h^2 E_f} + \frac{1}{5G_{LT}}\right]. \tag{5}$$

Therefore, G_I can be determined only from the load vs. displacement data ($P - \delta$) without the need for measurements of a during the DCB test [36], being a reasonable alternative applicable to wood [11].

2.4. Cohesive law: Direct method

The cohesive laws for pure mode I loading describe the evolution of tractions as a function of the crack tip opening ($\sigma = f(w)$) and can be determined according to the following expression [37],

$$G_I = \int_0^{\bar{w}} \sigma\,(w)\,\mathrm{d}w. \tag{6}$$

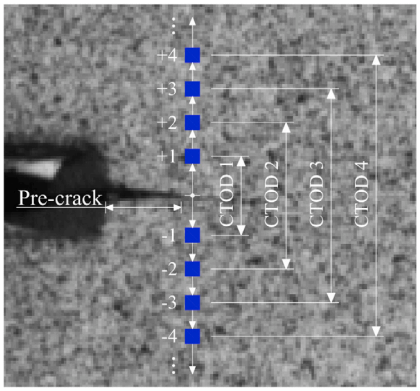

Fig. 5. Scheme of subsets pair location (blue squares) used for the determination of CTOD measurements.

Differentiating Eq. (6), the tractions can be directly defined as,

$$\sigma(w) = \frac{dG_I}{dw}. \tag{7}$$

To apply this methodology, it is necessary to determine the evolution of strain energy release rate in mode I (G_I) as a function of the crack tip opening displacements (CTOD). In this work, the evolution of G_I was found from Eq. (5) and CTOD was directly monitored using the ARAMIS 3D DIC system. The CTOD (w) was obtained by post-processing the recorded displacements. To this end, the pre-crack tip was identified at the initial stage image and pairs of facet pairs symmetrical to the fracture plane were carefully selected (Fig. 5). According to this each top subset (+1, +2, ...) was paired with its lower symmetrical (−1, −2, ...). Determination of the CTOD was always started using the subsets closest to the crack tip (+1 and −1) and then the next subsets were automatically selected sequentially until a subsets of facets is read in each of the test images successfully. It should be noted that the first subset of facets are typically rejected since they often contain erroneous measurements. These errors can be observed as discontinuities in $w-\delta$ curve. Moreover, each subset was verified to be on an opposite side of the crack during propagation since the crack growth could place them on the same side. Finally, w was determined for each loading step by evaluating the relative displacement between both subsets [38,39],

$$w = \left\| w^+ - w^- \right\|, \tag{8}$$

where w^+ and w^- are the displacement components perpendicular to the crack surface (Figure 6) associated with the subsets described above and $\|\cdot\|$ represents the Euclidean norm.

There are eventually several ways to carry out the numerical differentiation given in Eq. (7), with advantages and drawbacks. The approximation of a continuous function based on a least-square regression strategy has been successfully applied in other relevant research available in literature (e.g. [11,13,40,41]) and is adopted in this work. To obtain σ, a logistic function was fitted to $G_I - w$ curve by least squares through successive approximations according to the next expression,

$$G_I = \frac{A_1 - A_2}{1 + (w/w_0)^p} + A_2, \tag{9}$$

where A_1, A_2, w_0 and p are fitting constants by the regression analysis. This function does not have a particular physical meaning, however it is used as a tool to smooth the noise before deriving Eq. (7). In this way, σ can be determined as follows,

$$\sigma = -\frac{p(A_1 - A_2)(w/w_0)^{p-1}}{w_0\left(1 + (w/w_0)^p\right)^2}. \tag{10}$$

The A_2 parameter in Eqs (9) and (10) should provide an estimation of the critical strain energy release rate according to Eq. (11),

$$A_2 = \lim_{w\to\infty} G_I = G_{Ic}. \tag{11}$$

In alternative to the employment of a continuous function in a global fitting approach, a local least-square fitting algorithm can be used considering, for instance, a smoothing spline [42,43].

2.5. A three-linear cohesive law model

In order to validate the experimental procedure, 2D finite element analyses were performed using ABAQUS software. A plane stress analysis together with quadratic isoparametric 8-node (CPS8R) solid element were used to model the DCB test. The damage zone was implemented as a user subroutine of the ABAQUS software and using 6 nodes elements located at half-height of the specimen according to the scheme in Fig. 7. A total displacement (δ) of 16 mm was applied, which was introduced in increments no greater than 0.02 mm in order to obtain numerically stable crack growth and accurate results.

A three-linear cohesive law model with a bilinear softening relationship (Fig. 8) was implemented to reproduce the crack growth in Mode I according to the experimental tests. Recent research shows good agreements on the application of a trilinear cohesive law to simulate crack growth in wood [11,20,30].

Two different parts can be distinguished in this fracture behavior model. Firstly, an initial branch where the material behaves elastically until the maximum traction σ_u is attained for a corresponding crack opening in mode I (w_0). It is defined by Eq. (12),

$$\sigma = kw, \tag{12}$$

where k is the initial stiffness of the cohesive elements and is known as the penalty parameter. It normally takes a high value (10^6 N/mm^3) to avoid undesirable interpenetrations and difficulties to achieve the model convergence [44]. Although this penalty stiffness value reveals to be higher than the ones estimated in the cohesive laws obtained experimentally, it should be noted that the goal in this work is to properly address the softening region taking part after the local strength is achieved. In fact, the rigorous simulation of damage initiation and its propagation are the main objectives to achieve. In this context, the second part of the trilinear cohesive law (Fig. 8) represents the development of the FPZ and damage initiation (microcracking in the first descending branch and fiber-bridging in the last one) and so the material behaves in a non-linear way after the local strength (σ_u) is attained. This part is defined by three parameters: the ultimate traction (σ_u), the traction at which fiber-bridging appears (σ_1) and the corresponding crack opening (w_1). The ultimate crack growing is defined from the fracture energy G_{Ic}. The traction–separation relationships at this part of the law are established according to Eq. (13),

$$\sigma = (1-d)kw, \tag{13}$$

where d is the damage parameter, which is updated at each loading increment during the iterative process and is obtained from the cohesive law as a function of w. This parameter assumes the value of Eqs. (14) and (15), depending on the branch to which it belongs. In this sense, if $w_0 < w < w_1$ then,

$$d = 1 - \frac{w_0}{w\sigma_u}\left[\frac{\sigma_1 - \sigma_u}{w_1 - w_0}(w - w_0) + \sigma_u\right], \tag{14}$$

and when $w_1 < w < w_u$ then,

$$d = 1 - \frac{w_0}{w\sigma_u}\left[\frac{\sigma_1 (w - w_u)}{(w_u - w_1)}\right]. \tag{15}$$

It should be noted that knowing G_{Ic}, the ultimate crack tip separation can be obtained as follows,

$$w_u = \frac{2G_{Ic} - \sigma_u w_1 + \sigma_1 w_0}{\sigma_1}. \tag{16}$$

The values of the parameters defining the cohesive law are shown in Table 1, which correspond to the average values obtained in Section 3. Furthermore, in order to explain the scatter of wood properties and

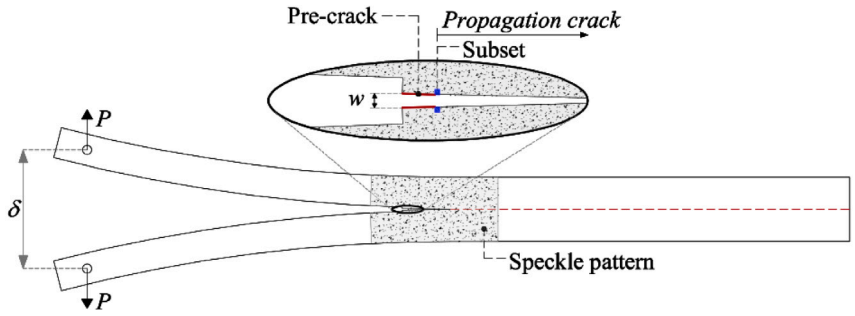

Fig. 6. Scheme of data measurement at the crack tip area of the specimen using DIC.

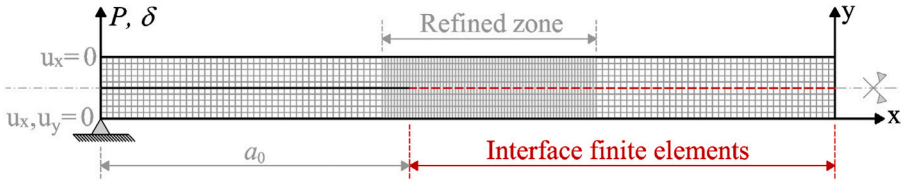

Fig. 7. Scheme of the numerical model and finite mesh.

Table 1
Numerical parameters of trilinear cohesive law. Maximum traction strength (σ_u), traction at which fiber-bridging appears (σ_1), displacement at which fiber-bridging appears (w_1) and critical fracture energy (G_{Ic}).

	σ_u (N/mm^2)	σ_1 (N/mm^2)	w_1 (mm)	G_{Ic} (kJ/m^2)	G_μ/G_{Ic} micro-cracking	G_b/G_{Ic} fiber-bridging
Average	8.29	1.00	0.080	0.46	70.28%	29.72%
upper limit	8.29	1.20	0.097	0.56	70.32%	29.68%
lower limit	8.29	0.80	0.063	0.36	70.23%	29.77%

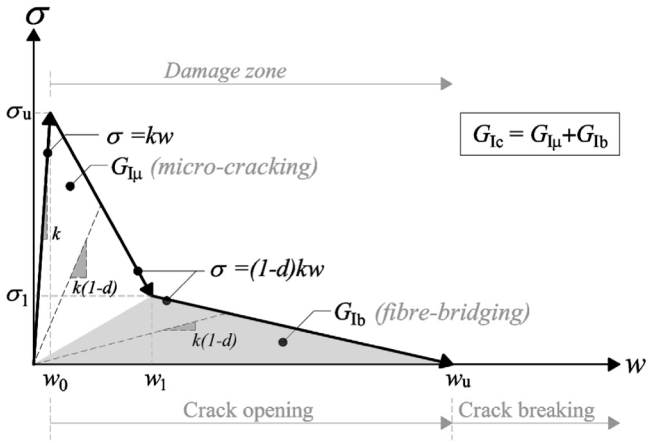

Fig. 8. Trilinear cohesive law.

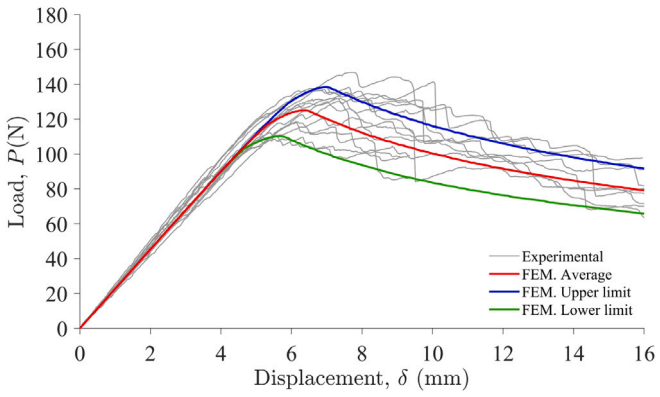

Fig. 9. Experimental and numerical $P-\delta$ curves from DCB test on beech.

knowing that the damage propagation is governed by the fracture energy, two additional cohesive laws have been implemented in FEM, representing the upper and lower limits of the fracture energy, whose values have been obtained by applying the St. Dev. to the mean value of G_{Ic}. It should be noted that these extreme cohesive laws were defined considering the same σ_u and keeping constant the proportionality between the micro-cracking and fiber-bridging fracture energy components obtained in the average cohesive law. This assumption relies on the fact that crack growth is essentially governed by fracture energy, not being much affected by σ_u.

The mean values of elastic constants of European beech used as input data in the numerical models were taken from [31] and are summarized in Table 2.

3. Results and discussion

3.1. R-Curves

Fig. 9 shows the $P-\delta$ curves obtained from the experimental DCB tests (in gray) and from the numerical analysis using the elastic constants specified in Table 2 and the fracture properties compiled in Table 1. The numerical curve derived using the average values of both elastic and fracture properties is shown in red, together with the numerical upper and lower limits by applying the standard deviation (St. Dev.) to the mean values (blue and green lines, respectively).

The experimental curves show consistent results taking into account the typical variability of wood. The numerical curve derived using the mean material properties is shown as representative of the experimental results. Furthermore, the upper and lower limit curves could explain

Table 2
Average elastic constants of European beech used as input data in the numerical models [31].

	E_L (MPa)	E_R (MPa)	E_T (MPa)	υ_{LR} (-)	υ_{LT} (-)	υ_{TR} (-)	G_{LR} (MPa)	G_{LT} (MPa)	G_{RT} (MPa)
Average	13811	1590	832	0.51	0.44	0.32	1108	706	349
St. Dev.	(1323)	(541)	(115)	(0.030)	(0.015)	(0.041)	(202)	(139)	(53)

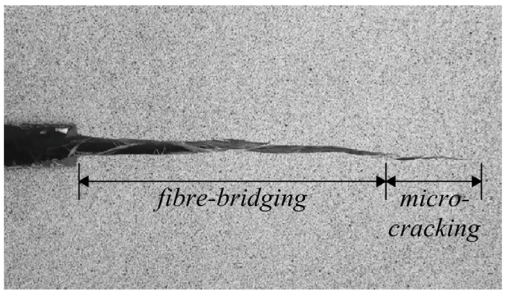

Fig. 10. Toughening mechanisms during crack propagation of the "*TL 06*" DCB specimen.

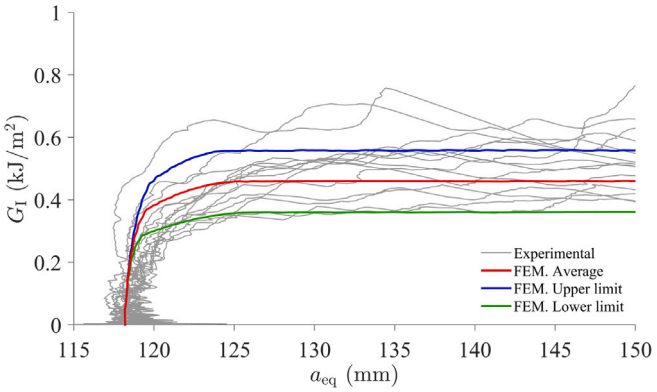

Fig. 11. *R*-curves from experimental DCB test in the TL propagation system and the numerical solutions.

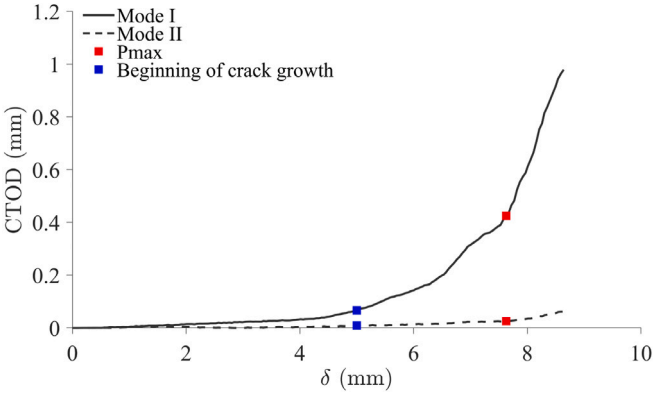

Fig. 12. Evaluation of the normal (Mode I) and parallel (Mode II) CTOD with regard to the applied displacement (δ).

the scatter of the wood properties. Accordingly, it is confirmed that finite element models using a trilinear cohesive law applied to CZM are a useful tool to predict the fracture behavior in mode I of beech. These statements are in agreement with other author's research using other wood species [11,45].

Non-linear behavior can be observed both in the experimental and numerical curves before the maximum load is attained. This is a typical feature of quasi-brittle materials like wood, due to the appearance of the aforementioned micro-cracking and fiber-bridging [13], as can be seen in Fig. 10. This fact verifies the existence of the FPZ ahead of the crack tip and therefore cannot be neglected. In addition, Fig. 10 reveals the difficulty of accurately monitoring crack growth during the tests, which supports the convenience of applying the CBBM scheme based on the equivalent crack length concept to assess the fracture energy [46].

The straight branch of the $P-\delta$ curves was used to calibrate the initial compliance (C_0), which was fitted by linear regression performed with Matlab® attaining coefficients of determination $R^2 > 0.999$. This value, together with the additional crack length ($a = a_0 + \delta$), were used to fit the corrected flexural modulus (E_f) and thus avoid measurement of this property in each DCB tests. The results for both C_0, E_f and maximum load (P_{max}) obtained for each DCB tests in addition to the mean, standard deviation (St. Dev.) and coefficient of variation (CoV) values are shown in Table 3. In the numerical models, an average value of E_L was used as input data, which seems to be quite consistent with the experimental tests as could be observed in Fig. 9. The dispersion of the results is within the expected range in wood.

The *R*-curves obtained from both experimental and numerical $P-\delta$ curves are shown in Fig. 11. These curves describe the evolution of the energy release rate (G_I) as a function of the equivalent crack length (a_{eq}), both parameters derived by applying the CBBM.

The scatter between curves is due to the typical wood variability. Overall, the G_I grows vertically until it steadies at a point represented by the plateau of the curves. This plateau indicates the critical fracture energy (G_{Ic}) and match to the beginning of the material damage, and therefore to the crack growth. A non-linear transition can be observed between the vertical and the horizontal part representing the development of the FPZ. However, in all cases, a plateau can be clearly seen in the *R*-curves, which shows a stable crack growth and therefore justifies the application of the proposed method. Given the length and dispersion of the points that generate the plateau of the *R*-curves, the G_{Ic} value was determined as the average value of the points that belong to this horizontal branch. The results are included also in Table 3. It should be highlighted that the numerical *R*-curves (average, upper limit and lower limit) obtained from the numerical $P-\delta$ fit quite well with the experimental results. Therefore, the use of cohesive elements to model the onset and evolution of damage seems to be a useful and simple tool whose applicability in beech wood (*Fagus sylvatica* L.) has been demonstrated.

The mean value of G_{Ic} (TL) for *Fagus sylvatica* L. resulted in 0.46 kJ/m^2 (22.1% COV). This value is higher than that of softwood species such as Picea abies, which according to [20] has a G_{Ic} value of 0.301 kJ/m^2. However, it is lower than the value obtained for other hardwoods species such as *Eucalyptus globulus* L., which applying the same methodology showed a G_{Ic} value of 0.77 kJ/m^2 according to [13].

3.2. Cohesive laws

The cohesive laws were determined from G_I (applying the CBBM) and the CTOD (w) measured using the DIC technique. In order to identify the eventual presence of spurious mode II loading, the evolution of CTOD (the normal component to the crack plane (Mode I) and the parallel component to the propagation system (Mode II)) with regard to the applied displacement (δ) for a representative experimental test is shown in Fig. 12.

As can be seen in the figure, the displacements belonging to Mode II are negligible. Therefore, the use of DCB specimens loaded in the

Table 3
Density (ρ), corrected flexural modulus (E_f), maximum load (P_{max}), initial compliance (C_0) and critical fracture energy (G_{Ic}) for each DCB specimen, and mean, standard deviation (St. Dev.) and coefficient of variation (CoV) values.

Specimen Ref	ρ (kg/m^3)	E_f (N/mm^2)	P_{max} (N)	C_0 (mm/N)	G_{Ic} (kJ/m^2)
TL_01	696	13500	108.74	0.044	0.36
TL_02	713	12914	134.70	0.048	0.45
TL_05	774	13283	146.95	0.046	0.65
TL_06	689	14797	132.09	0.042	0.49
TL_07	722	15375	135.19	0.041	0.44
TL_08	700	13817	129.97	0.044	0.51
TL_09	710	13164	108.74	0.045	0.34
TL_10	738	15183	136.50	0.041	0.54
TL_12	699	14804	118.70	0.043	0.27
TL_14	676	14735	110.05	0.044	0.35
TL_15	683	16012	138.95	0.041	0.53
TL_16	678	15536	131.93	0.042	0.52
TL_17	691	14910	118.37	0.044	0.41
TL_20	690	16524	137.64	0.040	0.51
Mean	**704**	**14611**	**127.75**	**0.043**	**0.46**
St. Dev.	26	1115	12.46	0.002	0.10
CoV (%)	3.7%	7.6%	9.8%	5.1%	22.1%

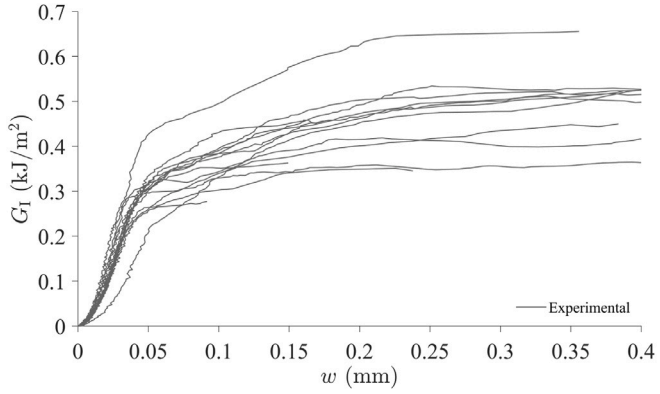

Fig. 13. Experimental $G_I - w$ curves.

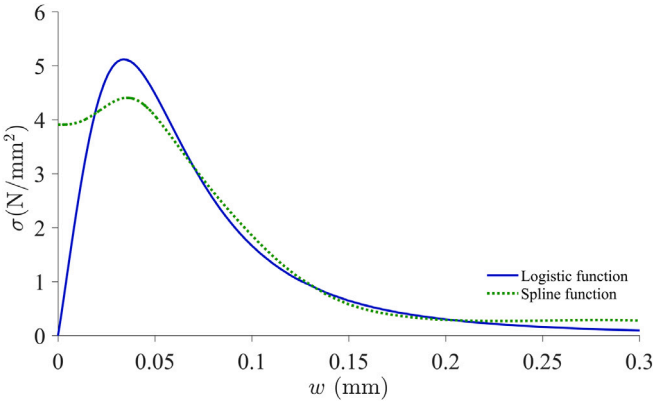

Fig. 15. Logistic and spline cohesive laws obtained for the "*TL 07*" DCB specimen.

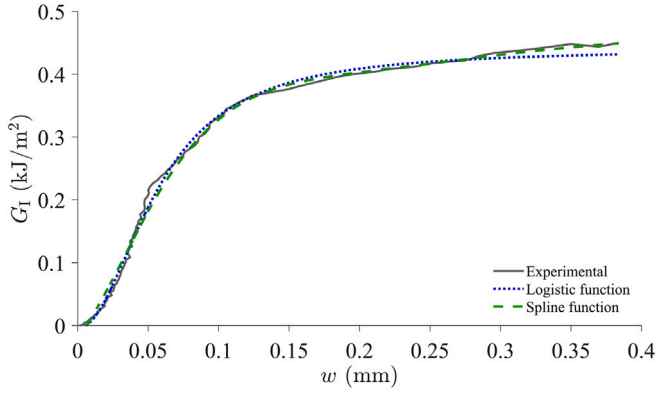

Fig. 14. Logistic and spline function fitting to the experimental $G_I - w$ curve obtained for the "*TL 07*" DCB specimen.

direction perpendicular to the grain seems to be a good test setup to determine G_{Ic} since the influence of mode II is very low.

The $G_I - w$ curves from the experimental tests are shown in Fig. 13. In order to have a continuous function that can be derived to obtain the cohesive laws, during data processing, both a logistic type function (Eq. (9)) and a spline type function were fitted. A representative example of this fit is shown in Fig. 14, which shows a good approximation of both functions. Nonetheless, it can be observed that the spline function fits better to the experimental curve due to its degrees of freedom. However, it has the disadvantage of being quite stiff at the beginning. Fig. 15 shows a representative example of the cohesive law obtained for each function. In this figure it can be seen how the spline function presents problems at the beginning due to the initial stiffness mentioned above. Therefore, in this study the cohesive laws were determined from the logistic function, since it proves to be a smoother and continuous function. It should be noted that only the data points from the start of the test to the beginning of crack propagation have been taken into account, since that point corresponds to the critical fracture energy.

All the experimental and the average cohesive laws of beech are shown in Fig. 16. The corresponding fitting parameters (A_1, A_2, w_0, p) of the logistic curves according to Eq. (10), the maximum traction (σ_u), fracture energy of the cohesive law ($G_{law,I}$) and maximum relative displacement (w_u) are summarized in Table 4. In particular, A_2 value is an estimate of G_{Ic}, which can be verified by comparing these values with those determined from the experimental R-curves shown in Table 3. It is also interesting to note that the σ_u values obtained from the cohesive laws are in agreement with the perpendicular tensile strength value in the tangential direction of 8.9 MPa for beech reported in the literature [47].

Table 4
Fitting parameters of the logistic function (A_1, A_2, w_0, p), maximum traction (σ_u), fracture energy ($G_{law,I}$) and maximum relative displacement (w_u) of the cohesive laws for each DCB specimen. Mean, standard deviation (St. Dev.) and coefficient of variation (CoV) values.

Specimen Ref	A_1 (kJ/m^2)	A_2 (kJ/m^2)	w_{10} (mm)	**p** (-)	$G_{law,I}$ (kJ/m^2)	σ_u (N/mm^2)	w_u (mm)
TL_01	0.007	0.35	0.029	3.12	0.34	10.07	0.024
TL_02	0.003	0.46	0.034	2.42	0.45	9.65	0.024
TL_05	−0.002	0.61	0.036	2.18	0.61	11.41	0.023
TL_06	−0.009	0.49	0.047	1.51	0.50	6.56	0.016
TL_07	−0.004	0.44	0.057	2.06	0.44	5.12	0.034
TL_08	−0.013	0.51	0.041	1.64	0.51	7.81	0.018
TL_09	0.008	0.35	0.024	3.16	0.34	12.57	0.020
TL_10	−0.023	0.54	0.045	1.45	0.55	7.72	0.014
TL_12	0.008	0.29	0.026	3.25	0.28	9.76	0.021
TL_14	0.004	0.33	0.031	2.48	0.33	7.83	0.022
TL_15	−0.013	0.53	0.043	1.66	0.53	7.71	0.019
TL_16	−0.020	0.52	0.040	1.43	0.53	8.21	0.012
TL_17	−0.009	0.39	0.026	2.04	0.40	10.10	0.015
TL_20	−0.007	0.51	0.042	1.84	0.51	7.77	0.022
Mean	**−0.005**	**0.46**	**0.037**	**2.16**	**0.46**	**8.74**	**0.020**
St. Dev.	0.010	0.09	0.009	0.64	0.10	1.97	0.005
CoV (%)	–	20.9%	25.5%	29.8%	21.3%	22.5%	27.1%

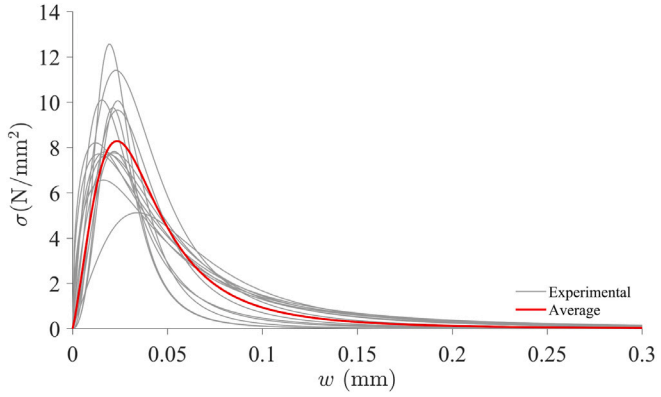

Fig. 16. Experimental cohesive laws (in gray) and average cohesive law (in red) in mode I for beech.

4. Conclusions

The *R*-curves and the cohesive laws in mode I and TL crack propagation system were determined for European beech by means of DCB tests. To derive G_I, the CBBM data reduction scheme, based on beam theory and equivalent crack length concept (a_{eq}), was applied. This method only requires the monitoring of the $P-\delta$ curve, which is an advantage relative to classical procedures. The CTOD (w) was measured directly by the DIC technique. A logistic function was fitted to the $G_I.-w$ curves to obtain the cohesive laws after differentiation of this relation. A mean G_{Ic} value of 0.46 kJ/m^2 was determined for this hardwood species. Furthermore, the mean σ_u value of 8.74 N/mm^2 obtained from the average cohesive law is consistent with the perpendicular tensile strength available in the literature.

The methodology proposed in this work was validated by finite elements model implementing a mean trilinear cohesive law with a bilinear softening relationship using CZM to simulate the crack growth under loads in Mode I. Two additional cohesive laws corresponding to the upper and lower limits of the critical fracture energy were proposed, resulting in a band capable of representing the scatter of wood properties in a simple way. The fracture properties obtained are fundamental to develop reliable numerical models for timber engineering design purposes using European beech.

CRediT authorship contribution statement

J.L. Gómez-Royuela: Conceptualization, Methodology, Software, Validation, Formal analysis, Investigation, Resources, Writing – original draft, Writing – review & editing.. **A. Majano-Majano:** Conceptualization, Methodology, Investigation, Resources, Writing – review & editing, Supervision, Funding acquisition. **A.J. Lara-Bocanegra:** Conceptualization, Methodology, Investigation, Resources, Writing – review & editing, Supervision. **J. Xavier:** Conceptualization, Methodology, Software, Validation, Resources, Writing – review & editing, Supervision, Funding acquisition. **M.F.S.F. de Moura:** Conceptualization, Methodology, Software, Validation, Resources, Writing – review & editing, Supervision, Funding acquisition.

Declaration of competing interest

The authors declare that they have no known competing financial interests or personal relationships that could have appeared to influence the work reported in this paper.

Acknowledgments

Part of the work was undertaken during a short-term scientific stay by the first author at the Faculty of Engineering (University of Porto) in 2021, with the financial support of *Programa Propio de I+D+i 2021 de la Universidad Politécnica de Madrid*. The authors acknowledge Fundação para a Ciência e a Tecnologia (FCT-MCTES) for the financial support of the *Laboratório Associado de Energia*, Transportes e Aeronáutica (LAETA) by the project UID/EMS/50022/2019 and the Research and Development Unit for Mechanical and Industrial Engineering (UNIDEMI) by the project UIDB/00667/2020.

References

[1] UNEP, Buildings and climate change. Summary for decision-makers, United Nation Environ. Programme (2009) 1–62.
[2] L. Gustavsson, R. Sathre, Variability in energy and carbon dioxide balances of wood and concrete building materials, Build. Environ. 41 (7) (2006) 940–951.
[3] L.O. Eriksson, L. Gustavsson, R. Hänninen, M. Kallio, H. Lyhykäinen, K. Pingoud, J. Pohjola, R. Sathre, B. Solberg, J. Svanaes, L. Valsta, Climate change mitigation through increased wood use in the European construction sector-towards an integrated modelling framework, Eur. J. Forest Res. 131 (1) (2012) 131–144.
[4] A.H. Buchanan, S.B. Levine, Wood-based building materials and atmospheric carbon emissions, Environ. Sci. Policy 2 (6) (1999) 427–437.
[5] A.H. Buchanan, B.G. Honey, Energy and carbon dioxide implications of building construction, Energy Build. 20 (3) (1994) 205–217.
[6] T. Ehrhart, European Beech glued laminated timber, 2019, 26173.
[7] European Committee for Standardization (CEN), EN 1995-1-1:2004 design of timber structures. Brussels, Belgium, 2016.
[8] T.A.C.M. Van der Put, A.J.M. Leitjen, Evaluation of perpendicular to grain failure of beams caused by concentrated loads of joints, CIB-W18, Meeting Thirty-Three, Paper 33-7-7, Delft, The Netherlands, 2000.

[9] T.A.C.M. Van der Put, Tension perpendicular to the grain at notches and joints, in: Proceedings Of CIB-W18 Conference, Paper 23-10-1, Lisbon, Portugal., 1990.
[10] J. Xavier, P. Monteiro, J.J. Morais, N. Dourado, M.F. De Moura, Moisture content effect on the fracture characterisation of *Pinus pinaster* under mode I, J. Mater. Sci. 49 (21) (2014) 7371–7381.
[11] J. Xavier, M. Oliveira, P. Monteiro, J.J. Morais, M.F. de Moura, Direct evaluation of cohesive law in mode I of *Pinus pinaster* by digital image correlation, Exp. Mech. 54 (5) (2014) 829–840.
[12] N.M. Dourado, M.F. De Moura, J.J. Morais, M.A. Silva, Estimate of resistance-curve in wood through the double cantilever beam test, Holzforschung 64 (1) (2010) 119–126.
[13] A. Majano-Majano, A.J. Lara-Bocanegra, J. Xavier, J. Morais, Measuring the cohesive law in mode I loading of *Eucalyptus globulus*, Materials 12 (1) (2019) 23.
[14] R.A. Luimes, A.S. Suiker, C.V. Verhoosel, A.J. Jorissen, H.L. Schellen, Fracture behaviour of historic and new oak wood, Wood Sci. Technol. 52 (5) (2018) 1243–1269.
[15] Y. Yu, R. Xin, W. Zeng, W. Liu, Fracture resistance curves of wood in the longitudinal direction using digital image correlation technique, Theor. Appl. Fract. Mech. 114 (2021) 102997.
[16] K. Ostapska, K.A. Malo, Crack path tracking using DIC and XFEM modelling of mixed-mode fracture in wood, Theor. Appl. Fract. Mech. 112 (January) (2021).
[17] M.F. de Moura, N. Dourado, Mode I fracture characterization of wood using the TDCB test, Theor. Appl. Fract. Mech. 94 (September 2017) (2018) 40–45.
[18] A. Majano-Majano, M. Hughes, J.L. Fernandez-Cabo, The fracture toughness and properties of thermally modified beech and ash at different moisture contents, Wood Sci. Technol. 46 (2012) 5–21.
[19] M. Merhar, D.G. Bučar, B. Bučar, Faktor kritičnog intenziteta naprezanja (i. mod) bukovine (*Fagus sylvatica*) u TL presjeku: Usporedba različitih metoda, Drvna Ind. 64 (3) (2013) 221–229.
[20] N. Dourado, M.F. de Moura, S. Morel, J. Morais, Wood fracture characterization under mode I loading using the three-point-bending test. Experimental investigation of *Picea abies l.*, Int. J. Fract. 194 (2015) 1–9.
[21] A. Reiterer, G. Sinn, S.E. Stanzl-Tschegg, Fracture characteristics of different wood species under mode I loading perpendicular to the grain, Mater. Sci. Eng. A 332 (1–2) (2002) 29–36.
[22] S.E. Stanzl-Tschegg, D.M. Tan, E.K. Tschegg, New splitting method for wood fracture characterization, Wood Sci. Technol. 29 (1) (1995) 31–50.
[23] H. Yoshihara, T. Kawamura, Mode I fracture toughness estimation of wood by DCB test, Composites A 37 (11) (2006) 2105–2113.
[24] M.F. de Moura, J.J. Morais, N. Dourado, A new data reduction scheme for mode I wood fracture characterization using the double cantilever beam test, Eng. Fract. Mech. 75 (13) (2008) 3852–3865.
[25] D.S. Dugdale, Yielding of steel, J. Mech. Phys. Solids 8 (1960) 100–104.
[26] A. Hillerborg, M. Modéer, P.-E. Petersson, Analysis of crack formation and crack growth in concrete by means of fracture mechanics and finite elements, Cem. Concr. Res. 6 (1976) 773–782.
[27] P.-E. Petersson, Crack Growth and Development of Fracture Zones in Plain Concrete and Similar Materials, Report TVBM, Division Of Building Materials, Lund Institute Of Technology, Lund, Sweden, 1981.
[28] L. Boström, Method of determination of the softening behaviour of wood and the applicability of a nonlinear fracture mechanics model, Lund (PhD thesis), (TVBN-1012) 1992, p. 148.
[29] L. Boström, The stress-displacement relation of wood perpendicular to the grain - part 1. Experimental determination of the stress-displacement relation, Wood Sci. Technol. 28 (4) (1994) 309–317.
[30] N. Dourado, S. Morel, M.F. de Moura, G. Valentin, J. Morais, Comparison of fracture properties of two wood species through cohesive crack simulations, Composites A 39 (2) (2008) 415–427.
[31] J.L. Gómez-Royuela, A. Majano-Majano, A.J. Lara-Bocanegra, T.P.S. Reynolds, Determination of the elastic constants of thermally modified beech by ultrasound and static tests coupled with 3D digital image correlation, 302, 302 (2021) 124270.
[32] GOM mbH, ARAMIS Commercial software. Aramis 6.0.2; GOM mbH: Braunschweig, Germany, 2007.
[33] J. Xavier, A. de Jesus, J. Morais, J. Pinto, Stereovision measurements on evaluating the modulus of elasticity of wood by compression tests parallel to the grain, Constr. Build. Mater. 26 (1) (2012) 207–215.
[34] J. Pereira, J. Xavier, B. Ghiassi, J. Lousada, J. Morais, On the identification of earlywood and latewood radial elastic modulus of pinus pinaster by digital image correlation: A parametric analysis, J. Strain Anal. Eng. Des. 53 (8) (2018) 566–574.
[35] J. Williams, The fracture mechanics of delamination tests, 1989.
[36] F.A. Pereira, J.J. Morais, M.F. de Moura, N. Dourado, M.I. Dias, Evaluation of bone cohesive laws using an inverse method applied to the DCB test, Eng. Fract. Mech. 96 (2012) 724–736.
[37] J.R. Rice, A path independent integral and the approximate analysis of strain concentration by notches and cracks, J. Appl. Mech. Trans. ASME 35 (2) (1968) 379–388.
[38] A.M. Sousa, J. Xavier, J.J. Morais, V.M. Filipe, M. Vaz, Processing discontinuous displacement fields by a spatio-temporal derivative technique, Opt. Lasers Eng. 49 (12) (2011) 1402–1412.
[39] J. Xavier, A.M.R. Sousa, J.J.L. Morais, V.M.J. Filipe, M. Vaz, Measuring displacement fields by cross-correlation and a differential technique: experimental validation, Opt. Eng. 51 (4) (2012) 043602.
[40] J. Xavier, J.R. Fernandes, O. Frazão, J.J. Morais, Measuring mode I cohesive law of wood bonded joints based on digital image correlation and fibre bragg grating sensors, Compos. Struct. 121 (2015) 83–89.
[41] J. Oliveira, J. Xavier, F. Pereira, J. Morais, M. de Moura, Direct evaluation of mixed mode I+II cohesive laws of wood by coupling MMB test with DIC, Materials 14 (2) (2021) 374.
[42] F. Pereira, M. de Moura, N. Dourado, J. Morais, J. Xavier, M. Dias, Direct and inverse methods applied to the determination of mode I cohesive law of bovine cortical bone using the DCB test, Int. J. Solids Struct. 128 (2017) 210–220.
[43] F. Silva, M. de Moura, N. Dourado, J. Xavier, F. Pereira, J. Morais, M. Dias, Mixed-mode I+II fracture characterization of human cortical bone using the single leg bending test, J. Mech. Behav. Biomed. Mater. 54 (2016) 72–81.
[44] C.G. Dávila, P.P. Camanho, M.F. De Moura, Mixed-mode decohesion elements for analyses of progressive delamination, in: 19th AIAA Applied Aerodynamics Conference, May 2014, 2001.
[45] N. Dourado, M.F. de Moura, Effect of temperature on the fracture toughness of wood under mode I quasi-static loading, Constr. Build. Mater. 223 (2019) 863–869.
[46] J. Xavier, J. Morais, N. Dourado, M.F. De Moura, Measurement of mode I and mode II fracture properties of wood-bonded joints, J. Adhes. Sci. Technol. 25 (20) (2012) 2881–2895.
[47] T. Ozyhar, S. Hering, P. Niemz, Moisture-dependent elastic and strength anisotropy of European beech wood in tension, J. Mater. Sci. 47 (16) (2012) 6141–6150.

Publicación III

Shear traction-separation laws of European beech under mode II loading by 3D digital image correlation

José Luis Gómez-Royuela, Almudena Majano-Majano, Antonio José Lara-Bocanegra, José Xavier, M. F. S. F. de Moura.

Wood Science and Technology, 56: 1631-1655, 2022
DOI: https://doi.org/10.1007/s00226-022-01429-3
Q1 (JCR). Impact factor: 3,4

Wood Science and Technology (2022) 56:1631–1655
https://doi.org/10.1007/s00226-022-01429-3

ORIGINAL

Shear traction–separation laws of European beech under mode II loading by 3D digital image correlation

José Luis Gómez-Royuela[1] · Almudena Majano-Majano[1] · Antonio José Lara-Bocanegra[1] · José Xavier[2] · M. F. S. F. de Moura[3]

Received: 29 June 2022 / Accepted: 28 October 2022 / Published online: 21 November 2022

Abstract

An experimental and numerical study on mode II fracture behaviour of European beech (*Fagus sylvatica* L.) in the RL and TL crack propagation systems is performed. It is a hardwood species that has attracted increasing interest for structural use in Europe in recent years. Three-point end notched flexure tests are performed. The *R*-curves of both crack propagation systems are obtained, from which the critical strain energy release rate (G_{IIc}) is derived by applying the compliance-based beam method. This data reduction scheme avoids crack length monitoring during its propagation, which is an advantage in wood. Using a direct method, the shear traction-separation laws in mode II loading are determined. Full field displacements around the crack tip are monitored by 3D digital image correlation technique, and the crack tip shear displacements are analysed. The proposed method is numerically validated by finite element analysis. Cohesive zone models are developed implementing a shear traction–separation law with exponential damage evolution zone and the average value of the experimental elastic and fracture properties. The numerical results for the different properties including upper and lower limits represent well the experimental data.

Introduction

Wood is one of the most important and least polluting natural resources in the world. Currently, concern about greenhouse gas emissions is growing steadily. This results in sustainability policies strongly betting on the use of wood as a construction material and being interested in carrying out a sustainable exploitation of forests. In response, the research community is accompanying this change by developing products and tools that allow building in an environmentally friendly way, deepening the use of wood as a structural material.

✉ José Luis Gómez-Royuela
joseluis.gomez.royuela@upm.es

Extended author information available on the last page of the article

Technological development and the better use of natural resources in recent years have sparked interest in the use of hardwood species in the building sector. Part of this concern is due to the high mechanical performance of hardwoods compared to softwoods. In this sense, one of the hardwood species that has recently gained a great deal of attention for structural purposes in Europe is beech (*Fagus sylvatica* L.) (Enders-Comberg et al. 2015; Kovryga et al. 2020; Ehrhart et al. 2021), on which this study will focus.

In the context of timber structures, there are common design situations where brittle failures can occur due to stress concentrations, for example, in beams with holes, joints, notched beams, etc. (Ardalany et al. 2016; Dourado et al. 2018; Majano-Majano et al. 2022) producing critical situations that require special attention. Therefore, it is necessary to establish adequate failure criteria and to accurately characterise the fracture properties of the material. In this context, conventional methods relying on the strength of materials and failure criteria have limitations. To overcome these drawbacks, fracture mechanics based approach can offer advantages, since this theory appeared as a tool to explain the failure mechanisms associated with the propagation of pre-existing cracks. The first model developed was only able to satisfactorily explain the behaviour of brittle materials such as glass (Inglis 1913; Griffith et al. 1921) and therefore did not arouse much enthusiasm in the research community. However, the theory underwent a great development after the Second World War (Irwin and Washington 1957; Dugdale 1960; Barenblatt 1962; Rice 1968; Bažant and Planas 1998) and managed to explain the failure of materials such as steel, concrete, or wood, which is characterised by the development of strain energy dissipation mechanisms before failure, such as plastic deformation around the crack tip, friction, microcracking, or fibre-bridging. These softening mechanisms in wood can be modelled with the concept of Fracture Process Zone (FPZ) ahead of the crack tip (de Moura et al. 2006). There is experimental research in the literature that suggests a quasi-brittle behaviour of wood, with fibre-bridging being the major crack tip toughening mechanism (Vasic and Smith 2002).

Numerical simulations using finite element analysis (FEA) are becoming a useful and powerful tool to better understand the fracture behaviour of many timber structural applications, such as end notched beams, beams with holes or bolted connections (Rautenstrauch et al. 2008; Caldeira 2011; Franke and Quenneville 2011, 2012; Ardalany et al. 2016; Dourado et al. 2018). In this sense, cohesive zone models (CZM) constitute one of the simplest methods to take into account the aforementioned toughening phenomena and whose precision has been sufficiently demonstrated (Dugdale 1960; Barenblatt 1962; Hillerborg et al. 1976; Petersson 1981; Boström 1992; Coureau et al. 2007; de Moura et al. 2009a; Dourado et al. 2013; de Moura et al. 2015; Pereira et al. 2018). The CZM applies a strength criterion based on limit stresses to determine the start of the damage, and later implements a traction-separation law to describe the progressive damage of the material according to a fracture mechanics criterion. However, the drawback of using CZM is that they must be associated with geometrically defined damage paths in the numerical model and, therefore, it is essential to know them previously. Moreover, knowledge of the different material properties is necessary to develop FEA models accurately. Relevant information on the properties of *Fagus sylvatica* L. can be found in the

literature, such as the elastic orthotropic constants (Ozyhar et al. 2013a, c; Gómez-Royuela et al. 2021) and viscoelastic characterisation (Ozyhar et al. 2013b). However, CZMs also require the material fracture properties, such as the fracture energy and the cohesive law. These properties can be obtained experimentally by direct methods (Xavier et al. 2014b) or by inverse methods using numerical simulations (Dourado et al. 2012).

Various fracture test arrangements have been proposed to study pure fracture modes (mode I, mode II, mode III) (Cramer and Pugel 1987; Stanzl-Tschegg et al. 1995; Ehart et al. 1998; Frühmann et al. 2002b, a; Qiao et al. 2003; Yoshihara 2004; Brunner et al. 2008; Ardalany et al. 2012; Majano-Majano et al. 2019, 2012; Xavier et al. 2014a; Dourado et al. 2015; Luimes et al. 2018; Crespo et al. 2018). Although there is still no globally accepted method for each of them, the double cantilever beam (DCB) (Yoshihara and Kawamura 2006) and the three-point end notched flexure (ENF) (Yoshihara and Ohta 2000) tests are widely applied to pure modes I and II, respectively. Much research has focused mainly on the wood fracture behaviour under mode I, as it is considered to be the most predominant one. However, many elements are designed to withstand high shear loads, so knowing the fracture behaviour under mode II becomes an important key issue.

The objective of this work is to experimentally determine the main fracture properties in mode II loading of European beech wood (*Fagus sylvatica* L.) using ENF specimens for both tangential-longitudinal (TL) and radial-longitudinal (RL) crack propagation systems. For the first time, to the best of the authors' knowledge, the shear traction-separation laws of *Fagus sylvatica* L. are provided, which are derived directly from the relationship between the strain energy release rate (G_{II}) obtained from the *R*-curves and the crack tip shear displacements (CTSD) monitored during testing by means of the 3D digital image correlation (DIC) technique. The compliance-based beam method (CBBM) is applied as a data reduction scheme, which is based on the beam theory and on the equivalent crack length (a_{eq}) concept. It has the advantage that only the load–displacement curve is needed and does not require measuring crack growth during the test, which would be a complex task in wood, particularly under mode II loading. Numerical validation by FEA using cohesive zone models with exponential softening relationship of the shear traction–separation law is also performed.

Materials and methods

Raw material

Fagus sylvatica L. from Europe was the wood species tested in this work. The specimens were machined and carefully cut from knot-free boards and oriented according to the RL and TL crack propagation systems (Fig. 1). The material was stored in a climate chamber at 20 °C and 65% relative humidity until an equilibrium moisture content was reached. The density of each specimen was measured, resulting in average values of 721 kg/m^3 and 708 kg/m^3 for the batches corresponding to RL and TL systems, respectively. Main moisture contents of 10% and 9.9% were achieved

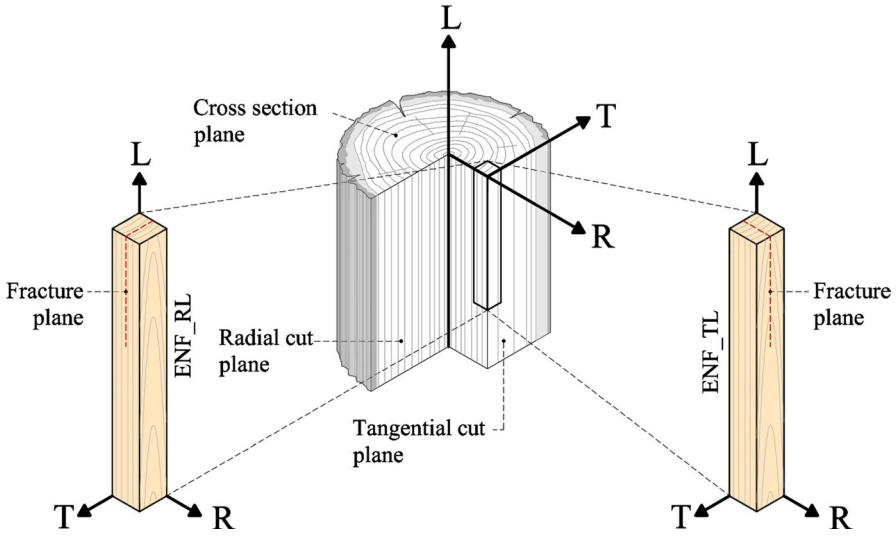

Fig. 1 RL and TL crack propagation systems of the specimens

for the RL and TL groups of specimens, respectively. Constant values for the shear modulus in LR plane, $G_{LR} = 1108$ MPa, and the shear modulus in LT plane, $G_{LT} = 706$ MPa, were taken from Gómez-Royuela et al. (2021).

Three-point end notched flexure tests coupled with 3D digital correlation

Twelve ENF specimens with RL orientation and fourteen with TL were tested according to the geometry schematically shown in Fig. 2. These are small rectangular-shaped beams with nominal dimensions $2L_1 \times 2h \times B$ (500 mm × 20 mm × 20 mm). An initial crack was performed at mid-cross section height using a band saw.

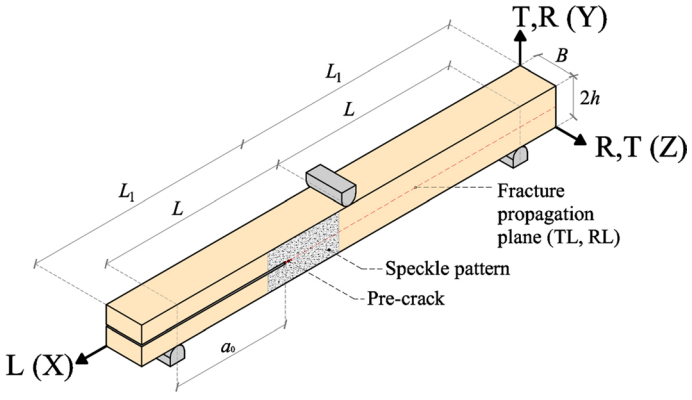

Fig. 2 ENF geometry

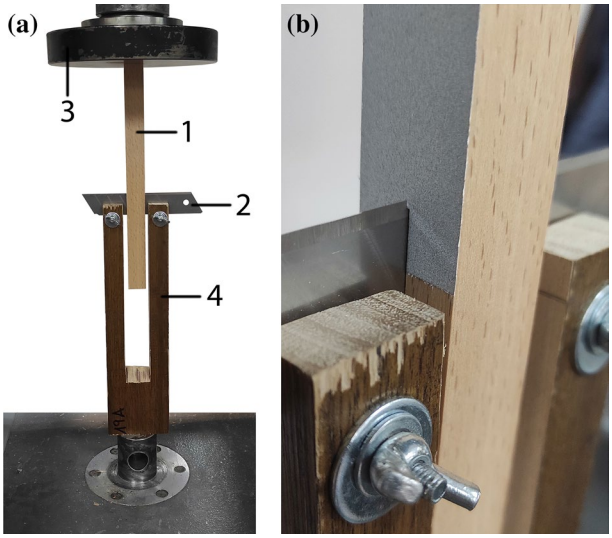

Fig. 3 **a** Cutting setup: 1- ENF specimen, 2- sharp thin blade, 3- loading plate, 4- cutting support; **b** pre-crack

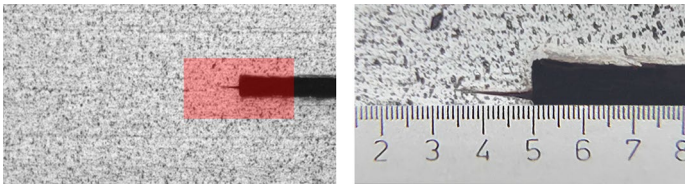

Fig. 4 Pre-crack measurement: measuring area marked in the highlighted square (left); measuring area viewed with a precision magnifying glass (right)

This procedure was carried out in two steps: first, a notch with an initial length a_0 (161 mm) was machined, and just prior to testing this notch was lengthened 1 mm more using a very sharp thin blade. This delicate process was controlled using a universal testing machine (Fig. 3) with a cross-head speed of 10 mm/min, since the shape of the pre-crack surface plays an important role and could significantly influence the results, as reported in Dias et al. (2013). The pre-crack length was measured with a precision magnifying glass as shown in Fig. 4.

The ENF specimens were subjected to three point bending tests using an electromechanical universal testing machine with a load cell of 5 kN maximum capacity (Fig. 5). The beam span was 2*L* (460 mm). The load was introduced at the mid-span under a constant crosshead speed of 2 mm/min. To avoid friction effects during the tests, two sheets of Teflon were introduced between the upper and lower sides of the crack at the support zone. The load displacement curves (P-δ) were recorded during the tests with a frequency of 1 Hz. The deflection of the specimen was obtained by means of a linear variable differential transformer (LVDT) measuring the loading

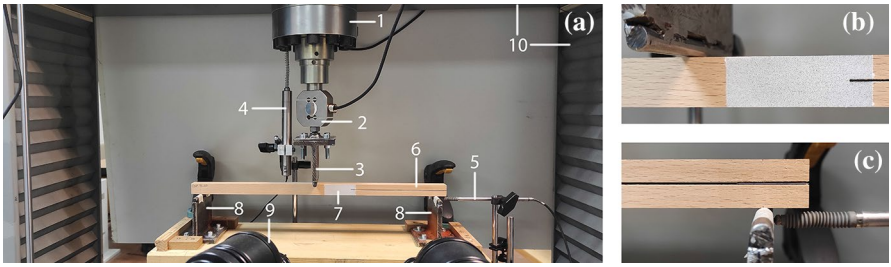

Fig. 5 **a** ENF test set-up coupled with 3D DIC: (1) 300 kN load cell, (2) 5 kN load cell, (3) loading nose, (4) LVDT, (5) LVDT, (6) beech specimen, (7) speckle pattern, (8) supports, (9) DIC system equipment, (10) electro-mechanical testing machine frame; **b** detail of speckle pattern; **c** detail of the support

plate displacement (element 4 in Fig. 5), as this LVDT was synchronised with both the 5 kN load cell and the DIC system. It should be noted that the loading nose did not produce any indentation on the specimens. An additional LVDT was used to verify that the supports showed no horizontal displacements (Fig. 5c). The maximum displacement recorded was approximately 0.01 mm, which was considered negligible. The initial test setup and the completed test result are shown in Figs. 5 and 6, respectively.

3D DIC is an optical technique capable of measuring full field displacements of a speckled pattern, applied on the surface of interest (Sutton et al. 2009). An advantage of the 3D system over the 2D system is the ability to take measurements of an area within a volume, avoiding measurement errors arising from poor positioning of the specimen with respect to the cameras. The 3D DIC system ARAMIS® 3D (GOM mbH 2007) was used and coupled to the universal testing machine to record synchronized data of crack tip shear displacements with a frequency of 1 Hz. To ensure the accuracy of the measurements, a speckle pattern with appropriate contrast and granulometry was created on the surface of interest of the ENF specimens. This pattern was made in two stages: first, a thin, homogeneous layer of matte white paint was applied by spray, and then a pattern of black dots was projected on the surface using an airbrush. The optical system consisted of two front cameras with a resolution of 5 megapixels, coupled with 35 mm lenses. The optical system was calibrated according to the specifications described by the manufacturer (GOM mbH 2007). For this proposal, 13 images were taken and the calibration results were verified to

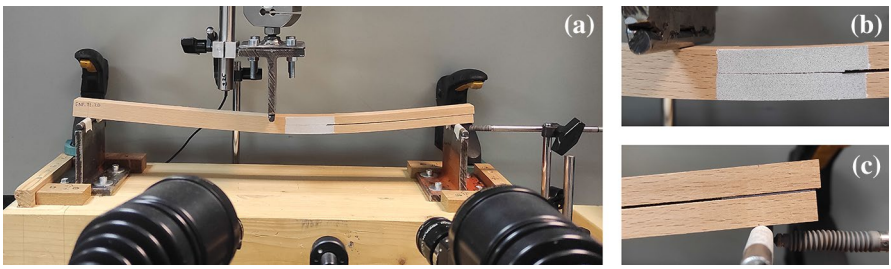

Fig. 6 **a** ENF specimen being tested; **b** detail of the fracture zone; **c** detail of the support

be within the acceptable range established by GOM company. The calibration procedure was carried out using a CP20 according to the size of the study area. A subset size of 15×15 pixel^2 and a subset step of 13×13 pixel^2 were selected to improve the spatial resolution in a compromise with respect to accuracy. To achieve accurate measurements, the cameras were placed 400 mm from the surface of interest and set up for a field of view of 80×65 mm^2. Consequently, an angle of 25° was established between the cameras. The separation between them and the reference axis was locked at 138 mm. In addition, to ensure the correct focus of the specimen surface, the device incorporated two white-light spotlights with adjustable light intensity to avoid insufficient or excessive light exposure. The spotlights and the shutter time were set to ensure adequate contrast and illumination of the specimen.

Experimental direct data reduction method

The shear traction–separation laws for pure mode II loading describe the relationship between the strain energy release rate (G_{II}), the shear stresses (τ) and the crack tip shear displacements (CTSD) according to the following expression (Leffler et al. 2007)

$$G_{II} = \int_0^{\bar{u}} \tau(u) du \tag{1}$$

where u is the CTSD, which was directly monitored during the test using the ARAMIS 3D DIC system. The differentiation of Eq. (1) provides directly the shear traction-separation law ($\tau = f(w)$) as

$$\tau(u) = \frac{dG_{II}}{du} \tag{2}$$

To apply this equation, it is necessary to determine the evolution of G_{II} during the test. However, nonlinear phenomena such as microcracks, cracks-branching and fibre-bridging appear in the area around the crack tip. These toughening mechanisms influence the fracture behaviour of wood and therefore cannot be neglected. This zone is known as FPZ and is located ahead of the crack tip. To overcome this difficulty, in this study, the G_{II} was determined from the crack growth resistance curves (R-curves), which are a useful tool that allows quantifying the influence of the FPZ. The G_{IIc} is given by the plateau value of these curves. According to this, G_{II} can be obtained by the Irwin-Kies equation:

$$G_{II} = \frac{P^2}{2B} \frac{dC}{da} \tag{3}$$

where P, B, C and a are the applied load, the width of the specimen, the compliance ($C = \delta/P$) and the crack length, respectively. In this work, dC/da was determined applying the CBBM (de Moura et al. 2006). This data reduction scheme is based on the equivalent crack length (a_{eq}) concept and accounts for the energy dissipated due

to the toughening mechanisms. These phenomena are developed in the FPZ and are not negligible in wood. In this context, considering the Timoshenko beam theory for the ENF test, the specimen compliance can be written as (de Moura et al. 2006)

$$C = \frac{3a^3 + 2L^3}{8Bh^3E_L} + \frac{3L}{10BhG_{Li}},\ i = R, T \tag{4}$$

being E_{L} and $G_{\mathrm{L}i}$ the longitudinal and shear elastic moduli, respectively. In the last one, i can be either R or T and refer to the radial and tangential orthotropic directions. L, B, h and a are the dimensions of the specimens identified in Fig. 2. To take into account the effects that the inherent variability of wood has on the elastic properties, a corrected bending modulus E_{f} is considered instead of E_{L}. For this purpose, the E_{f} value can be determined from Eq. (4) using the initial values of the crack length $a = a_0$ and compliance $C = C_0$. It should be clarified that C_0 was estimated by linear regression of the P-δ curve applying the least-squares method. Consequently, E_{f} can be determined according to the following expression

$$E_f = \frac{3a_0^3 + 2L^3}{8Bh^3C_{0,\mathrm{corr}}} \tag{5}$$

where $C_{0,\mathrm{corr}}$ is given by

$$C_{0,\mathrm{corr}} = C_0 - \frac{3L}{10BhG_{Li}},\ i = R, T \tag{6}$$

It should be highlighted that no significant errors are made when neglecting the influence of inherent variability of $G_{\mathrm{L}i}$ on the result of C, as shown in de Moura et al. (2006). Therefore, in this research work, a typical value of G_{L} summarized in "Raw material" section was considered in Eq. (6). On the other hand, accurate crack length measurements during the ENF test is a difficult task since crack tends to grow with their faces in close contact (Schuecker and Davidson 2000). Furthermore, the specimen compliance ($C = \delta/P$) recorded during the test can be quite influenced by the effects that the FPZ causes in the vicinity of the crack tip. Because of this, an amount of energy can be dissipated that is not accounted for in G_{II}, when real crack length is used as a calculation parameter. Consequently, important errors can occur in the characterisation of the fracture energy. To overcome these difficulties, an equivalent crack length (a_{eq}) is used in Eq. (4) instead of the real one and can be written as (de Moura et al. 2006)

$$a_{\mathrm{eq}} = a + \Delta a_{\mathrm{FPZ}} = \sqrt[3]{\frac{C_{\mathrm{corr}}}{C_{0,\mathrm{corr}}}a_0^3 + \frac{2}{3}\left(\frac{C_{\mathrm{corr}}}{C_{0,\mathrm{corr}}} - 1\right)L^3} \tag{7}$$

where C_{corr} is given by

$$C_{\mathrm{corr}} = C - \frac{3L}{10BhG_{\mathrm{L}i}},\ i = R, T \tag{8}$$

Finally, combining Eqs. (3) and (7), the evolution of G_{II} as a function of a_{eq} can be determined as follows

$$G_{II} = \frac{9P^2 a_{eq}^2}{16B^2 h^3 E_f} \tag{9}$$

In order to obtain the shear traction–separation law, CTSD were rigorously measured using the ARAMIS 3D DIC system. For this purpose, the pre-crack tip was identified in the first image and subsequently pairs of symmetrical facets to the expected fracture plane in the initial picture were carefully selected. According to this, each top subset (+1, +2, +3, …) was paired with its lower symmetrical subset (− 1, − 2, − 3, …) (Fig. 7). The displacements in the direction of the fracture plane were then post-processed for each loading step and for each selected pair of facets. It should be noted that the CTSD determination was always started considering the subsets pair closest to the crack tip (+1 and − 1). However, to avoid facets near discontinuities and damage areas, each subset of data was verified to be recognized successfully in each of the recorded images. A sensitivity analysis was therefore systematically performed. This validation process was carried out by observing if there were discontinuities in the u-δ curve. In addition, it was verified that each facet of a subset pair was on the opposite side of the crack during the test, as the crack propagation could place them on the same arm.

Finally, CTSD (u) was evaluated as the relative displacement between each set of facets as follows (Sousa et al. 2010, 2011)

$$u = \left\| u^+ - u^- \right\| \tag{10}$$

where u^+ and u^- are the displacement components parallel to the crack surface (Fig. 8) associated with the subsets described above and $\| \cdot \|$ represents the Euclidean norm.

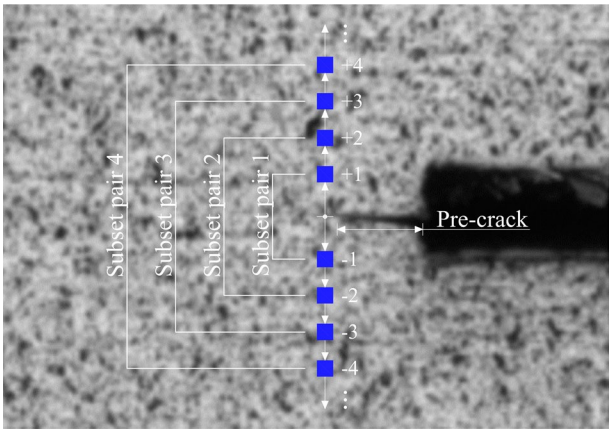

Fig. 7 Scheme of the subsets pair location (squares) used for the determination of CTSD

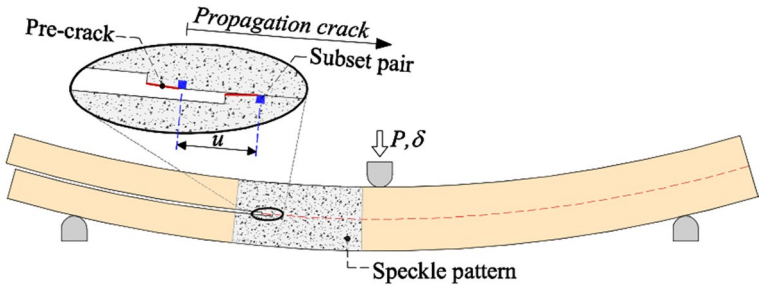

Fig. 8 Scheme of the ENF test with the speckle pattern at the crack tip area of the specimen during testing

In order to obtain τ, a continuous function was fitted to G_{II}-u. There are different ways to address this problem adequately.

In this sense, relevant research available in the literature (Oliveira et al. 2021; Gómez-Royuela et al. 2022) has shown that a 4-parameter logistic model is a useful tool for fitting calibration curves of this shape. Therefore, in this study, a 4-parameter logistic function (Rodbard 1974; Rodbard and Hutt 1974) was fitted by least squares through successive approximations according to the following expression

$$G_{II} = \frac{A_1 - A_2}{1 + \left(u/u_0\right)^p} + A_2 \tag{11}$$

where A_1, A_2, u_0 and p are fitting constants by regression analysis. It should be noted that this function is used as a tool to smooth the noise before deriving Eq. (2). In this way, τ can be determined as follows

$$\tau = -\frac{p(A_1 - A_2)(u/u_0)^{p-1}}{u_0\left(1 + (u/u_0)^p\right)^2} \tag{12}$$

The A_2 parameter in Eqs. (11) and (12) should provide an estimation of the critical strain energy release rate according to Eq. (13).

$$A_2 = \lim_{u \to \infty} G_{II} = G_{IIc} \tag{13}$$

On the other hand, this methodology has been successfully applied in other relevant research available in the literature (e.g. Pereira et al. 2018; Majano-Majano et al. 2020).

Numerical validation

In order to verify the appropriateness of the experimental procedure followed to determine the shear traction–separation law according to the direct method (Eq. (12)), a numerical law similar to the experimental one (Eq. (12)) was implemented in ABAQUS® v2021 (Abaqus 2021), a commercial finite element

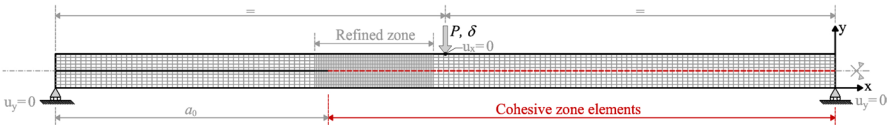

Fig. 9 Scheme of the numerical model with the refined mesh

Table 1 Numerical parameters of the exponential shear traction–separation law. Maximum shear strength (τ_u), initial stiffness (k), ultimate displacement at which fibre breaks (u_u), rate of damage evolution (α) and critical fracture energy in mode II (G_{IIc})

Propagation system	τ_u (N/mm^2)	K (N/mm^3)	u_u (mm)	G_{IIc} (N/mm)
RL				
Average	27.95	662	0.413	2.29
Upper limit	36.46	995	0.333	2.46
Lower limit	21.86	487	0.499	2.12
TL				
Average	18.65	454	0.298	1.17
Upper limit	22.43	546	0.304	1.43
Lower limit	14.86	362	0.289	0.91

software. Since the fracture plane will remain the same throughout the thickness of the specimen, a 2D analysis was performed using CZM. To obtain accurate results, a refined mesh was performed in the crack growth region according to the scheme in Fig. 9. A total of 2070 8-node (CPS8R) quadratic plane stress elements were used to model the ENF specimen. 148 6-node quadratic cohesive surfaces were used to simulate fracture propagation at the plane located at half-height, as shown in Fig. 9. 73 of these 148 elements belong to the refined zone. The Newton–Cotes integration scheme was used in the elements (Gonçalves et al., 2000). The analyses were carried out considering nonlinear geometric behaviour. Implicit nonlinear analysis was considered and the Newton–Raphson convergence method was used to solve the systems of nonlinear equilibrium equations. The model was loaded applying 20 mm displacement (δ) at the mid-span of the specimen in increments no greater than 0.02 mm in order to obtain a smooth crack growth and accurate results.

Recent research available in the literature uses simple shapes to define the softening region of the shear traction–separation law, such as linear or bilinear softening, to simulate crack growth in wood (de Moura et al. 2009b; Xavier et al. 2014b; de Moura et al. 2018). In this study, an exponential softening relationship (Fig. 10) was implemented using standard items in ABAQUS to reproduce stable propagation of the crack in Mode II according to the experimental test. This shape provides very good fit to the experimental cohesive laws.

This fracture behaviour is characterised by an initial undamaged linear elastic branch until the maximum shear stress τ_u is reached at the peak of the curve,

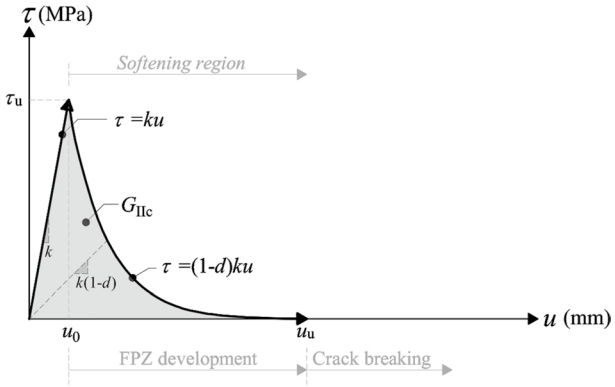

Fig. 10 Exponential shear traction–separation law implemented in ABAQUS. Separation (u) and shear traction (τ)

which is associated with the corresponding crack opening u_0. This undamaged stage is defined by Eq. (14).

$$\tau = k\,u \tag{14}$$

where u is the CTSD and k is the initial interface stiffness considered by the user, usually known as the *penalty parameter*. It should be noted that being rigorous with the proposed data reduction scheme in "Experimental direct data reduction method" section the initial stiffness implemented in the numerical model could be taken directly from the second derivative of Eq. (11). However, this would lead to a greater consumption of computational resources and also in many situations to use unsound values of k, since the logistic curve shape leads to a stiffness close to zero in the first loading step, something that has no physical meaning in this material. According to this, the initial stiffness used in the numerical solution was the slope of the fitted line between the origin ($u=0$ and $\tau=0$) and the peak of the curve given by Eq. (12) ($u=u_0$ and $\tau=\tau_u$). The k values used are summarized in Table 1.

The second branch of the shear traction–separation law is a softening stage corresponding to the development of the FPZ. After achieving maximum local strength (τ_u), the material behaves in a nonlinear way and the largest slope zone (first descending branch) and the lowest slope zone represent microcracking and fibre-bridging, respectively. The ultimate crack growing (u_u) is defined from the fracture energy G_{IIc}. The shear traction–separation relationships at this part of the law are established according to Eq. (15):

$$\tau = (1-d)k\,u \tag{15}$$

where d is the damage parameter, which is determined from the shear traction–separation law as a function of u according to Eq. (16). It varies between 0 and 1, with 0 if there is no material damage and 1 when the rupture is reached.

$$d = \frac{1 - e^{-\alpha\left(\frac{u-u_0}{u_u-u_0}\right)}}{1 - e^{-\alpha}} \tag{16}$$

being α a nondimensional parameter that defines the rate of damage evolution. A value of $\alpha = 6$ was adopted, since it turned out to be a representative value that fits the damage branch given by Eq. (12). Knowing G_{IIc}, the final CTSD (u_u) can be obtained by integrating the area under the function given in Fig. 10. The values considered to determine the shape of the shear traction–separation law are listed in Table 1, which correspond to the average experimental values obtained in "Results and discussions" section. To consider the inherent variability of wood properties, two additional separation laws were implemented in the numerical validation, which are listed in Table 1 and represent the upper and lower limits of the shear traction–separation laws. These additional laws were derived by applying the standard deviation (St. Dev.) to the mean values, as detailed in "Shear traction-separation laws" section.

The mean values of the elastic constants of European beech used as input data in the numerical models were taken from previous work by the authors (Gómez-Royuela et al. 2021) and E_L was altered in such a way that the initial slope of the experimental P-δ curves was correctly predicted. These values are summarized in Table 2.

Results and discussions

R-curves

The experimental P-δ curves (in grey) obtained from the ENF tests for the RL and TL propagation systems are shown in Fig. 11. They also include the numerical P-δ curves using the exponential shear traction–separation laws and elastic constants specified in Tables 1 and 2. Likewise, numerical P-δ curves considering the upper and lower limits of the experimental shear traction–separation laws are represented (dotted and dashed lines, respectively), whose values are summarized in Table 1 and the laws can be seen in "Shear traction-separation laws" section.

The experimental curves of both crack propagation systems show consistent results despite the typical variability that surrounds a material such as wood. It should be noted that RL propagation system shows higher ultimate load and less scatter in the curves than the TL direction. In addition, the stiffness of both groups is quite similar. Initial compliance (C_0) was calibrated using the straight branch of the

Table 2 Elastic properties of *Fagus sylvatica* L. used in numerical validation (Gómez-Royuela et al. 2021)

	E_L (MPa)	E_R (MPa)	E_T (MPa)	ν_{RL} (−)	ν_{TL} (−)	ν_{RT} (−)	G_{LR} (MPa)	G_{LT} (MPa)	G_{RT} (MPa)
Average	13,811	1590	832	0.51	0.44	0.32	1108	706	349
St. Dev	(1323)	(541)	(115)	(0.030)	(0.015)	(0.041)	(202)	(139)	(53)

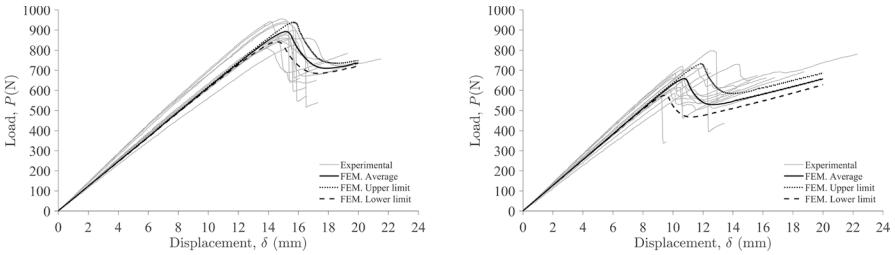

Fig. 11 Experimental and numerical P-δ curves from ENF tests in both RL (left) and TL (right) propagation systems

experimental P-δ curves. This procedure was addressed by linear regression applying the least-squares method obtaining coefficients of determination $R^2 > 0.999$. This value is used to fit E_f and thus avoid determining this property in each ENF test. The numerical curves obtained are consistent with the experimental ones. Furthermore, the numerical curves that represent the upper and lower limits of the shear traction-separation laws prove to be able to explain the variability of the wood.

In Fig. 11, it can be seen that both groups showed nonlinear behaviour before the curve reached the maximum load. This fact reveals that the influence of the FPZ developed ahead of the crack tip cannot be ignored. This is a typical behaviour of quasi-brittle materials such as wood. This phenomenon has also been observed by other authors for different wood species (Xavier et al. 2014b; Majano-Majano et al. 2020) and develops microcracks and fibre-bridging. This fact highlights the difficult task of accurately monitoring crack propagation during testing. In this sense, it seems appropriate to use the data reduction scheme based on an equivalent crack length concept to determine G_{II} (de Moura et al. 2006). Typical macroscopic visualisation of the different stages during crack propagation and the absolute displacement fields (X,Y,Z) of the crack tip corresponding to the maximum load state (point 3) are shown in Fig. 12a, b, respectively.

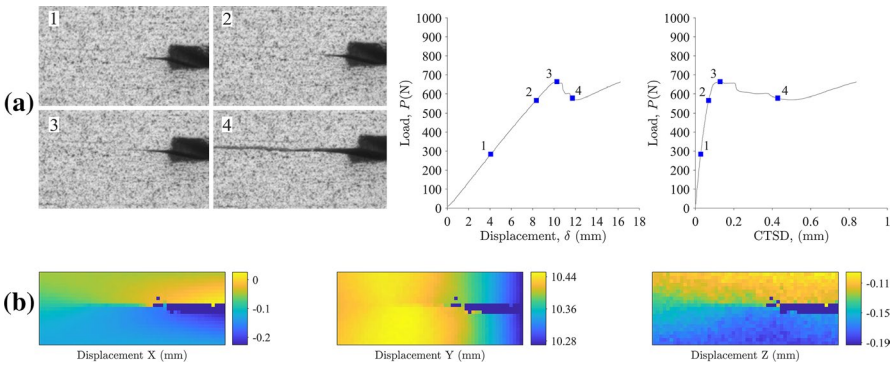

Fig. 12 **a** Macroscopic visualization of the different stages during crack propagation of the ENF TL 14 specimen and corresponding P-δ and P-CTSD curves; **b** absolute displacement fields (X,Y,Z) of the crack tip corresponding to point 3

From Fig. 12b, it can be deduced that the relative displacements in the Y and Z directions are negligible. This fact verifies that the choice of an ENF test set-up is adequate to evaluate fracture mode II, since the relevant displacements occur in the X direction. Therefore, disregarding the displacements in the Y and Z directions does not imply a significant error.

The experimental and numerical *R*-curves obtained from both crack propagation systems are shown in Fig. 13. These curves describe the evolution of G_{II} as a function of a_{eq} and are a useful tool to determine the critical fracture energy. According to them, G_{II} increases its value until it stabilizes, drawing a plateau. The transition between these two branches is not linear and, therefore, the influence of the FPZ can again be observed. However, in all cases, a horizontal branch is clearly evident, revealing stable crack growth. This fact verifies the suitability of the proposed method (CBBM).

G_{IIc} was determined as the average value of the points that belong to the horizontal branch. Numerical *R*-curves were obtained using the numerical *P*-δ curves. As can be observed, the numerical *R*-curves fit quite well with the experimental ones. In addition, the upper and lower limit curves encompass the dispersion of the experimental curves. These results justify the validity of the experimental procedure followed to obtain the fracture properties of *Fagus sylvatica* L.

The results of C_0, E_f, maximum load (P_{max}) and critical fracture energy (G_{IIc}) obtained from each ENF test in both RL and TL crack propagation systems are listed in Tables 3 and 4, respectively. Additionally, the mean, St. Dev., and coefficient of variation (CoV) values are also shown in those tables. The average value of the critical fracture energy obtained in RL system is significantly higher than in TL system. In particular, G_{IIc} in RL is twice that of G_{IIc} in TL. Furthermore, it should be noted that RL system shows less variability than TL. This can also be observed in Fig. 13. The maximum load (P_{max}) in RL is again higher than in TL but, in this case, the difference is only 32%. On the other hand, the differences of C_0 and E_f between the two fracture propagation systems are negligible.

The average value of G_{IIc} for *Fagus sylvatica* L. resulted in 2.29 N/mm (7.5% CoV) and 1.17 N/mm (22.1% CoV) in RL and TL crack propagation systems, respectively. This mean value in RL system is higher than that of other species such as *Pinus pinaster*, which according to Xavier et al. (2014b) has a G_{IIc} value

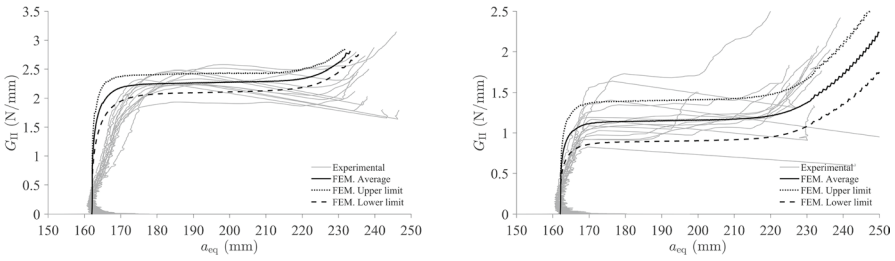

Fig. 13 R-curves from experimental and numerical ENF tests in both RL (left) and TL (right) crack propagation systems

Table 3 Density (ρ), corrected flexural modulus (E_f), maximum load (P_{max}), initial compliance (C_0) and critical fracture energy (G_{IIc}) obtained in RL crack propagation system from the *R*-curves

Specimen Ref	ρ (kg/m^3)	E_f (N/mm^2)	P_{max} (N)	C_0 (mm/N)	G_{IIc} (N/mm)
ENF_RL_01	718	13,561	810	0.016	1.91
ENF_RL_02	702	14,705	932	0.014	2.47
ENF_RL_03	711	13,050	898	0.016	2.29
ENF_RL_04	720	14,931	941	0.014	2.44
ENF_RL_05	678	13,591	876	0.016	2.25
ENF_RL_06	704	13,725	860	0.016	2.21
ENF_RL_07	664	13,096	858	0.016	2.55
ENF_RL_08	680	13,950	849	0.015	2.15
ENF_RL_09	741	14,741	955	0.014	2.42
ENF_RL_10	694	13,261	858	0.016	2.31
ENF_RL_11	746	15,452	942	0.014	2.22
ENF_RL_12	736	12,271	823	0.017	2.21
Average	708	13,861	883	0.015	2.29
St. Dev	26	928	49	0.001	0.17
CoV (%)	3.7%	6.7%	5.6%	6.8%	7.5%

Table 4 Density (ρ), corrected flexural modulus (E_f), maximum load (P_{max}), initial compliance (C_0) and critical fracture energy (G_{IIc}) obtained in TL crack propagation system from the *R*-curves

Specimen Ref	ρ (kg/m^3)	E_f (N/mm^2)	P_{max} (N)	C_0 (mm/N)	G_{IIc} (N/mm)
ENF_TL_01	757	12,329	731	0.018	1.71
ENF_TL_02	706	13,968	607	0.016	0.93
ENF_TL_03	735	14,256	572	0.015	0.83
ENF_TL_04	704	13,745	717	0.016	1.37
ENF_TL_05	820	15,311	687	0.014	1.06
ENF_TL_06	714	14,347	647	0.015	1.09
ENF_TL_07	715	15,057	703	0.014	1.17
ENF_TL_08	639	13,145	584	0.017	0.93
ENF_TL_09	672	13,342	616	0.016	1.01
ENF_TL_10	714	13,949	612	0.016	0.97
ENF_TL_11	772	15,056	798	0.015	1.60
ENF_TL_12	757	15,026	715	0.015	1.32
ENF_TL_13	707	14,962	720	0.014	1.21
ENF_TL_14	679	14,457	665	0.014	1.15
Average	721	14,211	670	0.015	1.17
St. Dev	45	865	66	0.001	0.26
CoV (%)	6.3%	6.1%	9.8%	6.8%	22.1%

of 1.15 N/mm, or *Eucalyptus globulus* L., which according to Majano-Majano et al. (2020) shows a G_{IIc} value of 1.54 N/mm.

Representative pictures of the specimen cross section and the fractured surface observed after crack propagation for both RL and TL propagation systems can be seen in Fig. 14. The fracture surface shows the rays crossing the wood in the radial direction, significantly affecting crack propagation in the RL system, which may explain the considerably higher values of fracture energy in RL with respect to the TL.

Shear traction-separation laws

The shear traction-separation law describes the evolution of τ as a function of CTSD (u). The area under the τ-u curve corresponds to the G_{IIc} value. To guarantee a correct characterization of the fracture properties in mode II, the presence of crack tip opening displacement (CTOD) during the test must be negligible, as otherwise part of the energy in mode I would be erroneously computed as fracture energy in mode II. This is a relevant aspect in the proposed data reduction scheme. To verify this, the influence of CTSD and CTOD was analysed as a function of the displacement (δ) applied to the ENF specimen. The CTOD measurement method is detailed in Gómez-Royuela et al. (2022). The results of a representative test in both RL and TL crack propagation systems are shown in Fig. 15.

The results reveal that CTOD in Mode I is negligible, which means that the ENF test set-up followed is appropriate to determine G_{IIc}, since the influence of Mode I on Mode II is very low. The evolution of G_{II} as a function of u from the experimental tests is shown in Fig. 16. Such evolution of G_{II} until reaching G_{IIc} (plateau value in the *R*-curves) is smoother in the RL crack propagation system compared to TL, where the transition is more abrupt. This fracture behaviour

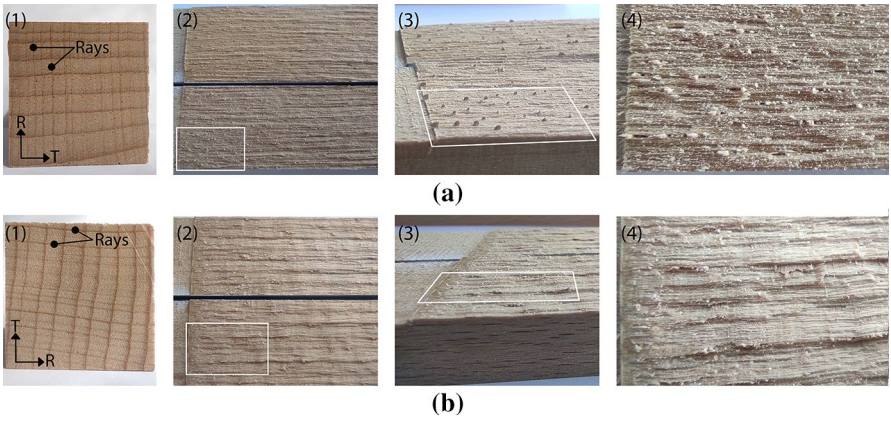

Fig. 14 Representative ENF specimens after testing in RL (**a**) and TL (**b**) crack propagation systems: (1) cross section; (2) fracture surface of the two parts of the specimen; (3) oblique view of the fracture surface; (4) detail of the fracture surface

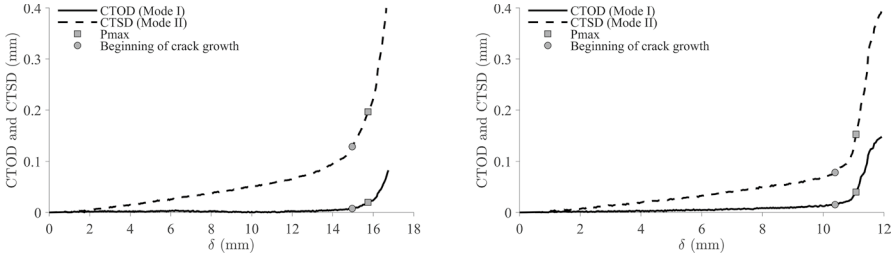

Fig. 15 Evaluation of normal CTOD (Mode I) and parallel CTSD (Mode II) with respect to applied displacement (δ) in both RL (left) and TL (right) crack propagation systems

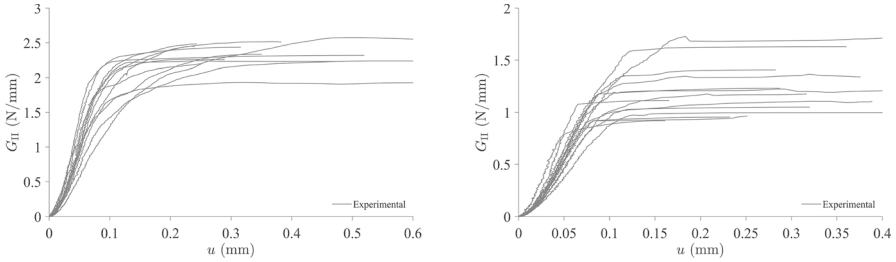

Fig. 16 Experimental G_{II}-u relationship in both the RL (left) and TL (right) crack propagation systems

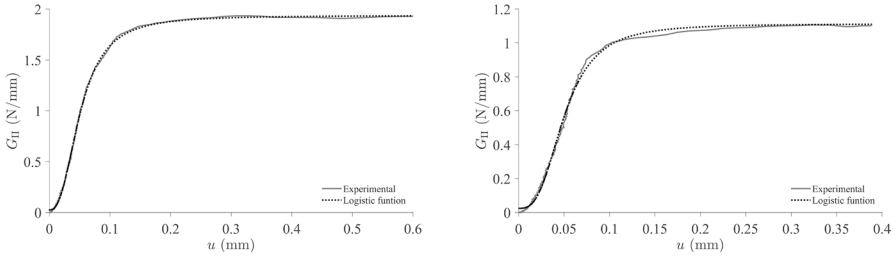

Fig. 17 Logistic function fitting to the ENF RL 01 (left) and ENF TL 06 (right) test results

reveals a greater influence of the FPZ in the RL system than in the TL, as a result of the toughening mechanisms such as microcracks and fibre-bridging.

With the main objective of reducing the noise from the experimental data and having a continuous and smooth function that can be derived to determine the shear traction–separation law, a logistic-type function (see "Experimental direct data reduction method" section) was fitted to each experimental G_{II}-u curve. A representative example in both crack propagation systems is shown in Fig. 17, from which a good approximation can be observed. It should be noted that the same set of data points considered for determining G_{IIc} according to "R-curves" section has been taken into account for this fitting procedure.

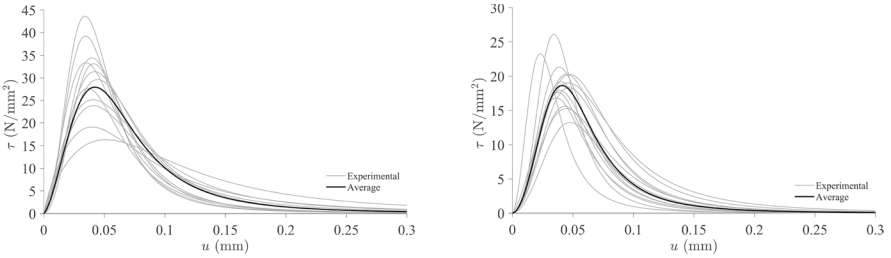

Fig. 18 Experimental (in grey) and average (in black) shear traction–separation laws in mode II for RL (left) and TL (right) crack propagation systems

All the experimental and the average shear traction-separation laws of both RL and TL fracture systems of *Fagus sylvatica* L. are shown in Fig. 18. Consistent results can be observed. The fitting parameters A_1, A_2, u_0 and p of the logistic curves for the RL and TL systems are listed in Tables 5 and 6, respectively. It should be clarified that the fit parameter A_2 is a direct estimate of G_{IIc}. Furthermore, $G_{\mathrm{law,II}}$ corresponds to the area under the logistic fit curve shown in Fig. 18. It should be noted that the mean curve (black line) shown in Fig. 18 is obtained using the average values of parameters A_1, A_2, u_0 and p listed in Tables 5 and 6. However, this mean curve does not result in the mean values of $G_{\mathrm{law,II}}$, τ_{u} and u_{u}. The average value of the maximum local shear stress (τ_{u}) in the RL direction resulted in 57% higher than in the TL.

Table 5 Parameters of the logistic function (A_1, A_2, u_0, p), maximum shear stress (τ_{u}), fracture energy of the shear traction–separation law ($G_{law,II}$) and maximum relative displacement (u_{u}) for RL crack propagation system

Specimen Ref	A_1 (N/mm)	A_2 (N/mm)	u_0 (mm)	p (−)	$G_{\mathrm{law,II}}$ (N/mm)	τ_{u} (N/mm^2)	u_{u} (mm)
ENF_RL_01	0.023	1.94	0.051	2.50	1.91	27.71	0.615
ENF_RL_02	0.034	2.54	0.062	2.51	2.48	29.65	0.383
ENF_RL_03	0.049	2.46	0.044	2.82	2.40	43.64	0.316
ENF_RL_04	0.044	2.60	0.060	2.47	2.48	31.38	0.243
ENF_RL_05	0.043	2.35	0.053	2.74	2.29	34.44	0.289
ENF_RL_06	0.000	2.27	0.075	1.87	2.23	19.09	0.617
ENF_RL_07	-0.008	2.68	0.102	1.80	2.58	16.35	0.627
ENF_RL_08	0.051	2.20	0.053	2.89	2.12	33.14	0.253
ENF_RL_09	0.007	2.65	0.069	2.05	2.45	25.17	0.240
ENF_RL_10	0.008	2.32	0.065	2.15	2.26	23.83	0.350
ENF_RL_11	0.046	2.31	0.049	2.46	2.25	33.40	0.482
ENF_RL_12	0.078	2.37	0.046	2.73	2.29	39.22	0.520
Average	0.031	2.39	0.061	2.42	2.31	29.75	0.411
St. Dev	0.025	0.21	0.016	0.37	0.18	7.89	0.153
CoV (%)	81.3%	8.8%	26.7%	15.3%	7.9%	26.5%	37.3%

Table 6 Parameters of the logistic function (A_1, A_2, u_0, p), maximum shear stress (τ_u), fracture energy of the shear traction–separation law ($G_{law,II}$) and maximum relative displacement (u_u) for TL crack propagation system

Specimen Ref	A_1 (N/mm)	A_2 (N/mm)	u_0 (mm)	p (−)	$G_{law,II}$ (N/mm)	τ_u (N/mm^2)	u_u (mm)
ENF_TL_01	0.008	1.77	0.067	2.41	1.76	19.04	0.434
ENF_TL_02	0.023	1.02	0.047	2.81	1.00	16.84	0.251
ENF_TL_03	0.023	0.95	0.031	2.70	0.92	23.30	0.161
ENF_TL_04	0.028	1.47	0.058	2.87	1.43	20.31	0.283
ENF_TL_05	0.034	1.19	0.041	3.39	1.15	26.11	0.165
ENF_TL_06	0.024	1.11	0.050	2.94	1.09	17.91	0.389
ENF_TL_07	0.038	1.28	0.049	3.00	1.24	21.34	0.288
ENF_TL_08	0.028	1.01	0.047	3.06	0.97	17.64	0.232
ENF_TL_09	0.028	1.08	0.055	2.91	1.05	15.61	0.320
ENF_TL_10	0.033	1.02	0.061	2.90	0.99	13.22	0.428
ENF_TL_11	0.040	1.70	0.063	2.69	1.64	20.28	0.360
ENF_TL_12	0.036	1.41	0.061	2.84	1.37	18.33	0.376
ENF_TL_13	0.036	1.26	0.052	2.86	1.24	19.18	0.471
ENF_TL_14	0.022	1.23	0.060	2.63	1.19	15.26	0.317
Average	0.029	1.25	0.053	2.86	1.22	18.88	0.320
St. Dev	0.008	0.26	0.010	0.23	0.25	3.34	0.096
CoV (%)	29.4%	20.5%	18.3%	7.9%	20.9%	17.7%	30.2%

In order to explain the inherent variability of this wood species, three numerical laws (average, upper limit and lower limit) were fitted to the experimental ones by applying the St. Dev. to the average law. The three logistic experimental laws (dashed lines) and exponential numerical laws fitted to the logistic experimental laws (solid lines) are shown in Fig. 19. It should be noted that the numerical laws implemented in FEA have the same G_{IIc} value as that determined according to the experimental method detailed in "Experimental direct data reduction method" section and obtained as follows: first, logistic curves (Eq. (12)) were obtained varying the values of parameters A_1, A_2, u_0 and p so that the area under the curves obtained

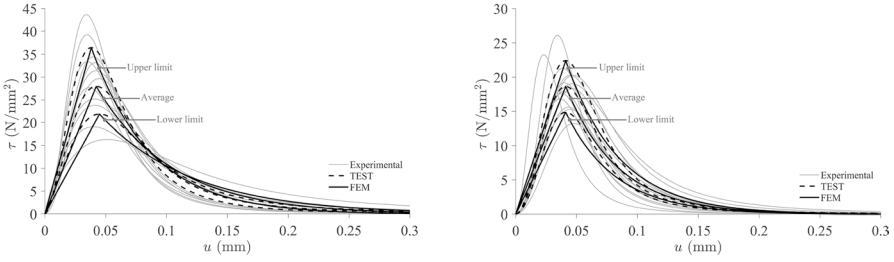

Fig. 19 Shear traction–separation laws: experimental laws (in grey); average, upper limit and lower limit of the logistic experimental laws (dashed lines); and exponential numerical laws fitted to the logistic experimental laws (solid lines). RL (left) and TL (right) crack propagation systems

(average law, upper limit law and lower limit law) is equal to G_{IIc} determined according to the experimental method. The average value of the parameters A_1, A_2, u_0 and p coincides with the average values given in Tables 5 and 6. The upper and lower limits of these parameters were determined by adding or subtracting a percentage (55% in this research work) of the St. Dev. to the mean values. The average value of G_{IIc} coincides with the average value shown in Table 3 and Table 4. Likewise, the upper and lower limits of G_{IIc} were determined by adding and subtracting, respectively, the St. Dev. to the average value of G_{IIc} (Tables 3, 4). Then, for simplicity in FEA, the logistic curves were simplified to exponential curves (see Fig. 10), so that the area under the exponential curve is equal to the area of the logistic curve, thus ensuring that the G_{IIc} implemented in the FEA is the same as that obtained from the experimental test. Furthermore, as a design criterion of the exponential curve, it was imposed that the point located at the tip of the logistic curve coincides with the point where the damage of the exponential curve begins (coordinates u_0, τ_u). The parameters defining each of the exponential laws are summarised in Table 1. The load–displacement curves and respective *R*-curves ensuing from the numerical laws were obtained and included for comparison with the experimental results in Figs. 11 and 13. Overall, it can be settled that the limiting curves define well the observed experimental range, which reinforces the suitability of the proposed methodology.

Conclusion

The experimental shear traction–separation law was obtained by the direct method, and CTSD was analysed by 3D DIC technique. This data reduction scheme was validated by finite element analysis implementing an exponential softening relationship. A cohesive zone model was used to reproduce crack propagation. Two additional shear traction–separation laws were implemented in the numerical validation, representing the upper and lower limits of the average law determined by applying the standard deviation to the mean value of G_{IIc}. These additional laws prove to be able to explain the variability of the wood.

The G_{II} fracture energy of European beech was derived by applying the CBBM, a data reduction method based on beam theory and on the equivalent crack length concept that only requires the P-δ curves data and not the measurement of crack propagation during the test, which would be a difficult task in wood and in the ENF test.

The average G_{IIc} values were approximately twice as high in the RL crack propagation system (2.29 N/mm) as in TL (1.17 N/mm). However, the maximum load reached in the RL direction only represented 32% more than in TL. The ultimate shear stress (τ_u) of the shear traction–separation law in the RL system resulting from a logistic curve fitting was 57% higher than in the TL direction.

The results of G_{IIc} and the shear traction–separation laws presented in this work are of great interest for the design of timber structures made of beech with the possibility of brittle failure involving mode II (e.g. dowel connections loaded at an angle to the grain, or beams with holes or notches), both for use in analytical expressions based on energy approaches for the prediction of load carrying capacity, and in

numerical FEM using cohesive zone models where damage initiation and propagation need to be analysed.

Acknowledgements Part of the work was undertaken during a short-term scientific stay by the first author at the Faculty of Engineering (University of Porto) in 2021, with the financial support provided by *Programa Propio de I+D+i 2021 de la Universidad Politécnica de Madrid*. The work is part of the R&D&I Project PID2020-112954RA-I00 funded by MCIN/AEI/10.13039/501100011033. The authors gratefully acknowledge also Fundação para a Ciência e a Tecnologia (FCT-MCTES) for the financial support of the *Laboratório Associado de Energia, Transportes e Aeronáutica* (LAETA) by the project UID/EMS/50022/2020 and the Research and Development Unit for Mechanical and Industrial Engineering (UNIDEMI) by the project UIDB/00667/2020.

Funding Open Access funding provided thanks to the CRUE-CSIC agreement with Springer Nature.

Declarations

Conflict of interest The authors declare that they have no conflict of interest.

References

Abaqus (2021) ABAQUS 2021 documentation, Dassault Systèmes Simulia Corp., Johnston, RI, USA.

Ardalany M, Deam B, Fragiacomo M (2012) Experimental results of fracture energy and fracture toughness of Radiata Pine laminated veneer lumber (LVL) in mode I (opening). Mater Struct Constr 45:1189–1205. https://doi.org/10.1617/s11527-012-9826-1

Ardalany M, Fragiacomo M, Moss P (2016) Modeling of laminated veneer lumber beams with holes using cohesive elements. J Struct Eng 142:04015102. https://doi.org/10.1061/(asce)st.1943-541x.0001338

Barenblatt GI (1962) The mathematical theory of equilibrium cracks in brittle fracture. Adv Appl Mech 7:55–129. https://doi.org/10.1016/S0065-2156(08)70121-2

Bažant ZP, Planas J (1998) Fracture and size effect in concrete and other quasibrittle materials. CRC, Boca Raton

Boström L (1992) Method of determination of the softening behaviour of wood and the applicability of a nonlinear fracture mechanics model. Lund PhD:148

Brunner AJ, Blackman BRK, Davies P (2008) A status report on delamination resistance testing of polymer-matrix composites. Eng Fract Mech 75:2779–2794. https://doi.org/10.1016/j.engfracmech.2007.03.012

Caldeira T (2011) Caracterização experimental e numérica do comportamento frágil de ligações com cavilhas em estruturas de madeira (in English: Experimental and numerical characterisation of the brittle behaviour of dowel connections in timber structures). Dissertation, Universidade de Trás-os-Montes e Alto Douro.

Coureau JL, Morel S, Gustafsson PJ, Lespine C (2007) Influence of the fracture softening behaviour of wood on load-COD curve and R-curve. Mater Struct Constr 40:97–106. https://doi.org/10.1617/s11527-006-9122-z

Cramer SM, Pugel AD (1987) Compact shear specimen for wood mode II fracture investigations. Int J Fract 35:163–174. https://doi.org/10.1007/BF00015586

Crespo J, Majano-Majano A, Xavier J, Guaita M (2018) Determination of the resistance-curve in *Eucalyptus globulus* through double cantilever beam tests. Mater Struct 51:77. https://doi.org/10.1617/s11527-018-1209-9

de Moura MFSF, Silva MAL, de Morais AB, Morais JJL (2006) Equivalent crack based mode II fracture characterization of wood. Eng Fract Mech 73:978–993. https://doi.org/10.1016/j.engfracmech.2006.01.004

de Moura MFSF, Campilho RDSG, Gonçalves JPM (2009a) Pure mode II fracture characterization of composite bonded joints. Int J Solids Struct 46:1589–1595. https://doi.org/10.1016/j.ijsolstr.2008.12.001

de Moura MFSF, Silva MAL, Morais JJL et al (2009b) Data reduction scheme for measuring G_{IIc} of wood in end-notched flexure (ENF) tests. Holzforschung 63:99–106. https://doi.org/10.1515/HF.2009.022

de Moura MFSF, Fernandes R, Silva FGA, Dourado N (2015) Mode II fracture characterization of a hybrid cork/carbon-epoxy laminate. Compos Part B Eng 76:44–51. https://doi.org/10.1016/j.compositesb.2015.02.010

de Moura MFSF, Silva MAL, Morais JJL, Dourado N (2018) Mode II fracture characterization of wood using the Four-Point End-Notched Flexure (4ENF) test. Theor Appl Fract Mech 98:23–29. https://doi.org/10.1016/j.tafmec.2018.09.008

Dias GF, de Moura MFSF, Chousal JAG, Xavier J (2013) Cohesive laws of composite bonded joints under mode I loading. Compos Struct 106:646–652. https://doi.org/10.1016/j.compstruct.2013.07.027

Dourado N, de Moura MFSF, de Morais AB, Pereira AB (2012) Bilinear approximations to the mode II delamination cohesive law using an inverse method. Mech Mater 49:42–50. https://doi.org/10.1016/j.mechmat.2012.02.004

Dourado N, Pereira FAM, de Moura MFSF et al (2013) Bone fracture characterization using the end notched flexure test. Mater Sci Eng C 33:405–410. https://doi.org/10.1016/j.msec.2012.09.006

Dourado N, de Moura MFSF, Morel S, Morais J (2015) Wood fracture characterization under mode I loading using the three-point-bending test. Experimental investigation of *Picea abies* L. Int J Fract 194:1–9. https://doi.org/10.1007/s10704-015-0029-y

Dourado N, Silva FGA, de Moura MFSF (2018) Fracture behavior of wood-steel dowel joints under quasi-static loading. Constr Build Mater 176:14–23. https://doi.org/10.1016/j.conbuildmat.2018.04.230

Dugdale DS (1960) Yielding of steel. J Mech Phys Solids 8:100–104

Ehart RJA, Stanzl-Tschegg SE, Tschegg EK (1998) Crack face interaction and mixed mode fracture of wood composites during mode III loading. Eng Fract Mech 61:253–278. https://doi.org/10.1016/S0013-7944(98)00033-2

Ehrhart T, Steiger R, Frangi A (2021) European beech glued laminated timber. Bautechnik 98:104–114

Enders-Comberg M, Frese M, Blaß HJ (2015) Beech LVL for trusses and reinforced glulam. Bautechnik 92:9–17

Franke B, Quenneville P (2011) Numerical modeling of the failure behavior of dowel connections in wood. J Eng Mech 137:186–195

Franke, Quenneville (2012) Prediction of the load capacity of dowel-type connections loaded perpendicular to grain for solid wood and wood products. Proc 12th World Conf Timber Eng New Zeland

Frühmann K, Reiterer A, Tschegg EK, Stanzl-Tschegg SS (2002a) Fracture characteristics of wood under mode I, mode II and mode III loading. Philos Mag A Phys Condens Matter, Struct Defects Mech Prop 82:3289–3298. https://doi.org/10.1080/01418610208240441

Frühmann K, Tschegg EK, Dai C, Stanzl-Tschegg SE (2002b) Fracture behaviour of laminated veneer lumber under mode I and III loading. Wood Sci Technol 36:319–334. https://doi.org/10.1007/s00226-002-0142-8

GOM Metrology GmbH (2007) ARAMIS commercial software. Aramis 6.0.2; GOM Metrology GmbH: Braunschweig, Germany

Gómez-Royuela JL, Majano-Majano A, Lara-Bocanegra AJ, Reynolds TPS (2021) Determination of the elastic constants of thermally modified beech by ultrasound and static tests coupled with 3D digital image correlation. Constr Build Mater. https://doi.org/10.1016/j.conbuildmat.2021.124270

Gómez-Royuela JL, Majano-Majano A, Lara-Bocanegra AJ et al (2022) Evaluation of *R*-curves and cohesive law in mode I of European beech. Theor Appl Fract Mech 118:103220. https://doi.org/10.1016/j.tafmec.2021.103220

Gonçalves JPM, De Moura MFSF, De Castro PMST, Marques AT (2000) Interface element including point-to-surface constraints for three-dimensional problems with damage propagation. Eng Comput (swansea, Wales) 17:28–47. https://doi.org/10.1108/02644400010308053

Griffith AA (1921) The phenomena of rupture and flow in solids. Philos Trans R Soc London Ser a, Contain Pap a Math or Phys Character 221:163–198

Hillerborg A, Modéer M, Petersson P-E (1976) Analysis of crack formation and crack growth in concrete by means of fracture mechanics and finite elements. Cem Concr Res 6:773–782

Inglis CE (1913) Stress in a plate due to the presence of cracks and sharp corners. Spring Meet. Fifty-fourth Sess. Inst. Nav. Archit. 219–241

Irwin GR, Washington DC (1957) Analysis of stresses and strains near the end of a crack traversing a plate. J Appl Mech 24:361–364

Kovryga A, Stapel P, van de Kuilen JWG (2020) Mechanical properties and their interrelationships for medium-density European hardwoods, focusing on ash and beech. Wood Mater Sci Eng 15:289–302. https://doi.org/10.1080/17480272.2019.1596158

Leffler K, Alfredsson KS, Stigh U (2007) Shear behaviour of adhesive layers. Int J Solids Struct 44:530–545. https://doi.org/10.1016/j.ijsolstr.2006.04.036

Luimes RA, Suiker ASJ, Verhoosel CV et al (2018) Fracture behaviour of historic and new oak wood. Wood Sci Technol 52:1243–1269. https://doi.org/10.1007/s00226-018-1038-6

Majano-Majano A, Hughes M, Fernandez-Cabo JL (2012) The fracture toughness and properties of thermally modified beech and ash at different moisture contents. Wood Sci Technol 46:5–21. https://doi.org/10.1007/s00226-010-0389-4

Majano-Majano A, Lara-Bocanegra AJ, Xavier J, Morais J (2019) Measuring the cohesive law in mode I loading of *Eucalyptus globulus*. Materials (basel) 12:23. https://doi.org/10.3390/ma12010023

Majano-Majano A, Lara-Bocanegra AJ, Xavier J, Morais J (2020) Experimental evaluation of mode II fracture properties of *Eucalyptus globulus* L. Materials (basel) 13:1–13. https://doi.org/10.3390/ma13030745

Majano-Majano A, Lara-Bocanegra AJ, Xavier J, Guaita M (2022) Splitting capacity of *Eucalyptus globulus* beams loaded perpendicular to the grain by connections. Mater Struct 55:147. https://doi.org/10.1617/s11527-022-01983-z

Oliveira J, Xavier J, Pereira F et al (2021) Direct evaluation of mixed mode I+II cohesive laws of wood by coupling mmb test with dic. Materials (Basel) 14:374. https://doi.org/10.3390/ma14020374

Ozyhar T, Hering S, Niemz P (2013a) Moisture-dependent orthotropic tensioncompression asymmetry of wood. Holzforschung 67:395–404. https://doi.org/10.1515/hf-2012-0089

Ozyhar T, Hering S, Niemz P (2013b) Viscoelastic characterization of wood: Time dependence of the orthotropic compliance in tension and compression. J Rheol (n Y N y) 57:699–717. https://doi.org/10.1122/1.4790170

Ozyhar T, Hering S, Sanabria SJ, Niemz P (2013c) Determining moisture-dependent elastic characteristics of beech wood by means of ultrasonic waves. Wood Sci Technol 47:329–341. https://doi.org/10.1007/s00226-012-0499-2

Pereira FAM, de Moura MFSF, Dourado N et al (2018) Determination of mode II cohesive law of bovine cortical bone using direct and inverse methods. Int J Mech Sci 138–139:448–456. https://doi.org/10.1016/j.ijmecsci.2018.02.009

Petersson P-E (1981) Crack growth and development of fracture zones in plain concrete and similar materials. Rep TVBM, Div Build Mater Lund Inst Technol Lund, Sweden

Qiao P, Wang J, Davalos JF (2003) Analysis of tapered ENF specimen and characterization of bonded interface fracture under mode-II loading. Int J Solids Struct 40:1865–1884. https://doi.org/10.1016/S0020-7683(03)00031-3

Rautenstrauch, K and Franke, B and Franke, S and Schober, KU (2008) A new design approach for end-notched beams: View in code. In: Paper No. CIB-W18/41–6–2, Proc., Meeting

Rice JR (1968) A path independent integral and the approximate analysis of strain concentration by notches and cracks. J Appl Mech Trans ASME 35:379–388. https://doi.org/10.1115/1.3601206

Rodbard D (1974) Statistical quality control and routine data processing for radioimmunoassays and immunoradiometric assays. Clin Chem 20:1255–1270. https://doi.org/10.1093/clinchem/20.10.1255

Rodbard D, Hutt DM (1974) Statistical analysis of radioimmunoassay and immunoradiometric (labeled antibody) assays:A generalized, weighted, iterative, least-squares method for logistic curve fitting. In: Symposium on RIA and Related Procedures in Medicine, Int. Atomic Energy Agency. New York: Uniput, pp 209–233

Schuecker C, Davidson BD (2000) Evaluation of the accuracy of the four-point bend end-notched flexure test for mode II delamination toughness determination. Compos Sci Technol 60:2137–2146. https://doi.org/10.1016/S0266-3538(00)00113-5

Sousa AMR, Xavier J, Vaz M et al (2010) Cross-correlation and differential technique combination to determine displacement fields. Strain 47:87–98. https://doi.org/10.1111/j.1475-1305.2010.00740.x

Sousa AMR, Xavier J, Morais JJL et al (2011) Processing discontinuous displacement fields by a spatio-temporal derivative technique. Opt Lasers Eng 49:1402–1412. https://doi.org/10.1016/j.optlaseng.2011.07.007

Stanzl-Tschegg SE, Tan DM, Tschegg EK (1995) New splitting method for wood fracture characterization. Wood Sci Technol 29:31–50. https://doi.org/10.1007/BF00196930

Sutton MA, Orteu J-J, Schreier HW (2009) Image correlation for shape, motion and deformation measurements. Springer, New York.

Vasic S, Smith I (2002) Bridging crack model for fracture of spruce. Eng Fract Mech 69:745–760. https://doi.org/10.1016/S0013-7944(01)00091-1

Xavier J, Oliveira M, Monteiro P et al (2014a) Direct evaluation of cohesive law in mode I of *Pinus pinaster* by Digital image correlation. Exp Mech 54:829–840. https://doi.org/10.1007/s11340-013-9838-y

Xavier J, Oliveira M, Morais JJL, De Moura MFSF (2014b) Determining mode II cohesive law of *Pinus pinaster* by combining the end-notched flexure test with digital image correlation. Constr Build Mater 71:109–115. https://doi.org/10.1016/j.conbuildmat.2014.08.021

Yoshihara H (2004) Mode II R-curve of wood measured by 4-ENF test. Eng Fract Mech 71:2065–2077. https://doi.org/10.1016/j.engfracmech.2003.09.001

Yoshihara H, Kawamura T (2006) Mode I fracture toughness estimation of wood by DCB test. Compos Part A Appl Sci Manuf 37:2105–2113. https://doi.org/10.1016/j.compositesa.2005.12.001

Yoshihara H, Ohta M (2000) Measurement of mode II fracture toughness of wood by the end-notched flexure test. J Wood Sci. https://doi.org/10.1007/BF00766216

Authors and Affiliations

José Luis Gómez-Royuela[1] · Almudena Majano-Majano[1] · Antonio José Lara-Bocanegra[1] · José Xavier[2] · M. F. S. F. de Moura[3]

Almudena Majano-Majano
almudena.majano@upm.es

Antonio José Lara-Bocanegra
antoniojose.lara@upm.es

José Xavier
jmc.xavier@fct.unl.pt

M. F. S. F. de Moura
mfmoura@fe.up.pt

[1] Department of Building Structures and Physics, ETS of Architecture, Universidad Politécnica de Madrid (UPM), Avda. Juan de Herrera, 4, 28040 Madrid, Spain

[2] UNIDEMI, Department of Mechanical and Industrial Engineering, NOVA School of Science and Technology, Universidade NOVA de Lisboa, 2829-516 Caparica, Portugal

[3] Departamento de Engenharia Mecânica e Gestão Industrial, Faculdade de Engenharia da Universidade do Porto, Rua Dr. Roberto Frias, 4200-465 Porto, Portugal

Capacidad de carga frente a la hienda de uniones con clavijas

Este trabajo se presenta en la publicación IV.

Publicación IV

Experimental and numerical research on the splitting capacity of European beech beams loaded perpendicular to the grain by connections: influence of different geometrical parameters.

José Luis Gómez-Royuela, Almudena Majano-Majano, Antonio José Lara-Bocanegra, José Xavier, M. F. S. F. de Moura.

Applied Sciences, 14: 900, 2024
DOI: https://doi.org/10.3390/app14020900
Q1 (JCR). Impact factor: 2,5

applied sciences

MDPI

Article

Experimental and Numerical Research on the Splitting Capacity of European Beech Beams Loaded Perpendicular to the Grain by Connections: Influence of Different Geometrical Parameters

José Luis Gómez-Royuela [1], Almudena Majano-Majano [1], Antonio José Lara-Bocanegra [1], José Xavier [2,3,*] and Marcelo F. S. F. de Moura [4]

[1] Department of Building Structures and Physics, ETS of Architecture, Universidad Politécnica de Madrid (UPM), Avda. Juan de Herrera 4, 28040 Madrid, Spain; joseluis.gomez.royuela@upm.es (J.L.G.-R.); almudena.majano@upm.es (A.M.-M.); antoniojose.lara@upm.es (A.J.L.-B.)
[2] UNIDEMI, Department of Mechanical and Industrial Engineering, NOVA School of Science and Technology, Universidade NOVA de Lisboa, 2829-516 Caparica, Portugal
[3] Laboratório Associado de Sistemas Inteligentes, LASI, 4800-058 Guimarães, Portugal
[4] Department of Mechanical Engineering and Industrial Management, Faculty of Engineering, University of Porto, Rua Dr. Roberto Frias, 4200-465 Porto, Portugal; mfmoura@fe.up.pt
* Correspondence: jmc.xavier@fct.unl.pt

Abstract: In the present work, single- and double-dowel joints following different geometric configurations are experimentally and numerically investigated to derive the splitting behaviour of beech wood (*Fagus sylvatica* L.), one of the most widespread hardwood species in Europe for structural purposes. The influence of the spacing between dowels, their distance to the supports, and the slenderness of the beams is analysed. The correlation of the experimental failure loads with those predicted numerically by cohesive zone finite element-based models using the fracture properties of the species is discussed. The experimental results are also compared with those obtained from the normative expression included in Eurocode 5 and two other design models reported in the literature. The splitting failure loads predicted by both the analytical and numerical models were found to be conservative, the latter being closer to the experimental values.

Keywords: dowel connection; hardwood; numerical model; fracture mechanics; timber structures; Fagus sylvatica; cohesive zone modelling

Citation: Gómez-Royuela, J.L.; Majano-Majano, A.; Lara-Bocanegra, A.J.; Xavier, J.; de Moura, M.F.S.F. Experimental and Numerical Research on the Splitting Capacity of European Beech Beams Loaded Perpendicular to the Grain by Connections: Influence of Different Geometrical Parameters. *Appl. Sci.* **2024**, *14*, 900. https://doi.org/10.3390/app14020900

Academic Editor: Laurent Daudeville

Received: 19 December 2023
Revised: 17 January 2024
Accepted: 18 January 2024
Published: 20 January 2024

1. Introduction

In recent decades, there has been significant growth in the development of renewable and environmentally sustainable building materials, spurred by the imperative to address the impacts of climate change. The building sector is a significant consumer of primary energy, contributing significantly to the release of substantial amounts of carbon dioxide (CO_2) into the atmosphere [1,2]. In this context, wood and wood-based products have attracted great interest in architecture and civil engineering because of their renewable resource potential when sustainably managed [3], their savings in primary energy and CO_2 emissions during the manufacturing process [1,4], and the added value they bring to buildings. Furthermore, among the main structural building materials, wood is the only one composed of substantial amounts of carbon captured from the atmosphere during the tree growth process (around 50% of its dry weight) [5]. Currently, most structural timber products are made from softwoods, but in recent years, there has been growing interest in the use of hardwoods for structural purposes. The reasons for this are multiple and may be due, among others, to the under-use of aged hardwood forests and the high mechanical properties compared to softwoods [6,7].

In this respect, *Fagus sylvatica* L., or European beech, is one of the most important and widespread hardwood species in Europe (from southern Scandinavia to northern Sicily

and from northwestern Turkey to northwestern Spain), with an average height of about 30–40 m. [8,9]. The large beech reserves available in European forests have aroused the interest of the scientific community. Several investigations have been carried out on this material for structural purposes, both on solid wood in terms of determining its elastic constants [10–13], mechanical properties [14–16], or fracture behaviour [17,18], as well as on structural products made of beech such as glulam [19] or laminated veneer lumber (LVL) [20]. European beech also offers good strength and stiffness compared to softwoods, which makes it an excellent choice for the design of timber structures, especially in the assessment of high-performance scenarios, such as connections with fasteners or large span elements, allowing for a reduction in the cross-section of the main members.

Mechanical connections with steel dowel-type fasteners are among the most widely used connections in timber structures [21–23] because of their simplicity of manufacture and assembly and the possibility of being designed to have a ductile connection failure. However, there are certain situations where brittle failure of the timber member may occur at load levels below the bearing capacity for desirable ductile behaviour, especially in designs with connections loaded at an angle to grain where tension stresses perpendicular to the grain are induced, for which timber inherently exhibits relatively low strength and stiffness. This brittle splitting failure is, therefore, one of the most critical in timber structures and deserves particular concern in design.

Eurocode 5 [24] includes the so-called European Yielding Model (EYM) originally formulated by Johansen [25], which is used to predict the load carrying capacity of dowel-type connections subjected to shear force. This model always considers the plastic behaviour of timber and also the possible plastic behaviour of the dowel depending on the failure mode of the connection. However, this model can dangerously overestimate the ultimate load in connections if splitting failure occurs. Concerning the prediction of the splitting capacity of connections loaded at an angle to the grain, Eurocode 5 provides a relatively simple relationship developed theoretically by Van der Put and Leijten [26,27] following an energetic approach in the framework of linear elastic fracture mechanics (LEFM). The expression only applied to softwood and considered the timber member width, the distance from the fastener to the loaded edge of the member, and the ratio of the latter to the member depth (commonly known as the α parameter). It is widely demonstrated and specified in some design codes that when $\alpha \geq 0.7$, splitting may be neglected. The expression also includes a constant value arising from the fracture energy calibration parameter. However, the scientific literature suggests that this value is a considerable overestimation for some wood species commonly used in Europe [28]. The expression disregards the influence of other parameters, such as the number and geometry of groups of fasteners.

Further experimental and numerical research has been carried out to propose alternative analytical formulations to the normative expression, taking into account the effect of different geometrical parameters of the connection and material properties. Most of these experimental studies have been conducted on softwoods, e.g., the first studies reported in [29–32] used to calibrate the analytical model proposed by Van der Put and Leijten or later relevant studies on sawn spruce and glulam [33–36], radiata pine LVL [37], southern pine LVL [38,39], and southern pine MSR lumber [38]. However, very little research has focused on the splitting behaviour of dowel connections in hardwood species. Recent studies can be found on *Eucalyptus globulus* sawn wood [40] and yellow poplar PSL [38]. There is a work on beech beams loaded perpendicularly to the grain by connections, although the α values considered were higher than 0.7 [23].

In terms of numerical investigations, several authors have developed finite element models (FEMs) to realistically replicate the behaviour of structural timber elements with fastener connections [22,34,41–43]. One method involves utilising cohesive zone models (CZMs) incorporating traction–separation laws, which are treated as inherent material properties. These models require predefining possible damage paths. Strength criteria based on limit stresses are applied to indicate the onset of the damage. Damage evolves as described by the traction–separation law following the principles of fracture mechanics.

This method was first applied to wood in [44], and its capability has been sufficiently demonstrated in subsequent studies [41,42,45], as well as in previous work by the authors focusing on the simulation of crack propagation in double cantilever beams (DCBs) [17] and end-notched flexure (ENF) tests [18] in beech wood, offering good agreement with experimental results.

The main objective of the present research is to determine the splitting capacity of *Fagus Sylvatica* L. (European beech) solid wood beams loaded perpendicular to the grain by connections, considering α values lower than 0.7. An experimental campaign is carried out on connections consisting of one and two dowels placed at various positions along beams of different lengths and depths aiming to study the influence of these geometrical parameters. Cohesive zone finite element-based models using the fracture properties of the species are also developed, which are capable of reproducing crack development. Finally, the results are compared with the theoretical splitting failure loads obtained by applying the analytical expression included in Eurocode 5 [24] and two other alternative design models reported in the literature [46,47], which offer a more complete formulation regarding the consideration of different geometrical parameters of the connection.

2. Materials and Methods

2.1. Experimental Test

European beech (*Fagus sylvatica* L.) solid wood from Austria was used in the experimental tests. The boards were obtained from heartwood and cut in the tangential direction. Before testing, the boards were conditioned in a climatic chamber at 20 °C and 65% relative humidity until equilibrium moisture content (MC) was reached. After conditioning, all boards were visually graded according to the German standard DIN 4074-5:2008 [48]. The specimens were free from knots and cracks. All specimens met the requirements for the LS13 strength class [48], which would allow a strength class assignment of D40 according to EN 1912:2012 [49]. MC was determined using the oven-drying method using a section taken from each board following EN 13183-1:2002 [50]. This resulted in an average value of 10.3%. The density (ρ) was also measured using a section taken from each board according to EN 408:2012 [51] and adjusted to the reference moisture content of 12% [52], giving a mean value of 732 kg/m^3.

The beams were subjected to 3- or 4-point bending tests depending on the connection layout studied (Figure 1), at a constant crosshead displacement rate set between 0.75 and 3.50 mm/min, so that failure took place in approximately 5 min.

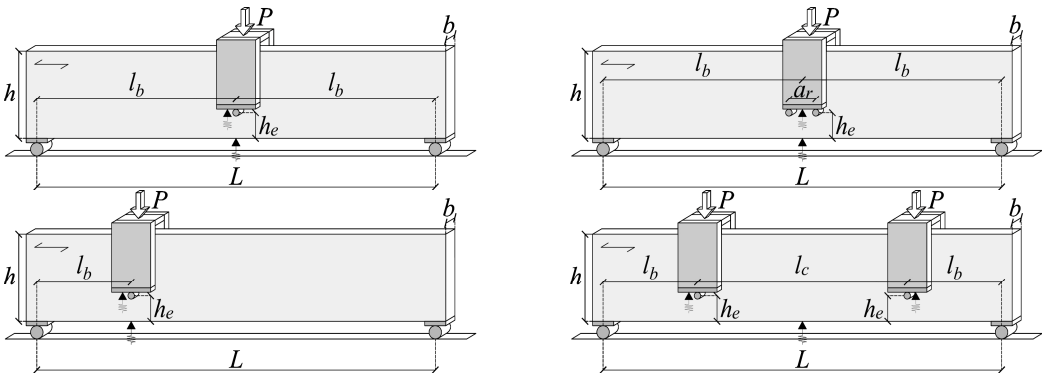

Figure 1. Bending test set-ups.

Displacements (δ) were measured using linear variable differential transformers (LVDTs) and recorded at a frequency of 1 Hz during the tests. To analyse joint behaviour and dowel sliding, LVDTs were placed both at the bottom of the loading plates, as close as possible to the dowel, and at the bottom of the beam (black triangles in Figure 1). Holes of the same diameter as the dowels were drilled in the timber beams so that there was no clearance between them.

The experimental programme was divided into two groups of specimens according to the beam depth (h): group 1 with h = 100 mm and group 2 with h = 200 mm. The beam width (b) was 48 mm for all specimens. In all tests, dowels with a diameter (d) of 16 mm and 120 mm length made of S355-grade steel were used. With this diameter, the dowel slenderness (b/d) was small, and steel yielding was avoided.

The distance to the loaded edge (h_e) was set at $4d$ (minimum distance established in Eurocode 5 [24]), remaining constant in all tests, resulting in joints with two different values of the α parameter ($\alpha = h_e/h$), namely 0.64 for group 1 and 0.32 for group 2. In each of the groups, beams with one dowel (1D) and two dowels (2D) were tested in order to analyse the influence of the number of dowels and connections on the splitting capacity.

As a reference configuration, a span L of 950 mm (1000 mm specimen length) and one connection with 1D and 2D (spaced $a_r = 4d$ apart) located at mid-span were established. In order to analyse the influence of the distance l_b from the connection to the support and the distance l_c between the connections on the splitting capacity, different l_b values were considered (360 mm, 240 mm, and 120 mm), which corresponded to support spacings of approximately 0.38, 0.25, and 0.13 times the span. In order to also analyse the influence of the slenderness of the beam on the splitting capacity, beams with the connection at mid-span but with L of 450 mm (500 mm specimen length) were also tested. Figure 2 illustrates the set of reference configurations and their variations.

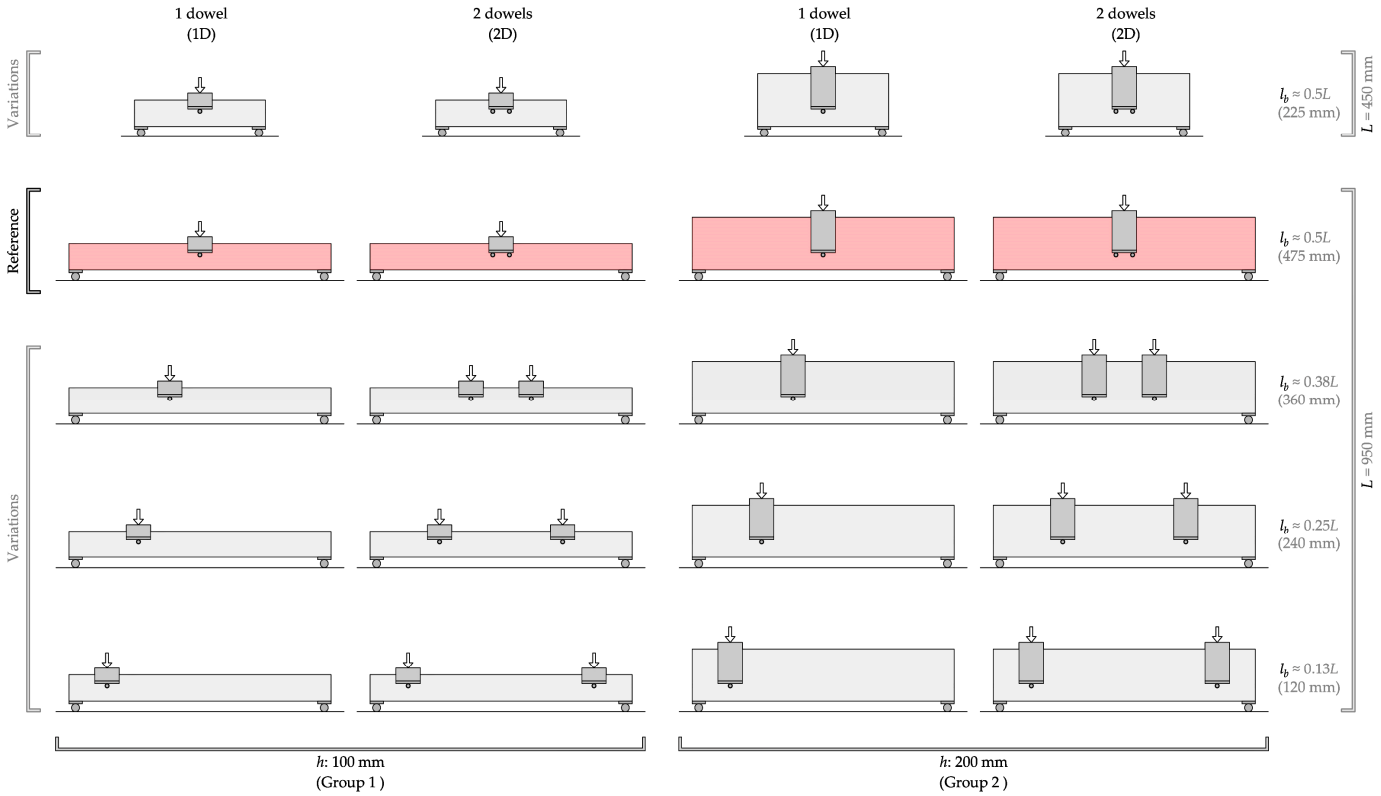

Figure 2. Experimental configurations tested: reference configurations (in red) with one- and two-dowel connections placed at mid-span for each beam depth group and variations (in grey) regarding connection position and beam slenderness.

Table 1 summarises, for each series of tests, the geometrical parameters of the beam (span and depth), as well as the density and moisture content, the position of the connection in terms of distance to the support l_b and the spacing between connections l_c (in case of two connections), the position of the connection in relation to the beam depth by means of the α parameter, and the number of replicates tested.

2.2. Numerical Analysis

Numerical finite element analyses of all configurations studied in the experimental campaign (Figure 2) were carried out using ABAQUS v2021 software [53]. Brittle splitting failure is addressed as simply as possible and in a way that provides sufficiently safe results from a structural design point of view.

Since the dowel had low slenderness, it showed very small deformations, and the authors did not observe any yield hinges, so a simplified 2D model was developed in which a cohesive zone model (CZM) was implemented to reproduce the crack growth. The timber beam and the steel elements (supports and dowels) were defined by 8-node quadratic plane stress elements (CPS8R). The model mesh was refined in the crack propagation region, as well as in the dowel and support locations (Figure 3a,b), using a minimum and maximum mesh size of 1 mm × 1 mm and 4 mm × 4 mm, respectively. To simulate crack growth and propagation, 6-node quadratic cohesive surfaces were used together with the Newton–Cotes integration scheme [54]. To reduce the computational time and in accordance with the findings in [55], only one fracture plane at mid-height of the dowel was modelled. The contact between the steel elements and wood was introduced using 6-node quadratic contact surfaces with a friction coefficient of 0.15 [56]. The analyses were carried out considering a non-linear geometrical behaviour of the beams. The Newton–Raphson convergence method was applied to solve the systems of non-linear equilibrium equations. An isotropic material was considered for steel elements and an orthotropic material for wood. The yielding behaviour of wood was neglected for the sake of the simplification intended by the model. Consequently, a linear elastic constitutive response of the materials was assumed. The application of the load was performed by a uniform vertical displacement imposed at the central node of the dowels in the range of 6 and 20 mm introduced in increments of no more than 0.01 mm to reproduce stable crack growth and to obtain accurate results.

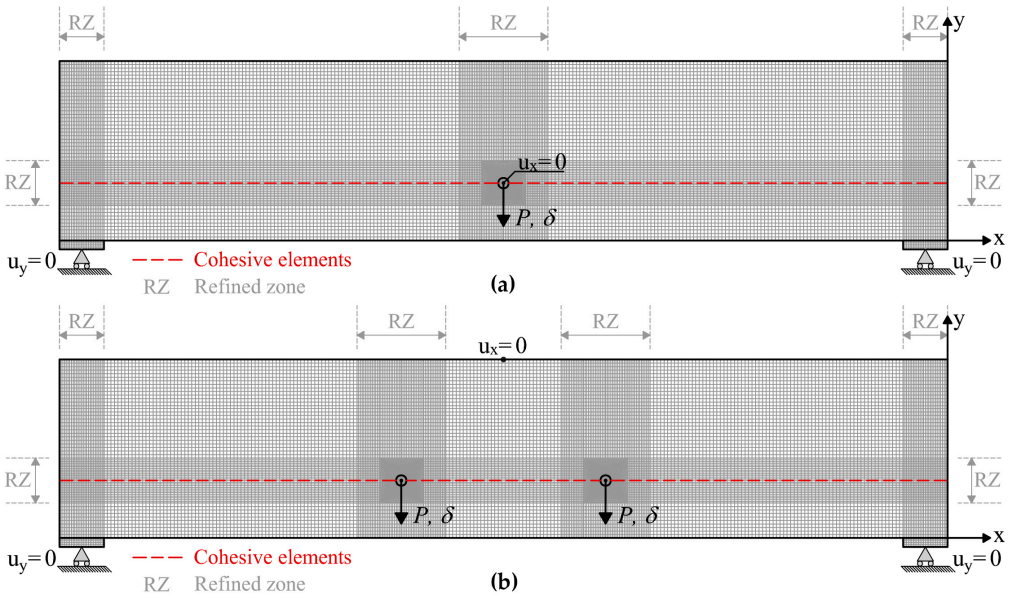

Figure 3. Numerical model: (**a**) single connection; (**b**) double connection.

Table 1. Experimental test program.

	Number of Dowels (no.dowels)	Span L (mm)	Connection–Support Distance l_b (mm)	Series h/no.dowels/L/l_b	Number of Specimens	Density ρ (kg/m^3)	Moisture Content (%)	Connection Spacing l_c (mm)	α h_e/h
Group 1 (h: 100 mm)	1D	450	225	100/1D/450/0.5L	4	747	9.7	-	0.64
		950	475	100/1D/950/0.5L	4	734	11.1		
			360	100/1D/950/0.38L	3	708	10.4		
			240	100/1D/950/0.25L	3	727	10.4		
			120	100/1D/950/0.13L	3	730	10.1		
	2D	450	225	100/2D/450/0.5L	4	727	10.2	-	0.64
		950	475	100/2D/950/0.5L	4	710	10.7	230	
			360	100/2D/950/0.38L	3	748	10.7		
			240	100/2D/950/0.25L	3	738	11.5	470	
			120	100/2D/950/0.13L	3	717	10.9	710	
Group 2 (h: 200 mm)	1D	450	225	200/1D/450/0.5L	4	756	9.7	-	0.32
		950	475	200/1D/950/0.5L	3	744	10.0		
			360	200/1D/950/0.38L	3	716	9.7		
			240	200/1D/950/0.25L	3	730	10.1		
			120	200/1D/950/0.13L	3	758	9.9		
	2D	450	225	200/2D/450/0.5L	4	730	9.6	-	0.32
		950	475	200/2D/950/0.5L	4	713	10.0	230	
			360	200/2D/950/0.38L	3	741	10.0		
			240	200/2D/950/0.25L	3	742	10.9	470	
			120	200/2D/950/0.13L	3	716	10.3	710	

A bilinear cohesive law model with a linear softening relationship was used to reproduce the fracture process in mixed-mode I + II (Figure 4) [57,58].

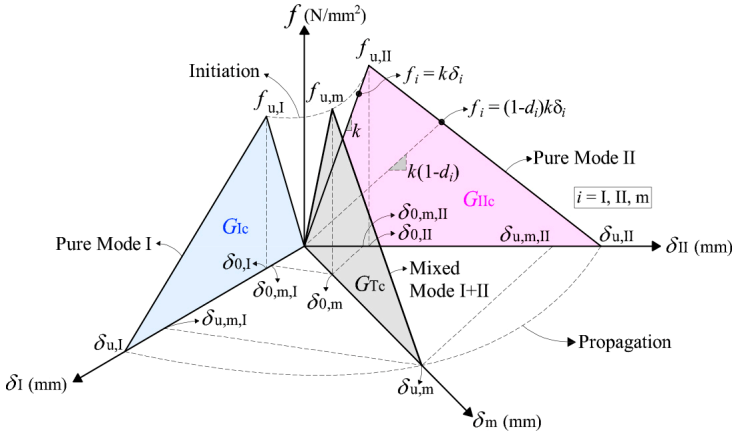

Figure 4. Bilinear cohesive law in mixed−mode I + II implemented in ABAQUS. Separation (δ) and traction (f).

The proposed damage model is characterised by two branches. The first one describes the elastic behaviour of the undamaged material until the stress limit ($f_{u,i}$, i = I, II, m) is reached, and the second one defines the softening behaviour under damage (Figure 4). Under mixed−mode I + II, an equivalent relative displacement combining the two loading modes is defined (Figure 4) according to Equation (1):

$$\delta_m = \sqrt{\delta_I^2 + \delta_{II}^2} \tag{1}$$

which can be written as

$$\delta_m = \delta_I \sqrt{1 + \beta^2} \tag{2}$$

being

$$\beta = \frac{|\delta_{II}|}{\delta_I} \tag{3}$$

In the first branch, the constitutive relationship is given by

$$f_m = k\delta_m \tag{4}$$

where f_m is the resulting mixed−mode I + II traction and k is the initial interface stiffness usually known as the penalty parameter which is set by the user. In this study, the value of 10^6 N/mm^3 [54,59] was adopted in all modes (I, II, mixed) to avoid undesirable interpenetration of the crack faces and numerical problems. A quadratic stress criterion is assumed to simulate damage onset under mixed-mode loading:

$$\left(\frac{f_I}{f_{u,I}}\right)^2 + \left(\frac{f_{II}}{f_{u,II}}\right)^2 = 1 \tag{5}$$

where (f_I, f_{II}) are the current mode I and II loading components and ($f_{u,I}$, $f_{u,II}$) are the corresponding local strengths (Figure 4). After some algebraic manipulation involving Equations (1)–(5), the relative displacement at damage onset becomes

$$\delta_{0,m} = \frac{\delta_{0,I}\delta_{0,II}\sqrt{1 + \beta^2}}{\sqrt{\beta^2\delta_{0,I}^2 + \delta_{0,II}^2}} \tag{6}$$

where $\delta_{0,i}$ (i = I, II) are the relative displacements at damage onset under pure mode loading (Figure 4). During propagation, the traction–separation relationship can be directly defined as

$$f_{\mathrm{m}} = (1 - d_{\mathrm{m}})k\delta_{\mathrm{m}} \tag{7}$$

where d_{m} is the damage parameter defined from the linear softening relationship between $\delta_{0,\mathrm{m}}$ and the ultimate relative displacement $\delta_{\mathrm{u,m}}$ according to

$$d_{\mathrm{m}} = \frac{\delta_{\mathrm{u,m}}(\delta_{\mathrm{m}} - \delta_{0,\mathrm{m}})}{\delta_{\mathrm{m}}(\delta_{\mathrm{u,m}} - \delta_{0,\mathrm{m}})} \tag{8}$$

The ultimate relative displacement $\delta_{\mathrm{u,m}}$ is calculated by means of the linear energetic criterion used to simulate damage propagation under mixed-mode I + II loading:

$$\frac{G_{\mathrm{I}}}{G_{\mathrm{Ic}}} + \frac{G_{\mathrm{II}}}{G_{\mathrm{IIc}}} = 1 \tag{9}$$

where G_{ic} (i = I, II) are the critical fracture energy and G_i (i = I, II) are the energy components of the current mode mixity given by

$$G_i = \frac{1}{2}k\delta_{0,\mathrm{m},i}\delta_{\mathrm{u,m},i} \tag{10}$$

with $\delta_{0,\mathrm{m},i}$ and $\delta_{\mathrm{u,m},i}$ representing the critical mode i components of the relative displacements at damage onset and at failure, respectively. From Equations (3) and (10), the strain energy release rate under mixed-mode loading can be written as

$$G_{\mathrm{Tc}} = G_{\mathrm{I}} + G_{\mathrm{II}} = G_{\mathrm{I}}\left(1 + \beta^2\right) \tag{11}$$

Combining Equations (11) and (9) yields

$$G_{\mathrm{Tc}} = \frac{G_{\mathrm{Ic}}G_{\mathrm{IIc}}(1 + \beta^2)}{G_{\mathrm{IIc}} + \beta^2 G_{\mathrm{Ic}}} \tag{12}$$

Knowing the critical strain energy release rate (G_{Tc}), $\delta_{\mathrm{u,m}}$ can be determined as follows:

$$\delta_{\mathrm{u,m}} = \frac{2G_{\mathrm{Tc}}}{k\delta_{0,\mathrm{m}}} \tag{13}$$

which makes it possible to define the damage parameter (Equation (8)) that represents the progressive propagation of damage under mixed-mode I + II loading. It should be noted that this general formulation also addresses the pure mode loading cases (I or II) since they are particular cases of the mixed-mode loading scenario.

The mean values of the fracture parameters of European beech defining the mode I and II cohesive laws in the TL crack propagation system, as well as the elastic constants of the material, were obtained from previous work by the authors [10,17,18] and are compiled in Tables 2 and 3. For the dowel steel, a modulus of elasticity of 210,000 N/mm^2 and a Poisson's ratio of 0.3 were considered. These material properties were used as input data in the numerical models.

Table 2. Average values and standard deviation of the elastic constants of European beech [10].

	E_{L} (N/mm^2)	E_{R} (N/mm^2)	E_{T} (N/mm^2)	ν_{RL} (-)	ν_{TL} (-)	ν_{RT} (-)	G_{LR} (N/mm^2)	G_{LT} (N/mm^2)	G_{RT} (N/mm^2)
Average	13,811	1590	832	0.51	0.44	0.32	1108	706	349
St. Dev.	1323	541	115	0.030	0.015	0.041	202	139	53

Table 3. Numerical parameters of the bilinear cohesive law: maximum traction (f_u) and critical fracture energy (G_c) in fracture modes I and II and TL crack propagation system for beech [17,18].

	$f_{I,u}$ (N/mm^2)	$f_{II,u}$ (N/mm^2)	G_{Ic} (N/mm)	G_{IIc} (N/mm)
Average	8.74	18.88	0.46	1.17
St. Dev.	1.97	3.34	0.10	0.26

2.3. Design Models

Several design proposals can be found in the literature to predict the splitting capacity of timber connections loaded perpendicular to the grain. However, there is much discussion on the parameters influencing the splitting behaviour, and no solid proposal has yet been developed that is widely accepted by the research community. A comprehensive review of most of the existing models, their theoretical basis, and their scope in the design of timber connections can be found in [34,60]. A summary of simple analytical models and the relationships between them is compiled in [61]. The three design models used in this work to predict the splitting failure load of the European beech are described below.

The first is the model formulated by Van der Put [26]. It is one of the first analytical models to predict the maximum shear force for the splitting failure of a simply supported beam. The model was developed using an energy approach in the framework of linear elastic fracture mechanics (LEFM). A single force acting at the mid-span of the beam was considered a starting point regardless of the type of fastener used to transfer the load to the beam. Subsequently, Van der Put and Leijten [27] calibrated the original model [26] for softwood using experimental results available in the literature. Some other considerations for this model can be found in [62]. The proposal has been widely discussed, mainly because of its simplicity. Jensen [63,64] published an extended model without any simplifying assumptions and including the contribution of normal forces in the section equilibrium, in which the original model of Van der Put appears as a special case. In addition, following the same approach, models for beams with two connections were developed. Also based on the original proposal, Ballerini [65] presented a semi-empirical expression taking into account the geometry of the connection. But despite successive proposals, the original model of Van der Put forms the basis of the design expression given in Eurocode 5 [24] (Equations (14)–(17)), which will be used to calculate the theoretical failure loads for beech in the present work:

$$F_{v,\mathrm{Ed}} \leq F_{90,\mathrm{Rd}} \tag{14}$$

$$F_{v,\mathrm{Ed}} = \max\begin{Bmatrix} F_{v,\mathrm{Ed},1} \\ F_{v,\mathrm{Ed},2} \end{Bmatrix} \tag{15}$$

$$F_{90,\mathrm{Rd}} = \frac{F_{90,\mathrm{Rk}}}{\gamma_{\mathrm{M}}} k_{\mathrm{mod}} \tag{16}$$

$$F_{90,\mathrm{Rk}} = 14 b\, w \sqrt{\frac{h_e}{1 - \frac{h_e}{h}}} \tag{17}$$

where $F_{\mathrm{v,Ed},1}$ and $F_{\mathrm{v,Ed},2}$ are the shear forces in the main beam on both sides of the connection, $\mathrm{F}_{90,\mathrm{Rk}}$ is the characteristic splitting capacity, k_{mod} is the modification factor considering load duration and moisture content, γ_{M} is the partial factor for material properties, b is the width of the beam, h is the depth of the beam, h_e is the distance from the fastener to the loaded edge of the beam, and w is a factor depending on the type of fastener (1 for dowels). It is important to underline that Equation (17) includes also a constant 14 value. According to the original work of Van der Put and Leijten [27], this 14 value is derived from the expression $C_1 = (GG_c/0.6)^{0.5}$, where the so-called *apparent fracture parameter* $(GG_c)^{0.5}$ was used as a fitting parameter by taking test results from a limited number of sources in the literature with different connection types. A value of $C_1 = 10$ N/mm$^{1.5}$ was suggested for use in the code design expression, somewhat lower than the $C_1 = 14$ N/mm$^{1.5}$ finally

adopted. Since the expression of the code is only valid for softwoods, in the present work it was decided to apply the original relationship and determine the C_1 value for European beech instead of C_1 = 14 N/mm$^{1.5}$, by means of the shear modulus G and critical fracture energy G_c of the material obtained experimentally, resulting in C_1 = 23.27 N/mm$^{1.5}$.

The second design model that was applied to estimate European beech's carrying capacity in the present work is the model formulated by Jensen [46]. It relies on Timoshenko's beam theory for elastic foundations (BEFs) and the quasi-non-linear fracture mechanics. For its development, a beam is considered with a cracking layer modelled by springs to which the material fracture properties are assigned. Upon cracking, the beam below this layer is considered to be resting on elastic Wrinkler springs connected to the upper part, which is assumed to be infinitely rigid. For a single load acting far from the beam end and small crack lengths, Equations (18)–(22) result:

$$P_u = \gamma \, P_{u,LEFM} \tag{18}$$

$$P_{u,LEFM} = 2bC_1\sqrt{\frac{h_e}{1-\frac{h_e}{h}}} \tag{19}$$

$$\gamma = \frac{\sqrt{2\zeta+1}}{\zeta+1} \tag{20}$$

$$\zeta = \frac{C_1}{f_t}\sqrt{10\frac{G}{E}\frac{1}{h_e}} \tag{21}$$

$$C_1 = \sqrt{\frac{5}{3}GG_f} \tag{22}$$

with P_u being the splitting load of the connection, E the longitudinal modulus of elasticity, G the shear modulus of elasticity, and G_f the fracture energy. One of the differentiating features of this model compared to previous proposals is that it takes into account the perpendicular tensile strength of the timber, f_t.

The third of the design approaches selected to estimate the theoretical splitting failure load of European beech is the one postulated by Franke and Quenneville [47] given by Equations (23)–(26). The design approach was developed through experimental investigations and finite element numerical simulations considering numerous connection arrangements, in the framework of non-linear fracture mechanics. It is one of the most comprehensive models in the literature, which for the first time considers mixed-mode I + II (tension and shear) failure criteria that represent a more realistic situation and not only mode I, as most of the previous models conservatively do:

$$F_{90} = \frac{b\cdot 10^3}{\left(\frac{G_{\text{I, norm}}}{G_{\text{Ic}}}+\frac{G_{\text{II, norm}}}{G_{\text{IIc}}}\right)}\cdot k_r \tag{23}$$

$$G_{\text{I, norm}} = e^{(h^{-1}(200-10h_e\cdot h^{-0.25}-a_r))} \tag{24}$$

$$G_{\text{II, norm}} = \left(0.05+0.12\frac{h_e}{h}+1\cdot 10^{-3}a_r\right) \tag{25}$$

$$k_r = \begin{cases} 1 & \text{for } n=1 \text{ dowel} \\ 0.1+(\arctan(n))^{0.6} & \text{for } n>1 \text{ dowels} \end{cases} \tag{26}$$

with F_{90} being the splitting load of the connection, G_{Ic} and G_{IIc} the critical fracture energy of the material in mode I and II, respectively, and $G_{\text{I, norm}}$ and $G_{\text{II, norm}}$ the normalised fracture energy in mode I and II, respectively. The model also includes other parameters concerning the connection layout, such as the width of the connection (a_r) and the number of rows of fasteners parallel to the grain through the k_r factor.

The material properties of the European beech that are used as input data in the three above-mentioned models to calculate the corresponding theoretical splitting ultimate loads were obtained from previous work of the authors and are presented in Tables 2 and 3. A value of 8.9 N/mm^2 is used for the tensile strength perpendicular to the grain (f_t) [13].

3. Results and Discussion

3.1. Experimental Results

3.1.1. Splitting Loads and Failure Modes

The results on ultimate loads and failure modes from the experimental work on European beech are presented here.

Splitting was the type of failure that governed the collapse of most of the beams tested. However, some specimens failed in bending. Table 4 shows the percentage of failures due to splitting or bending per test series, as well as the mean values of the connection failure load (P_{exp}) and the maximum shear force corresponding to P_{exp} ($V_{shear,max}$) for each of these two failure modes. The location of P_{exp} is represented in Figure 1.

Table 4. Experimental results: percentage of beams with splitting/bending failure per series (%); average values of the connection failure load (P_{exp}) and the maximum shear force corresponding to the P_{exp} ($V_{shear,max}$) for each failure mode; coefficient of variation (COV); ratio between the distance of the connection to the support (l_b) and the beam depth (h).

	Failure Mode					
	Series	**Splitting/Bending**				
	***h*/no.dowels/*L*/l_b**	**%**	**P_{exp} (kN)**	**$V_{shear.max}$ (kN)**	**COV (%)**	**l_b/h**
Group 1 (*h*: 100 mm)	100/1D/450/0.5L	100/-	32.5/-	16.3/-	5.1/-	2.25
	100/1D/950/0.5L	25/75	31.0/30.3	15.5/15.2	-/4.1	4.75
	100/1D/950/0.38L	67/33	26.7/33.3	16.6/20.7	7.4/0	3.60
	100/1D/950/0.25L	67/33	26.3/28.3	19.7/21.1	5.7/0	2.40
	100/1D/950/0.13L	100/-	23.9/-	20.9/-	6.0/-	1.20
	100/2D/450/0.5L	100/-	49.0/-	24.5/-	10.5/-	1.93
	100/2D/950/0.5L	-/100	-/37.6	-/18.8	-/8	4.43
	100/2D/950/0.38L	33/67	23.7/23.9	23.7/23.9	0/0.4	3.60
	100/2D/950/0.25L	67/33	27.1/21.5	27.1/21.5	8.7/0	2.40
	100/2D/950/0.13L	100/-	25.0/-	25.0/-	10.1/-	1.20
Group 2 (*h*: 200 mm)	200/1D/450/0.5L	100/-	27.2/-	13.6/-	7.8/-	1.13
	200/1D/950/0.5L	100/-	30.8/-	15.4/-	11/-	2.38
	200/1D/950/0.38L	100/-	24.3/-	15.1/-	10.0/-	1.80
	200/1D/950/0.25L	100/-	20.5/-	15.3/-	14.2/-	1.20
	200/1D/950/0.13L	100/-	27.4/-	23.9/-	6.5/-	0.60
	200/2D/450/0.5L	100/-	29.2/-	14.6/-	20.5/-	0.97
	200/2D/950/0.5L	100/-	33.6/-	16.8/-	5.1/-	2.22
	200/2D/950/0.38L	100/-	22.8/-	22.8/-	20.1/-	1.80
	200/2D/950/0.25L	100/-	26.9/-	26.9/-	18.9/-	1.20
	200/2D/950/0.13L	100/-	28.5/-	28.5/-	24.1/-	0.60

It should be noted that all the tested connections have the same distance from the loaded edge (h_e) but different values of α. This leads to the fact that all tested series in group 2 failed by splitting but not the series in group 1. In particular, all beams in the reference series of group 1 failed in bending, except for one beam in the reference series with one dowel. In addition, in the series of group 1 with the off-centre connection, some beams also failed by bending, except in the series with the connection closer to the support, where all beams failed by splitting. The closer the connection is to the supports, the more predominant the splitting failure. This trend is logical since the moment generated by the

load decreases with the proximity of the connection to the support. It is worth noting that bending failure only occurred in the beams with the greatest slenderness and α ratio of 0.64, where the ultimate loads shown in Table 4 caused stresses in the outermost wood fibres of around 90 N/mm^2, which are in line with the limit values reported in the literature [15].

It was observed that the experimental tests reached the maximum load by developing two different fracture patterns: one completely brittle (pure splitting) and the other in a combination of failure modes (a non-negligible plastic behaviour of the wood develops before splitting occurs), as shown in Figure 5. The behaviour of the combined failure mode is directly related to the formation of small cracks in the wood at the bottom of the dowel and, in some cases, to the yielding of the wood around the connection, as these areas are singular points subjected to high stress concentrations perpendicular to the grain.

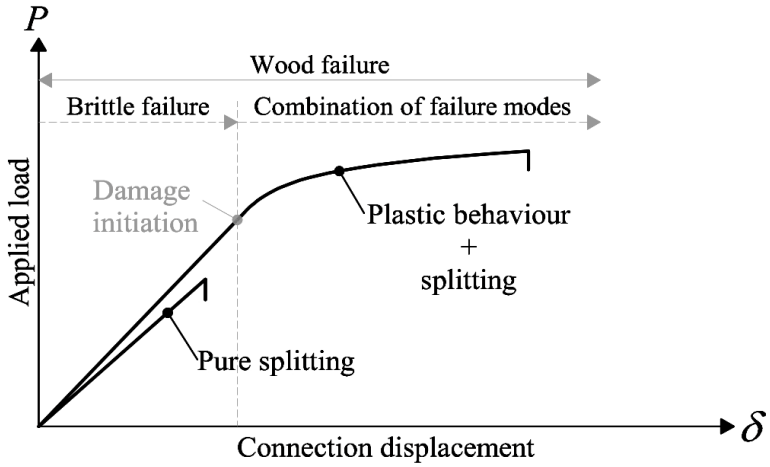

Figure 5. Governing failure modes in the experimental tests.

A summary of the load–displacement curves (P-δ) for each of the tested specimens is shown in Figures 6 and 7. In these graphs, the load and displacement of the connection are plotted, according to the placement of LVDTs depicted in Figure 1. However, in Figure 7b, the total load on the beam ($2P$) is plotted in order to compare the results between the graphs depicted in Figure 7.

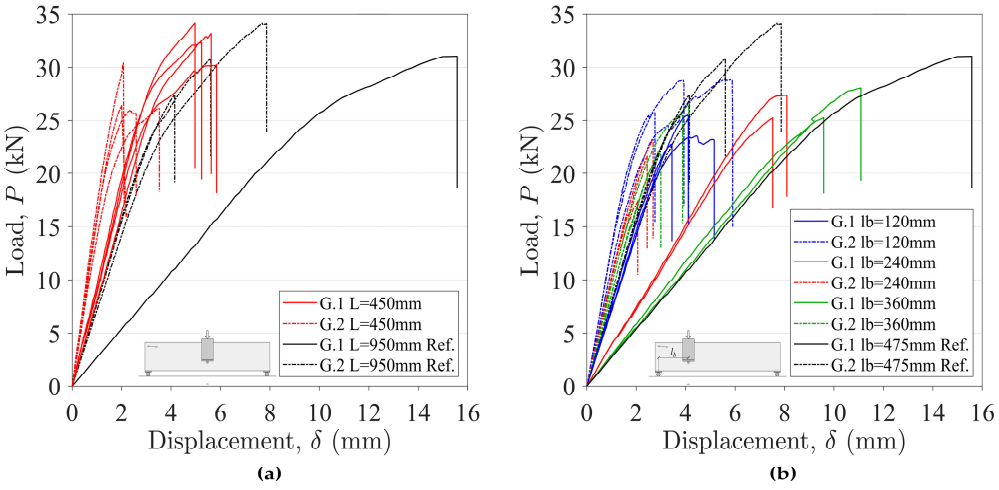

Figure 6. Experimental P-δ curves of beams with one dowel: (**a**) 1D with connection at mid-span; (**b**) 1D with the connection placed at off-centre of the beam.

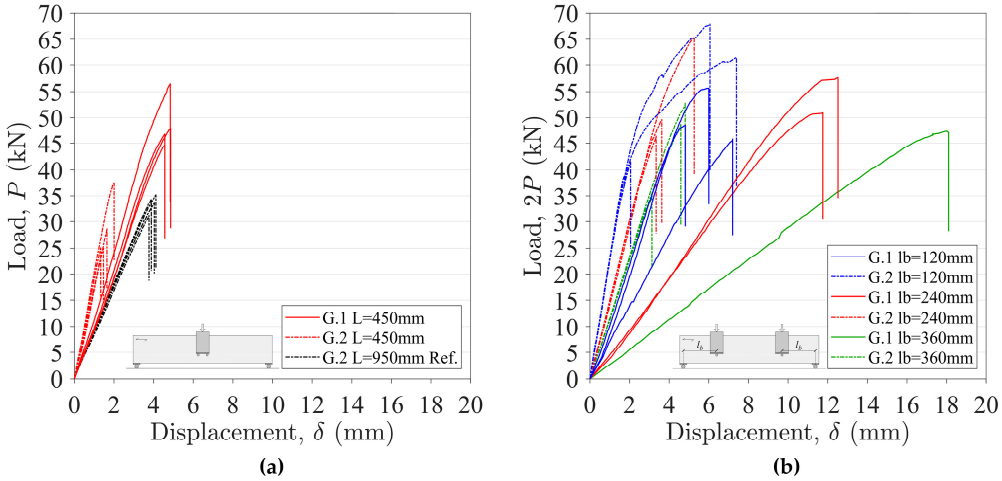

Figure 7. Experimental P-δ curves of beams with two dowels: (**a**) 2D with connection at mid-span; (**b**) 2D with the connection placed at off-centre of the beam.

As can be seen, a single-dowel-type connection tends to develop a mixed-mode behaviour, but a double-dowel-type connection tends to collapse in a brittle manner. In particular, all beams with two dowels located in the centre of the span and those with two off-centre connections closer to the centre of the span break in a completely brittle manner. However, the rest of the beams showed a mixed-mode behaviour. This difference in behaviour depends on the configuration of the connection and is in line with the results of other research in the literature for other wood species [29,34,38,40,66].

In the series investigated, the splitting failure was characterised by the propagation of a main crack, which extended along the beam length and through the full entire thickness. This failure mode appeared suddenly and in a brittle manner. In some tests, the splitting failure was preceded by the formation of small cracks around the dowel, but eventually only one crack propagated and in a forceful manner. In some specimens, the crack shape that developed along the beam was very straight and continuous (see Figure 8a), but in other cases, the shape was oblique and/or discontinuous (see Figure 8b). The crack propagation patterns across the width of the beam also exhibited similar differences between the specimens (see Figure 9). However, the results showed that the less straight and continuous the crack propagation was, both longitudinally and transversely, the higher the splitting capacity.

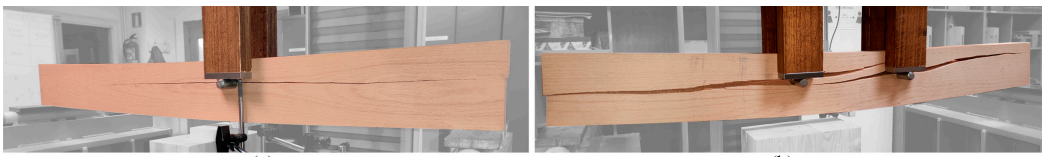

Figure 8. Typical failures: (**a**) straight and continuous crack; (**b**) oblique and discontinuous crack.

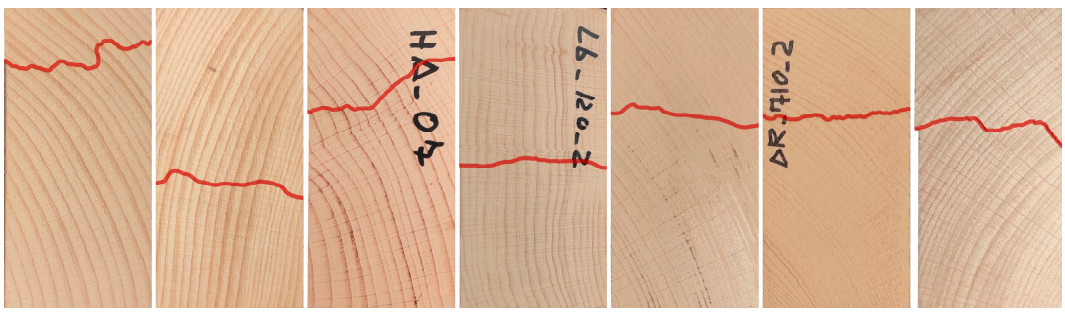

Figure 9. Typical crack patterns.

In all the series with two dowels and a span of 950 mm in group 2, the crack was propagated to the end of the beam, splitting it into two parts. In addition, this also happened in the beams of group 1 with a span of 450 mm and in all the series with two connections except for the one where the connections are closer to the supports (100/2D/950/0.13L). However, this did not happen in the rest of the series, where the crack did not reach the ends. Some of these crack patterns are shown in Figure 10.

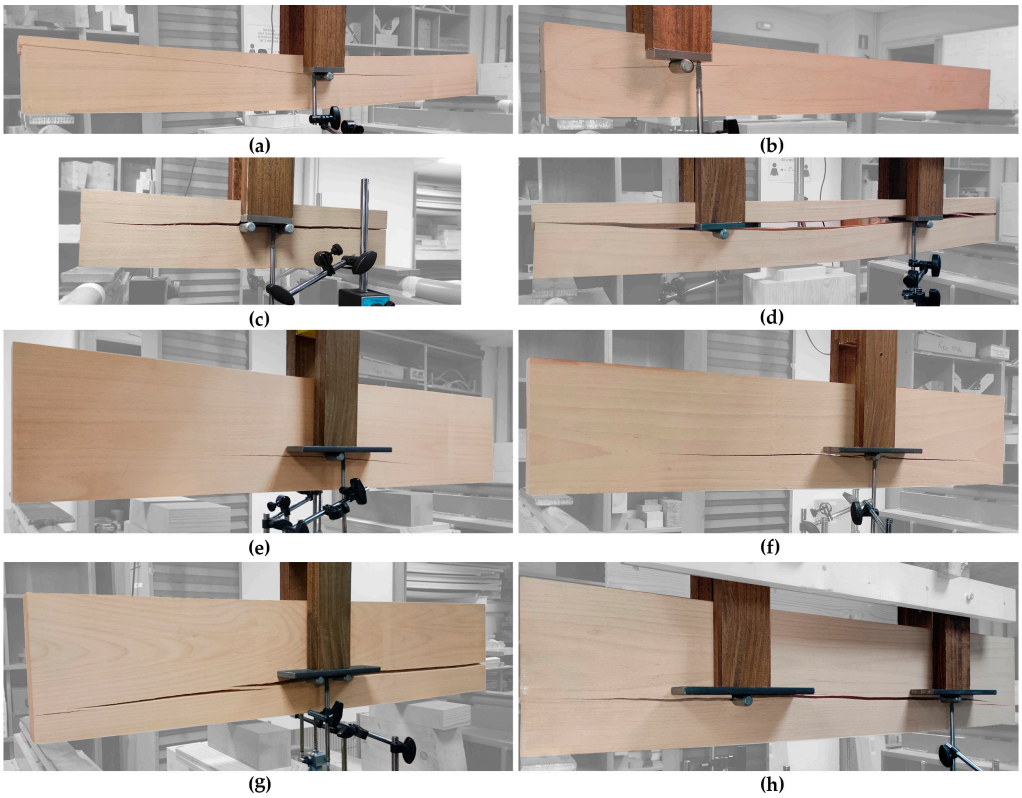

Figure 10. Typical splitting failure of series with h = 100 mm (group 1 (**a**–**d**)) and h = 200 mm (group 2 (**e**–**h**)): (**a**,**e**) 1D with connection at mid-span; (**b**,**f**) 1D with the connection placed at off-centre of the beam; (**c**,**g**) 2D with connection at mid-span; (**d**,**h**) 2D with the connections placed at off-centre of the beam.

3.1.2. Influence of the Number of Dowels at the Connection

To study the influence of the number of dowels on the connection, the series with the connection located at mid-span with one and two dowels and beam spans of 450 mm and 950 mm were considered.

Table 5 summarises the results of the series studied, including the mean value of the splitting failure load, the parameter α, the slenderness of the beam, and the percentage load increase in the connections with two dowels with respect to their counterparts with one dowel.

As can be seen, the load gain of 2-dowel connections relative to single-dowel connections never reaches twice the value.

The influence of the parameter α can be analysed by comparing the series with different values of α and similar slenderness (4.75 slenderness for α = 0.32 and 4.5 slenderness for α = 0.64). The results show that the load gain for α = 0.32 is very small, only 9%. However, for the series with α = 0.64, the load gain attained is much higher, 51%, although still far from the expected doubling. Note that in this case α is doubled, but the load gain is more than five times higher.

Table 5. Load increase in series with two-dowel connections compared to one-dowel connections.

Number of Dowels (no.dowels)	Series h/no.dowels/L/l_b	L (mm)	Slenderness (L/h)	h_e (mm)	α h_e/h	P_{exp} (kN)	Load Increase (%)
1D	100/1D/450/0.5L	450	4.50	64	0.64	32.5	51%
2D	100/2D/450/0.5L					49.0	
1D	200/1D/450/0.5L	450	2.25	64	0.32	27.2	7%
2D	200/2D/450/0.5L					29.2	
1D	200/1D/950/0.5L	950	4.75	64	0.32	30.8	9%
2D	200/2D/950/0.5L					33.6	

The effect of the span can be analysed by comparing the results of the series with the same depth (h = 200 mm) but different spans (450 mm and 950 mm). It can be observed that, as the span increases, the load gain for using two dowels instead of one is almost negligible, from 7% for the series with a 450 mm span to 9% for the series with a 950 mm span. These results show that span has hardly any influence, at least for low α values such as the one studied (α = 0.32).

The increase in load obtained as a function of the number of dowels in the connection is consistent with other research [34,40,67], where increasing the number of dowels led to an increase in splitting failure load.

It is worth mentioning that the load carrying capacity of the connection increases slightly with increasing beam span. Figure 11 shows the ultimate splitting loads in relation to the beam span for the series of single- and double-dowel connections at mid-span for h = 200 mm.

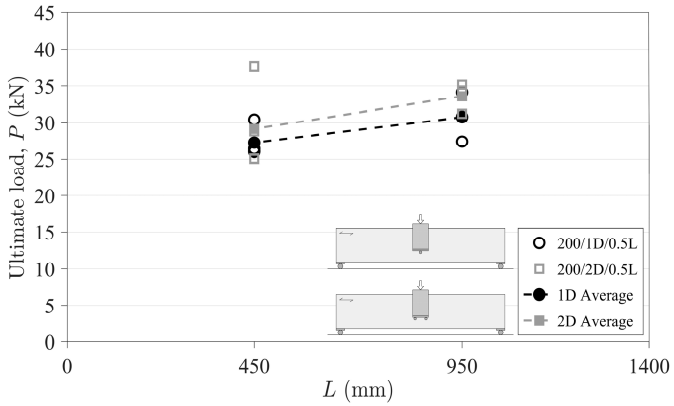

Figure 11. Splitting failure loads for one- and two-dowel connections in relation to beam span, for h = 200 mm.

According to the results, it follows that the larger the span, the higher the splitting loads (13% for 1D and 15% for 2D). In terms of beam slenderness (L/h), the higher the slenderness, the higher the load carrying capacity, which is in agreement with the results for spruce glulam available in [34,68]. In the case of the series with h = 100 mm, this comparison is not possible because the beams with larger spans failed in bending.

3.1.3. Influence of Distances l_b and l_c

The evolution of the maximum splitting load for the beams with one-dowel connections placed at different distances from the nearest support (l_b) is shown in Figure 12a. Figure 12b shows the load evolution for beams with two-dowel connections as a function of the spacing between the dowels (l_c). The results in both graphs are given for beams with h = 100 mm and h = 200 mm.

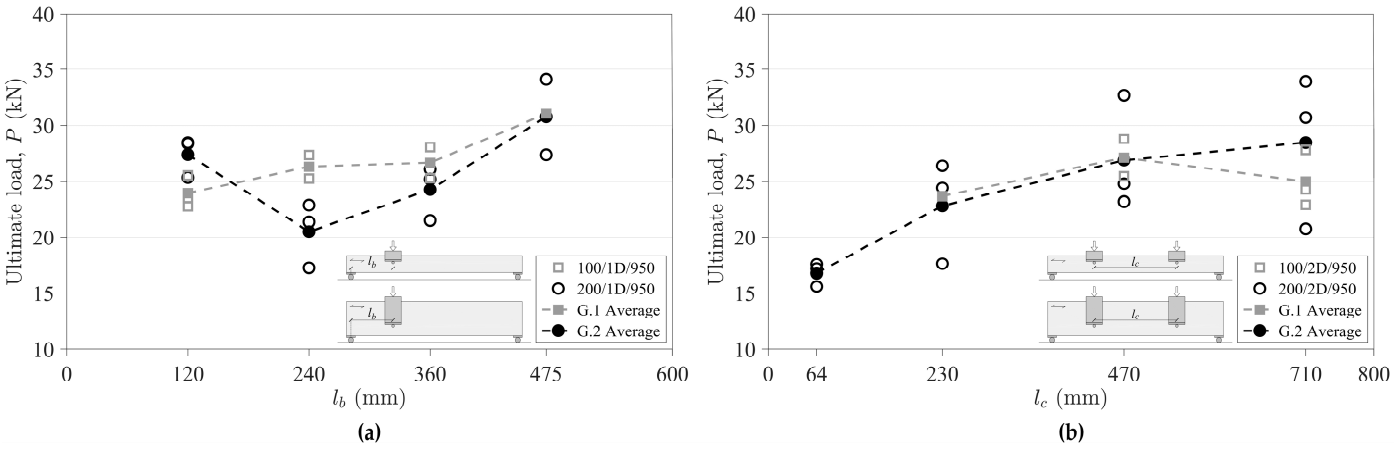

Figure 12. (**a**) Splitting failure loads of single-dowel connections versus the distance between the connection and the support l_b, for the two different beam depths; (**b**) splitting failure loads of two-dowel connections versus dowel spacing l_c, for the two different beam depths.

When looking at the evolution of the splitting capacity as a function of l_b for beech beams with one-dowel connections (Figure 12a), the series of h = 200 mm shows a decrease in splitting failure loads with the proximity of the dowel to the support, up to the distance l_b = 240 mm. However, the load increases again when the dowel is at the closest distance to the support of those studied (l_b = 120 mm). The specific l_b distance at which this trend change occurs is difficult to determine with accuracy as many tests would be necessary. However, a value of $l_b \approx h$ seems a good approximation. This apparent increase in the splitting capacity of the beam may be due to the fact that, for distances of $l_b \approx h$, part of the load is transferred directly to the supports [62]. However, the splitting failure is not negligible even if $l_b < h$.

A similar trend is observed for beams with h = 100 mm, with a decrease in ultimate load with decreasing l_b, although in this case with no increase in load for the lowest l_b. This observation may be related to the fact that the smallest value of l_b tested is greater than h and therefore the dowel is not close enough to the support to transfer the load directly to it.

There are not many experimental studies in the literature focusing on the influence of l_b. Some literature sources report that splitting capacity is independent of l_b [35,61], contrary to the results of the present study, where the influence was evident. Other studies with off-centre dowel connections in sawn spruce, spruce glulam, Douglas fir glulam, or Radiata pine LVL can be found in [28,34,69]. However, due to the limited results and geometries addressed, it is difficult to draw clear conclusions.

When comparing the test results between the two beam depths, it can be seen that the h = 100 mm series tends to attain higher splitting loads than the h = 200 mm series. This gain in load may be explained, to some extent, by the difference in the α ratios, so that the higher the α, the higher the ultimate load. This influence of the parameter α is in line with the findings described in Section 3.1.1.

Regarding the evolution of the ultimate splitting loads as a function of l_c for beech beams with two-dowel connections (Figure 12b), it can be seen that the loads increase with the dowel spacing, which is in agreement with the test results reported in [34,36,66,67,70].

The results from the h = 200 mm series show that the ultimate loads measured for beams with small dowel spacings ($l_c = 4d$) do not differ significantly from the loads reached for beams with a single dowel placed at mid-span, and the larger the dowel spacing, the higher the splitting load. Small increases in the l_c spacing lead to load increases, but this tends to stabilise at large l_c spacings. A similar trend is observed for the series with h = 100 mm, although many of the specimens in this series failed in bending (Table 4). It should be noted that the average values of the loads reached are practically identical between the two groups, except for the series with an l_c spacing of 710 mm, where the specimens with h = 100 mm showed lower splitting capacity. In this case, it seems that α

does not influence the ultimate load, even though the series with h = 100 mm have twice the α ratio of those with h = 200 mm.

It is interesting to note that series with $l_b/h < 2.4$ failed by splitting and those with $l_b/h \geq 2.4$ were susceptible to fail by bending. Furthermore, when $l_b/h \geq 4.40$, the governing failure mode appears to be primarily bending. However, these values are influenced by the number of dowels with which the connection is loaded, as beams with two dowels can transfer more load to the beam before splitting occurs. This favours bending as the dominant failure mode.

3.1.4. Influence of the Number of Connections

The effect of placing another connection symmetrically to the centre of the beam is discussed here. Figure 13 shows the evolution of the load per connection as a function of l_b for beams with single (1D) and double symmetrical (2D) connections, for the two groups of beam depths tested (100 and 200 mm). It is observed that the load of beams with a single connection is higher than that of beams with two connections in the case of l_b of 360 mm, i.e., a connection spacing l_c of 230 mm. Considering the linear relationship plotted in Figure 13, the value of l_c required for a multiconnection beam to exceed the load corresponding to its single-connection counterpart would be approximately 420 mm and 280 mm for h = 100 mm and h = 200 mm, respectively ($l_c \approx 4.2h$ and $1.4h$, respectively). This could be due to an influence of the α parameter, suggesting that a higher α requires higher l_c connection spacing.

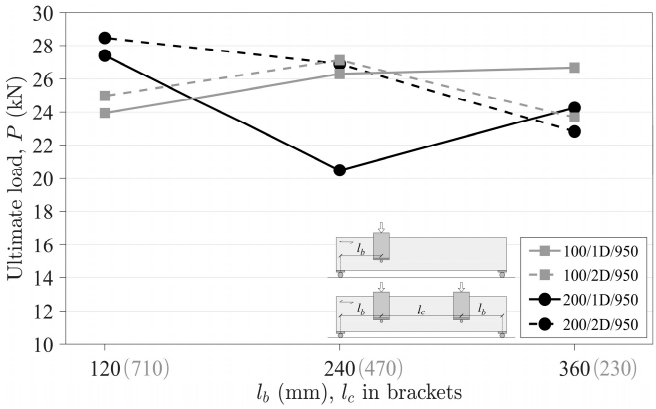

Figure 13. Splitting failure load per connection for single and double symmetrical connections as a function of the distance to the support l_b, for the two different beam depths.

In the case of beams with h = 100 mm, it is observed that the load per connection in beams with multiple connections corresponding to l_b distances of 120 mm and 240 mm ($l_c \geq 470$ mm) is approximately 4% higher than the equivalent case with a single connection. However, in the case of beams with h = 200 mm, this increase does not remain constant and amounts to 4% and 31% for l_b distances of 120 mm and 240 mm, respectively. In this case, there is a significant gain for l_b = 240 mm. It should be noted that this distance l_b corresponds to the geometry for which the most critical case of its equivalent with one connection occurs. In both groups of beam depths, for a certain distance between connections (l_c), there is an inflexion point at which beams with multiple connections reach more load than their counterparts with a single connection. Therefore, a beam with multiple connections arranged symmetrically to the centre of the beam reaches more than twice the splitting load than its counterpart with a single connection.

According to the findings in Section 3.1.3, the total load of a beam with two dowels located at off-centre of the beam does not double the load of the reference connection, i.e., a connection with two dowels located at mid-span. However, when comparing similar geometries, there is a certain connection spacing (l_c) where the stresses introduced into the beam by each connection do not interfere with each other and, in such cases, the total load

of a beam with multiple connections can be more than twice the load of its counterpart with a single connection.

3.2. Comparison between Experimental, Numerical, and Theoretical Failure Loads

The adequacy of the numerical and design models described in Sections 2.2 and 2.3 for the prediction of the splitting failure loads of beech beams loaded perpendicular to the grain by the connections is discussed here in relation to the experimental results. The material properties of the European beech used as input values in the models were also presented in Section 2.2, which corresponded to the tangential direction of the wood as this was the main orientation of the cross-section of the beams.

Figure 14 shows representative results of the experimental (grey lines) and numerical (black lines) load–displacement curves, depicting both the dowel displacement (dashed lines) and the beam bottom face displacement (solid lines). As can be seen, the numerical results agree well with the experimental results for the main parameters, such as stiffness and ultimate load. Still, the numerical curves were able to better reproduce the experimental behaviour of the beams with a brittle failure than those with a mixed-mode failure pattern (see Figure 5). The good agreement between the experimental and numerical initial stiffness shows that the average values of the elastic constants used are representative of the material. This consistency between the numerical and experimental initial stiffness is more evident in the curves plotted considering the displacement of the bottom of the beam than in those plotted with the displacement under the dowel, where the numerical ones show a higher stiffness. The maximum splitting capacity of the geometries of group 1 (h = 100 mm) matches the experimental results, but in the case of group 2 (h = 200 mm), the predicted loads are always lower than the experimental ones.

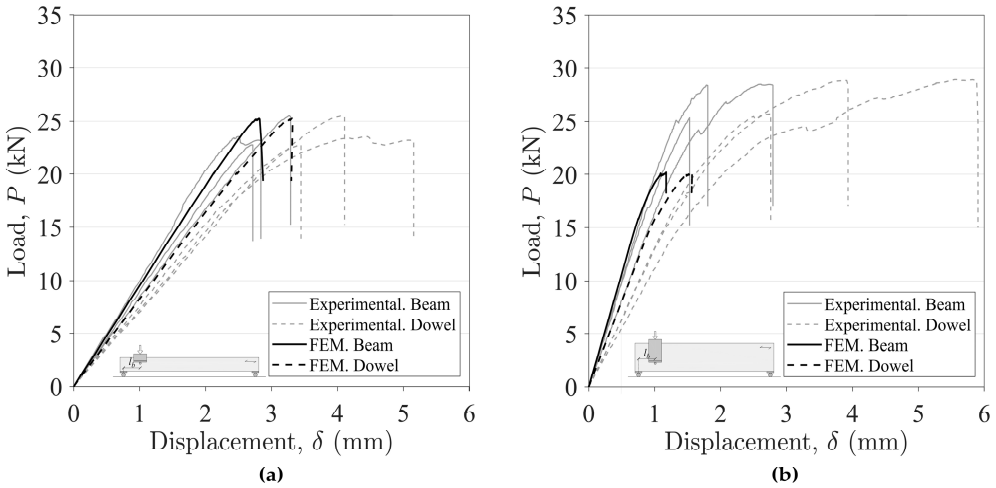

Figure 14. Representative experimental and numerical P-δ curves: (**a**) series with h = 100 mm (100/1D/950/0.13L); (**b**) series with h = 200 mm (200/1D/950/0.13L).

It should be highlighted that the expression in Eurocode 5 [24] focuses on the prediction of the maximum shear force, so the maximum splitting capacity of the connection has been obtained by applying beam theory. Thus, the maximum splitting capacity foreseen by Eurocode 5 [24] is twice the value of the shear force (Equations (14)–(17)) for all series, except for series 1D with the connection located at off-centre of the beam, where the maximum load carrying capacity was determined according to the following expression:

$$P_{\text{pre}} = V_{s,\max} \frac{L}{L - l_b} \tag{27}$$

where $V_{\text{s,max}}$ is the maximum shear force obtained directly from Equation (14), L is the beam span, and l_b is the distance from the connection to the nearest support. It should be

noted that only Eurocode 5 [24] and the numerical models take into account the position of the connection with respect to the beam.

The results of the predicted failure loads from the numerical finite element analysis and the three design models studied are presented in Table 6. The predicted values normalised to the experimental results for all cases are also included. These ratios are also shown graphically in Figure 15. A ratio ≤ 1 represents a safe prediction and a ratio > 1 an unsafe prediction.

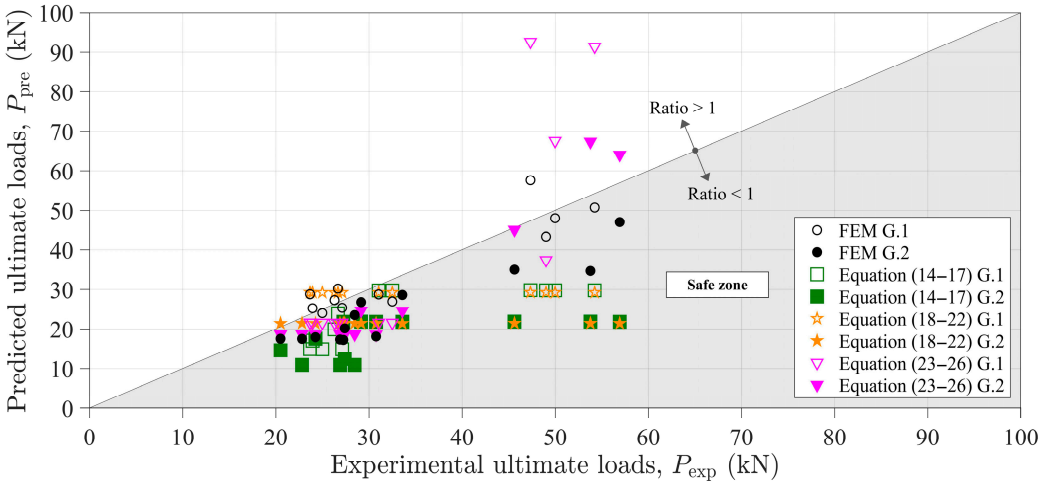

Figure 15. Experimental failure loads versus values predicted by FEM (black symbols) and by the design models (symbols in colours) for the European beech.

As can be seen from the results, in general terms, the best theoretical predictions were found for low experimental loads (between 20 and 35 kN), and there was more dispersion at higher experimental loads (between 45 and 60 kN).

When the connection is located at the centre of the beam (l_b = 0.5L), all models provide safe predictions for all the cases studied (one and two dowels and the two beam edges). Specifically, in the case of one dowel (1D), the Eurocode 5 base model and the Jensen model similarly give the best predictions. However, when there are two dowels (2D), it is FEM that stands out with theoretical loads closer to the experimental ones when applying the three design models, and it is precisely the Eurocode 5 base model and Jensen that offer the worst predictions this time, contrary to the previous case. This is consistent with the models that do not consider the number of fasteners in their formulation.

When the connection is off-centre (l_b = 0.38L, 0.25L, and 0.13L) and considering 1D, the Eurocode 5 model is the one that gives the predictions least adjusted to the experimental values in most cases, although always on the safe side. The closer the dowel is to the support, the more conservative it is. It should be noted that the C_1 value used in the expression corresponds to beech. If the fixed value C_1 = 14 given in the Eurocode 5 expression (Equations (14)–(17)) for softwoods had been used, the predicted loads would have been even more conservative.

In the case of off-centre connection, but focusing now on 2D, two assumptions have been considered for the analysis of results: each dowel as part of a separate connection (i.e., the beam would have two connections with 1D each) and the two dowels as part of the same connection. The results of this second assumption are marked with * in Table 6.

According to the first scenario of two separate connections, the Eurocode 5 model seems to be too conservative again, this time with predictions below 63% of the experimental load. The FEM appears to give theoretical values closer to the experimental ones.

Table 6. Experimental (P_{exp}) vs. predicted (numerical and theoretical, P_{pre}) splitting capacity.

	Series	Exp. Test	Numerical Analysis		Design Models					
					Eurocode 5 [24] Equations (14)–(17)		Jensen [46] Equations (18)–(22)		Franke and Quenneville [47] Equations (23)–(26)	
	h/no.dowels/L/l_b	P_{exp} (kN)	P_{pre} (kN)	P_{pre}/P_{exp}	P_{pre} (kN)	P_{pre}/P_{exp}	P_{pre} (kN)	P_{pre}/P_{exp}	P_{pre} (kN)	P_{pre}/P_{exp}
G.1	100/1D/450/0.5L	32.5	27.0	0.83	29.8	0.92	29.2	0.90	21.6	0.66
	100/1D/950/0.5L	31.0	28.8	0.93	29.8	0.96	29.2	0.94	21.6	0.70
	100/1D/950/0.38L	26.7	30.2	1.13	24.0	0.90	29.2	1.10	21.6	0.81
	100/1D/950/0.25L	26.3	27.3	1.04	19.9	0.76	29.2	1.11	21.6	0.82
	100/1D/950/0.13L	23.9	25.3	1.06	17.0	0.71	29.2	1.22	21.6	0.90
	100/2D/450/0.5L	49.0	43.4	0.89	29.8	0.61	29.3	0.60	37.4	0.76
	100/2D/950/0.5L	-	-	-	-	-	-	-	-	-
	100/2D/950/0.38L	23.7	28.8	1.22	14.9	0.63	29.3	1.24	21.6	0.91
	100/2D/950/0.25L	27.1	25.4	0.94	14.9	0.55	29.2	1.08	21.6	0.80
	100/2D/950/0.13L	25.0	24.0	0.96	14.9	0.60	29.2	1.17	21.6	0.86
G.1 * ($P = 2P$)	100/2D/950/0.38L	47.3	57.6	1.22	29.8	0.63	29.3	0.62	92.6	1.96
	100/2D/950/0.25L	54.2	50.7	0.94	29.8	0.55	29.2	0.54	91.4	1.69
	100/2D/950/0.13L	50.0	48.0	0.96	29.8	0.60	29.2	0.58	67.6	1.35
G.2	200/1D/450/0.5L	27.2	17.2	0.63	21.8	0.80	21.4	0.79	18.6	0.68
	200/1D/950/0.5L	30.8	18.1	0.59	21.8	0.71	21.4	0.70	18.6	0.60
	200/1D/950/0.38L	24.3	17.9	0.74	17.6	0.72	21.4	0.88	18.6	0.77
	200/1D/950/0.25L	20.5	17.5	0.85	14.6	0.71	21.4	1.05	18.6	0.91
	200/1D/950/0.13L	27.4	20.2	0.74	12.5	0.46	21.4	0.78	18.6	0.68
	200/2D/450/0.5L	29.2	26.8	0.92	21.8	0.75	21.5	0.74	24.7	0.85
	200/2D/950/0.5L	33.6	28.6	0.85	21.8	0.65	21.4	0.64	24.6	0.73
	200/2D/950/0.38L	22.8	17.5	0.77	10.9	0.48	21.5	0.94	18.6	0.82
	200/2D/950/0.25L	26.9	17.3	0.64	10.9	0.41	21.5	0.80	18.6	0.69
	200/2D/950/0.13L	28.5	23.5	0.83	10.9	0.38	21.4	0.75	18.6	0.65
G.2 * ($P = 2P$)	200/2D/950/0.38L	45.6	35.0	0.77	21.8	0.48	21.5	0.47	45.1	0.99
	200/2D/950/0.25L	53.8	34.7	0.64	21.8	0.41	21.5	0.40	67.4	1.25
	200/2D/950/0.13L	56.9	47.1	0.83	21.8	0.38	21.4	0.38	64.1	1.13

* This comparison is made considering that the beam has only one connection, i.e., $P = 2P$.

Under the second assumption of considering the two dowels as part of the same connection, the theoretical failure loads predicted by the FEM and by the Eurocode 5 model double their value, but the ratio between these and the experimental ones is the same as that obtained under the first assumption, thus making the Eurocode 5 model quite conservative, as mentioned above.

However, the load ratios resulting from applying the models of Jensen (Equations (18)–(22)) and Franke and Quenneville (Equations (23)–(26)) differ between the two assumptions. Specifically, Jensen's model leads to the same theoretical loads for both scenarios, and therefore, the ratios are halved when only one connection is considered, which means overly conservative predictions with theoretical values below 62% of the experimental load, similar to those obtained by applying the Eurocode 5 model (it should be remembered that both models disregard the number of dowels in the connection in their formulation). On the other hand, if the connections were considered independent, Jensen's model gives results closer to the experimental ones but sometimes in a non-conservative way, as was the case for beams of h = 100 mm.

Focusing on the Franke and Quenneville model, the difference in behaviour between both assumptions is the reverse: the consideration of independent connections is the one that gives conservative results, while the second assumption of considering a single connection with two dowels results for most of the cases unsafe, with some theoretical values far away from the experimental ones, especially in the beams of h = 100 mm. Therefore, the Franke and Quenneville design model considering two independent connections, as well as the FEM model, would be the most appropriate when off-centre multidowel connections are presented.

4. Conclusions

The numerical and experimental splitting capacity results for European beech (*Fagus sylvatica* L.) beams loaded perpendicular to the grain by single- and double-dowel connections with different locations along the beam span are provided.

The use of an additional dowel slightly increases the splitting capacity at low α (h_e/h) values (0.32) but significantly increases it at high α values (0.64), by about 50%. For the same test configuration, the larger the beam span, the higher the splitting load. For single-dowel connections, the position of the dowel along the beam span influences the splitting capacity, which is lower the closer the connection is to the supports. For double-dowel connections, the greater the distance between the dowels, the greater the splitting load, but in no case will the increased load from an additional dowel double the ultimate load of a single-dowel connection. Beams with $l_b/h < 2.4$ fail by splitting, and those with an l_b/h ratio ≥ 2.4 are susceptible to fail by bending, but these values are influenced by the number of dowels loaded into the connection, as beams with two dowels can transfer more load to the beam before splitting occurs. This fact favours bending as the dominant failure mode.

A 2D finite element model was developed for each geometry in the experimental programme, using a cohesive element model and a bilinear cohesive law to reproduce the mode I and II fracture process.

The proposed finite element model successfully replicated the behaviour of beams exhibiting purely brittle failure patterns more effectively than those displaying mixed-mode failure.

The numerical P-δ curves are in good agreement with the experimental ones. The proposed numerical model demonstrates its efficacy as a powerful tool for predicting the splitting capacity of timber connections with various arrangements. Moreover, it proves to be structurally safe from a design standpoint.

Of the three design models based on fracture mechanics (including the Eurocode 5 expression), the models based on elastic and linear fracture energy generally give good load predictions for single-dowel arrangements. For two-dowel layouts, where the two dowels are considered as part of the same connection, design models that include fracture properties only in mode I provide too conservative values. The model that considers mode

I and II fracture and the influence of joint width (l_c) predicts overestimated values for high l_c configurations.

Further experimental research on the splitting behaviour considering other connection geometries and hardwood species would be desirable in order to obtain a general expression valid for all of them.

Author Contributions: Conceptualisation, J.L.G.-R., A.J.L.-B. and A.M.-M.; methodology, J.L.G.-R., A.J.L.-B., A.M.-M., J.X. and M.F.S.F.d.M.; validation, J.L.G.-R.; formal analysis, J.L.G.-R.; investigation, J.L.G.-R., A.J.L.-B. and A.M.-M.; writing—original draft preparation, J.L.G.-R.; writing—review and editing, J.L.G.-R., A.J.L.-B., A.M.-M., J.X. and M.F.S.F.d.M.; visualisation, J.L.G.-R.; supervision, A.M.-M., J.X. and M.F.S.F.d.M.; funding acquisition, A.M.-M., J.X. and M.F.S.F.d.M. All authors have read and agreed to the published version of the manuscript.

Funding: Part of the work was undertaken during a short-term scientific stay by the first author at the Faculty of Engineering (University of Porto) in 2021, with the financial support provided by Programa Propio de I+D+i 2021 de la Universidad Politécnica de Madrid. This work is part of the R&D&I Project PID2020-112954RA-I00 funded by MCIN/AEI/10.13039/501100011033. The authors gratefully acknowledge Fundação para a Ciência e a Tecnologia (FCT-MCTES) for the financial support of the Laboratório Associado de Energia, Transportes e Aeronáutica (LAETA) by the project UID/EMS/50022/2020 and the Research and Development Unit for Mechanical and Industrial Engineering (UNIDEMI) by the projects UIDB/00667/2020 and UIDP/00667/2020.

Institutional Review Board Statement: Not applicable.

Informed Consent Statement: Not applicable.

Data Availability Statement: The original contributions presented in the study are included in the article material, further inquiries cab be directed to the corresponding author/s.

Conflicts of Interest: The authors declare no conflict of interest.

References

1. Gustavsson, L.; Sathre, R. Variability in Energy and Carbon Dioxide Balances of Wood and Concrete Building Materials. *Build. Environ.* **2006**, *41*, 940–951. [CrossRef]
2. UNEP. *Buildings and Climate Change: Summary for Decision-Makers*; UNEP DTIE, Sustainable Consumption & Production Branch: Paris, France, 2009; ISBN 987-9-28073-064-7.
3. Buchanan, A.H.; Honey, B.G. Energy and Carbon Dioxide Implications of Building Construction. *Energy Build.* **1994**, *20*, 205–217. [CrossRef]
4. Sathre, R.; Gustavsson, L. Using Wood Products to Mitigate Climate Change: External Costs and Structural Change. *Appl. Energy* **2009**, *86*, 251–257. [CrossRef]
5. UNECE; FAO. *Circularity Concepts in Wood Construction*; United Nations Publication: Geneva, Switzerland, 2023; ISBN 978-9-21117-328-4.
6. Aicher, S.; Christian, Z.; Dill-Langer, G. Hardwood Glulams—Emerging Timber Products of Superior Mechanical Properties. In Proceedings of the World Conference on Timber Engineering (WCTE), Quebec City, QC, Canada, 10–14 August 2014.
7. Camú, C.T.; Aicher, S. A Stochastic Finite Element Model for Glulam Beams of Hardwoods. In Proceedings of the World Conference on Timber Engineering, Seoul, Republic of Korea, 20–23 August 2018.
8. De Rigo, D.; Caudullo, G. Fagus Sylvatica in Europe: Distribution, Habitat, Usage and Threats. In *European Atlas of Forest Tree Species*; Publication Office of the European Union: Luxembourg, 2016; pp. 94–95, ISBN 978-9-27617-291-8.
9. Antonucci, S.; Santopuoli, G.; Marchetti, M.; Tognetti, R.; Chiavetta, U.; Garfì, V. What Is Known About the Management of European Beech Forests Facing Climate Change? A Review. *Curr. For. Rep.* **2021**, *7*, 321–333. [CrossRef]
10. Gómez-Royuela, J.L.; Majano-Majano, A.; Lara-Bocanegra, A.J.; Reynolds, T.P.S. Determination of the Elastic Constants of Thermally Modified Beech by Ultrasound and Static Tests Coupled with 3D Digital Image Correlation. *Constr. Build. Mater.* **2021**, *302*, 124270. [CrossRef]
11. Ozyhar, T.; Hering, S.; Niemz, P. Viscoelastic Characterization of Wood: Time Dependence of the Orthotropic Compliance in Tension and Compression. *J. Rheol.* **2013**, *57*, 699–717. [CrossRef]
12. Ozyhar, T.; Hering, S.; Sanabria, S.J.; Niemz, P. Determining Moisture-Dependent Elastic Characteristics of Beech Wood by Means of Ultrasonic Waves. *Wood Sci. Technol.* **2013**, *47*, 329–341. [CrossRef]
13. Ozyhar, T.; Hering, S.; Niemz, P. Moisture-Dependent Orthotropic Tension-Compression Asymmetry of Wood. *Holzforschung* **2013**, *67*, 395–404. [CrossRef]
14. Ozyhar, T.; Hering, S.; Niemz, P. Moisture-Dependent Elastic and Strength Anisotropy of European Beech Wood in Tension. *J. Mater. Sci.* **2012**, *47*, 6141–6150. [CrossRef]

15. Widmann, R.; Fernandez-Cabo, J.L.; Steiger, R. Mechanical Properties of Thermally Modified Beech Timber for Structural Purposes. *Eur. J. Wood Wood Prod.* **2012**, *70*, 775–784. [CrossRef]
16. Franke, S.; Magnière, N. The Embedment Failure of European Beech Compared to Spruce Wood and Standards. In *Materials and Joints in Timber Structures*; Aicher, S., Reinhardt, H.-W., Garrecht, H., Eds.; RILEM Bookseries; Springer: Dordrecht, The Netherlands, 2014; pp. 221–229, ISBN 978-9-40077-810-8.
17. Gómez-Royuela, J.L.; Majano-Majano, A.; Lara-Bocanegra, A.J.; Xavier, J.; de Moura, M.F.S.F. Evaluation of R-Curves and Cohesive Law in Mode I of European Beech. *Theor. Appl. Fract. Mech.* **2022**, *118*, 103220. [CrossRef]
18. Gómez-Royuela, J.L.; Majano-Majano, A.; Lara-Bocanegra, A.J.; Xavier, J.; de Moura, M.F.S.F. Shear Traction-separation Laws of European Beech under Mode II Loading by 3D Digital Image Correlation. *Wood Sci. Technol.* **2022**, *56*, 1631–1655. [CrossRef]
19. Ehrhart, T.; Steiger, R.; Frangi, A. European Beech Glued Laminated Timber. *Bautechnik* **2021**, *98*, 104–114. [CrossRef]
20. Blass, H.; Frese, M.; Enders-Comberg, M. Beech LVL—High Strength Material for Engineered Timber Structures. In *Structures and Architecture: Beyond Their Limits*, 1st ed.; Cruz, P.J., Ed.; CRC Press: Boca Raton, FL, USA, 2016; pp. 102–109. ISBN 978-1-31573-076-9.
21. Lara-Bocanegra, A.J. Láminas Reticulares de Madera Deformadas Elásticamente. Del Material a La Construcción (In English: Elastic Timber Gridshells. From Material to Construction). Ph.D. Thesis, Universidad Politécnica de Madrid, Madrid, Spain, 2022. [CrossRef]
22. Caldeira, T. Caracterização Experimental e Numérica Do Comportamento Frágil de Ligações Com Cavilhas Em Estruturas de Madeira (In English: Experimental and Numerical Characterisation of the Brittle Behaviour of Dowel Connections in Timber Structures). Ph.D. Thesis, Universidade de Trás-os-Montes e Alto Douro, Vila Real, Portugal, 2011.
23. Franke, S.; Franke, B.; Heubuch, S.; Frangi, A.; Jockwer, R. *Anschlüsse in Buchenholz. Ermittlung von Grundlagen Zur Bemessung von Anschlüssen Für Die Marktimplementierung in Der Schweiz*; Berner Fachhochschule: Bern, Switzerland, 2019; ISBN 978-3-90687-806-5.
24. *EN 1995-1-1*; Eurocode 5: Design of Timber Structures. Part 1-1: General. Common Rules and Rules for Buildings. European Committee for Standardization: Brussels, Belgium, 2016.
25. Johansen, K.W. Theory of Timber Connections. *Int. Assoc. Bridge Struct. Eng.* **1949**, *9*, 249–262.
26. Van der Put, T.A.C.M. Tension Perpendicular to the Grain at Notches and Joints. In Proceedings of the International Council for Research and Innovation in Building and Construction (CIB-W18), Lisbon, Portugal, 10–14 September 1990.
27. Van der Put, T.A.C.M.; Leitjen, A.J.M. Evaluation of Perpendicular to Grain Failure of Beams Caused by Concentrated Loads of Joints. In Proceedings of the International Council for Research and Innovation in Building and Construction (CIB-W18), Delft, The Netherlands, 28–30 August 2000.
28. Jensen, J.L.; Quenneville, P. Splitting of Beams Loaded Perpendicular to Grain by Connections. Some Issues with EC5. In Proceedings of the International Council for Research and Innovation in Building and Construction (CIB-W18), Alghero, Italy, 29 August–1 September 2011.
29. Ballerini, M. A New Set of Experimental Tests on Beams Loaded Perpendicular to Grain by Dowel Type Joints. In Proceedings of the International Council for Research and Innovation in Building and Construction (CIB-W18), Graz, Austria, 23–25 August 1999.
30. Möhler, K.; Lautenschläger, R. *Großflächige Queranschlüsse Bei Brettschichtholz*; Forschungsbericht des Lehrstuhls für Ingenieurholzbau und Baukonstruktionen, Univ. Karlsruhe: Karlsruhe, Germany, 1978.
31. Möhler, K.; Siebert, W. *Ausbildung von Queranschlüssen Bei Angehängten Lasten an Brettschichtholzträger*; Forschungsbericht des Lehrstuhls für Ingenieurholzbau und Baukonstruktionen, Univ. Karlsruhe: Karlsruhe, Germany, 1980.
32. Ehlbeck, J.; Görlacher, R. *Tragverhalten von Queranschlüssen Mittels Stahlblechformteilen, Insbesondere Balkenschuhen, Im Holzbau*; Forschungsbericht der Versuchsanstalt für Stahl, Holz und Steine, Abt. Ingenieurholzbau, Univ. Karlsruhe: Karlsruhe, Germany, 1983.
33. Ballerini, M. Beams Transversally Loaded by Dowel-Type Joints: Influence on Splitting Strength of Beam Thickness and Dowel Size. In Proceedings of the International Council for Research and Innovation in Building and Construction (CIB-W18), CO, USA, 11–14 August 2003.
34. Schoenmakers, J.C.M. Fracture and Failure Mechanisms in Timber Loaded Perpendicular to the Grain by Mechanical Connections. Ph.D. Thesis, Technische Universiteit Eindhoven, Eindhoven, The Netherlands, 18 May 2010.
35. Jensen, J.L.; Girhammar, U.A.; Quenneville, P.; Källsner, B. Splitting of Beams Loaded Perpendicular to Grain by Connections: Simple Fracture Mechanics Models. In Proceedings of the World Conference on Timber Engineering (WCTE), Auckland, New Zealand, 15–19 July 2012.
36. Leijten, A.J.M. Splitting of Timber Beams Caused by Perpendicular to Grain Forces of Multiple Connections. *Eng. Struct.* **2018**, *171*, 10–14. [CrossRef]
37. Franke, S.; Franke, B.; Quenneville, P. Analysis of the Failure Behaviour of Multiple Dowel-Type Connections Loaded Perpendicular to the Grain in LVL. In Proceedings of the World Conference on Timber Engineering (WCTE), Auckland, New Zealand, 16–19 July 2012.
38. Hindman, D.P.; Finkenbinder, D.E.; Loferski, J.R.; Line, P. Strength of Sawn Lumber and Wood Composite Dowel Connections Loaded Perpendicular to Grain. I: NDS Design Equations. *J. Mater. Civ. Eng.* **2010**, *22*, 1217–1225. [CrossRef]
39. Patel, M.C.; Hindman, D.P. Comparison of Single- and Two-Bolted LVL Perpendicular-to-Grain Connections. I: National Design Specification for Wood Construction Equations. *J. Mater. Civ. Eng.* **2012**, *24*, 339–346. [CrossRef]
40. Majano-Majano, A.; Lara-Bocanegra, A.J.; Xavier, J.; Guaita, M. Splitting Capacity of Eucalyptus Globulus Beams Loaded Perpendicular to the Grain by Connections. *Mater. Struct.* **2022**, *55*, 147. [CrossRef]

41. Franke, B.; Quenneville, P. Analyses of the Failure Behaviour of Transversely Loaded Dowel Type Connections in Wood. In Proceedings of the World Conference on Timber Engineering (WCTE), Trentino, Italy, 20–24 June 2010.
42. Dourado, N.; Silva, F.G.A.; de Moura, M.F.S.F. Fracture Behavior of Wood-Steel Dowel Joints under Quasi-Static Loading. *Constr. Build. Mater.* **2018**, *176*, 14–23. [CrossRef]
43. Shi, D.; Huang, H.; Li, N.; Liu, Y.; Demartino, C. Bolted Steel to Laminated Timber and Glubam Connections: Axial Behavior and Finite-Element Modeling. *Int. J. Mech. Sci.* **2023**, *252*, 108364. [CrossRef]
44. Boström, L. Method of Determination of the Softening Behaviour of Wood and the Applicability of a Nonlinear Fracture Mechanics Model. Ph.D. Thesis, Lund University, Lund, Sweden, 1992.
45. Franke, S.; Franke, B.; Magnière, N. Load Carrying Capacity of Cracked Beams. In Proceedings of the World Conference on Timber Engineering (WCTE), Vienna, Austria, 22–25 August 2016.
46. Jensen, J.L.; Gustafsson, P.J.; Larsen, H.J. A Tensile Fracture Model for Joints with Rods or Dowels Loaded Perpendicular to Grain. In Proceedings of the International Council for Research and Innovation in Building and Construction (CIB-W18), Colorado, CO, USA, 11–14 August 2003.
47. Franke, B.; Quenneville, P. Design Approach for the Splitting Failure of Dowel-Type Connections Loaded Perpendicular to Grain. In Proceedings of the International Council for Research and Innovation in Building and Construction (CIB-W18), Vancouver, BC, Canada, 26–29 August 2013.
48. *DIN 4074-5:2008*; Strength Grading of Wood-Part 5: Sawn Hard Wood. DIN: Berlin, Germany, 2008. (In German)
49. *EN 1912:2012*; Structural Timber. Strength Classes. Assignment of Visual Grades and Species. European Committee for Standardization: Brussels, Belgium, 2012.
50. *EN 13183-1:2002*; Moisture Content of a Piece of Sawn Timber. Part 1: Determination by Oven Dry Method. European Committee for Standardization: Brussels, Belgium, 2002.
51. *EN 408:2010+A1:2012*; Timber Structures. Structural Timber and Gluedlaminated Timber. Determination of Some Physical and Mechanical Properties. European Committee for Standardization: Brussels, Belgium, 2012.
52. *EN 384:2016+A1*; Structural Timber. Determination of Characteristic Values of Mechanical Properties and Density. European Committee for Standardization: Brussels, Belgium, 2019.
53. *ABAQUS 2021 Documentation*; Dassault Systèmes Simulia Corp.: Johnston, RI, USA, 2021.
54. Gonçalves, J.P.M.; de Moura, M.F.S.F.; de Castro, P.M.S.T.; Marques, A.T. Interface Element Including Point-to-surface Constraints for Three-dimensional Problems with Damage Propagation. *Eng. Comput.* **2000**, *17*, 28–47. [CrossRef]
55. Franke, B.; Quenneville, P. Numerical Modeling of the Failure Behavior of Dowel Connections in Wood. *J. Eng. Mech.* **2011**, *137*, 186–195. [CrossRef]
56. McKenzie, W.M.; Karpovich, H. The Frictional Behaviour of Wood. *Wood Sci. Technol.* **1968**, *2*, 139–152. [CrossRef]
57. Durão, L.M.P.; de Moura, M.F.S.F.; Marques, A.T. Numerical Simulation of the Drilling Process on Carbon/Epoxy Composite Laminates. *Compos. Part A Appl. Sci. Manuf.* **2006**, *37*, 1325–1333. [CrossRef]
58. Silva, F.G.A.; de Moura, M.F.S.F.; Dourado, N.; Xavier, J.; Pereira, F.A.M.; Morais, J.J.L.; Dias, M.I.R. Mixed-Mode I+II Fracture Characterization of Human Cortical Bone Using the Single Leg Bending Test. *J. Mech. Behav. Biomed. Mater.* **2016**, *54*, 72–81. [CrossRef]
59. Davila, C.; Camanho, P.; de Moura, M.F. Mixed-Mode Decohesion Elements for Analyses of Progressive Delamination. In Proceedings of the 19th AIAA Applied Aerodynamics Conference, Reston, VA, USA, 16–19 April 2001.
60. Jockwer, R.; Dietsch, P. Review of Design Approaches and Test Results on Brittle Failure Modes of Connections Loaded at an Angle to the Grain. *Eng. Struct.* **2018**, *171*, 362–372. [CrossRef]
61. Jensen, J.L.; Quenneville, P.; Girhammar, U.A.; Källsner, B. Brittle Failures in Timber Beams Loaded Perpendicular to Grain by Connections. *J. Mater. Civ. Eng.* **2015**, *27*, 4015026. [CrossRef]
62. Leijten, A.J.M.; Jorissen, A.J.M. Splitting Strength of Beams Loaded by Connections Perpendicular to Grain, Model Validation. In Proceedings of the International Council for Research and Innovation in Building and Construction (CIB-W18), Venice, Italy, 22–24 August 2001.
63. Jensen, J.L. Splitting Strength of Beams Loaded by Connections. In Proceedings of the International Council for Research and Innovation in Building and Construction (CIB-W18), CO, USA, 11–14 August 2003.
64. Jensen, J.L. Splitting Strength of Beams Loaded Perpendicular to Grain by Dowel Joints. *J. Wood Sci.* **2005**, *51*, 480–485. [CrossRef]
65. Ballerini, M. A New Prediction Formula for the Splitting Strength of Beams Loaded by Dowel-Type Connections. In Proceedings of the International Council for Research and Innovation in Building and Construction (CIB-W18), Edinburgh, Scotland, 31 August–3 September 2004.
66. Habkirk, R.; Quenneville, J.H.P. Bolted Wood Connections Loaded Perpendicular-to-Grain: Effect on Wood Species. In Proceedings of the World Conference on Timber Engineering (WCTE), Portland, OR, USA, 6–10 August 2006.
67. Reshke, R.G. Bolted Timber Connections Loaded Perpendicular-to-Grain. Influence of Joint Configuration Parameters on Strength. Ph.D. Thesis, Royal Military College of Canada, Kingston, ON, Canada, 11 May 1999.
68. Yasumura, M. Criteria for Damage and Failure of Dowel-Type Joints Subjected To Force Perpendicular To the Grain. In Proceedings of the International Council for Research and Innovation in Building and Construction (CIB-W18), Venice, Italy, 22–24 August 2001.

69. Jensen, J.L.; Quenneville, P.; Girhammar, U.A.; Källsner, B. Beams Loaded Perpendicular to Grain by Connections—Combined Effect of Edge and End Distance. In Proceedings of the International Council for Research and Innovation in Building and Construction (CIB-W18): Meeting Forty-Five, Växjö, Sweden, 27–30 August 2012. CIB-W18/45-7-2.
70. Kasim, M.; Quenneville, P. Effect of Row Spacing on the Capacity of Bolted Timber Connections Loaded Perpendicular-to-Grain. In Proceedings of the International Council for Research and Innovation in Building and Construction (CIB-W18), Kyoto, Japan, 16–19 September 2002.

Anexo A. Resumen de los fundamentos teóricos

A.1. Propiedades resistentes y criterios de fallo

El comportamiento resistente de la madera depende completamente del tipo de solicitación y del ángulo que forma ésta con la dirección de las fibras. En consecuencia, la resistencia de la madera a esfuerzos en la dirección paralela a la fibra (L) es muy alta, pero muy débil en las direcciones perpendiculares (R, T). Esta diferencia de resistencia queda reflejada en la Figura A.1.1, la cual muestra las formas típicas de la relación constitutiva para cargas de tracción y compresión en las tres direcciones de ortotropía. En general, estas curvas se caracterizan por tener una rama inicial lineal donde el material se comporta de manera elástica y por tanto hay proporcionalidad entre las tensiones (σ) y las deformaciones (ε), una rama intermedia curvilínea donde el material desarrolla un comportamiento no lineal hasta que alcanza la tensión máxima en el pico de la curva y una rama final posterior al fallo del material. Esta última se ha identificado con una línea a trazos en la Figura A.1.1 cuya forma depende del tipo de esfuerzo.

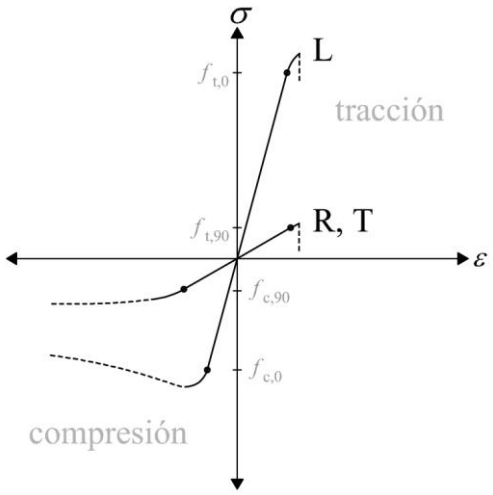

Figura A.1.1: Curvas tensión deformación del comportamiento habitual de la madera sometida a carga uniaxial (Adaptada de (Danielsson, 2013)).

Ante solicitaciones de compresión paralela y perpendicular a la fibra la respuesta del material es elastoplástica, identificándose muy bien las tres ramas de la curva y desarrollando una descarga suave después del fallo. Sin embargo, ante solicitaciones de tracción, la madera manifiesta una rotura mucho más frágil y suele desarrollar una pequeña región de comportamiento no lineal antes del fallo, así como una caída abrupta de la resistencia tras el fallo. El punto donde la curva inicial se desvía de una línea recta se conoce como límite de proporcionalidad o límite elástico $f_{j,\mathrm{L}}$, $f_{j,\mathrm{R}}$ y $f_{j,\mathrm{T}}$ donde el subíndice j representa tracción (j = t) o compresión (j = c). En la práctica no se suele hacer distinción entre la dirección R y T, siendo más habitual utilizar la notación $f_{j,i}$, donde i indica el ángulo que forma la tensión con la dirección de la fibra (i = 0 (L), i = 90 (R, T)).

Al diseñar elementos estructurales de madera, normalmente se utiliza un análisis de tensión en régimen elástico y lineal junto con un criterio de rotura basado en la tensión. En consecuencia, se asume que la resistencia del material cae a cero una vez que se alcanza el criterio de rotura. No obstante, en la modelización del comportamiento no lineal a escala macro, los criterios de rotura se utilizan para indicar

el inicio del daño del material y, por lo tanto, introducir endurecimiento o ablandamiento en el material aplicando la teoría de la plasticidad o teorías relacionadas con la mecánica de fractura no lineal, la cual se emplea en esta tesis. En la literatura existen numerosas propuestas de criterios de rotura basados en tensiones. A continuación, se muestran brevemente algunos de ellos.

A.1.1.Criterio de fallo lineal

El modelo lineal es la comprobación de interacción de resistencia más sencillo para un estado de tensión biaxial en materiales ortotrópicos (Aicher & Klöck, 2001), el cual se rige por la siguiente expresión:

$$\frac{\sigma_i}{f_i}+\frac{\sigma_j}{f_j}+\frac{\tau_{ij}}{f_{ij}}=1; \qquad i\neq j; \qquad i,\ j=\mathrm{L},\mathrm{R},\mathrm{T} \tag{21}$$

siendo f_i, f_j y f_{ij} los valores de resistencia del material en el plano de ortotropía *ij*.

A.1.2.Criterio de fallo cuadrático

La mayoría de los modelos para comprobar la interacción de resistencia son polinomios cuadráticos. El más sencillo para un estado de tensión biaxial resulta en una envolvente de resistencia elipsoidal de acuerdo con (Aicher & Klöck, 2001):

$$\left(\frac{\sigma_i}{f_i}\right)^2+\left(\frac{\sigma_j}{f_j}\right)^2+\left(\frac{\tau_{ij}}{f_{ij}}\right)^2=1; \qquad i\neq j; \qquad i,\ j=\mathrm{L},\mathrm{R},\mathrm{T} \tag{22}$$

Sin embargo, este modelo no tiene en cuenta la interacción entre las tensiones normales σ_i y σ_j.

A.1.3.Criterio de Tsai-Hill

Hill (Hill, 1950) desarrolló un criterio de plastificación para materiales metálicos anisotrópicos basándose en la teoría de distorsión de energía de von Mises para materiales isotrópicos, de manera que el criterio de Hill se reduce al criterio de von Mises cuando la anisotropía es extremadamente pequeña. Posteriormente, Azzi y Tsai (Azzi & Tsai, 1965) relacionaron los parámetros del criterio de plastificación de Hill con las resistencias mecánicas en las tres direcciones principales en materiales compuestos. Como resultado, establecieron de forma general que el fallo de un material ortótropo, para casos de carga en 3D, sucedía cuando se satisface la siguiente igualdad:

$$F(\sigma_\mathrm{R}-\sigma_\mathrm{T})^2+G(\sigma_\mathrm{T}-\sigma_\mathrm{L})^2+H(\sigma_\mathrm{L}-\sigma_\mathrm{R})^2+2L\tau_{\mathrm{RT}}^2+2M\tau_{\mathrm{LT}}^2+2N\tau_{\mathrm{LR}}^2=1 \tag{23}$$

donde *F*, *G*, *H*, *L*, *M*, *N* son constantes que dependen de las resistencias del material:

$$2F = \frac{1}{f_{\mathrm{R}}^2} + \frac{1}{f_{\mathrm{T}}^2} - \frac{1}{f_{\mathrm{L}}^2}; \qquad 2G = \frac{1}{f_{\mathrm{T}}^2} + \frac{1}{f_{\mathrm{L}}^2} - \frac{1}{f_{\mathrm{R}}^2}; \qquad 2H = \frac{1}{f_{\mathrm{L}}^2} + \frac{1}{f_{\mathrm{R}}^2} - \frac{1}{f_{\mathrm{T}}^2};$$
$$2L = \frac{1}{f_{\mathrm{RT}}^2}; \qquad 2M = \frac{1}{f_{\mathrm{LT}}^2}; \qquad 2N = \frac{1}{f_{\mathrm{LR}}^2}; \tag{24}$$

Este criterio de rotura para materiales ortotrópicos asume que las resistencias a tracción y compresión del material son las mismas, por lo que presenta algunas limitaciones para su aplicación en madera. Azzi y Tsai también sugirieron una versión simplificada de la ecuación (23) para el caso de tensión plana y considerando que el material es transversalmente isotrópico, es decir, que las propiedades mecánicas en las direcciones perpendiculares (R, T) respecto de la dirección principal (L) son las mismas, de modo que:

$$\frac{\sigma_{\mathrm{L}}^2}{f_{\mathrm{L}}^2} - \frac{\sigma_{\mathrm{L}}\sigma_{\mathrm{R}}}{f_{\mathrm{L}}^2} + \frac{\sigma_{\mathrm{R}}^2}{f_{\mathrm{R}}^2} + \frac{\tau_{\mathrm{LR}}^2}{f_{\mathrm{LR}}^2} = 1 \tag{25}$$

la cual define una superficie elíptica si se cumplen las restricciones definidas.

A.1.4.Criterio de Tsai-Wu

En la teoría de von Mises se asume que una presión hidrostática infinita no cambia la forma del cuerpo. Sin embargo, esta suposición no es válida para el caso de la madera (Kasal & Leichti, 2005). Para tener en cuenta esta diferencia, Tsai y Wu (Tsai & Wu, 1971) desarrollaron un criterio de rotura definido por un polinomio cuadrático tensorial que contiene términos lineales, los cuales permiten tener en cuenta las diferentes resistencias a tracción y compresión del material en cada una de las direcciones principales, por lo que el criterio de Tsai-Wu a menudo se propone como un criterio de fallo adecuado para madera. Este criterio se puede expresar en términos de tensores de fuerza en forma polinómica con la siguiente expresión general:

$$F_{ij}\sigma_{ij} + F_{ijkl}\sigma_{ij}\sigma_{kl} = 1; \qquad i,\ j,\ k,\ l = \mathrm{L,R,T} \tag{26}$$

donde F_{ij} y F_{ijkl} son tensores de resistencia de segundo y cuarto rango, los cuales se determinan experimentalmente. Se han propuesto formas simplificadas de la expresión general, ya que ésta es demasiado compleja para su uso práctico. En el caso especial de materiales ortotrópicos sometidos a tensión plana, por ejemplo en el plano LR, la ecuación (26) se simplifica y da como resultado:

$$\left(\frac{1}{f_{\mathrm{t,L}}} - \frac{1}{f_{\mathrm{c,L}}}\right)\sigma_{\mathrm{L}} + \left(\frac{1}{f_{\mathrm{t,R}}} - \frac{1}{f_{\mathrm{c,R}}}\right)\sigma_{\mathrm{R}} + \frac{\sigma_{\mathrm{L}}^2}{f_{\mathrm{t,L}} f_{\mathrm{c,L}}} + \frac{\sigma_{\mathrm{R}}^2}{f_{\mathrm{t,R}} f_{\mathrm{c,R}}} + 2F_{\mathrm{LR}}\sigma_{\mathrm{L}}\sigma_{\mathrm{R}} + \frac{\sigma_{\mathrm{LR}}}{f_{\mathrm{LR}}} = 1 \tag{27}$$

donde los subíndices t y c se refieren a tracción y compresión respectivamente. Esta expresión define un elipsoide en el espacio de tensiones y tiene en cuenta las interacciones entre las tensiones normales. No obstante, para asegurar que la superficie es cerrada (elipsoidal) y no se abre como un hiperboloide, es necesario que se cumpla la siguiente condición de estabilidad:

$$F_{\mathrm{LL}}F_{\mathrm{RR}} - F_{\mathrm{LR}}^2 \geq 0; \qquad F_{\mathrm{ii}} = \left(\frac{1}{f_{\mathrm{t},\,i}} - \frac{1}{f_{\mathrm{c},\,i}} \right); \qquad i = \mathrm{L}, \mathrm{R} \tag{28}$$

Las resistencias del material requeridas en este modelo pueden ser determinadas fácilmente con ensayos uniaxiales. Sin embargo, el coeficiente de interacción de tensiones F_{LR} es difícil de obtener experimentalmente ya que requiere de un ensayo de carga biaxial con tensiones normales en las direcciones L y R, el cual es muy complejo de realizar con precisión en madera. Aun así, la falta de homogeneidad del material daría como resultado tanta dispersión de datos que implicaría una incertidumbre considerable en la determinación de F_{LR}. Para superar este inconveniente algunos autores han propuesto aproximaciones. Liu (Liu, 1984) basándose en las fórmulas empíricas de Hankinson (Hankinson, 1921) propuso la siguiente ecuación para determinar F_{LR}:

$$F_{\mathrm{LR}} = \frac{1}{2}\left(\frac{1}{f_{\mathrm{t,\,L}}\, f_{\mathrm{c,\,R}}} + \frac{1}{f_{\mathrm{c\,L}}\, f_{\mathrm{t,\,R}}} - \frac{1}{f_{\mathrm{LR}}^2} \right) \tag{29}$$

De modo que se satisface la condición de estabilidad dada por la ecuación (28).

A.2. Mecánica de fractura

A.2.1.Antecedentes

La resistencia de los materiales está inherentemente relacionada con los defectos presentes en los mismos. La mecánica de fractura es una rama de la mecánica de materiales que aborda explícitamente la relación entre las fisuras o defectos de un material y su resistencia, por lo que su aplicación para abordar problemas estructurales en madera parece natural, ya que las fisuras son inherentes a la madera. Aun así, el diseño de uniones de madera con clavijas no se ha basado en la mecánica de fractura, ya que las formas de mecánica de fractura disponibles hasta la década de 1980 sólo eran aplicables a materiales frágiles homogéneos, como el vidrio.

El impulso para desarrollar la teoría de mecánica de fractura lo proporcionó Inglis hace más de un siglo. En su investigación (Inglis, 1913) obtuvo la solución para determinar las tensiones originadas en el vértice de una cavidad elipsoidal de un cuerpo infinito utilizando la teoría clásica de la elasticidad y observó que las tensiones en los vértices de un agujero con forma elíptica eran finitas Figura A.2.1a. Sin embargo, tendían a infinito cuando la forma de la cavidad se aproximaba a una fisura recta Figura A.2.1b, es decir, cuanto más afilada se convertía la punta de la fisura. Este hallazgo atrajo la atención de Griffith (Griffith, 1921, 1924) quien concluyó que en presencia de una fisura, el valor de tensión no puede usarse como criterio de fallo ya que las tensiones en la punta de la fisura, teóricamente, tienden a infinito. En consecuencia, cualquier cuerpo con una discontinuidad colapsaría, independientemente de la magnitud de la carga aplicada. Esto llevó a Griffith a proponer un criterio de análisis de la estabilidad de las fisuras basado en el equilibrio energético, el cual forma las bases de la mecánica de fractura elástica y lineal (LEFM, por sus siglas en inglés *Linear Elastic Fracture Mechanics*). Este enfoque estableció que una fisura se propagaría si la energía disponible en el sistema para extender la fisura una unidad de superficie fuese igual a la energía requerida para hacerlo.

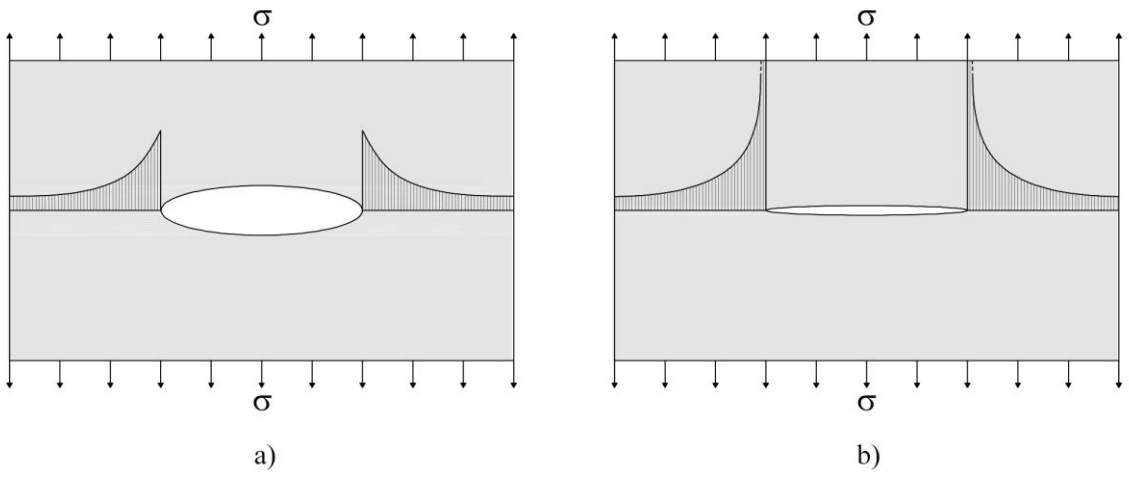

Figura A.2.1: Distribución de tensiones según la solución de Inglis: a) tensión finita en los vértices de un agujero con forma elíptica; b) tensiones que tienden a infinito cuando la cavidad se aproxima a una fisura recta.

A pesar de que los primeros trabajos de Griffith forman las bases fundamentales de la teoría de fractura moderna, inicialmente se consideraron de naturaleza muy académica ya que los modelos desarrollados sólo eran capaces de explicar adecuadamente el comportamiento de materiales muy frágiles, como el vidrio, por lo que no despertaron mucho entusiasmo en la comunidad investigadora. Sin embargo, la teoría experimentó un gran desarrollo en la segunda mitad del siglo XX estimulada, entre otras cosas, por el colapso de los cascos de los buques "Liberty" de la Marina de los Estados Unidos durante la Segunda Guerra Mundial. En ese periodo de tiempo se generalizaron las ideas de Griffith para extender su aplicación tanto a materiales dúctiles (acero) como cuasifrágiles (hormigón y madera). Estos materiales se caracterizan por desarrollar, en mayor o menor medida, mecanismos de disipación de la energía de deformación antes de romper, tales como la deformación plástica alrededor de la punta de la fisura, la fricción, la microfisuración o el puenteo de fibras. Estos avances llevaron a la mecánica de fractura a su estado actual de madurez siendo actualmente una rama muy importante de la mecánica de materiales.

Uno de los logros fundamentales en el desarrollo de LEFM se debió a Irwin (Irwin & Washington, 1957) que introdujo el concepto de factor de intensidad de tensiones (K) como un parámetro para medir la intensidad de las tensiones alrededor de la punta de la fisura y la relacionó con la tasa de liberación de energía de Griffith. Sin embargo, su aplicación se limitó a materiales elásticos y lineales, mientras que el enfoque basado en criterios de energía no.

LEFM es una herramienta básica para el análisis de muchos problemas estructurales relacionados con la propagación de fisuras. Sin embargo, poco después de asentar sus bases, se hizo evidente que sólo arrojaba buenas predicciones cuando el comportamiento del material a fractura se acercaba al idealmente frágil, es decir, el comportamiento no lineal del material debía estar limitado a una zona extremadamente pequeña localizada en la punta de la fisura permaneciendo de manera elástica, hasta el inicio de la fractura, el resto de la estructura. Por lo tanto, los materiales dúctiles o cuasifrágiles quedaban fuera del alcance de LEFM. Para superar esté inconveniente y extender la aplicación de la teoría de mecánica de fractura a materiales con comportamiento no lineal se desarrollaron varías teorías, de las cuales cabe mencionar el enfoque de los modelos de fisuras cohesivas, debido a su sencillez y aplicabilidad a la madera. Esté método ha sido propuesto bajo nombres diferentes (modelo de Dugdale-Barenblatt, modelo de fisura ficticia, modelo de fisuras puenteadas, etc.) y actualmente se conoce como modelo de zonas cohesivas (CZM, por sus siglas en inglés *Cohesive Zone Models*), el cual forma parte de lo que se conoce como mecánica de fractura no lineal (NLFM, por sus siglas en inglés *Non-Linear Fracture Mechanics*).

El CZM fue introducido por Dugdale y Barenblatt (Barenblatt, 1962; Dugdale, 1960) quienes de manera independiente desarrollaron un modelo para simular el comportamiento no lineal del material cerca de la punta de la fisura y evitar la singularidad de tensión. Aun así, el uso de la teoría de fractura o los CZMs estaba limitado a estructuras con una fisura preexistente. Sin embargo, la mecánica de fractura dio un salto considerable con el modelo de fisura ficticia desarrollado por Hillerborg *et al*. para hormigón (Hillerborg et al., 1976), ya que éste incluía reglas de iniciación de fisura y, por lo tanto, se podía aplicar a estructuras inicialmente no fisuradas. Desde su primer planteamiento se han desarrollado CZMs más elaborados para simular distintos mecanismos de fractura. Sin embargo, todos ellos comparten características comunes y, por lo tanto, se puede formular un modelo genérico de manera que cada uno de ellos se convierta en un caso particular. La primera aplicación de los CZMs en madera fue realizada por Boström (Boström, 1992) y actualmente es uno de los métodos más utilizados para analizar el comportamiento de estructuras fisuradas en madera.

A.2.2.Mecánica de fractura elástica y lineal

LEFM es la teoría básica de fractura cuyo origen se atribuye a la investigación de Griffith mencionada en el apartado anterior (Griffith, 1921). LEFM surgió como herramienta para explicar los mecanismos de fallo asociados a la propagación de fisuras preexistentes. Una característica importante de LEFM es que no se puede utilizar para predecir dónde y cuándo se producirá una fisura, pero si en la estructura existe una fisura, LEFM puede ser una buena herramienta para analizar si ésta se propagará o no.

Otro aspecto importante de LEFM es que considera que el material se comporta de manera elástica y lineal sin ninguna limitación de tensión o deformación, ya sea el material isotrópico, ortotrópico o anisotrópico. Además, aunque las cargas aplicadas en la estructura puedan ocasionar deformaciones arbitrariamente grandes sin que el material falle, en el análisis de las tensiones se adopta la teoría de pequeñas deformaciones, es decir, se aplica la ley de Hooke (Aicher et al., 2002). Sin embargo, está consideración conduce a que las tensiones y las deformaciones en la punta de la fisura sean singularmente grandes y tiendan teóricamente a infinito, tal como se muestra en la Figura A.2.2. Aun así, esto es algo que se acepta dentro de LEFM siempre y cuando la zona en proceso de fractura (FPZ, del inglés *Fracture Process Zone*), es decir, la zona de la punta de la fisura donde el material se comporta de manera no lineal sea infinitamente pequeña en comparación con la longitud real de la fisura, la distancia a los límites y los puntos donde se aplica la carga. Por lo tanto, el enfoque de LEFM puede arrojar buenas predicciones cuando el material se comporta de manera frágil. Sin embargo, cuando los mecanismos de disipación de energía en la FPZ no son despreciables, como ocurre claramente en los metales, los resultados de LEFM no serán precisos.

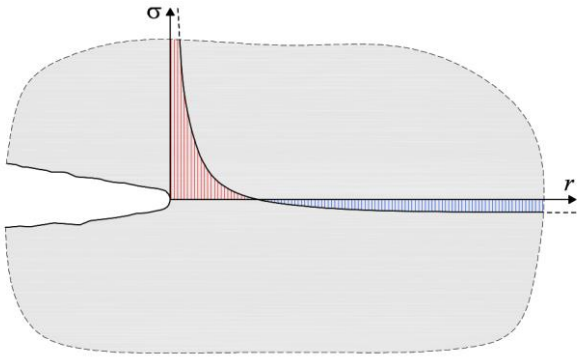

Figura A.2.2: Distribución de tensiones bajo el enfoque de la mecánica de fractura elástica y lineal.

La madera es un material que no se considera totalmente frágil sino cuasifrágil, ya que en la FPZ desarrolla mecanismos de disipación de energía que no pueden ser despreciados, tal como se verá en la sección A.2.3. Aun así, se pueden encontrar varias investigaciones sobre la aplicación de LEFM al análisis de la propagación de fisuras en vigas de madera con agujeros (Aicher et al., 1995; Riipola, 1995; Stefansson, 2001). Por otro lado, algunas de las principales normas de diseño de estructuras de madera incluyen comprobaciones de diseño basadas en LEFM. Concretamente, la comprobación de la capacidad de carga frente a la hienda de vigas cargadas perpendicularmente a la fibra mediante uniones con clavijas incluida en el Eurocódigo 5 (UNE EN 1995-1-1:2016) está basada en un enfoque de LEFM propuesto por van der Put and Leijten (Van der Put & Leijten, 2000).

Para analizar los problemas de fractura de acuerdo con LEFM existen dos enfoques: el enfoque de energía y el factor de intensidad de tensiones. A continuación, se muestra una breve visión general de ambos enfoques.

A.2.2.1.Enfoque basado en la energía

El criterio energético está basado en la suposición de que la propagación de una fisura ocurrirá si la energía disponible en el sistema para hacer crecer la fisura, la cual ha sido inducida por el sistema de cargas aplicadas, supera la resistencia del material (Anderson, 2017). De acuerdo con la primera ley de la termodinámica: cuando un sistema pasa de un estado de no equilibrio a un estado de equilibrio, se produce una disminución de la energía del sistema. Griffith aplicó esta idea en su principal contribución al estudio de la estabilidad de fisuras (Griffith, 1921) para formular una teoría de fractura basada en el balance de energía simple, de modo que la energía total del sistema (U_{Total}) puede escribirse como (Smith et al., 2003):

$$U_{\mathrm{Total}} = U_{\mathrm{e}} + U_{\mathrm{p}} + U_{\mathrm{s}} \tag{30}$$

donde U_{e} es la energía elástica de deformación, U_{s} es la energía superficial necesaria para formar la fisura y U_{p} es la energía potencial del sistema de cargas aplicadas, la cual es igual al trabajo negativo de las fuerzas aplicadas ($U_{\mathrm{p}} = -W$). Griffith concluyó que una fisura puede propagarse si la energía total de sistema disminuye o se mantiene constante. De acuerdo con esto, para un aumento infinitesimal del área de la fisura (dA) la ecuación (30) se puede expresar, en condiciones de equilibrio, de la siguiente manera:

$$\frac{dU_{\mathrm{s}}}{dA} = \frac{d}{dA}\left(W - U_{\mathrm{e}}\right) \tag{31}$$

Griffith propuso el criterio de energía para la fractura, pero Irwin es el principal responsable de desarrollar la versión actual de este enfoque. Irwin define el concepto de tasa de liberación de energía (G) de modo que la ecuación (31) puede reescribirse de la siguiente manera:

$$G = \frac{d}{dA}\left(W - U_{\mathrm{e}}\right) \tag{32}$$

Por lo tanto, G es la disminución de la energía potencial por aumento en el área de la fisura, pero también puede interpretarse como la energía disponible para hacer crecer la fisura una unidad de área, de modo que el criterio de propagación de una fisura se puede definir de acuerdo con la siguiente igualdad:

$$G = G_{\mathrm{c}} \tag{33}$$

donde G_c es la energía necesaria para hacer crecer la fisura una unidad de área. Este valor es conocido como la tasa crítica de liberación de energía, la cual es una propiedad del material. En consecuencia, la energía de fractura se puede calcular para un cuerpo cualquiera de acuerdo con la ecuación (32). Si

consideramos un cuerpo arbitrario de espesor constante (B) sometido a una carga normal al plano de fractura (P), entonces W y U_e pueden escribirse como:

$$W = P\delta; \qquad U_e = \frac{1}{2}P\delta \tag{34}$$

Combinando las ecuaciones (32) y (34) y usando la flexibilidad del cuerpo $C = \delta/P$, se obtiene una de las ecuaciones fundamentales de LEFM, conocida como la relación de Irwin-Kies (Irwin & Kies, 1954):

$$G = \frac{P^2}{2B}\frac{dC}{da} \tag{35}$$

Durante la propagación de la fisura, el valor de G proporcionado por la ecuación (35) establece la cantidad de energía necesaria (G_c) para propagar la fisura existente en el cuerpo.

A.2.2.2.Solución de Griffith

Griffith aplicó su enfoque para resolver el problema formulado por Inglis (Inglis, 1913). De acuerdo con la teoría de la elasticidad, si una fisura se propaga bajo un estado de carga constante el trabajo de las fuerzas exteriores es igual a dos veces la energía de deformación ($W = 2U_e$). Por lo tanto, la ecuación (31) puede reescribirse de la siguiente manera:

$$\frac{dU_s}{dA} = \frac{dU_e}{dA} \tag{36}$$

Griffith estableció que una fisura se propagaría si la energía disponible en el sistema para extender la fisura una unidad de superficie fuese igual a la energía requerida para hacerlo, la cual estableció en un valor igual a $2\gamma_s$, siendo γ_s la energía por unidad de superficie del material necesaria para formar una unidad nueva de área de fisura. En el caso concreto de una placa con agujero elíptico cuyo eje mayor coincide con la longitud de la fisura y de valor $2a$:

$$U_s = 4ab\gamma_s \tag{37}$$

donde a es la mitad de la longitud de fisura y b el ancho de la fisura. La solución de Inglis (Inglis, 1913) puede ser usada para resolver U_e, de modo que:

$$U_e = \frac{\pi\sigma^2 a^2 b}{E} \tag{38}$$

donde, σ es la tensión y E es el módulo de elasticidad del material. Sustituyendo las ecuaciones (37) y (38) en la ecuación (36) y siendo $dA = bda$, entonces:

$$\sigma_f = \sqrt{\frac{2E\gamma_s}{\pi a}} \tag{39}$$

Esto conduce a la determinación de la tensión de rotura (σ_f) de un sólido fisurado, la cual está directamente relacionada con la longitud de la fisura. Sin embargo, γ_s refleja la energía total de los enlaces rotos por unidad de área creada. Por lo tanto, está expresión sólo es válida para un sólido idealmente frágil, ya que en estos casos se puede propagar una fisura rompiendo sólo enlaces atómicos. Para superar esta limitación, Irwin y Orowan (Anderson, 2017) de manera independiente modificaron la expresión de Griffith para aplicarla a los metales incorporando en la ecuación (39) el comportamiento plástico:

$$\sigma_f = \sqrt{\frac{2E\,(\gamma_s + \gamma_{pl})}{\pi a}} \tag{40}$$

siendo γ_{pl} el trabajo plástico por unidad de área de superficie creada. Esto abrió la puerta a la generalización del modelo de Griffith teniendo en cuenta todo tipo de disipación de energía. Reescribiendo la ecuación (39):

$$\sigma_f = \sqrt{\frac{2E\,G_f}{\pi a}} \tag{41}$$

siendo G_f la energía de fractura, la cual puede incluir el comportamiento plástico, viscoelástico o viscoplástico. No obstante, para poder aplicar la ecuación (41), el comportamiento global de la estructura debe ser elástico, limitándose cualquier comportamiento no lineal a una pequeña zona cerca de la punta de la fisura.

A.2.2.3.Factor de intensidad de tensiones

Este criterio se basa en la suposición de que la propagación de una fisura ocurrirá si el factor de intensidad de tensiones (K) en la punta de la fisura alcanza un valor crítico (K_c).

Irwin (Irwin & Washington, 1957) basado en el método de Westergaard (Westergaard, 1939) reformuló el problema de LEFM en términos de los estados de tensión del material en las proximidades de la punta de la fisura (Figura A.2.3) en lugar de energéticamente y demostró que este enfoque era esencialmente equivalente al enfoque energético de Griffith. Además, mostró que las tensiones y desplazamientos cercanos a la punta de la fisura eran proporcionales a una constante que denominó factor de intensidad de tensiones (K), introduciendo así uno de los parámetros más relevantes de LEFM.

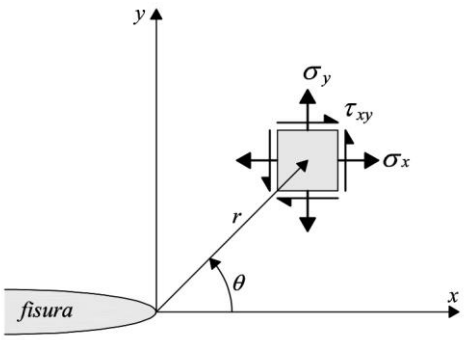

Figura A.2.3: Coordenadas de las componentes de tensión cercanas a la punta de la fisura para el caso de tensión plana.

En el caso de tensión plana y considerando el campo de tensiones mostrado en la Figura A.2.3, las tensiones en torno a la punta de la fisura de un cuerpo elástico y lineal bajo los modo de carga I y II quedan definas de acuerdo a las siguientes expresiones (Tada et al., 2000):

$$\text{Mode I} \quad \begin{cases} \sigma_x = \dfrac{K_{\mathrm{I}}}{\sqrt{2\pi r}} \cos\dfrac{\theta}{2}\left[1-\sin\dfrac{\theta}{2}\sin\dfrac{3\theta}{2}\right] \\ \sigma_y = \dfrac{K_{\mathrm{I}}}{\sqrt{2\pi r}} \cos\dfrac{\theta}{2}\left[1+\sin\dfrac{\theta}{2}\sin\dfrac{3\theta}{2}\right] \\ \tau_{xy} = \dfrac{K_{\mathrm{I}}}{\sqrt{2\pi r}} \sin\dfrac{\theta}{2}\cos\dfrac{\theta}{2}\cos\dfrac{3\theta}{2} \end{cases} \tag{42}$$

$$\text{Mode II} \quad \begin{cases} \sigma_x = -\dfrac{K_{\mathrm{II}}}{\sqrt{2\pi r}} \sin\dfrac{\theta}{2}\left[2+\cos\dfrac{\theta}{2}\cos\dfrac{3\theta}{2}\right] \\ \sigma_y = \dfrac{K_{\mathrm{II}}}{\sqrt{2\pi r}} \sin\dfrac{\theta}{2}\cos\dfrac{\theta}{2}\cos\dfrac{3\theta}{2} \\ \tau_{xy} = \dfrac{K_{\mathrm{II}}}{\sqrt{2\pi r}} \cos\dfrac{\theta}{2}\left[1-\sin\dfrac{\theta}{2}\sin\dfrac{3\theta}{2}\right] \end{cases} \tag{43}$$

donde K_{I} y K_{II} son los factores de intensidad de tensiones asociados a los modos de carga I y II, respectivamente. Estas expresiones ponen de manifiesto que los valores de tensión adoptan valores extremadamente altos cuando r tiende a 0, mostrando la singularidad de tensión en la punta de la fisura del tipo $1/\sqrt{r}$. Sin embargo, cada componente de tensión es proporcional al factor de intensidad de tensiones (K), el cual define completamente las condiciones de la punta de la fisura de un material elástico y lineal. Por lo tanto, si se conoce K es posible resolver todos los componentes de tensión, deformación y desplazamiento en función de r y θ. De acuerdo con (Brocks, 2018), el valor de K puede escribirse de manera generalizada como:

$$K = \beta\sigma_{\mathrm{R}}\sqrt{\pi a} \tag{44}$$

donde σ_{R} es la tensión nominal definida apropiadamente en el campo lejano de la fisura, a es la longitud de la fisura y β es un factor adimensional que depende de la geometría y la distribución de carga, el cual se puede determinar a partir de soluciones analíticas o numéricas. Por lo tanto, K depende de la carga aplicada, la geometría de la estructura y las condiciones de contorno. Sin embargo, K_{c}, también conocido como tenacidad a fractura, se considera una propiedad del material y define la resistencia a fractura del material. De acuerdo con esto, la fisura se propagará cuando el valor de intensidad de tensiones (K) alcanza un valor crítico (K_{c}):

$$K = K_{\mathrm{c}} \tag{45}$$

A.2.2.4.Relación entre *K* y *G*

Como se ha expuesto, existen dos parámetros fundamentales que describen el comportamiento a fractura de los materiales: la tasa de liberación de energía (G) y el factor de intensidad de tensiones (K). G describe el comportamiento global, y K es un parámetro local que caracteriza las tensiones, deformaciones y desplazamientos en torno a la punta de la fisura. A pesar de que cada parámetro se obtiene con un enfoque diferente, Irwin demostró que ambos caminos son equivalentes y consiguió relacionarlos entre sí. Para el modo de carga I y un material elástico lineal e isótropo, la relación entre ambos parámetros queda definida de la siguiente manera:

$$G = \frac{K_{\mathrm{I}}^2}{E} \tag{46}$$

En el caso especial de materiales ortotrópicos sometidos a tensión plana, por ejemplo en el plano LR, la relación para los modos de carga I y II es (Tada et al., 2000):

$$\begin{aligned} G_{\mathrm{I}} &= \frac{K_{\mathrm{I}}^2}{\sqrt{\frac{1}{2E_{\mathrm{L}}E_{\mathrm{R}}}}\sqrt{\sqrt{\frac{E_{\mathrm{L}}}{E_{\mathrm{R}}}}+\frac{E_{\mathrm{L}}}{2}\left(\frac{1}{G_{\mathrm{LR}}}-\frac{2\nu_{\mathrm{RL}}}{E_{\mathrm{R}}}\right)}} \\ G_{\mathrm{II}} &= \frac{K_{\mathrm{II}}^2}{\frac{1}{\sqrt{2}}\frac{1}{E_{\mathrm{L}}}\sqrt{\sqrt{\frac{E_L}{E_R}}+\frac{E_L}{2}\left(\frac{1}{G_{LR}}-\frac{2\nu_{RL}}{E_R}\right)}} \end{aligned} \tag{47}$$

A pesar de la similitud de ambos enfoques, el factor de intensidad de tensiones está limitado a elasticidad lineal, mientras que el concepto de tasa de energía liberada no.

A.2.3.Mecánica de fractura no lineal

La madera es un material cuyo comportamiento a rotura por tracción perpendicular a la fibra se considera frágil. Sin embargo, debido a su naturaleza fibrosa, desarrolla mecanismos de disipación de energía en la FPZ que no pueden ser despreciados, tales como el puenteo de fibras o las múltiples microfisuras, por lo que se clasifica como material cuasifrágil (de Moura & Dourado, 2018). Estos mecanismos de fractura implican que la madera no cumple con todos los requisitos necesarios para aplicar LEFM de manera rigurosa. De hecho, uno de los requisitos importantes para poder aplicar LEFM es que la FPZ debe ser lo suficientemente pequeña para que todas las no linealidades del material que puedan desarrollarse en la punta de la fisura sean despreciables. Si no se cumple esta consideración, los resultados de LEFM pueden ser imprecisos. Además, para poder aplicar LEFM es necesario que en algún punto de la estructura exista una prefisura, la cual dé lugar a una singularidad de tensión, es decir, si no hay prefisura LEFM no se debería utilizar. Sin embargo, estos inconvenientes pueden superarse aplicando el enfoque NLFM, ya que permite considerar el comportamiento no lineal del material en la FPZ mediante una relación constitutiva (ver sección 1.3.1.4) que describe los efectos de los mecanismos de ablandamiento del material. Este modelo utiliza tensiones finitas y considera una degradación progresiva de la resistencia del material en la punta de la fisura, tal como se muestra en el esquema de la Figura A.2.4.

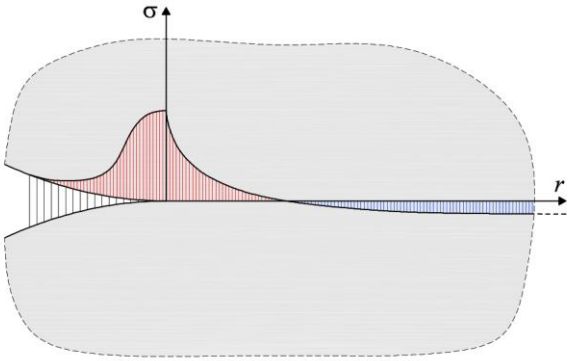

Figura A.2.4: Distribución de tensiones bajo el enfoque de la mecánica de fractura no lineal.

Una de las características más potentes de NLFM es que incluye reglas de iniciación de fisuras que permiten simular o predecir dónde y cuándo se creará una fisura dentro de una estructura y a partir de ahí analizar si ésta se propagará o no. Este aspecto es fundamental para analizar el comportamiento de estructuras de madera, ya que es un material propenso a desarrollar fisuras con frecuencia. Esta serie de ventajas hace que el enfoque NLFM sea más adecuado que el LEFM para analizar problemas en madera.

Desde su planteamiento, se han desarrollado diferentes métodos para abordar problemas de fractura bajo el enfoque de la NLFM. En este trabajo se aplica la NLFM a través de CZMs.

A.3. Bibliografía

Aicher, S., Gustafsson, P.J., Haller, P. & Petersson, H. (2002). Fracture Mechanics Models for Strength Analysis of Timber Beams with a Hole or a Notch: A Report of RILEM TC-133. Disponible online: https://lup.lub.lu.se/search/publication/127bb48d-c09b-471b-a9ff-bb6e48e03f5c.

Aicher, S. & Klöck, W. (2001). Linear versus quadratic failure criteria for in-plane loaded wood based panels. *Otto-Graf-Journal*, 12, 187–200.

Aicher, S., Schmidt, J. & Brunold, S. (1995). Design of timber beams with holes by means of fracture mechanics. En: *Proceedings of the International Council for Research and Innovation in Building and Construction (CIB-W18)*, Copenhagen, Denmark.

Anderson, T.L. (2017). Fracture Mechanics: Fundamentals and Applications (Fourth Edition). CRC Press. ISBN: 9781315370293.

Azzi, V.D. & Tsai, S.W. (1965). Anisotropic strength of composites. *Experimental Mechanics*, 5, 283–288. doi: https://doi.org/10.1007/BF02326292.

Barenblatt, G.I. (1962). The Mathematical Theory of Equilibrium Cracks in Brittle Fracture. *Advances in Applied Mechanics*, 7, 55–129. doi: https://doi.org/10.1016/S0065-2156(08)70121-2.

Boström, L. (1992). Method of determination of the softening behaviour of wood and the applicability of a nonlinear fracture mechanics model. PhD Thesis. Lund University, Sweden.

Brocks, W. (2018). Plasticity and Fracture. Springer International Publishing. ISBN: 978-3-319-62751-9.

Danielsson, H. (2013). Perpendicular to grain fracture analysis of wooden structural elements - Models and applications. PhD Thesis. Lund University, Sweden. Disponible online: https://portal.research.lu.se/en/publications/perpendicular-to-grain-fracture-analysis-of-wooden-structural-ele.

de Moura, M.F.S.F. & Dourado, N. (2018). Wood Fracture Characterization (First Edition). CRC Press. ISBN: 9781351106979.

Dugdale, D.S. (1960). Yielding of steel. *J. Mech. Phys. Solids*, 8, 100–104.

Griffith, A.A. (1921). The phenomena of rupture and flow in solids. Philosophical Transactions of the Royal Society of London. Series A, Containing Papers of a Mathematical or Physical Character, 221, 163–198. doi: https://doi.org/10.1098/rsta.1921.0006.

Griffith, A.A. (1924). The theory of rupture. En: *Proceedings of the First International Conference of Applied Mechanics*, 55–63.

Hankinson, R.L. (1921). Investigation of crushing strength of spruce at varying angles of grain. In Air Service Information Circular No. 259.

Hill, R. (1950). The Mathematical Theory of Plasticity. Clarendon Press. ISBN: 9780198503675.

Hillerborg, A., Modéer, M. & Petersson, P-E. (1976). Analysis of crack formation and crack growth in concrete by means of fracture mechanics and finite elements. *Cement and Concrete Research*, 6, 773–782.

Inglis, C.E. (1913). Stress in a plate due to the presence of cracks and sharp corners. *Spring Meetings of the Fifty-Fourth Session of the Institution of Naval Architects*, 55, 219–241.

Irwin, G.R. & Kies, J.A. (1954). Critical Energy Rate Analysis of Fracture Strength. *The Welding Journal*, 33, 193–198. Disponible online: https://archive.org/details/sim_welding-journal_1954-04_33_4/page/6/mode/1up.

Irwin, G.R. & Washington, D.C. (1957). Analysis of stresses and strains near the end of a crack traversing a plate. *Journal Applied Mechanics*, 24, 361–364.

Kasal, B. & Leichti, R.J. (2005). State of the art in multiaxial phenomenological failure criteria for wood members. *Progress in Structural Engineering and Materials*, 7, 3–13. doi: https://doi.org/10.1002/pse.185.

Liu, J. Y. (1984). Evaluation of the Tensor Polynomial Strength Theory for Wood. *Journal of Composite Materials*, 18, 216–226. doi: https://doi.org/10.1177/002199838401800302.

Riipola, K. (1995). Timber Beams with Holes: Fracture Mechanics Approach. *Journal of Structural Engineering*, 121, 225–239. doi: https://doi.org/10.1061/(ASCE)0733-9445(1995)121:2(225).

Smith, I., Landis, E. & Gong, M. (2003). Fracture and Fatigue in Wood. John Wiley & Sons Ltd, The Atrium, Chichester, England. ISBN: 0471487082.

Stefansson, F. (2001). Fracture Analysis of Orthotropic Beams. Linear Elastic and Non-Linear Methods. Disponible online: https://portal.research.lu.se/en/publications/fracture-analysis-of-orthotropic-beams-linear-elastic-and-non-lin.

Tada, H., Paris, P.C. & Irwin, G.R. (2000). The Stress Analysis of Cracks Handbook (Third Edition). ASME Press. doi: https://doi.org/10.1115/1.801535.

Tsai, S.W. & Wu, E.M. (1971). A General Theory of Strength for Anisotropic Materials. *Journal of Composite Materials*, 5, 58–80. doi: https://doi.org/10.1177/002199837100500106.

UNE-EN 1995-1-1:2016 Eurocódigo 5: Proyecto de estructuras de madera. Parte 1-1: Reglas generales y reglas para edificación. AENOR.

Van der Put, T.A.C.M. & Leijten, A.J.M. (2000). Evaluation of perpendicular to grain failure of beams caused by concentrated loads of joints. En: *Proceedings of the International Council for Research and Innovation in Building and Construction (CIB-W18)*, Delft, The Netherlands.

Westergaard, H.M. (1939). Bearing Pressures and Cracks. *Journal of Applied Mechanics*, 6, A49–A53. doi: https://doi.org/10.1115/1.4008919.

Anexo B. Listado de contribuciones relacionadas con la tesis

A continuación, se detalla el listado de contribuciones del autor realizadas durante el periodo de la Tesis Doctoral.

Artículos en revistas indexadas en JCR

1. Gómez-Royuela, J. L., Majano-Majano, A., Lara-Bocanegra, A. J., Xavier, J. & de Moura, M. F. S. F. (2024). Experimental and Numerical Research on the Splitting Capacity of European Beech Beams Loaded Perpendicular to the Grain by Connections: Influence of Different Geometrical Parameters. *Applied Sciences*, 14, 900.
   DOI: https://doi.org/10.3390/app14020900

2. Gómez-Royuela, J. L., Majano-Majano, A., Lara-Bocanegra, A. J., Xavier, J. & de Moura, M. F. S. F. (2022). Shear traction-separation laws of European beech under mode II loading by 3D digital image correlation. *Wood Science and Technology*, 56, 1631-1655.
   DOI: https://doi.org/10.1007/s00226-022-01429-3

3. Gómez-Royuela, J. L., Majano-Majano, A., Lara-Bocanegra, A. J., Xavier, J. & de Moura, M. F. S. F. (2022). Evaluation of *R*-curves and cohesive law in mode I of European beech. *Theoretical and Applied Fracture Mechanics*, 118, 103220.
   DOI: https://doi.org/10.1016/j.tafmec.2021.103220

4. Gómez-Royuela, J. L., Majano-Majano, A., Lara-Bocanegra, A. J. & Reynolds, T. P. S. (2021). Determination of the elastic constants of thermally modified beech by ultrasound and static tests coupled with 3D digital image correlation. *Construction and Building Materials*, 302, 124270.
   DOI: https://doi.org/10.1016/j.conbuildmat.2021.124270

Comunicaciones en congresos

1. Gómez-Royuela, J. L., Majano-Majano, A., Lara-Bocanegra, A. J., Xavier, J. & de Moura, M. F. S. F. (2024). Capacidad a hendido de vigas de haya cargadas perpendicularmente a la fibra mediante conexiones con pasadores: influencia de las propiedades de fractura. Congreso Ibero-Latinoamericano de la Madera en la Construcción (CIMAD 2024), Madrid, España.

2. Majano-Majano, A., Gómez-Royuela, J. L., Lara-Bocanegra, A. J. (2018). Elastic constants of thermally treated beech by ultrasound tests. World Conference on Timber Engineering (WCTE 2018), Seoul, Republic of Korea.